Imperial College of Science, Technology and Medicine
Department of Materials

# Theory and Simulation of Electronic and Optical Properties of Charged Defects in Two-Dimensional Semiconductors

Martik Aghajanian

*Submitted in partial fulfilment of the requirements for the degree of Doctor of Philosophy in the*
Centre for Doctoral Training for the Theory and Simulation of Materials
Department of Materials
Imperial College London
August 2021

# Abstract

Charged defects are frequently observed in quasi two-dimensional (2D) semiconductors such as monolayer transition-metal dichalcogenides (TMDCs) and few-layer black phosphorus (BP), and can have a significant effect on the performance of such materials in transport and optical applications. To aid the development of nanoscale devices fabricated using 2D materials, a detailed understanding of charged defects in these systems is needed. In this thesis, isolated charged defects are modelled in 2D semiconductors using the tight-binding approach which allows the use of large supercells which are required to capture the bound states that arise. The screened defect potential is described through an external potential determined via first-principles random-phase approximation. The binding energies and wavefunctions of bound states induced by charged defects in monolayer forms of $MoS_2$, $WS_2$, and BP as well as bilayer BP, were studied and the effect of varying the defect charge, defect height and the dielectric constant of possible substrates was investigated. It was found that for shallow defects in TMDCs, the binding energies of bound states can be mostly understood using effective mass theory. However, the presence of multiple low-energy valleys in the conduction and valence bands with different effective masses results in an interplay and competition between defect levels originating from different valleys. This results in resonant states that hybridise with the continuum bands, which has implications for transport, and results in the optical conductivity exhibiting excitonic resonances at energies below the optical band gap. Applying a similar analysis to monolayer BP, it was found that the substrate dielectric constant presents a promising means of control over both the donor and acceptor binding energies. In both monolayer and bilayer BP, it was found that the large difference between the armchair and zigzag effective masses of holes and electrons results in highly anisotropic wavefunctions of the defect states.

## Acknowledgements

First and foremost, I would like give my immeasurable thanks to my supervisors, Johannes and Arash, for the invaluable scientific insight, excellent academic guidance, and thoughtful advice as I carried out my work. Throughout the many projects that have filled my PhD, I have been inspired by their dedication and brilliance, which has bolstered my intrigue and motivation in the topic. I also greatly appreciate the immense patience and support they have shown me throughout my time away undertaking an internship and in the tough year that followed.

During my PhD I have had the pleasure of interacting and collaborating with a wide variety of inspiring individuals, each of which has positively influenced me and helped me along this challenging but rewarding academic adventure. I cannot begin to express how grateful I am to all my friends including those I have met at university, those from my glorious hometown of Scarborough, and those who I have had the pleasure of living with. They have helped to make my time as a PhD student the absolute thrill that it has proven to be.

Finally, I would like to thank my family whose love and support has kept me going. I am forever grateful to my wonderful mother for always being available to talk to me in times of stress, doubt or worry. I am forever thankful to my father for, throughout my life, setting for me a constant example of resilience and hard work. And I would like to give my deepest thanks to my brother, who I am very proud of, for loving me no matter what and for using his great talent as a craftsman to make our family home an even more beautiful and pleasant place to retreat to.

## Statement of Originality

I, Martik Aghajanian, confirm that the research included within this thesis is my own work or that, where it has been carried out in collaboration with, or supported by others, this is duly acknowledged and my contribution indicated. Previously published material is also acknowledged.

I attest that I have exercised reasonable care to ensure that the work is original, and does not to the best of my knowledge break any UK law, infringe any third party's copyright or other Intellectual Property Right, or contain any confidential material.

I accept that the college has the right to use plagiarism detection software to check the electronic version of this thesis.

I confirm that this thesis has not been previously submitted for the award of a degree by this or any other university. The copyright of this thesis rests with the author. Unless otherwise indicated, its contents are licensed under a Creative Commons Attribution-Non Commercial 4.0 International Licence (CC BY-NC).

Under this licence, you may copy and redistribute the material in any medium or format. You may also create and distribute modified versions of the work. This is on the condition that: you credit the author and do not use it, or any derivative works, for a commercial purpose.

When reusing or sharing this work, ensure you make the licence terms clear to others by naming the licence and linking to the licence text. Where a work has been adapted, you should indicate that the work has been changed and describe those changes. Please seek permission from the copyright holder for uses of this work that are not included in this licence or permitted under UK Copyright Law.

# Contents

**Abstract** **i**

**Acknowledgements** **iii**

**1 Introduction** **1**

1.1 Defects in Semiconductors . . . . . 1

1.2 Motivation for 2D Materials and Aims . . . . . 5

1.3 Summary of Chapters . . . . . 8

**2 Introduction to Monolayer Transition Metal Dichalcogenides** **10**

2.1 Fabrication and Devices . . . . . 11

2.2 Properties of Monolayer Transition Metal Dichalcogenides . . . . . 15

2.2.1 Modelling TMDCs with Tight-binding Models . . . . . 19

2.3 Charged Defects in Transition Metal Dichalcogenides Observed in Experiments . 23

2.4 Modelling Defects in Two-dimensional Materials . . . . . 28

2.4.1 First-principles Methods . . . . . 28

2.4.2 Tight-binding Methods to Model Charged Defects in TMDCs . . . . . 30

2.4.3 Treatment of Screening in TMDCs . . . . . 32

2.5 Optical Properties of Monolayer TMDCs . . . . . 37

2.5.1 Excitons in Pristine Crystals: Theory and Experiment . . . . . 37

2.5.2 Defect-induced Optical Properties of Monolayer TMDCs . . . . . 42

**3 Methods: Monolayer TMDCs 45**

3.1 Density Functional Theory . . . . . 46

3.1.1 Theoretical Concept . . . . . 46

3.1.2 Functionals, Pseudo-potentials and Convergence Parameters . . . . . 48

3.2 Defect Potentials . . . . . 51

3.2.1 Linear Response and the Random-Phase Approximation . . . . . 51

3.2.2 Calculating the Dielectric Function . . . . . 54

3.2.3 Screened Defect Potentials . . . . . 55

3.2.4 Substrate Screening: Doped Graphene and the Image Effect . . . . . 56

3.3 Variational Effective Mass Model . . . . . 58

3.4 Tight-Binding Calculations . . . . . 62

3.4.1 Fundamental Concept . . . . . 62

3.4.2 Constructing a Supercell . . . . . 64

3.4.3 Applying Defect Potentials . . . . . 68

3.4.4 Calculating the Electronic Properties of the Supercell Model . . . . . 70

3.5 Optical Properties and the Bethe-Salpeter Equation . . . . . 74

3.5.1 Velocity Matrix Element and Optical Conductivity . . . . . 74

3.5.2 Bethe-Salpeter Equation . . . . . 75

**4 Defects in Monolayer $MoS_2$ 80**

4.1 Electronic Structure of $MoS_2$ . . . . . 81

4.2 Screened Defect Potentials in Monolayer $MoS_2$ . . . . . 82

4.3 Wavefunctions of Defect States . . . . . 86

4.4 Theory of Defect State Binding Energies . . . . . 95

4.4.1 Acceptor State Binding Energies with Defect Charge . . . . . 96

4.4.2 Acceptor State Binding Energy with Defect Height . . . . . 100

4.4.3 Variational Effective Mass Model for Acceptor States . . . . . 101

4.4.4 Donor State Binding Energies with Defect Charge . . . . . 102

4.4.5 Variational Effective Mass Model for Donor States . . . . . 104

4.4.6 Variation of Defect Binding Energy with Substrate . . . . . 106

4.5 Local Density of States . . . . . 108

4.6 Optical Properties of Charged Defects on $MoS_2$ . . . . . 111

4.6.1 Pristine System Calculations . . . . . 111

4.6.2 Defect Cell Calculations . . . . . 114

4.6.3 Inclusion of Exchange . . . . . 117

**5 Bound and Resonant States of Charged Defects on $WS_2$ 119**

5.1 Properties of Monolayer $WS_2$ . . . . . 120

5.2 Experimentally Observed Defect States . . . . . 124

5.3 Defect States Calculated from the Tight-binding Model . . . . . 125

5.3.1 Lifetimes of Resonant States . . . . . 130

5.3.2 Sensitivity of the Binding Energies to Defect Height . . . . . 132

5.3.3 Other Defect States in the Spectrum . . . . . 133

**6 Defect States in Monolayer and Bilayer Black Phosphorus 135**

6.1 Introduction to Monolayer and Bilayer Black Phosphorus . . . . . 135

6.1.1 Electronic Properties and Applications . . . . . 135

6.1.2 Defects Observed in Few-Layer BP . . . . . 140

6.1.3 Previous Defect Modelling Approaches for BP . . . . . 142

6.1.4 Summary and Aims . . . . . 143

6.2 Methods for Studying Few-layer Black Phosphorus . . . . . 144

6.2.1 Screened Defect Potential . . . . . 145

6.2.2 Tight-binding Model . . . . . 149

6.2.3 Anisotropic Variational Effective Mass Model . . . . . 151

6.3 Results and Discussion . . . . . 152

6.3.1 Band Structure and Defect Potential . . . . . 152

6.3.2 Monolayer BP Defect Wavefunctions . . . . . 155

6.3.3 Monolayer BP Binding Energies . . . . . 158

6.3.4 Monolayer BP Local Density of States . . . . . 163

6.3.5 Bilayer BP Defect Wavefunctions . . . . . 165

6.3.6 Bilayer BP Adsorbate Binding Energies . . . . . 167

6.3.7 Bilayer BP Local Density of States . . . . . 169

**7 Conclusions and Outlook** **173**

7.1 Conclusions . . . . . 173

7.2 Further Work . . . . . 177

7.2.1 Further Study of Optical Properties of Charged Defects on Monolayer TMDCs . . . . . 177

7.2.2 Doped Systems: Formulation of Thomas-Fermi Screening . . . . . 178

**Bibliography** **180**

**A Copyright Permissions** **197**

# List of Tables

3.1 Hopping integral $T_{i,j}^{(\nu)}$ from orbitals $i$ to $j$ at different neighbouring sites connected by inter-orbital vector $\mathbf{v}$, in the monolayer $MoS_2$ model by Liu *et al.* [1], in terms of the hopping parameters of the model. . . . . 68

3.2 Values of the energy cutoff $E_{\text{cut}}^{\text{BSE}}$ used for the donor and acceptor defect calculations for the two substrates considered in the section of this work that looks at the optical properties of charged defects on monolayer $MoS_2$. . . . . 78

4.1 Effective masses $m_x^*$ and $m_y^*$ (in units of the free electron mass $m_0$) along the $k_x$ and $k_y$ reciprocal-space directions, respectively, for $MoS_2$, shown for the valence band (subscript $v$) and conduction band (subscript $c$), at valence band maxima and conduction band minima. . . . . 81

4.2 Identity of the labelled states in Fig. 4.7(a), showing the VBM in the BZ from which the state is most strongly constructed from, and the hydrogenic label of the state relating to its nodal structure. In the middle column, "Upper" and "Lower" refer to the upper and lower energy valence band in the spin-split region near $K/K'$. . . . . 95

4.3 Identity of the labelled states in Fig. 4.11(a), showing the CBM in the BZ from which the state is most strongly constructed from, and the hydrogenic label of the state relating to its nodal structure. In the middle column, "Upper" and "Lower" refer to the upper and lower energy conduction band in the spin-split region near the six $Q$ points. . . . . 103

4.4 Identity of the labelled states in Fig. Fig. 4.16(b, d) and Fig.4.17(b, d), in the form of the hydrogenic label and the band extremum/extrema from which the state is most strongly constructed from. "Upper" and "Lower" refer to the upper and lower energy in regions of the band structure where spin-splitting is significant.113

5.1 Effective masses $m_x^*$ and $m_y^*$ (in units of the free electron mass $m_0$) along the $k_x$ and $k_y$ reciprocal-space directions, respectively, for $WS_2$, shown for the valence band (subscript $v$) and conduction band (subscript $c$), at valence band maxima and conduction band minima. . . . . 120

5.2 Comparison of experimentally determined and theoretically calculated binding energies of three observed resonances: A, B, and C. Values are listed with respect to the K and Γ valence band edges. Positive binding energies indicate a lower energy with respect to the band edge [2]. . . . . 127

6.1 Effective masses at the Γ point in the Brillouin zone for Monolayer and Bilayer BP, calculated from the tight-binding models using a 4th-order accurate finite difference approximation to the second derivative of the bands. . . . . 155

# List of Figures

2.1 (a) Top view of a TMDC, with transition metal atom $M$ and chalcogen atom $X$ labelled. (b) In-plane view of TMDC. (c) Top lateral view of TMDC. . . . . 14

2.2 (a) Photoluminescence spectra, normalised by the intensity of peak A, of thin layers of $MoS_2$ for $N = 1 - 6$. Mak *et al.* [3] magnify feature I for $N = 4 - 6$ for clarity. (b) Absorption spectra of $MoS_2$ normalised by layer number (left axis, black solid) and the corresponding PL spectra (right axis, red solid), normalised by the intensity of the peak A [3]. Plots are displaced for clarity. Reprinted with permission from [3], Copyright 2010 by the American Physical Society. . . . . 16

2.3 (a) ARPES spectra of monolayer $MoSe_2$ along the $\Gamma - K$ direction in the BZ. and (b) corresponding theoretical first-principles band structure [4]. Reprinted by permission from [4], Nature 2014. . . . . 17

2.4 (a-c) Orbital projected band structures for monolayer $MoS_2$ (without spin-orbit coupling) from first-principles calculations. Symbol size is proportional to its population in corresponding state. (d,e) Orbital contribution to the (c) lowest energy conduction band and (d) highest energy valence band [5] of $WSe_2$. (f) Brillouin zone of TMDCs with high symmetry points indicated and $b_1$ and $b_2$ representing the reciprocal lattice vectors [5]. Republished with permission of the Royal Society of Chemistry, from [5]; permission conveyed through Copyright Clearance Center, Inc. . . . . 18

2.5 (a) Comparison of the tight-binding bands (red) from reference [6] and first-principles bands (blue). Republished with permission of the IOP Publishing, Ltd., from [6]; permission conveyed through Copyright Clearance Center, Inc. (b-d) Tight-binding bands (blue) for the third-nearest neighbour three-band model in reference [1] compared to first-principles calculations (red) for (b) $MoS_2$, (c) $MoSe_2$, and (d) $MoTe_2$. Reprinted with permission from [1], Copyright 2013 by the American Physical Society. . . . . 20

2.6 STM images of defects found on $MoS_2$: (a) $V_{\text{bias}} = -300$ mV images of dark halos around bright defects. (b) $V_{\text{bias}} = -20$ mV and (c) $V_{\text{bias}} = -150$ mV image of bright cluster defect with some depression. (d) $V_{\text{bias}} = -200$ mV image of two structured bright defects. (e) $V_{\text{bias}} = -1$ V image of shows ring-structured defect signatures. (f) $V_{\text{bias}} = +50$ mV image of bright defects resonances [7]. Reprinted with permission from [7], Copyright 2015 by the American Chemical Society. . . 24

2.7 High-resolution STM images of $MoSe_2$ at $V_{\text{bias}} = 1.25$ V, (a) both kinds of dominant defects (b) a single chalcogen antisite defect, and (c) a single metal vacancy defect. $\frac{\mathrm{d}I}{\mathrm{d}V_{\text{bias}}}$ curves obtained at various distances from a (d) chalcogen antisite and (e) single metal vacancy. (f) STEM imaging of metal vacancy defects [8]. Reprinted with permission from [8], Copyright 2019 by the American Chemical Society. . . . . 26

2.8 STM images of $n_1$ and $n_2$ defects on a $22 \times 22$ nm$^2$ with (a) $V_{\text{bias}} = -1.0$ V, and (b) $V_{\text{bias}} = 1.0$ V. (c) STM image of $n_2$ defect a $12 \times 12$ nm$^2$ at $V_{\text{bias}} = -1.0$ V [9]. Reprinted with permission from [9], Copyright 2020 by the American Chemical Society. . . . . 27

2.9 Comparison of the effective 2D dielectric function found from Eq. (3.19) (red) with the screening obtain from the Keldysh formalism in Eq. (2.3) (black), in (a) real-space and (b) reciprocal-space [10]. Reprinted with permission from [10], Copyright 2016 by the American Physical Society. . . . . 35

2.10 Imaginary dielectric function obtained from optical reflectance experiments by Li *et al.* [11] for (a) $MoS_2$, (b) $WS_2$, (c) $MoSe_2$, and (d) $WSe_2$ on silica substrate. Reprinted with permission from [11], Copyright 2014 by the American Physical Society. . . . . 39

2.11 Absorbance for $MoS_2$ using ab initio *GW* calculations for (a) without and (b) with the inclusion of broadening from the quasi-particle lifetimes [12]. Reprinted with permission from [12], Copyright 2013 by the American Physical Society. . . 40

2.12 (a) PL intensity at 0, 20 and 30 seconds of plasma argon bombardment. (b) Spectral weight of the defect bound excitons $X_D$, neutral excitons $X_O$ and charged excitons $X_T$ as a function of exposure time. (c) PL intensity as a function of Raman shift. (d) Normalised PL as a function of photon energy absorbed. (e) Spectral weight of the defect bound excitons $X_D$, neutral excitons $X_O$ and charged excitons $X_T$, as a function of laser power [13]. Reprinted with permission from [13], Copyright 2015 by the American Chemical Society. . . . . 42

3.1 $6 \times 6$ supercell of monolayer TMDC shown with just $M$ atoms (green circles) representing the sites in the three-band tight-binding model. The unit cell of the $MoS_2$ is shown as a black rhombus, and the first, second and third nearest neighbour hopping vectors (positive directions only) are shown in green, red and magenta, respectively. . . . . 67

3.2 Schematic of the rhombic supercell (black) shown along with the lines (red dashed) across which the defect potential is reflected within the triangular corners. 69

3.3 (left) Schematic of the band folding of reciprocal lattice vectors (grey circles), with the central circle representing the Γ point and the red dashed lines are the sectants of the hexagon. Each hexagon labelled by supercell size $N$, corresponds to the relative size of the unit cell BZ when the smallest hexagon is the supercell BZ. (right) Example of tree algorithm to determine folding points for $N = 6$, where the dashed lines are only counted for the first three sectants of the hexagonal BZ and the green circle indicates the $K/K'$ which should only be counted in two neighbouring sectants. . . . . 71

4.1 (a) Band structure along the $\Gamma KM\Gamma$ line in the $MoS_2$ Brillouin zone, along with the (b) corresponding density of states (DOS). . . . . 81

4.2 (a) Dielectric function obtained from the random-phase approximation, compared to screening in the Keldysh model. (b) Schematic for screening at different length scales. . . . . 82

4.3 Defect potential of monolayer $MoS_2$ for a $1e$ charge, derived from first principles within the random-phase approximation (a) for $d = 2$ Å compared to both the Keldysh model and the unscreened Coulomb potential (both with $d = 2$ Å), as well as (b) for multiple values of the defect height $d$. Insets show the log-log form of the potentials in the main plot. . . . . 83

4.4 (a) Defect state wavefunctions (modulus square) and (b) corresponding defect state projections for an acceptor defect on monolayer $MoS_2$ for a charge of $-0.3e$ and a defect height of $d = 2$ Å. States are labelled by their order $n_{\text{def}}$ in the defect series, with $n_{\text{def}} = 1$ being the most strongly bound. Each unique $n_{\text{def}}$ corresponds to a spin-degenerate pair of states. . . . . 87

4.5 Defect state wavefunctions (modulus square) and for a donor defect on monolayer $MoS_2$ for a charge of $0.3e$ and a defect height of $d = 2$ Å. States are labelled by their order $n_{\text{def}}$ in the defect series, with $n_{\text{def}} = 1$ being the most strongly bound. Each unique $n_{\text{def}}$ corresponds to a spin-degenerate pair of states. . . . . 93

4.6 Schematic of the hybridisation present in the conduction band of $MoS_2$ in the presence of an impurity potential. Shows a sketch of the conduction band structure at $K$ and $K'$, with zero spin-orbit coupling at the $K/K'$ points. The positive energy axis $E$ is shown in the top left. This is only shown for the $1s$ and $1s'$ states. 95

4.7 (a) Acceptor binding energies in $MoS_2$ as a function of charge size $Z$ for a defect at 2 Å above the $M$ site. The identity of the states is given in Table 4.2. (b) Acceptor binding energies of the $1s$ states from $K/K'$ and $\Gamma$ as a function of $Z$ for the same height and defect site, with power law fittings shown in the legend. All energies are referenced from the valence band maximum at $K/K'$, and $\Delta_{K\Gamma} = 0.0711$ eV is the energy difference between the valence band maxima at $\Gamma$ and $K/K'$. . . . . 96

4.8 Tight-binding band structure, where bands with spin-up (spin-down) character are in red (blue) [14]. From [14] (own) under the Creative Commons License (subfig. (a) removed). . . . . 97

4.9 Variation of binding energy of the two most strongly bound $1s$ states with defect charge $Z$, referenced to the valence band, for a defect height of (a) $d$ =1.5 Å and (b) $d$ =2.5 Å above the Mo atom. $\Delta_{K\Gamma} = 0.0711$ eV is the energy difference between the valence band maxima at $\Gamma$ and $K/K'$. . . . . 99

4.10 Binding energies as a function of charge $Z$, calculated from the variational effective mass (VEM) model. This is done for a particle in a potential $V(r)$ of a charged defect a height $d$ above the Mo atom, screened by Keldysh dielectric function $1 + r_0 q$ with $r_0 = 41.71$ Å. The particle has either a mass $m_K^*$ of the VBM at $K/K'$ or mass $m_\Gamma^*$ of the VBM at $\Gamma$. Fitting parameters to the power law $AZ^\gamma$ are also shown, with the energy difference between the $\Gamma$ and $K/K'$ maxima given as $\Delta E_{K\Gamma}$. . . . . 101

4.11 (a) Donor binding energies in $MoS_2$ as a function of charge size $Z$ for a defect at 2 Å above the $M$ site. The identity of the states is given in Table 4.3. (b) Donor binding energies of the $1s$ states from $K/K'$ and $Q$ as a function of $Z$ for the same height and defect site, with power law fittings for the $1s$ states shown in the legend. All energies are referenced from the conduction band minimum at $K/K'$. . . . . 103

4.12 Donor binding energies as a function of charge $Z$, calculated from the variational effective mass model. This is done for a particle in a potential $V(r)$ of a charged defect a height $d$ above the Mo atom, screened by Keldysh dielectric function $1 + r_0 q$ with $r_0 = 41.71$ Å. The particle has either a mass $m_K^{*(1)}$ and $m_K^{*(2)}$ of the CBM at $K/K'$. Fitting parameters to the power law $AZ^\gamma$ are also shown. . . . . 105

4.13 Variation of the defect state binding energy with substrate dielectric constant $\varepsilon_{\text{sub}}$, for (a) the $1s(K)$ and $1s(\Gamma)$ states for an acceptor defect with unit charge, and (b) the hybridised $1s$ states from $K/K'$ and $Q$ for a donor defect with unit charge. The defects in both (a) and (b) are placed 2.0 Å above the Mo atom layer. . . . . 107

4.14 (a,b) LDOS of a carbon (C) adatom on $MoS_2$ (+$SiO_2$ substrate) near the (a) valence band and (b) conduction band edge. (c,d) LDOS of a lithium (Li) adatom on $MoS_2$ (+$SiO_2$ substrate) near the (c) valence band and (d) conduction band edge. Results are shown for several distances from the impurity. In each graph, the zero of energy is set to the band edge of the unperturbed $MoS_2$ [14]. From [14] (own) under the Creative Commons License. . . . . 110

4.15 Optical conductivity of the pristine $MoS_2$ monolayer on a $SiO_2$ substrate (black) and a diamond substrate (red), using an interaction potential determined from the random-phase approximation. The optical conductivity found from exclusion of the electron-hole interaction is shown as a black dashed line. . . . . 112

4.16 (a) Optical conductivity and (b) exciton projections of monolayer $MoS_2$ on a $SiO_2$ ($\varepsilon_{sub} = 3.8$) substrate in the presence of an acceptor defect of unit charge situated $d = 2$ Å above the transition metal atom. (c) Optical conductivity and (d) exciton projections for the same setup but on a diamond ($\varepsilon_{sub} = 5.7$) substrate. The size of the blue (valence band) and red dots (conduction band) in (b, d) indicate the relative strength of the projection. . . . . 114

4.17 (a) Optical conductivity and (b) exciton projections of monolayer $MoS_2$ on a $SiO_2$ ($\varepsilon_{sub} = 3.8$) substrate in the presence of a donor defect of unit charge situated $d = 2$ Å above the transition metal atom. (c) Optical conductivity and (d) exciton projections for the same setup but on a diamond ($\varepsilon_{sub} = 5.7$) substrate. The size of the blue (valence band) and red dots (conduction band) in (b, d) indicate the relative strength of the projection. . . . . 115

4.18 Optical conductivity for a $12 \times 12$ supercell of $MoS_2$ on an $SiO_2$ substrate, in the presence of a charged acceptor defect with unit charge situated 2 Å above a Mo site, comparing the calculation with the inclusion of the exchange (black) and without exchange (red). The conductivity has not been rigidly shifted to align with the pristine case. . . . . 118

5.1 (a) Band structure along the $\Gamma - K - M - \Gamma$ line in the $WS_2$ Brillouin zone, along with the (b) corresponding density of states (DOS). . . . . 121

5.2 (a) Dielectric function for the combined system (red) of $WS_2$, which sits $z_g$ = 4.9 Å above a layer of doped graphene ($v_F = 1.15 \times 10^6$ ms$^{-1}$) which itself lies $z_s$ = 1.7 Å above a silicon carbide (SiC) substrate ($\varepsilon_{SiC} = 9.7$). This model takes into account the Lindhard screening present in the polarisation function of doped graphene and the image effect that occurs between the $WS_2$ and SiC. The dielectric function of a freestanding monolayer is also shown (black) for comparison. (b) Defect potential using the dielectric function in (a) of the combined system, for a charged defect of charge $1e$ sat $z_d$ = 2.4 Å above the transition metal layer of $WS_2$ (red), compared to the freestanding monolayer case (black) and the unscreened Coulomb case (green dashed). . . . . 122

5.3 (a-b) STS spectra of a charged defect on $WS_2$, where upward bending of the conduction band due to the negatively charged defect is indicated with a dashed white line, and the onset of the $K/K'$ and Γ valleys of pristine $WS_2$ are indicated with white dotted lines. Note that the spectra in (a) and (b) were taken on different defects. (c) STS of a CD. (d) Constant height d$I$/d$V$ of the defect corresponding to electronic states A, B, and C [2]. Reprinted with permission from [2] (own), Copyright 2020 by the American Physical Society. . . . . 123

5.4 (a),(b) Calculated local density of states of a negatively charged defect in $WS_2$ on graphene/SiC substrate. In (a), the onset of the $K/K'$ and Γ valleys are indicated by dashed lines. In (b), the defect states are labelled by their hydrogenic quantum numbers and valley. (c) Simulated STS images of defect states. (d) Projections of defect wave functions onto unperturbed $WS_2$ states [2]. Reprinted with permission from [2] (own publication), Copyright 2020 by the American Physical Society. . . . . 126

5.5 (a) Real-space wavefunctions and (b) reciprocal-space projections of the resonant defect states seen ≈ 80 meV above the Γ point. . . . . 128

5.6 (a) Schematic of the electronic structure of a negatively charged defect in $WS_2$. Shown are the primary valence band maximum at $K$ (a second degenerate maximum exists at $K'$) and the secondary maximum at $\Gamma$ as well as the bound and resonant defect states. The states labelled 1s ($K$), 1s ($\Gamma$), and 2p ($K$) correspond to the experimental features A, B, and C, respectively. (b) Schematic of the system consisting of a $WS_2$ layer on graphene on a silicon carbide substrate with a substitutional impurity with charge $Z$ [2]. Reprinted with permission from [2] (own publication), Copyright 2020 by the American Physical Society. . . . . 130

5.7 Dependence of the binding energy (measured with respect to the secondary valence band maximum at $\Gamma$) of various defect states on the parameter $z_d$ [2]. Reprinted with permission from [2] (own publication), Copyright 2020 by the American Physical Society. . . . . 133

6.1 (a) Scanning tunnelling microscopy image of the upper atoms of the topmost sublayer of BP. From [15] under the Creative Commons License. (b, c) Crystal structure of bulk BP, shown for the side view and the top view [15]. Reprinted with permission from [16], Copyright 2014 by the American Chemical Society. . 136

6.2 (a) Band structure and projected density of states (PDOS) for the $p_z$-orbitals calculated for monolayer BP by using $GW$, where the bands are coloured in accordance with their composition of $p_z$-orbitals [17]. Reprinted with permission from [17], Copyright 2016 by the American Physical Society. (b) Scanning tunnelling spectra of the black phosphorus surface, showing band gap at approximately 2 eV, with red and blue spectra found from different sublayers and marked in the STM image of the surface in the inset [18]. Reprinted with permission from [18], Copyright 2014 by the American Chemical Society. (c, d) Experimental band dispersions of bulk BP using ARPES with $s$-polarised light along the $X - \Gamma - X$ line in the BZ [19]. Reprinted with permission from [19], Copyright 2014 by the American Physical Society. . . . . 137

6.3 (a) Schematic of the BP field effect transistor and (b) field effect mobility as a function of temperature [20]. Reprinted with permission from [20], Copyright 2016 by the American Chemical Society. (b) has been adapted by removing the inset and curves corresponding to the hall mobility which are unrelated to this discussion. (c) Schematic of the BP-$MoS_2$ heterojunction $p-n$ diode, on $p+$ silicon wafer capped with $SiO_2$ as the global back gate and Ni/Au as contacts [21]. Reprinted with permission from [21], Copyright 2014 by the American Chemical Society. . . . . 139

6.4 STM images of the spatial structures of the bound hole states showing (a) an ellipse shape for the ground state and (b) dumbbell shape. (c,d) Simulated top view of the squared wave function of $1s$ and $2p_x$ states calculated using an anisotropic hydrogen-like model [22]. Reprinted with permission from [22], Copyright 2017 by the American Chemical Society. . . . . 140

6.5 (a) Crystal structure of a black phosphorus monolayer, with armchair and zigzag directions labelled. The unit cell of the pristine crystal is outlined in red. (b) Schematic of the effective charge layer in the monolayer screening model, where $d$ is the defect height from the top sublayer. (c) Schematic of the placement of the intercalated defect in bilayer BP, where $d_{\text{int}} = 2.72$ Å is the out-of-plane distance of the defect below the effective charge sheet of the top layer (red dashed). 145

6.6 Tight-binding electronic band structure of black phosphorus in (a) the monolayer and (b) bilayer structure in the Brillouin zone (BZ). Inset of (a) depicts the high symmetry points of the BZ. All energies are referenced to the valence band maximum at $\Gamma$. . . . . 153

6.7 Defect potential for monolayer BP for a charged defect sitting $d = 2$ Å above the top sublayer, shown for the top sublayer (black) and the bottom sublayer (red), compared to the unscreened potential (green dashed). Inset displays the log-log form of this figure. . . . . 154

6.8 Defect potential for bilayer BP for a charged defect placed 2 Å above the top sublayer of the top layer, shown for all four sub-layers in the system. Inset displays the log-log form of this figure. . . . . 154

6.9 Wavefunctions of the six most bound acceptor defect states on monolayer black phosphorus, from (i) to (vi) in order of decreasing binding energy. This is shown for a defect height of $d = 2$ Å above the top sublayer and $\varepsilon_{\text{sub}} = 2$. . . . . 156

6.10 Projections of the six most bound acceptor defect states on monolayer black phosphorus, from (i) to (vi) in order of decreasing binding energy. This is shown for a defect height of $d = 2$ Å above the top sublayer and $\varepsilon_{\text{sub}} = 2$. . . . . 157

6.11 Wavefunctions of the six most bound acceptor defect states on monolayer black phosphorus, from (i) to (vi) in order of decreasing binding energy. This is shown for a defect height of $d = 2$ Å above the top sublayer and $\varepsilon_{\text{sub}} = 8$. . . . . 158

6.12 Projections of the six most bound acceptor defect states on monolayer black phosphorus, from (i) to (vi) in order of decreasing binding energy. This is shown for a defect height of $d = 2$ Å above the top sublayer and $\varepsilon_{\text{sub}} = 8$. . . . . 159

6.13 (a,b) Binding energy variation of (a) donor and (b) acceptor 1s defect states with $\varepsilon_{\text{sub}}$ and $d$, extracted from the tight-binding model with isotropic defect potential. (c,d) Variational 1s energy extracted from the effective mass model inserting the effective masses of (c) the conduction band minimum and (d) the valence band maximum. (e,f) Average parabolic energy deviation $\Delta E_{\text{EMA}}$ of the 1s state for the case of (e) acceptor and (f) donor, shown as a function of substrate dielectric constant for the same defect heights as (a-d). . . . . 160

6.14 Local density of states for a charged defect a distance $d = 2$ Å above the top sublayer, for monolayer BP on a substrate with $\varepsilon_{\text{sub}} = 2$ for (a,b) acceptor defects and (c,d) donor defects. This is shown separately along the (a,c) armchair and (b,d) zigzag directions. . . . . 163

6.15 Local density of states for a charged defect a distance $d = 2$ Å above the top sublayer, for monolayer BP on a substrate with $\varepsilon_{\text{sub}} = 8$ for (a,b) acceptor defects and (c,d) donor defects. This is shown separately along the (a,c) armchair and (b,d) zigzag directions. . . . . 164

6.16 Top layer wavefunction of bilayer BP for acceptor states for a charged adsorbate with height $d = 2$ Å from the top sublayer of the top layer, in order a-e of most to least strongly bound. Binding energy is displayed in the top left, and the bottom layer wavefunction is shown in the inset. . . . . 166

6.17 Top layer wavefunction of bilayer BP for acceptor states for a charged intercalated defect placed $d_{\text{int}} = 2.7$ Å below the top effective layer, in order a-e of most to least strongly bound. Binding energy is displayed in the top left, and the bottom layer wavefunction is shown in the inset. . . . . 167

6.18 Defect energy levels as a function of defect height $d$ above the top sublayer of freestanding monolayer BP (dashed) and freestanding bilayer BP (solid) for (a) donor and (b) acceptor defects, showing the monolayer band gap (dashed) and bilayer band gap (solid). . . . . 168

6.19 Local density of states (LDOS) for a defect charge placed 2 Å above the top sublayer in the top layer of bilayer BP, shown for the acceptor case along the (a) armchair and (b) zigzag directions, and shown for the donor case along the (c) armchair and (d) zigzag directions. . . . . 170

6.20 Local density of states (LDOS) for a charged intercalated defect placed $d_{\text{int}} = 2.7$ Å below the top layer of bilayer BP, shown for the acceptor case along the (a) armchair and (b) zigzag directions, and shown for the donor case along the (c) armchair and (d) zigzag directions. . . . . 171

# Chapter 1

# Introduction

## 1.1 Defects in Semiconductors

In the theory of ideal, perfectly periodic systems, the electronic structure forms a series of bands, where the separation between the highest occupied band and lowest unoccupied band is known as the *band gap*. *Semiconductors* are non-metallic crystalline solids with a band gap small enough such that observable conductivity is present at temperatures lower than its melting point [23]. As with most idealised systems in physics, perfectly periodic semiconductors pose as an unrealistic simplification of the disordered truth of nature. In addition to the assumption of a countably infinite number of atoms, defects in these systems are critical to their stability, and occur in a material that participates in any physical process (including its own fabrication). The possible species of defects in most semiconductors can vary in their source and dimension, from substitutional point defects to vacancy line defects and stacking faults. However, their existence breaks the translational symmetry of the crystal, and can also significantly modify their electronic, thermal, mechanical, magnetic and optical properties. In this thesis, I will consider point defects, as compared to higher dimensional defects, they are highly common in semiconductor materials.

Electronically, the behaviour of a point defect in the crystal depends strongly on the species, which includes the size of the defect atom (or lack thereof), and the effective electronic valence

of the defect. For impurity atoms that have the same valence as the host atom site, known as *isovalent*, the resulting change to the electronic structure is typically one or more defect levels in the band gap, whose energy is reflective on the difference in energy of the relevant orbitals of the impurity and host atoms. In some cases, such as for GaN, isovalent substitutions of phosphorus were theoretically shown to induce deep in-gap levels which are both highly localised to the defect site and have a spatial electron distribution that conforms to the $3p$-orbital shape of the valence level of the P defect [24].

In this work I have studied the properties of charged defects, specifically defect species whose valence or effective valence (for the case of some vacancies) differs by a non-zero integer to that of the host. In semiconductors such as silicon and germanium, point defects such as substitutional phosphorus, aluminium and arsenic atoms have a different number of valence electrons in the outer shell compared to the host semiconductor [25]. Depending on the mismatch of electronic valence between the impurity and the host, this results in the impurity being able to donate electrons to the conduction band (known as a *donor*) or accept electrons from the valence band (known as an *acceptor*) upon a small thermal excitation. Due to energy differences between the valence orbitals of the impurity atom and the valence orbitals of the host atom that it replaces, the presence of these dopants typically results in the formation of an in-gap state. For example, an aluminium (Al) substitution in silicon (Si) will behave as an acceptor due to its lower valence, but will also form an unoccupied acceptor level (in the ground state) that sits above the valence band, since the empty $3p$ orbital in Al is higher (less strongly bound) than the $3p$ orbital of the host Si [25]. In the ground state of the semiconductor, the acceptor level remains unoccupied and is thus electrically neutral, while the valence band is fully occupied. For the donor case, the donor level remains occupied in the ground state and is also neutral. In laboratory conditions, it is typically the case that acceptor states and donor states are active, such that they are relinquished of their holes or electrons respectively, and the carrier is placed in an excited state. This excitation of the carrier from the defect results in a charged centre, which has an associated electrostatic potential that theoretically has a long-range (tens

of nanometres or greater) form of [26]:

$$V(\mathbf{r}) \approx \frac{-e^2}{4\pi\varepsilon_0\varepsilon|\mathbf{r}|}, \tag{1.1}$$

where $\varepsilon_0$ is the permittivity of free space and $\varepsilon$ is the relative dielectric constant of the semiconductor, which is static. While $\varepsilon$ is anisotropic for many materials, it is assumed to be isotropic in Eq. (1.1). The potential pulls back on the relinquished carriers, such that bound defect states form which can be approximated with an exciton model [23, 26]:

$$\left(-\frac{\hbar^2}{2m^*}\nabla^2 + V(\mathbf{r})\right) F(\mathbf{r}) = E_{\text{bind}} F(\mathbf{r}), \tag{1.2}$$

where $m^*$ is the effective mass of the carrier, $F$ is the envelope function of the bound state, and $E_{\text{bind}}$ is the energy of the bound state referenced from the conduction band minimum (for donors) or the valence band maximum (for acceptors), also known as the *binding energy*. The effective mass formulation in Eq. (1.2) is a valid approximation when $V(\mathbf{r})$ is slow varying and not strong enough to induce transitions that span the full band gap. The bound state energies of charged defects in bulk semiconductors are most easily predicted by substitution of Eq. (1.1) into Eq. (1.2), as this can be solved analytically in the exact same way that one solves the hydrogen model. Consequently, the bound state binding energies found from this approach are discretised, following a pattern of:

$$E_n = -\left(\frac{m^* Z^2}{\varepsilon^2}\right)\frac{13.6\text{eV}}{n^2}, \tag{1.3}$$

where $n$ is a positive integer and $Z$ is the charge of the defect. Since before the 1970s, this approach has been applied as a crude but valuable approximation to the case of charged defects in many bulk semiconductors, such as silicon (Si) and germanium (Ge). For Si and Ge, it is observed that for a variety of chemically distinct defect atoms, the ground state of the experimentally obtained defect levels does not conform to the theoretically obtained binding energies and varied with defect atom. However, for both donor and acceptor defects in silicon, the set of observed excited states that arose in the band gap exhibited a more striking similarity

to those obtained from Eq. (1.2) [27]. This demonstrated an independence of the excited defect levels from the chemical species of the defect, as the large theoretically-determined orbits would in principle make the states insensitive to electronic and structural features in the immediate vicinity of the defect [26]. This reflects on how the assumption of the defect potential in Eq. (1.1) removes all dependence of the theoretically obtained in-gap levels on the chemical nature of the defect. The true short-range behaviour of the potential associated with the defect will be substantially more dependent on which atom is being removed and/or which atom substitutes it, as well as the orbitals the doping carriers occupy at zero temperature. This is substantially more important when determining the ground state defect level, as these are typically more localised to the defect site itself, especially in the case of deep impurity states [28]. These types of problems cannot be approached with the effective mass approximation, because of a potential $V(\mathbf{r})$ which is particularly short-range (on the scale of the lattice parameter or less) such that the expansion of $V(\mathbf{r})$ and bound states in terms of Bloch states requires a larger section of the Brillouin zone with non-uniform effective mass and possibly other bands [29].

Defects are crucial to the function of some semiconductors in electronic devices such as $p-n$ junctions, field-effect transistors and photoelectric devices. The doping nature of donors and acceptors, fundamentally allows for direct control of a semiconductor's conductivity [28]. This is well-known for silicon, with groups having shown that the increase in defect concentration greatly enhances its conductivity [30]. In zinc oxide (ZnO), a favourable semiconductor for optoelectronic devices and thin-film transistors on account of its large band gap, it is found that the addition of Al defects results in $n$-doping which greatly enhances the conductivity of ZnO films, beyond the intrinsic $n$-doping present from oxygen vacancies or zinc interstitial defects [31]. It is clear that defects are important for improving desirable properties, and thus much effort has been placed in the research of ways to enhance such properties using defects, known as *defect engineering*. This method of material alteration is commonly used for fabrication of devices on the nanoscale, and has been driven by the need to control charge carrier type, carrier concentration and electrical current [32].

## 1.2 Motivation for 2D Materials and Aims

Over a decade ago, an atom-thick sheet of carbon known as graphene was experimentally isolated via repeated mechanical exfoliation of individual layers from graphite, resulting in a two-dimensional semimetal [33]. Up until the realisation of graphene, the idea of two-dimensional materials and their electronic properties had only been theorised in models for quasi-two-dimensional electronic accumulation at semiconductor-insulator interfaces [34]. It demonstrated exceptional properties for electronic applications, such as extremely high mobilities for both electrons and holes in excess of $2 \times 10^5$ cm$^2$/Vs, with easily tunable carrier concentrations [35, 36]. Since then, much work has gone into the development of graphene-base devices, such as functionalised graphene electrochemical double-layer capacitors [37], and metal-oxide-semiconductor field effect transistors (MOSFETs) [38]. In such transistors, experimental groups took advantage of graphene's high mobility and the fact that an electronic band gap could be engineered through the use of appropriately narrow nanoribbons, producing MOSFETs that have transconductances (rate of change of drain current with respect to the gate-source potential difference) comparable to state-of-the-art silicon MOSFETs [38, 39]. While graphene is promising for nanoelectronics, there are still several challenges in fabricating usable yields of graphene nanoribbons with distinct edges, and in introducing a band-gap that does not significantly impede carrier mobility [38, 40].

In addition to the work on its intrinsic properties and applications, there has been a large body of research into the effects of defects in graphene, such as vacancies and adatoms, and their ability to enhance its properties for better device functionality [41–44]. This work has led to the development of graphene-based devices, such as in transparent conductive films for photodetectors, touch screens, and light-emitting devices, in which the graphene is functionalised or doped [45]. Its versatility and strong performance in a variety of electronic and optoelectronic devices comes from a combination of flexibility and sensitivity to external surface effects, such that the correct manipulation of chemical doping and functionalisation can adapt it for specific tasks. Doping schemes in graphene are simpler than in three-dimensional systems, and the similarity of its surface chemistry to that of graphite means that it can weakly adsorb a variety

of atoms and molecules such as $NO_2$ and K, some of which act as dopants [46]. A handful of these benefits are inherent to the two-dimensional nature of graphene alone, indicating that other materials with this property may also demonstrate similar or more desirable properties for a variety of devices [47].

The discovery of materials held together by weak van der Waals (vdW) forces that could be "stripped" layer-by-layer presented an attractive avenue for materials research. This diverse collection of exfoliated, quasi-2D materials, share all the benefits of the low-dimensionality of graphene but exhibit different desirable properties for a variety of applications. One such property that is inherently lacking in graphene, and needs to be engineered, is a band-gap. Several quasi-2D materials that have been uncovered in the decade since graphene's discovery have been shown to have a sizeable, direct band-gap on the order of 100 meV or larger, which immediately makes them promising candidates for optical devices and field effect transistors. "Quasi-2D", in this context, refers to the fact that while the electrons in the material are confined to a single-layer, they are not confined to a perfect 2D plane and display some physics in the out-of-plane direction. However, they are often still referred to as "2D", as will be done in this thesis. In this work, I will focus on monolayer molybdenum disulfide ($MoS_2$), monolayer tungsten disulfide ($WS_2$), monolayer black phosphorus (BP) and bilayer BP, which are all known to be direct band-gap semiconductors with reasonably good carrier mobilities for transport applications. While their carrier mobilities are not intrinsically as high as those observed in graphene, it is possible to enhance carrier concentration and thus conductivity with intentional doping.

The effects charged defects have on the electronic structure of bulk 3D semiconductors is well known, and as a consequence, the development of microchips and sensors over the last few decades has become an essential element of technology in the modern age. Similarly, it becomes apparent that in order to efficiently develop 2D semiconductors for the purpose of future nanoscale circuits, the behaviour of defects in theses materials must factor into the design process, predominantly for charged defects which commonly arise in doping strategies. Hence, to guide experimental efforts to engineer and enhance the properties of 2D semiconductors for various transport and optoelectronic applications, a thorough understanding of how charged de-

fects behave in 2D semiconductors is needed. Simulation is a common and insightful approach to achieve this, allowing parameters and properties of the system in question to be gradually varied, which can provide a picture of the underlying principles that determine the electronic structure of charged defects in 2D semiconductors.

In this work, my general aim is to develop such an understanding by modelling isolated charged defects on samples of 2D semiconductors, and by studying the behaviour of bound states that arise in the band gap when the properties associated with both the defect and possible substrates are varied. While this will primarily focus on the adsorbate species of defects, the concepts presented and discussed apply to other charged point defects such as vacancies and substitutionals. In this work I consider several observable properties that are relevant to defect engineering and which are readily accessible in experiment. The binding energy of a defect state is a critical property to consider when engineering a material for application in devices such as $p-n$ junctions and photodetectors. Similarly, the extent of the wavefunction of the defect state can indicate how clusters of neighbouring defects interact with one another. This work aims to understand how these properties are influenced by the effective charge and height of the defect above the system, which are parameters that can vary depending on the adsorbate in question [48, 49]. Furthermore, I aim to make predictions of experimental signatures of the defect states in materials such as monolayer $MoS_2$, which can tie the findings in this work to observable quantities. For this purpose, the local density of states is a useful property for direct comparison between the results of simulation and scanning tunnelling experiments, in addition to the optical conductivity which can be measured in reflectivity experiments and is highly sensitive to the presence of defects.

A significant challenge in modelling charged defects on 2D semiconductors is the spatial range over which bound states can vary, which can be large for 2D materials on account of their reduced dimension [50]. To address this, I will present an approach that utilises tight-binding theory to model the electronic structure of a sample of a 2D semiconductor on length scales that can capture both the variation of the defect potential and the real-space behaviour of defect states. Using this approach, I aim to bridge the gap between the Ångstrom-scale description of atomic defects and features of impurity states on the order of tens of nanometres. On the

continuum scale, effective mass theories have successfully provided a framework with which to understand the electronic structure of charged defects and excitons in 3D semiconductors [29]. In this work, I define variational models for monolayer $MoS_2$ and monolayer BP within the effective mass approximation, that can be compared to the atomistic approach presented in this work. This is done with the aim of providing an insight into how well continuum models can be used for charged defects in these semiconductors across regions of the parameter space.

## 1.3 Summary of Chapters

- **Chapter 2** provides an introduction to the group of 2D semiconductors called monolayer transition metal dichalcogenides (TMDCs) and a review of literature concerning the experimental and theoretical study of charged defects in TMDCs. I attempt to further motivate the study of TMDCs and highlight shortcomings of previous attempts to model charged defects in TMDCs.

- **Chapter 3** provides details of the methods I used to model charged defects in monolayer TMDCs, including some relevant theory. This includes a review of density-functional theory, the effective mass approximation, tight-binding theory and linear response, then going on show how these were used to approximate an isolated charge in monolayer $MoS_2$ and monolayer $WS_2$.

- **Chapter 4** presents my results on the study of charged defects in monolayer $MoS_2$, which first looks into the static properties of the bound states that arise in the presence of a defect charge and how the binding energy can be controlled with the effective defect charge, the defect height, and the dielectric constant of the substrate. This ends with a brief look at how the charged defects are able to influence the optical properties of $MoS_2$.

- **Chapter 5** presents collaborative work which studied experimental signatures of defects in monolayer $WS_2$ with scanning tunnelling methods, and comparing them to tight-binding calculations to understand how the resonant states in the sample manifested in the tunnelling spectra.

- **Chapter 6** presents a literature review, discussion of methods, and discussion of results which studies the properties of charged defects in black phosphorus (BP). In this part of the investigation, charged defects are modelled in both monolayer and bilayer BP for several values of the defect height and substrate dielectric constant, applying the techniques and the understanding developed in chapters 3 and 4.

- **Chapter 7** gives conclusions of the research carried out in this thesis. This is followed by an outline of future endeavours that build on the achievements in this work.

# Chapter 2

# Introduction to Monolayer Transition Metal Dichalcogenides

This introductory section covers the topics in literature relevant to chapters 4 & 5, pertaining to the electronic and optical properties of monolayer group 6 transition metal dichalcogenides (TMDCs). To begin this chapter, I will first provide a brief overview of some of the various fabrication techniques for a particular group of monolayer TMDCs that are semiconductors, as they have been shown to have different merits relating to the quantity of the material produced and the quality of the produced samples. Fabrication techniques are in part responsible for some defect concentrations present in experimental samples, which result in different properties depending on the technique, some of which are desirable for device applications. I will also highlight how these properties relate to the performance of monolayer TMDCs in devices such as microprocessors, to motivate further study of the electronic properties of these materials in this work. I will then present a summary of the basic electronic properties of monolayer group 6 TMDCs as observed from experiment and computational modelling. I will then discuss some of the experimental study of neutral and charged defects in these materials, to both motivate their study in this work and highlight features of their effect on the properties of TMDCs. This will be followed by a discussion of the various ways these defects have been modelled, either through first-principles methods, continuum effective mass approaches, or through semi-

empirical tight-binding models, additionally outlining a particular example of modelling defects in graphene which has inspired a good portion of the work in the thesis. This example, requiring a description of the screening in the material, invokes a discussion into previous ways by which the screened Coulomb interaction in monolayer TMDCs has been modelled. Finally, I will review some of the literature concerning the optical properties of TMDCs and how defects have been observed in experiment to alter their optical response.

## 2.1 Fabrication and Devices

Monolayer transition metal dichalcogenides (TMDCs) are among the array of 2D materials that have emerged into academic focus since the advent of graphene. Bulk TMDCs consist of van der Waals (vdW) bonded monolayers, with the chemical formula $MX_2$, where $M$ is a transition metal atom and $X$ is an atom from the chalcogen column of the periodic table. Their versatility with respect to device fabrication and the strong dependence of their electronic properties on environmental modifications have driven years of intense study into both the theory of these materials and their many applications. There are several stable combinations of chalcogens (sulfur, selenium, tellurium, etc.) and transition metal atoms, resulting in a diverse range of properties in these materials. For example, monolayer TMDCs such as titanium diselenide ($TiSe_2$) are semimetals, while hafnium disulfide ($HfS_2$) is an insulator, and TMDCs such as tantalum disulfide can exhibit superconductivity in low-temperature conditions with externally applied pressure [47, 51, 52]. This arises due the variety of the occupancy of the $d$ valence orbitals within the transition metal group, and invokes a zoo of 2D materials with this chemical classification to be the subject of research showing many different desirable properties for device applications. Within this class of materials, there also exists a set of semiconducting TMDCs, known as group 6 TMDCs, which have molybdenum (Mo) or Tungsten (W) as their transition metal atom [5, 51]. While these are indirect band gap semiconductors in the bulk form, monolayers of these materials exhibit a direct band gap [5, 53].

Much like graphene, these materials can be stripped to yield a monolayer form using mechan-

ical exfoliation (ME) techniques [53]. While ME produces highly pure flakes of monolayer material, it provides no control of flake thickness and size, and is not a scalable means of synthesis. However, in experimental work, large continuous films are often required instead of flakes of uncontrolled size. Chemical exfoliation of monolayer TMDCs is also a very common method of obtaining nanosheets with a high yield and scalability [54]. By preparing TMDCs in a liquid phase, large sheets of monolayer material can be obtained, with additional benefits to flexibility of being able to create composite materials from the liquidation stage before any spray coating or inkjet printing takes place [53]. Another common form of synthesis is chemical vapour deposition (CVD), in which precursor materials are vaporised and allowed to pass over a suitable substrate where they react to form a chosen TMDC. CVD produces a high yield of randomly distributed monolayer TMDC flakes [55]. The diverse array of methods with which monolayers are synthesised brings with it varying propensities of lattice defects to form depending on the techniques used. In samples of $MoS_2$ grown through CVD, characterisation via photoluminescence revealed the presence of additional peaks below the band gap energy, caused by transitions between states associated with defects [56]. Defects have also been observed in CVD-grown sheets of $WS_2$ [57]. Electronic characterisation of these defects requires further study, both theoretically and experimentally, to understand which synthesis techniques create them in higher abundances and to explain how they change the electronic structure. Scanning tunnelling experiments and first-principles calculations have been widely performed on chalcogen vacancies, which are reported to be the most common point defects in samples of 2D TMDCs obtained through CVD or ME [58]. Conversely, transition metal antisite defects has also been found to be the dominant species in physical vapour deposition (PVD) [59].

Following fabrication, monolayer group 6 TMDCs have been shown to be a viable component for a range of applications, such as field effect transistors (FETs). The low dimensionality of these monolayers allows for more sensitive control of transport properties of gates in FETs, using external fields and surface modifications. While the carrier mobility of intrinsic TMDCs such as $MoS_2$ was found to be roughly three orders of magnitude less than that of graphene, the on-current/off-current ($I_{ON}/I_{OFF}$) ratio is remarkably high, due to a large band gap which gives rise to a low off-current [60]. $I_{ON}/I_{OFF}$ is a measure of the fractional change in current through

the FET when a current is supplied to the gate, which is important for any logical transistor in the interest of clearly distinguishing between a "1" or a "0". Also, the intrinsic defects that arise in TMDCs allow for a substantial $n$-type doping, such as in $MoS_2$. This has been demonstrated by Nipane *et al.* [61], by fabricating $n$-type (intrinsic) and $p$-type (through phosphorous implantation) transistors. Unaltered $MoS_2$ flakes exhibited strong electron conduction with an $I_{ON}/I_{OFF}$ ratio of $10^6$ assumed to be caused by intrinsic sulfur vacancies, while exhibiting a lesser $I_{ON}/I_{OFF}$ ratio of $10^2$ in the hole transport regime (with a negative gate voltage). A monolayer $MoS_2$ transistor, fabricated by Radisavljevic *et al.* [62], was shown to achieve values of $I_{ON}/I_{OFF}$ of $10^8$, compared to transistors made from bilayer graphene [63] which have been reported to achieve values of up to 100. The low mobilities that were originally found in TMDCs, such as $MoS_2$, can be readily improved using the sensitivity of quasi-two-dimensional materials to the environmental changes introduced by substrates or electrodes. Using strong insulating top-gate "high-$\kappa$" dielectrics, Radisavljevic *et al.* showed that $MoS_2$ based transistors have reasonable electron mobilities of approximately 200 $cm^2V^{-1}s^{-1}$, which compares well to that found in thin silicon films [62, 64]. In other experiments, mobilities of carriers in $MoS_2$ transistors as high as 700 $cm^2V^{-1}s^{-1}$ have been achieved with the use of scandium contacts [65]. In work by Wachter *et al.* [66], a microprocessor consisting of 115 $MoS_2$-based FETs has been produced, each with a mobility of $\sim 3$ $cm^2V^{-1}s^{-1}$ and a $I_{ON}/I_{OFF}$ of $10^8$. While this shows that monolayer TMDCs are promising candidates for next-generation microprocessing, the operating frequency of the microprocessor can be improved significantly with chemical doping [66].

Additional to the desirable transport properties of monolayer TMDCs for logic based applications, significant work has gone into the development and understanding of the optical applications of TMDCs, such as in photodetectors. The large direct optical band gap between 1 eV and 2.5 eV found in these monolayers makes them highly desirable for photonic applications that operate in the visible, near UV, and part of the IR range of the electromagnetic spectrum [67]. This is demonstrated with photodetectors constructed from $MoS_2$ that display an exceptional responsivity to light [68], far exceeding that achieved by graphene based photodetectors at the time [67]. The strong performance of $MoS_2$ in photodetection has been interpreted as originating from the existence of "band-tail" states, which are localised states close to the conduction

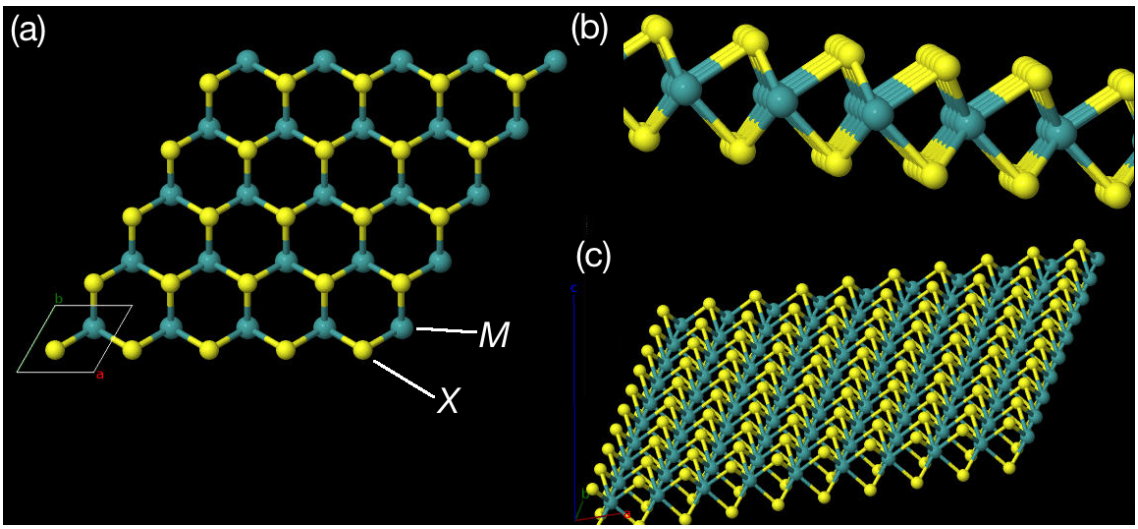



Figure 2.1: (a) Top view of a TMDC, with transition metal atom $M$ and chalcogen atom $X$ labelled. (b) In-plane view of TMDC. (c) Top lateral view of TMDC.

or valence band edge which arise from disorder and are associated with a lower mobility by inducing short-range scattering [69]. As a consequence, the trapping of electrons and holes by these states results in longer carrier lifetimes contributing to higher photoconductivity [67, 70].

In this brief overview, I have introduced the idea that depending on the synthesis technique, namely mechanical exfoliation and CVD, different concentrations of defects are present in the resulting samples. While mechanical exfoliation yields high quality samples but is not scalable, CVD can produce large amounts of samples while introducing a significant concentration of defects, such as chalcogen vacancies. For any commercial electronic device based on TMDCs, the usage of scalable techniques are a necessity and hence the study of defects is critical to the success of TMDCs in such applications. Furthermore, the understanding of their impact on a materials performance is an important and necessary step to the development of optimised and efficient nanoscale products like the above mentioned.

## 2.2 Properties of Monolayer Transition Metal Dichalcogenides

In their monolayer form, TMDCs adopt a honeycomb structure, shown in Fig. 2.1(a-c), in which the first site is occupied by an $M$ atom and the second site is occupied by two $X$ atoms aligned in the out-of-plane direction [53]. In contrast to the weaker vdW bonding holding monolayers together, strong covalent bonds hold $M$ and $X$ atoms together in the lattice, resulting in stable few-layer and monolayer samples at ambient conditions [5]. A key property of interest in monolayer TMDCs, is the large quasi-particle band gap, which can be measured as the energy needed for an electron and hole to separately tunnel into the material from a scanning tip in tunnelling experiments [5]. A common technique for analysing transition energies of emission following the absorption of a photon are photoluminescence (PL) experiments. The absorption of a photon creates an electron-hole pair which is bound together by the screened Coulomb interaction in the material [5], while the recombination of an electron and hole results in the emission of a photon. In PL experiments, the optical band gap is observed, which is the energy needed to excite an electron from the valence band maximum to the conduction band minimum. This is less than the quasi-particle band gap by an amount equal to the binding energy of this electron and the hole it leaves behind. In work by Mak *et al.* [3], the PL spectrum for monolayer $MoS_2$ shows a single peak (Fig 2.2(a), shown in red) at $\approx 1.9$ eV, contrasting with the multiple peaks seen in the bilayer case, the lowest of which being at $\approx 1.6$ eV. Furthermore, the intensity of the monolayer peak is two orders of magnitude larger than any of the bilayer PL peaks (not shown in the normalised PL spectra of Fig 2.2). This suggests that the lowest transition energy is indirect and phonon-assisted in the bilayer [3], whereas monolayer $MoS_2$ exhibits a direct optical band gap of $E_g \approx 1.9$ eV. Monolayer TMDCs have a larger band gap than their bulk counterparts because of quantum confinement and reduced screening [3]. Quantum confinement is a phenomenon that causes an electron's kinetic energy to increase when confined in the out-of-plane direction on a length scale comparable to or less than its de Broglie wavelength. Two strong peaks are observed in the absorption spectra of monolayer $MoS_2$ (Fig 2.2(b), shown in black), with the lower peak aligning with the optical band gap marked by the normalised

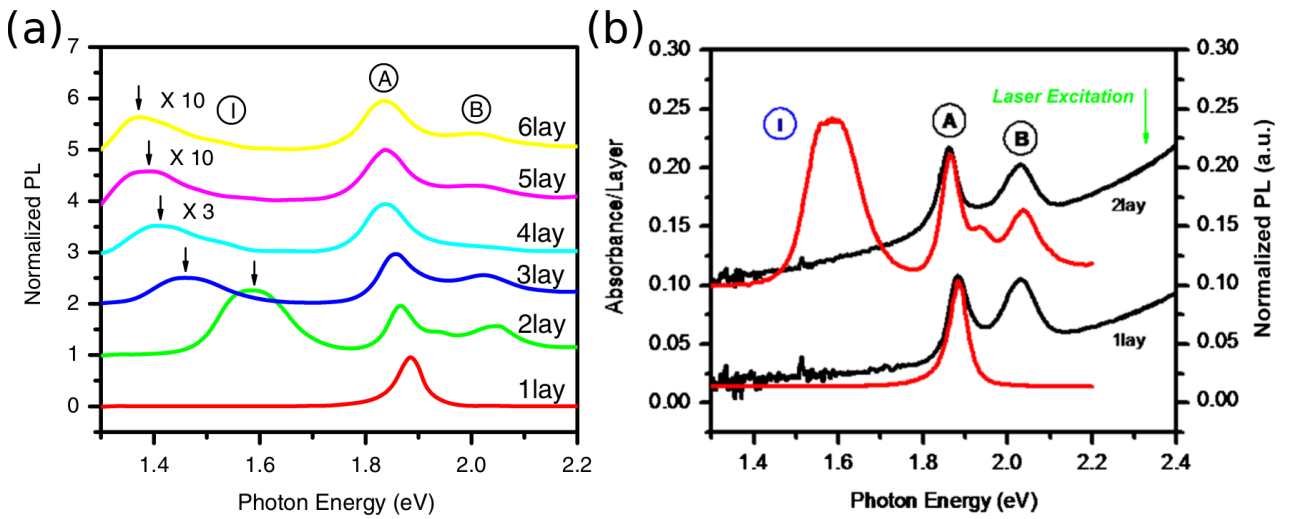



Figure 2.2: (a) Photoluminescence spectra, normalised by the intensity of peak A, of thin layers of $MoS_2$ for $N = 1-6$. Mak *et al.* [3] magnify feature I for $N = 4-6$ for clarity. (b) Absorption spectra of $MoS_2$ normalised by layer number (left axis, black solid) and the corresponding PL spectra (right axis, red solid), normalised by the intensity of the peak A [3]. Plots are displaced for clarity. Reprinted with permission from [3], Copyright 2010 by the American Physical Society.

PL peak in red [3]. In comparison, the quasi-particle band gap for suspended $MoS_2$ has been determined to be 2.5 eV [71], significantly larger than the optical band gap. Subtracting the two values gives an experimental estimate for the lowest exciton binding energy of $0.6 \pm 0.1$ eV in the monolayer system [4]. This is smaller than a binding energy of 0.96 eV that has been extracted from *GW* calculations [12].

The band structure of monolayer TMDCs has been both experimentally and computationally determined via angle-resolved photoemission spectroscopy (ARPES) and density functional theory (DFT) + *GW* calculations, respectively. ARPES experiments, performed for monolayer and multilayer $MoSe_2$ by Zhang *et al.* [4], shown in Fig. 2.3(a), demonstrate the primary VB maximum at a point labelled as $K$ in the first BZ, in the corner of the hexagonal Brillouin zone (BZ). This is in agreement with ab initio density-functional theory (DFT) shown in Fig. 2.3(b). When the system was doped with electrons, ARPES measurements found the conduction band (CB) state near $K$ are occupied, indicating that the direct band gap of $MoSe_2$ is at the $K$ point in the band structure. This is consistent with PL measurements of $MoSe_2$ and $MoS_2$ by Tongay *et al.* [72], which demonstrated large PL at low temperatures that are characteristic of a direct gap. A secondary VB maximum is found at the centre of the BZ, known as $\Gamma$, which is lower

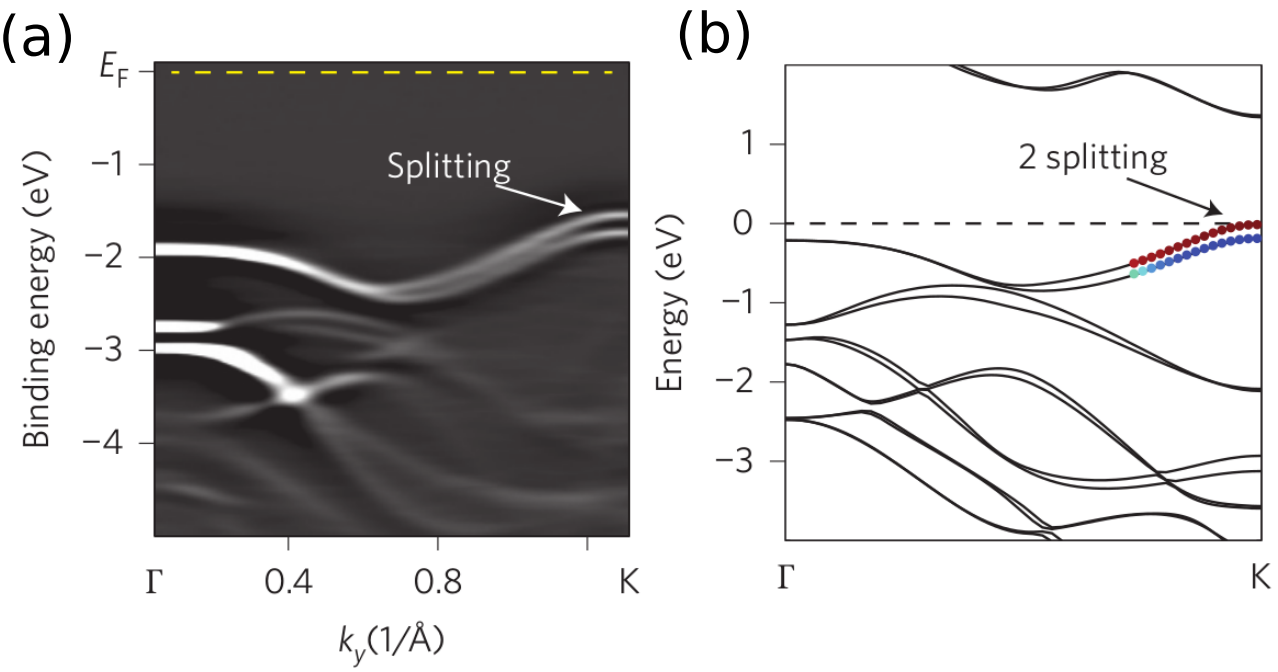



Figure 2.3: (a) ARPES spectra of monolayer $MoSe_2$ along the $\Gamma - K$ direction in the BZ. and (b) corresponding theoretical first-principles band structure [4]. Reprinted by permission from [4], Nature 2014.

in energy than that of the point $K$. Both Fig. 2.3(a) and (b) show that this maximum exhibits a much lower curvature than the primary maximum, indicating a significantly higher effective mass.

The electronic structure of monolayer $MoS_2$, as calculated from DFT, is shown in Fig 2.4(a-b) without spin-orbit splitting, with orbital contributions from the Mo-$d$ orbitals and S-$p$ orbitals indicated using coloured markers [5]. DFT calculations of monolayer $MoS_2$ in the generalised-gradient approximation (GGA) by Perdew Burke, and Ernzerhof (PBE) [73], showed that the dominant orbitals in the characterisation of the low-energy band structure are the $4d$-orbitals on the Mo atom and the $3p$-orbitals on the S atom. Contributions to the bands close to the gap from other orbitals, such as the $4p$ and $5s$ orbitals on the metal atom and $3s$ orbitals on the chalcogen, were exceptionally small. Furthermore, the direct gap at $K/K'$ is primarily characterised by the $d_{x^2-y^2}$, $d_{xy}$ and $d_{z^2}$ orbitals making them critical for the determining the low-energy physics [1,5]. This is also the case for $WSe_2$, where the orbital composition is shown in Fig. 2.4(d-e). Interestingly, the $p_z$-orbitals on the chalcogen atoms were found to be important for characterising the secondary CB minima at $Q$ and VB maximum at $\Gamma$. Since these orbitals

play a significant role in the bonding between neighbouring layers in bulk TMDCs, they mediate the transition to an indirect gap in the multilayer [5]. In addition to orbital characterisation, first-principles calculations have also indicated the presence of trigonal warping in the CB and VB extrema at $K/K'$, where the energy contour plots exhibit a triangular three-fold symmetric shape, arising from to the coupling between the CB and VB with other remote bands [74].

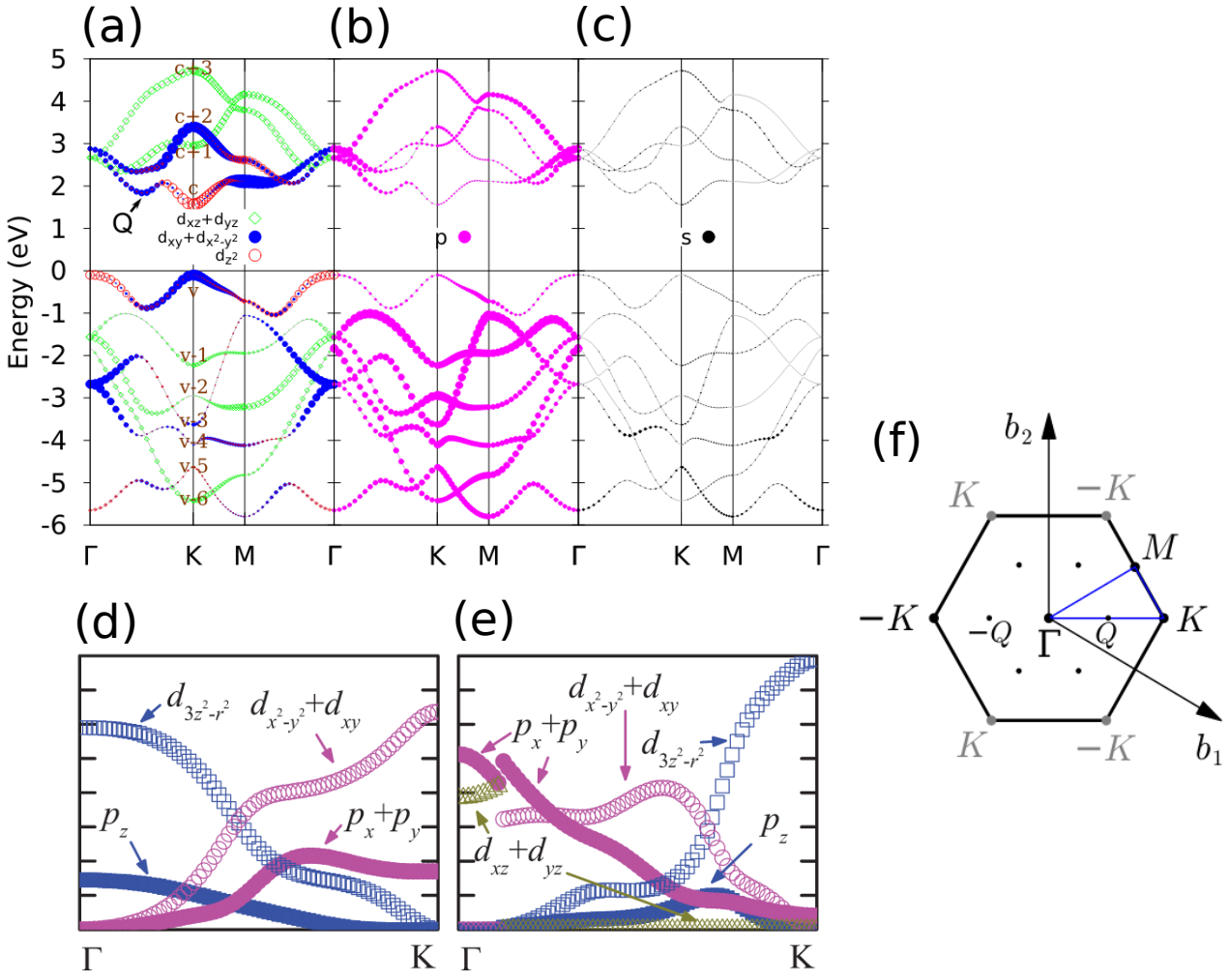



Figure 2.4: (a-c) Orbital projected band structures for monolayer $MoS_2$ (without spin-orbit coupling) from first-principles calculations. Symbol size is proportional to its population in corresponding state. (d,e) Orbital contribution to the (c) lowest energy conduction band and (d) highest energy valence band [5] of $WSe_2$. (f) Brillouin zone of TMDCs with high symmetry points indicated and $b_1$ and $b_2$ representing the reciprocal lattice vectors [5]. Republished with permission of the Royal Society of Chemistry, from [5]; permission conveyed through Copyright Clearance Center, Inc.

Another interesting feature of the band structure of monolayer TMDCs that separates them from other quasi 2D materials is the presence of a significant spin-splitting in some areas of the BZ. Spin-orbit coupling (SOC) comes as a result of the relativistic interaction between an

electron's spin and the magnetic field induced by the motion of the charged nucleus in the electron's frame [75]. The VB maxima at $K$ were found to have strong spin-orbit splitting that is not present in the VB maximum at $\Gamma$. This splitting is seen in both ARPES measurements and DFT calculations, as shown in Fig. 2.3(a) and Fig. 2.3(b), respectively. For monolayer group 6 TMDCs, this strong SOC arises from the $d$-orbitals of transition metal atoms [5]. Due to mirror reflection symmetry of TMDCs in the material plane, it is such that for every state with spin-up, there is a state with spin-down that has the same energy. On the other hand, time-reversal symmetry ensures that states with opposite momentum and opposite spin have the same energy. Hence, the energy difference between up and down spin is the same at the $K$ and $K'$ points but with opposite signs, which is a phenomenon known as spin-valley locking. Calculations using DFT (GGA) determined a SOC splitting in the VB maximum of 0.146-0.148 eV in $MoS_2$ and 0.425-0.430 eV in $WS_2$ which is consistent with the energy difference between peaks in absorption spectra [75, 76]. Spin-orbit splitting in the CB minimum at $K/K'$ is significantly smaller, because of the negligible SOC in the $d_{z^2}$ orbitals in the transition metal atom which predominantly characterises the CB at $K/K'$. In $MoS_2$ and $WS_2$, this splitting has been calculated using DFT to obtain 0.003 eV and 0.029 eV, respectively [5]. Since the contribution from the $M$-$d_{z^2}$ orbitals to the VB maximum at $\Gamma$ is relatively high in Fig. 2.4(a, e), this is potentially the reason for negligible splitting seen in $MoSe_2$ ARPES measurements [4]. It can be concluded that splitting in the VBM at $K/K'$ caused by SOC, cannot be simply neglected.

### 2.2.1 Modelling TMDCs with Tight-binding Models

In addition to DFT calculations, tight-binding models can be used to efficiently calculate the band structure and are especially useful when dealing with systems of many atoms (on the order of $10^2 - 10^4$) in nanoribbon or supercell calculations, offering a more lightweight alternative to the computational demands of ab initio calculations. A number of models have been constructed for TMDCs, with each having advantages and drawbacks depending on the chosen basis of atomic orbitals [5, 6, 77–79]. In the theory of tight-binding models, the overlap

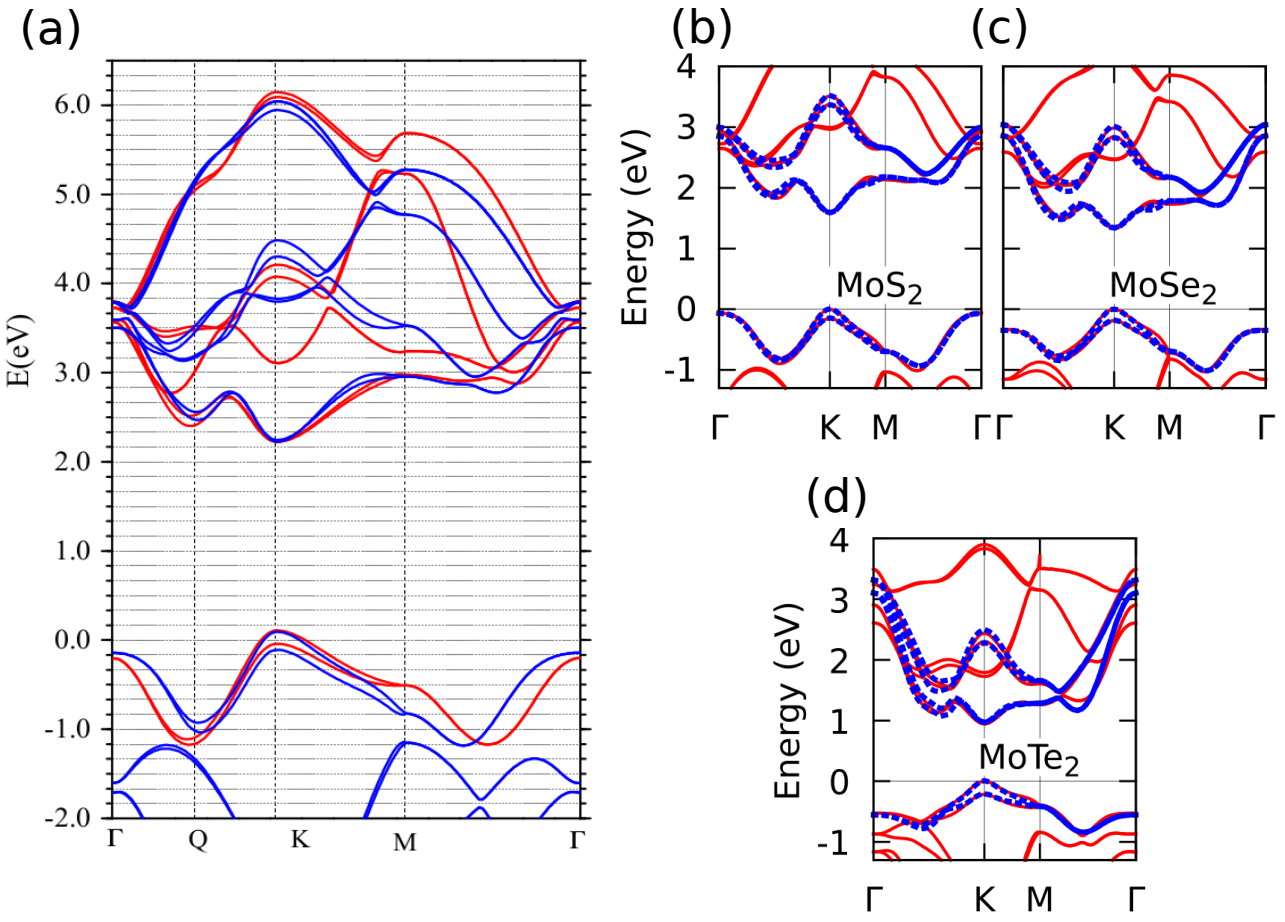



Figure 2.5: (a) Comparison of the tight-binding bands (red) from reference [6] and first-principles bands (blue). Republished with permission of the IOP Publishing, Ltd., from [6]; permission conveyed through Copyright Clearance Center, Inc. (b-d) Tight-binding bands (blue) for the third-nearest neighbour three-band model in reference [1] compared to first-principles calculations (red) for (b) $MoS_2$, (c) $MoSe_2$, and (d) $MoTe_2$. Reprinted with permission from [1], Copyright 2013 by the American Physical Society.

integrals between the orbitals on closely neighbouring atoms are converted into parameters, through which a formulaic approximation to the band structure of a material is obtained. Often, these parameters are obtained from ab initio methods such as density-functional theory. From first-principles calculations discussed in the previous subsection, it is apparent that an accurate band structure of monolayer TMDCs requires a set of important orbital states from the transition metal atoms and both chalcogen atoms. Hence, when considering a local orbital basis of tight-binding models, a significant subset of the outer valence orbitals of the constituent atoms must be selected such that the model can be sufficiently parameterised to best match the first-principles band structure.

An advantage of using a tight-binding model with a larger basis of orbitals from all atoms in

the motif of the lattice, is that the orbital composition of bands in the electronic structure found from DFT can be more accurately modelled. An eleven-band model of $MoS_2$ by Ridolfi *et al.* [6] was constructed using the $4d_{xy}$ $4d_{yz}$, $4d_{zx}$, $4d_{x^2-y^2}$, and $4d_{z^2}$ orbitals of the Mo atoms and the $3p_{x,y,z}$ of the S atoms in the top and bottom sublayers, and it was shown to successfully reproduce the orbital composition of the electronic structure at symmetry points, such as the $K/K'$ points and the $\Gamma$ point [6]. Unlike the $K/K'$ VB maxima which are mostly characterised by the $d_{xy}$ and $d_{x^2-y^2}$ orbitals, the VB maximum at $\Gamma$ is more complex in its composition, with the $p$-orbitals of the chalcogens having a minority contribution in addition to the $d_{z^2}$ orbitals [5]. The bands by Ridolfi *et al.* are shown in Fig. 2.5(a) compared to the DFT calculations, and demonstrate that the fit is reasonably good for the extrema of $K/K'$. Although the orbital composition of the states near the $\Gamma$ point is reproduced, a stark contrast in the effective mass (curvature) can be seen between the first-principles and tight-binding bands. This model also provided an insight into why the band gap is indirect in the bilayer and direct in the monolayer, demonstrating that the $4d_{x^2-y^2}$ orbitals on the Mo atoms and $3p_z$ orbitals of the S atoms were responsible for raising the energy of the secondary VB maximum at $\Gamma$ and lowering the energy of the secondary minimum at $Q$ in the transition from monolayer to bilayer, leading to an indirect band gap between the $\Gamma$ point in the VB and the $Q$ point in the CB [80]. There have previous attempts to construct models for a more light-weight approximation to the band structure, such as one constructed by Rostami *et al.*, which has a seven-orbital basis [79]. This however, results in flat bands that arise in the band gap which the model is not sufficiently parameterised to remove, due to the non-orthogonality of the basis and omission of key orbitals such as the $p_z$ orbitals of the chalcogen atoms [6, 79].

A tight-binding model by Zahid *et al.* includes the $4p$, $4d$, and $5s$ orbitals of Mo, and the $3p$ orbitals of both chalcogens, totalling 30 orbitals with the inclusion of spin-orbit coupling [77]. This exhibits excellent agreement with first-principles DFT calculations performed with the hybrid functional proposed by Heyd, Scuseria, and Ernzerhof [81]. However, it requires 96 fitting parameters to construct the model, meaning that along with the large basis size, construction of a supercell model would be costly and impractical for applications in which more than a few unit cells are required, such as in defect calculations or transport calculations [6]. From

the success and failures of these models, it is clear that a trade-off exists between a minimally complex calculation and exceptional agreement with electronic structure obtained from ab initio methods.

In calculations where only the bands close to the band gap need to be modelled accurately, the size of the basis can be reduced significantly. The orbitals $d_{xy}$, $d_{x^2-y^2}$ and $d_{z^2}$ on the transition metal atom demonstrate the strongest contributions to the band structure near the gap, known as the *low-energy* band structure as shown in Fig. 2.4(a) [5]. Conversely, the orbitals shown to be significant in obtaining the indirect gap in multilayer systems, such as the $p$-orbitals on the chalcogen, are less important in low-energy calculations of monolayer TMDCs. Liu *et al.* [1] used the $d_{xy}$, $d_{x^2-y^2}$ and $d_{z^2}$ orbitals on the transition metal atoms to create a three-band tight-binding model with up to third-nearest-neighbour hopping. This model was fit to the DFT (GGA) band structure using 19 free parameters, and was shown to accurately reproduce DFT bands at energies close to the band gap [1]. The simplified basis means that the model fails to obtain a non-zero spin-splitting at the CB minima at $K/K'$ (which is 3 meV). DFT calculations suggest that this is because the splitting is mediated by the $3p_{x,y}$-orbitals on the S atoms [1]. Fig. 2.5(b-d) clearly shows that this minimal-basis highly parameterised approach is able to capture the band extrema of all Mo-based monolayer group 6 TMDCs near $K/K'$, $\Gamma$ and $Q$ points in the Brillouin zone (BZ), including the effective masses associated with each extrema. It can be seen from the comparison of Fig. 2.5(a) and (b), that while the model in [1] is highly parameterised and captures the low-energy bands well, the model in [6] attempts to use a larger basis to capture the form of higher energy bands as well.

The tight-binding models discussed in this subsection highlight that in order to achieve accuracy and good agreement with first-principles methods across many bands, a large basis and large number of parameters are required. However, this can be costly to compute for supercell or nanoribbon forms of the tight-binding model, a problem which can be addressed by reducing the basis of orbitals used. However, by including subsets of local orbitals on each of the atoms in the unit cell, it is likely that errors in higher-energy bands from an incomplete basis choice can limit the accuracy of the fitting of low-energy bands to first-principles calculations. In the study of defects on monolayer TMDCs, the low-energy region of the band structure is the

most important region to accurately approximate, since the in-gap states are a common feature in defect calculations. Hence, models that can minimise the basis, omitting superfluous local orbitals, but provide a good numerical representation of the low-energy band structure, are an ideal means of capturing the properties of large enough systems that can approximate isolated defects. Of the various models presented here, these conditions have been best achieved by Liu *et al.* [1], devising a highly parameterised tight-binding model with only three orbitals in its basis.

## 2.3 Charged Defects in Transition Metal Dichalcogenides Observed in Experiments

Since the discovery of monolayer TMDCs, many experimental and theoretical groups have been trying to understand the plethora of point defects that can either arise in or be successfully added to monolayer TMDCs. Many point defects in these materials contribute to properties in the form of scattering centres and dopants [82], and much effort has been invested into the introduction of defects to these systems in order to study changes in observable quantities. This includes photoluminescence (PL) where optical resonance peaks are observed in addition to those known to be associated with the pristine system, and in scanning tunnelling spectroscopy where peaks are seen within the electronic band gap. Here I will outline several instances of observations of charged defects in TMDCs as seen from tunnelling experiments.

As mentioned, one of the most common intrinsic defects in monolayer TMDCs are chalcogen vacancies, which have been shown to act as electron donors in $MoS_2$ [58]. In addition to the many intrinsic defects that are present in TMDC materials, atoms can be introduced to the system through chemisorption, as an attempt to dope the system and engineer the electronic structure of 2D TMDCs. This has been performed with a variety of adsorbate candidates on molybdenum disulfide ($MoS_2$), including potassium adatoms which were shown through XPS to exhibit electron transfer to the system, resulting in $n$-doping [83], and sodium atoms which were also shown to behave as donors through an upward shifting of the Fermi level

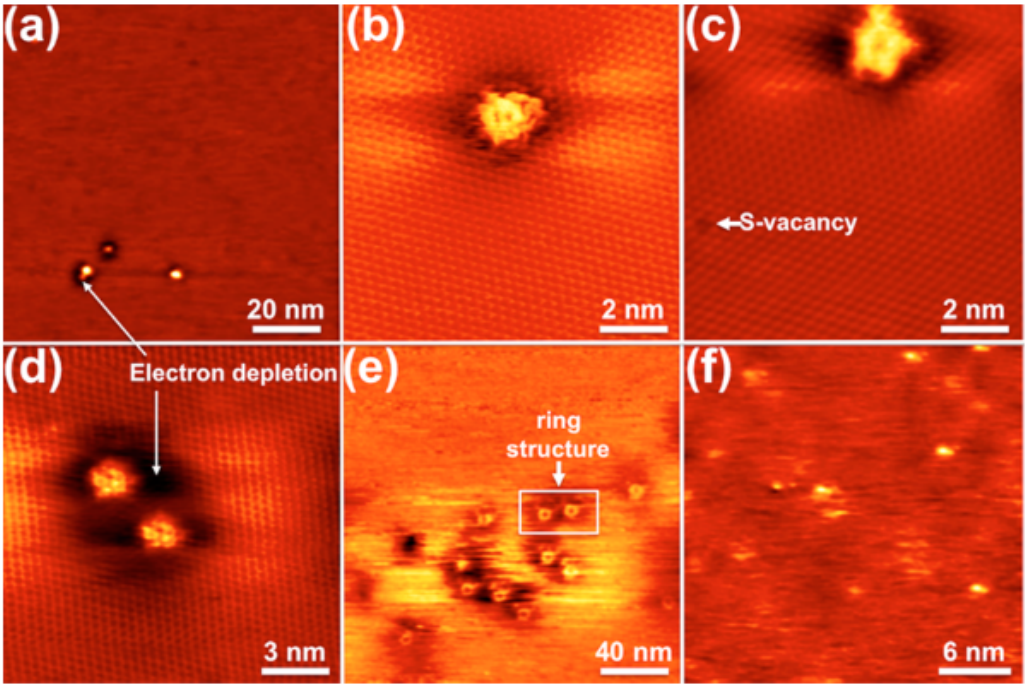



Figure 2.6: STM images of defects found on $MoS_2$: (a) $V_{bias} = -300$ mV images of dark halos around bright defects. (b) $V_{bias} = -20$ mV and (c) $V_{bias} = -150$ mV image of bright cluster defect with some depression. (d) $V_{bias} = -200$ mV image of two structured bright defects. (e) $V_{bias} = -1$ V image of shows ring-structured defect signatures. (f) $V_{bias} = +50$ mV image of bright defects resonances [7]. Reprinted with permission from [7], Copyright 2015 by the American Chemical Society.

seen in photoemission spectroscopy [84]. When carriers are excited from their dopant atoms into either the conduction or valence band, this leaves behind an unscreened charge. Hence, when considering doping strategies or intrinsic carrier concentrations, an understanding of how charged defects modify the electronic structure in monolayer TMDCs is important.

Tunnelling experiments, such as scanning tunnelling microscopy (STM), are a commonly used and insightful way to observe the local density of states in the vicinity of defects. STM operates by passing electrons through a tip into an underlying material sample via quantum tunnelling, which is biased using a tunable voltage to probe either above or below the Fermi level [85]. Through this operating principle, one can image the surface of the material in terms of the number of occupied or unoccupied electronic states depending on whether the bias voltage is negative or positive, respectively, or scan over a range of bias voltages at a particular location to obtain the density of states of the material. This has been performed by several groups, such as in work by Addou *et al.* [7], where molybdenum disulfide ($MoS_2$) crystals were exfoliated

and analysed at the (0001) surface level, which can provide insight into the behaviour of defects in the monolayer form. The STM images are shown in Fig 2.6, and demonstrate that defects can be identified electronically by localised patterns dispersed across the surface of the sample. In Fig 2.6(a) and (f) the bias voltage is negative, probing regions near the valence band, and demonstrates the existence of localised bright spots surrounded by dark halos, which appears for some defects and not others as seen in (b). While the bright spots may correspond to clusters of defects and a variety of chemical states, the dark regions are characteristic of electron depletion caused by a downward bending of the bands from the effects of Coulomb impurities (the effects of the scanning tip were excluded as a possibility) [7]. They propose that the cause of the electron depletion is Coulomb repulsion from a negatively charged S atom or impurity [7]. When a positive bias is applied to the sample, probing closer to the conduction band as electrons are biased to tunnel into the sample, it is found that a series of bright spots appear as seen in Fig 2.6(f). Here, the dark halos are not present and bright spots are instead seen spanning several nanometres, which have been attributed to donors in the chalcogen layer of the $MoS_2$ surface [7].

STM analysis has also been performed recently by Edelberg *et al.* [8] on naturally occurring $MoSe_2$ crystals. At a positive bias voltage, STM images of defects in these materials appear clearly in Fig. 2.7(a) as localised bright spots with radii on the nanometre scale, and dark spots on the same length-scale. The bright spots have been identified as single chalcogen antisite defects, as seen in Fig. 2.7(b), and the dark spots have been identified as metal atom vacancies, as seen in Fig. 2.7(c). These two defect species accounted for the majority of defects observed in the $MoSe_2$ sample, with chalcogen vacancies being two orders of magnitude less numerous than their antisite counterparts [8]. To complement the STM images, spectroscopic tunnelling data in Fig. 2.7(d) and 2.7(e), corresponding to the chalcogen antisite and metal atom vacancy, respectively, reveals further insight into the electronic nature of these defects, through analysis of the band-bending that takes place. In Fig. 2.7(d), the STS data demonstrates a broad resonance near the conduction band which shifts closer to the chalcogen antisite defect, identifying a band-bending most commonly associated with donors. For the metal atom vacancy, the STS reveals a localised state close to the valence band that shifts with distance to the defect,

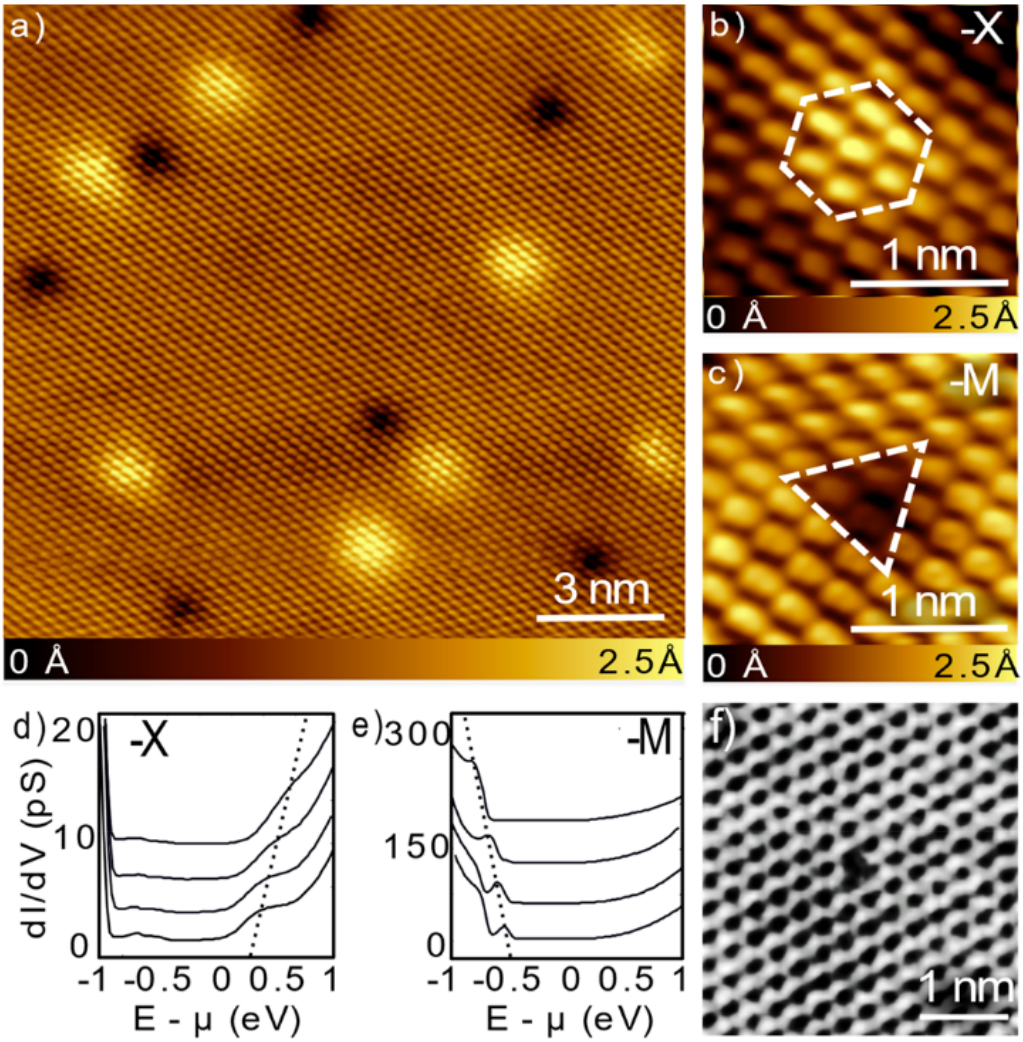



Figure 2.7: High-resolution STM images of $MoSe_2$ at $V_{bias} = 1.25$ V, (a) both kinds of dominant defects (b) a single chalcogen antisite defect, and (c) a single metal vacancy defect. $\frac{dI}{dV_{bias}}$ curves obtained at various distances from a (d) chalcogen antisite and (e) single metal vacancy. (f) STEM imaging of metal vacancy defects [8]. Reprinted with permission from [8], Copyright 2019 by the American Chemical Society.

indicating bending in the opposite direction and being consistent with acceptors [8].

From these two examples it can be seen that some defects in bulk crystals or few-layer samples, such as vacancies and antisite defects, can dope the system, which is verified by band-bending in tunnelling spectra. Along with the spatial extent of this band-bending, these features are characteristic of local Coulomb impurities. While it is informative to interpret the tunnelling spectra of these few-layer/bulk systems in the context of charged defects in the monolayer forms, on account of their similar band structure and identical chemistry, there will be some differences that are important to consider. As well as a larger, direct band gap, STM of

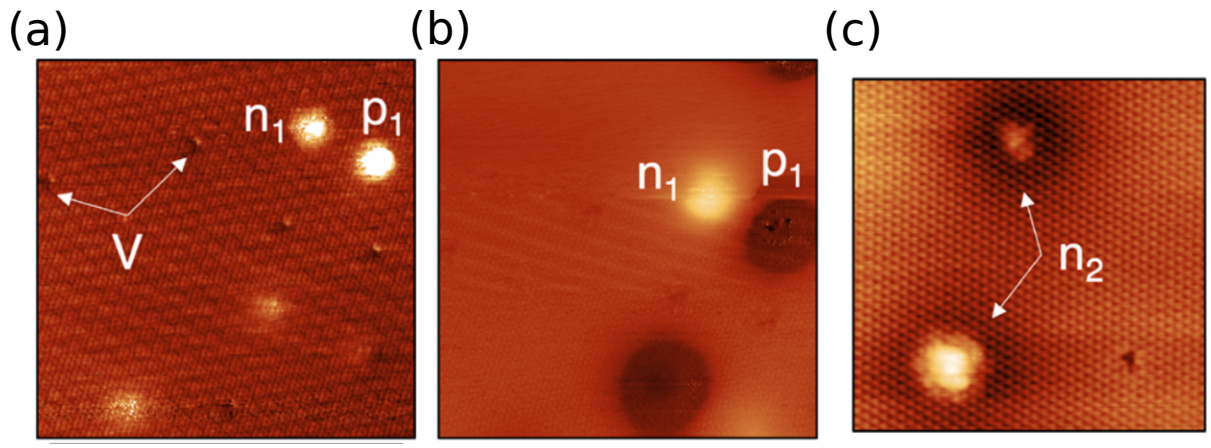



Figure 2.8: STM images of $n_1$ and $n_2$ defects on a $22 \times 22$ nm$^2$ with (a) $V_{\text{bias}} = -1.0$ V, and (b) $V_{\text{bias}} = 1.0$ V. (c) STM image of $n_2$ defect a $12 \times 12$ nm$^2$ at $V_{\text{bias}} = -1.0$ V [9]. Reprinted with permission from [9], Copyright 2020 by the American Chemical Society.

monolayers will show shifted shoulders in the density of states due to the shift of the secondary valence band extrema, caused by the increased quantum confinement. Recent work by Blades *et al.* [9] demonstrates the results of STS/STM measurements on defects that are thermally created in monolayer $WSe_2$. The observed defects are labelled by their electronic and structural features, as $n_1$, $n_2$ and $p_1$, and are identified as being an $n$-type, an $n$-type and a $p$-type dopant, respectively, in the $WSe_2$ monolayer [9]. The STM image of these defects in Fig. 2.8(a) shows that at negative bias voltage (-1.0 V), the defect labelled by $p_1$ shows an extended localised state associated with acceptor defects, while in Fig. 2.8(b) the application of a positive bias (1.0 V) shows that the defect exhibits a dark region. The defect species labelled as $n_1$ also shows a localised resonance at negative bias (Fig. 2.8(a)), but demonstrates downward bending of the conduction band [9]. The defect species $n_2$ is identified as a donor defect and exhibits a charge depletion region in Fig. 2.8(c) for negative bias (-1.0 V), characteristic of band-bending of the valence band from the Coulomb potential associated with a bare donor [9]. As with the study on bulk TMDC surfaces, this dark halo is indicative of a chemical state surrounded by charge depletion. Generally, in this high temperature study where the additional carriers are unbound from their dopant atoms, the charged nature of the defects is revealed. Subsequently, shifts of the conduction or valence band edges are observed in the STS measurements, and localised states with a spatial extent on the order of nanometres are imaged in the STM measurements. It should be noted that STS and STM do not necessarily identify the chemical nature of the

defects, which can be deduced in combination with input from other techniques such as X-ray photoelectron spectroscopy.

In summary, the observations in this section indicate that charged defects associated with dopants commonly present themselves in scanning tunnelling experiments as either bright nanometre-scale resonances or dark wells with an optional cluster spot in the centre, depending on the bias voltage and the electronic nature of the defect. It is seen that for donor defects, large positive biases that probe close to the conduction band show the defects as bright spots, and show as dark regions of electron depletion for negative bias voltages close to the valence band. The situation is reversed for acceptors, and these patterns are seen for both monolayer and surfaces of bulk crystals of TMDCs. While some aspects of these defect signatures can be explained through local band-bending by a Coulomb potential, an understanding of the mechanism by which such large bright spots manifest is currently unclear.

## 2.4 Modelling Defects in Two-dimensional Materials

### 2.4.1 First-principles Methods

Defects in two-dimensional (2D) materials, such as in graphene or in TMDCs, have been of significant interest over the last decade. The adsorption of metallic atoms on graphene is a promising approach [86] to defect engineering, as first-principles studies have indicated that the choice of adatom results in a diverse range of effects on graphene's electronic structure [86, 87], offering insight to the potential applications of graphene in transport experiments. However, for applications in logical electronic devices, the zero band gap of graphene is a strong hindrance [59]. On the other hand, as previously seen, the direct band gap in semiconducting monolayer TMDCs is believed to be a promising platform for nanoelectronics [48, 59]. The role that defects play in experimentally observed properties of TMDCs, and their potential application for optimising these materials for nanoelectronic devices, has been studied only within the last decade.

First-principles density functional theory (DFT) has been a widely-used tool for studying the interaction of adsorbed atoms and molecules with TMDCs, yielding important material-specific insights about adsorption geometries and adsorbate binding energies [48, 83, 88–90]. It is found that across these studies, trends exist between the groups of adatoms in the periodic table and their most energetically favourable bonding site on TMDCs. Atoms from groups 1-3, such as lithium or calcium, prefer to adsorb to the site directly above the transition metal atom [88] ($M$-site), and atoms from groups 5-7 favour the site above the chalcogen atoms [88, 89] ($X$-site). They also conclude no discernible trend in this respect for group 4 atoms or transition metal atoms. An important quantity when studying impurities in semiconductors is the charge transfer that occurs between the adatom and the 2D material upon adsorption. Significant charge transfer has been found to occur for most types of adatom due to the redistribution of the electron density near the bond between the adatom and 2D material [91]. These studies determine the charge transfer for various adatoms, which can be done by either partitioning the total electronic charge density [48, 83, 86] or by studying the partial Kohn-Sham density of states [86,91]. Charge transfer between adatoms on TMDCs, mainly $MoS_2$, has been determined in first-principles studies with notable trends between some adatoms from groups in the periodic table and the sign of the charge transfer. For example, calculations have shown that atoms from group 1 act as donors [89], transferring significant charge to the $MoS_2$ sheet, while atoms from groups 5-7 behave as slightly less effective acceptors. In work by Rastogi *et al.* [88], they find distinct differences in the effects on the electronic structure between group 1-2 and group 3, namely that group 3 adatoms result in in-gap donor states close to the conduction band minimum, while group 1-2 do not despite similar estimations of charge transfer to group 3.

While the first-principles approach to studying adatoms on TMDCs gives a qualitative description of the bonding that takes place, there are several limitations of the methods used for this analysis. Firstly, the supercells used for such calculations are severely limited by the poor system-size scaling of DFT, scaling with number $N$ of atoms as $\mathcal{O}(N^3)$. For example, Rastogi *et al.* [88] used a $3 \times 3$ unit cell, which had images of the defect in neighbouring supercells being separated by less than 10 Å. In 2D materials, adatoms strongly alter electron-electron interactions through a long-range weakly-screened Coulomb potential, which typical DFT supercells

cannot fully capture [91]. This has been observed in scanning tunnelling spectroscopy (STS) performed for Coulomb impurities on graphene [92], showing that the defect states associated with adatoms can extend up to 100 Å. While these systems are distinct from graphene, the 2D nature of these materials means that the electric field lines emanating from the impurity can leave the plane and avoid the screening charge, similarly resulting in weakly screened potentials [50]. Secondly, first-principles studies of adatoms on TMDCs are also limited in accuracy when discussing the charge transfer from adatoms. This can be clearly seen in the discrepancy between charge transfer obtained from different studies of the same system [48, 83, 88, 89]. Various techniques can be used for determining charge transfer, such as Bader's method [93] or Mulliken population analysis [94], which both involve the partitioning of the total electronic density. Despite the success of these methods for qualitative comparison amongst adatoms, the calculation of transferred charge by studying spatial electron densities with DFT, is ambiguous as there exists no definite dividing line to separate the TMDC+defect system [86, 95]. As an added complication, even DFT with the ideal exchange-correlation functional is only capable of accurately determining the total ground-state density, and not individual parts, which further highlights the arbitrariness and ambiguity of some of the practical definitions of charge transfer.

### 2.4.2 Tight-binding Methods to Model Charged Defects in TMDCs

Some recent studies of defects on 2D materials have been performed with the use of tight-binding models. This has been performed for $MoS_2$ by Salehi *et al.* [96], using a Hamiltonian with a basis set containing $s$, $p$, and $d$ orbitals from the $M$ and both $X$ atoms in the unit cell, which results in a 27-band model. They use supercells with sizes up to $11 \times 11$ to simulate vacancies in the system by removing an atom from the model, finding vacancy defect states arising in the band gap [96]. For Mo atom vacancies, they found acceptor behaviour, while they found donor behaviour for S atom vacancies. They show that a $5 \times 5$ supercell is sufficient to prevent vacancy-vacancy interactions, and this leads to convergence of the energy of the defect state. While the energy of vacancy defect states may converge for such supercells, the convergence of the density of states to that of the infinite system of TMDC+defect is not apparent, which

arises due to the orbital characterisation of the band extrema by the $4d$-orbitals of the $M$-atoms. This means that even for a large basis of orbitals in the unit cell, the low-energy band structure of this system is inefficiently modelled, since the basis contains many orbitals that are unnecessary for constructing the band extrema. Additionally, unlike for the case of vacancy defects with strong local potentials, the accuracy of electronic structure calculations performed with these supercell sizes will be limited for shallow defects, where the excess charge can be notably less than the electron charge and the localised states extend much further from the defect [91]. However, this demonstrates the computational efficiency of such electronic structure calculations for defect states, relative to DFT, and holds great promise for use in the study of other species of defects on TMDCs.

Corsetti *et al.* [91] developed a multi-scale method for studying calcium adatoms on graphene which accounted for the long-range extent of both the electrostatic potential associated with defects, and the resulting bound states of the system. In this framework, linear-scaling DFT was used for a calcium adatom on a $56 \times 56$ graphene supercell, from which the screened potential of the defect was extracted as a local average around each carbon atom in the system. This was used to parameterise various local screening models of the potential, namely the linear and non-linear Thomas-Fermi approximation, which provided a value for the effective charge transfer $Z$, and the chemical potential $\mu$. The aim of this parameterisation of the continuum potential, was the long-range extrapolation of the form of the defect potential extracted from linear-scaling DFT. Secondly, a large-scale tight-binding model of graphene that extends over tens of nanometres was constructed, in which the continuum defect potential was applied as an on-site term in the Hamiltonian. This approach allowed a comparison to be made between simulated local density of states and the $\mathrm{d}I/\mathrm{d}V$ found in scanning tunnelling experiments [92]. A benefit of using this multi-scale method for calcium adatoms on graphene opposed to using DFT alone [86] was the minimisation of the effects of the periodic defect images in neighbouring supercells. Near the Dirac point of graphene, this prevented the presence of electronic states that spatially occupy regions equidistant from neighbouring defects, known as impurity-impurity bonding states, which is a common problem in ab initio studies of charged defects [97]. Additionally, the calculation of the charge transfer from adatom to 2D

materials is determined from the parameterisation, and is free of the ambiguity associated with charge-partition methods such as Bader's method [93]. In the absence of explicit doping of the system, the Thomas-Fermi approach used in the work would reduce to the random-phase approximation (RPA) in graphene, for which the dielectric function is widely known in the linear band approximation [91]. This method of defect potential + large tight-binding model could be readily applied to a 2D semiconductor in which the doping by the impurity itself does not contribute to a significant carrier population, by determining a dielectric function within the RPA without linear response terms for carrier concentrations such as in the Lindhard model [98].

There is still much to understand about the general properties of TMDCs with adsorbates, such as the binding energies of bound states and the changes to the absorption spectra. While ab initio methods, such as DFT, provide a more accurate chemical description of a charged defect, the poor scaling of the method renders it less effective at fully utilising that accuracy for the purpose of determining its electronic structure. The current state of the field has provided insight into the need for computationally efficient methods for these systems that span large distances, in order to more accurately capture the effects of an isolated defect. Previous work on the effects of adsorbates on graphene has highlighted the success of a tight-binding approach, indicating that similar techniques should be considered for TMDCs. Such an approach, not directly pursued before, is useful for capturing the long-range properties of isolated defects and their experimental signatures. Work in this thesis attempts to address this gap in the understanding of adsorbates on TMDCs, in order to give an accurate picture of changes to electronic structure and optical properties such as absorption spectra.

### 2.4.3 Treatment of Screening in TMDCs

In order to apply the ideas implemented by Corsetti *et al.* to the novel electronic structure of defects in monolayer TMDCs, I will briefly review methods to capture the non-linear screening present in these materials. In this framework, an understanding of the screening in these materials is essential for predicting the electronic structure of charged defects in TMDCs. There are multiple approaches for approximating the screening, and in this subsection I will specifically

discuss the use and development of two approaches: The Keldysh form of the screening, which pertains more to a continuum treatment of the system, and through first-principles calculations on the atomic scale using the random-phase approximation (RPA).

Often, a quantum mechanical description of the screening is not necessary for the purpose of modelling sufficiently weak potentials in thin film semiconductors, and a long-wavelength continuum theory can adequately provide a model of impurity states or excitons in such materials. Keldysh [99] (and Rytova a decade prior [100]) devised a screened Coulomb interaction in thin film semiconductors (and semimetals) using an electrostatic approach, by considering a region of space with thickness $l$ and dielectric constant $\epsilon$, sandwiched between a substrate with constant $\epsilon_1$ and a medium of dielectric constant $\epsilon_2$. The expression for the potential experienced between two electrons, at out-of-plane positions $z$ and $z'$, in this medium is then given by:

$$V_{\text{Keld}}(\mathbf{r}, z, z') = \frac{e^2}{\varepsilon_0 \epsilon} \int \frac{\mathrm{d}^2\mathbf{k}}{(2\pi)^2}\, e^{i\mathbf{k}\cdot\mathbf{r}} \frac{\cosh\left(\left|\frac{\mathbf{k}}{2}\right| l + \eta_1\right) \cosh\left(\left|\frac{\mathbf{k}}{2}\right| l + \eta_2\right)}{|\mathbf{k}| \sinh(|\mathbf{k}| l + \eta_1 + \eta_2)}, \tag{2.1}$$

where $\eta_i = \frac{1}{2}\ln\left(\frac{\epsilon+\epsilon_i}{\epsilon-\epsilon_i}\right)$. Keldysh uses several assumptions to reach an expression for a simple screened potential, by first assuming $V_{\text{Keld}}$ is independent of $z, z'$, and focusing on the region where $|\mathbf{k}| l \ll 1$, so to be able to expand the hyperbolic functions in Eq. (2.1):

$$V_{\text{Keld}}(\mathbf{r}) \approx \frac{e^2}{4\varepsilon_0(\epsilon_1+\epsilon_2)} \left[\mathcal{H}\left(\frac{\epsilon_1+\epsilon_2}{\epsilon}\frac{r}{l}\right) - N_0\left(\frac{\epsilon_1+\epsilon_2}{\epsilon}\frac{r}{l}\right)\right], \tag{2.2}$$

where it is also assumed that $\epsilon_{1,2} \ll \epsilon$, as well as that $l$ is smaller than the effective Bohr radius $\tilde{a}_B = \frac{\hbar^2\epsilon}{me^2}$. In Eq. (2.2), $\mathcal{H}$ and $N_0$ are the Struve function and zeroth Bessel function of the second kind, respectively. This results in the effective Keldysh dielectric function [99]:

$$\varepsilon(q) = \frac{\epsilon_1+\epsilon_2}{2} + r_0 q, \tag{2.3}$$

where $r_0 = \frac{l\epsilon}{2}$ is the effective scale length of the screening. This simple formula can accurately capture the long-wavelength screening of many 2D semiconductors. In the long-range limit, this converges towards a Coulomb potential screened by the average dielectric constant, as is expected for quasi-2D materials and thin films. In the short range, the screened potential

scales logarithmically and is not typical of screening in semiconductors, in which the dielectric function converges to unity as the charges get closer together. This short range behaviour is expected for a dielectric function that diverges linearly with the wavevector, since it does not accurately capture the behaviour of the screening at large values of $q$.

The Keldysh potential has been successfully used in the application of several 2D semiconductors. The ab initio dielectric function of freestanding transition metal dichalcogenides (TMDCs) compares very well to the linear form at small values of the wavenumber, finding $r_0 = 35$ Å for $MoS_2$ [10]. This can be further applied to quickly and efficiently calculating binding energies of excitons in monolayer TMDCs as well as for localised three-particle excitations, known as trions, representing the electron-hole interaction in a variational model with the Hamiltonian [101]:

$$\hat{H}_X = -\frac{\hbar^2 \nabla_{\mathbf{r}}^2}{2\mu} - V_{\text{Keld}}(r), \tag{2.4}$$

where $\mu$ is the reduced effective mass of the electron-hole pair. When the electron-hole separation is long-range, such as in 2D materials with sufficiently weak screening, the Keldysh potential can in some circumstances approximate the interaction well.

In the random-phase approximation (RPA), the electrons are approximated as only interacting through the Hartree potential. Work by Qiu *et al.* [10] applied the RPA to the screening of monolayer $MoS_2$ and outlined computational challenges and key features of convergence with respect to the calculation of the dielectric matrix $\varepsilon^{-1}_{\mathbf{GG'}}(\mathbf{q})$. This first involved performing DFT calculations on a periodic system which, despite approximating the electronic system of a 2D material, was calculated for a 3D periodic system. In plane-wave DFT software packages, periodicity in all three directions must be maintained, and hence in order to simulate a 2D system, one must separate consecutive layers by a large enough distance $L_z$ such that electrons situated on two neighbouring periodic layers do not interact. This turns out to be on the order of 10 Ångstroms. A caveat of this approach is that the number of $\mathbf{G} \sim \frac{1}{L_z}$ vectors required to converge the system, which correlates to the number of unoccupied bands required for the calculation, increases substantially. The convergence of $\varepsilon_{\mathbf{GG'}}(\mathbf{q})$ with increasing $L_z$ is slow, and results in very inaccurate values for small $q$. A method around this is to incorporate a

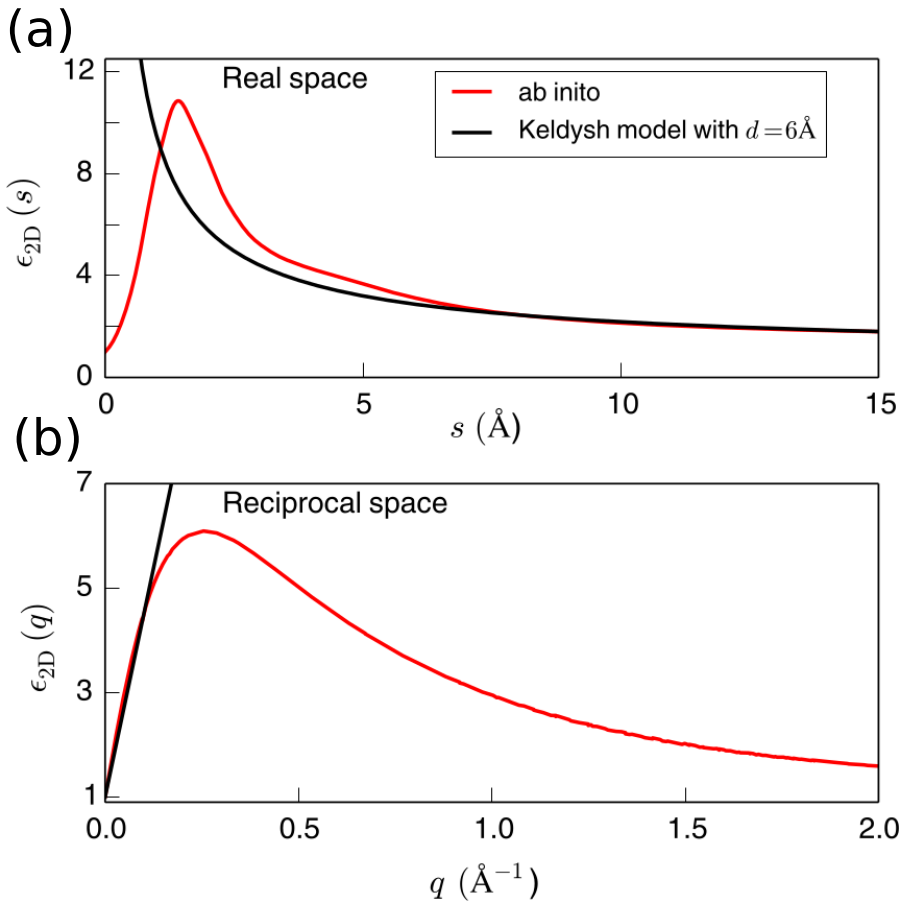



Figure 2.9: Comparison of the effective 2D dielectric function found from Eq. (3.19) (red) with the screening obtain from the Keldysh formalism in Eq. (2.3) (black), in (a) real-space and (b) reciprocal-space [10]. Reprinted with permission from [10], Copyright 2016 by the American Physical Society.

truncated form of the Coulomb potential into the calculation of the screening, developed by Ismail-Beigi [102], which takes the form of:

$$v_{\text{trunc}}(\mathbf{q}) = \frac{e^2}{\varepsilon_0 q^2}\left[1 - e^{-\frac{q_{xy}L_z}{2}}\cos\left(\frac{q_z L_z}{2}\right)\right], \tag{2.5}$$

where $q_{xy} = \sqrt{q_x^2 + q_y^2}$. For large values of $q$, corresponding to shorter distances in the monolayer, the second term in the square brackets in Eq. (2.5) vanishes, retaining the 3D interaction between electrons across distances similar to the lattice parameter. However, from Eq. (2.5) it can be seen that for small $q_z$ and $q_{xy}$, in turn corresponding to significantly larger distances on the order of $L_z$, the term in square brackets can be expanded and reduced to approximately $\frac{q_{xy}L_z}{2}$. This gives the Coulomb interaction purely 2D properties when considering interactions between monolayers and permits the use of reasonably low values of $L_z$ for the same accuracy

in $\varepsilon^{-1}_{\mathbf{G}\mathbf{G}'}(\mathbf{q})$.

From the inverse dielectric matrix $\varepsilon^{-1}_{\mathbf{G}\mathbf{G}'}(\mathbf{q})$, one can extract an effective dielectric function $\varepsilon_{2\mathrm{D}}(\mathbf{q})$ which gives a measure of the screening between two orbitals in the plane of the material. This is further demonstrated by Qiu *et al.* [10], where the interaction between two orbitals in the Mo layer is represented by:

$$W_{ij}(\mathbf{s}_i, \mathbf{s}_j) = \int \mathrm{d}^2 s_3 \; [\varepsilon^{-1}_{2\mathrm{D}}]_{ij}(\mathbf{s}_1, \mathbf{s}_3) v(|\mathbf{s}_3 - \mathbf{s}_2|) = \int \mathrm{d}\mathbf{r}_1 \mathrm{d}\mathbf{r}_2 \; \rho_i(\mathbf{r}_1 - \mathbf{s}_1) W(\mathbf{r}_1, \mathbf{r}_2) \rho_j(\mathbf{r}_2 - \mathbf{s}_2), \quad (2.6)$$

where $\rho(\mathbf{r})$ is the electronic density and $W(\mathbf{r}, \mathbf{r}')$ is the screened interaction. When Fourier-transformed, this allows us to write an effective 2D dielectric function:

$$[\varepsilon^{-1}_{2\mathrm{D}}(q)]_{ij} v^{2\mathrm{D}}_{\mathbf{q}} = \frac{1}{L_z} \sum_{\mathbf{G}_z \mathbf{G}'_z} \rho^*_i(\mathbf{q} + \mathbf{G}_z) W_{\mathbf{G}_z \mathbf{G}'_z}(q) \rho_j(\mathbf{q} + \mathbf{G}'_z) \quad (2.7)$$

$$\varepsilon^{-1}_{2\mathrm{D}}(q) = \frac{q}{2\pi e^2 L_z} \sum_{\mathbf{G}_z \mathbf{G}'_z} W_{\mathbf{G}_z \mathbf{G}'_z}(q) = \frac{q}{2\pi e^2 L_z} \sum_{\mathbf{G}_z \mathbf{G}'_z} \varepsilon^{-1}_{\mathbf{G}_z \mathbf{G}'_z}(\mathbf{q}) v_{\mathrm{trunc}}(\mathbf{q} + \mathbf{G}'_z), \quad (2.8)$$

where in the second line, the electronic density of orbital $i$ is approximated as $\rho_i(\mathbf{r}_1 - \mathbf{s}_1) = \delta(\mathbf{r}_1 - \mathbf{s}_1)$ and the orbital indices are dropped. This formula essentially provides the ratio between the screened interaction between two points in monolayer $MoS_2$ and the bare Coulomb potential, in line with the definition of Eq. (3.19).

Fig. 2.9 shows a comparison of the two approaches to modelling the screening in thin-film systems in Eq. (2.8) and Eq. (2.3), with (a) in real-space and (b) in reciprocal-space. This demonstrates good agreement at small wavevectors corresponding to distances on the nanoscale, which is consistent with continuum nature of the Keldysh formulation. Disagreement is observed in Fig. 2.9(a) beyond approximately 1 nm, where the dielectric function obtained from first-principles dips below the approximation by Keldysh. This likely arises from the uncertainty of the linear fit in Fig. 2.9(b) near $q = 0$ with the ab initio dielectric function, since the data in this region does not perfectly conform to a straight line. This means that while estimates of $r_0$ in the Keldysh dielectric function for $MoS_2$ lie somewhere close to 40 Å, the exact value depends on how the line fitting is performed. It can also be clearly seen from the real-space dielectric functions in Fig. 2.9(a) that the Keldysh function yields unphysically large

values of the screening at small distances, whereas the ab initio RPA dielectric function returns to unity as expected. This is a reflection on the approximations made to simplify the Keldysh integral to the quotient of the Coulomb potential and a linear dielectric function, as well as a lack of any quantum mechanical description of the system at short-range.

## 2.5 Optical Properties of Monolayer TMDCs

While the electronic properties of charged defects in monolayer transition metal dichalcogenides (TMDCs) are important in many applications, the effect that charged defects have on the interaction of fabricated TMDC samples with incident light is crucial to many experiments and devices. Modelling and understanding the excitation of an electron by light requires a description of excitons, which form as a result of the screened Coulomb interaction between an electron and a hole. The reduced dimensions and large band gap in monolayer TMDCs means that such interactions are long-range, unlike many three-dimensional semiconductors. This makes the behaviour of excitons in monolayer TMDCs a topic of great interest. Over the last decade, much academic work has gone into understanding excitons in these materials, but there is a gap in current understanding of how the presence of charged defects can change these intriguing properties.

### 2.5.1 Excitons in Pristine Crystals: Theory and Experiment

Excitons are bound states of the quasi-particles formed when light is imparted onto a material, emerging from the mutual Coulomb attraction between an electron excited into the conduction band from the absorption of light, and the corresponding hole that is left in the valence band upon excitation. Their mutual attraction can be described by the Hamiltonian [103]:

$$H_{e-h} = E_g + \frac{p_e^2}{2m_e} + \frac{p_h^2}{2m_h} + V_{\text{scr}}(|\mathbf{r}_e - \mathbf{r}_h|) \tag{2.9}$$

where $E_g$ is the band gap, $V_{\text{scr}}$ is the screened interaction, $p_i$, $m_i$, $\mathbf{r}_i$ are the momentum, mass and position, respectively, of electrons ($i = e$) and holes ($i = h$). In the basis of the centre-of-mass motion $\mathbf{R}$ and the relative motion $\mathbf{r}$, this is described by the expressions:

$$\mathbf{r} = \mathbf{r}_e - \mathbf{r}_h, \quad \mathbf{R} = \frac{m_e\mathbf{r}_e + m_h\mathbf{r}_h}{M} \longrightarrow \mathbf{r}_e = \mathbf{R} + \frac{m_h}{M}\mathbf{r}, \quad \mathbf{r}_h = \mathbf{R} - \frac{m_e}{M}\mathbf{r}, \tag{2.10}$$

where $M = m_e + m_h$. Substituting this into the Hamiltonian and using $\mathbf{p} = \hbar\mathbf{k}$, one obtains [103]:

$$\begin{aligned}
\frac{p_e^2}{2m_e} + \frac{p_h^2}{2m_h} &= \frac{1}{2}m_e\left(\dot{\mathbf{R}}^2 + \frac{m_h^2}{M^2}\dot{\mathbf{r}}^2 + 2\frac{m_h}{M}\dot{\mathbf{R}}\dot{\mathbf{r}}\right) + \frac{1}{2}m_h\left(\dot{\mathbf{R}}^2 + \frac{m_e^2}{M^2}\dot{\mathbf{r}}^2 - 2\frac{m_e}{M}\dot{\mathbf{R}}\dot{\mathbf{r}}\right) \\
&= \frac{(\mu\dot{\mathbf{r}})^2}{2\mu} + \frac{(M\dot{\mathbf{R}})^2}{2M} \longrightarrow \frac{\hbar^2k^2}{2\mu} + \frac{\hbar^2Q^2}{2M} \\
H_{e-h} &= E_g - \frac{\hbar^2}{2\mu}\nabla^2 + V_{\text{scr}}(r) + \frac{\hbar^2Q^2}{2M}
\end{aligned}$$

where $\mu = \frac{m_e m_h}{M}$ and $-i\nabla$ has been used as the real-space operator of $k$. The last term in $H_{e-h}$ vanishes for direct transitions with $Q = |\mathbf{Q}| = 0$. It should also be noted that the momentum of the hole $\mathbf{p}_h$ has an opposite sign to that of the valence band electron that it replaces, while the position of the hole has the same sign as that from the corresponding valence band electron. In the case of monolayer TMDCs, this resembles the 2D hydrogen model more closely in energy level multiplicity and ordering, while deviating significantly from the analytic solution on account of the unique dielectric screening present in the material. The interaction between an electron and hole consists of a direct component and an exchange component. The direct interaction is primarily associated with the electron and hole charge distributions, being dictated at long-range by the envelope function of the electron-hole pair, whilst being determined at short range by the Bloch functions of the material which vary uniquely at the Ångstrom-scale [104]. The exchange interaction however, is a consequence of the Pauli exclusion principle combined with the requirement for the many-body wavefunction to be anti-symmetric. The combination of opposing spin wavefunctions in the Coulomb integral accounts for the indistinguishable nature of electrons in the many-body wavefunction. This interaction energy tends to be an order of magnitude smaller than the direct interaction and is

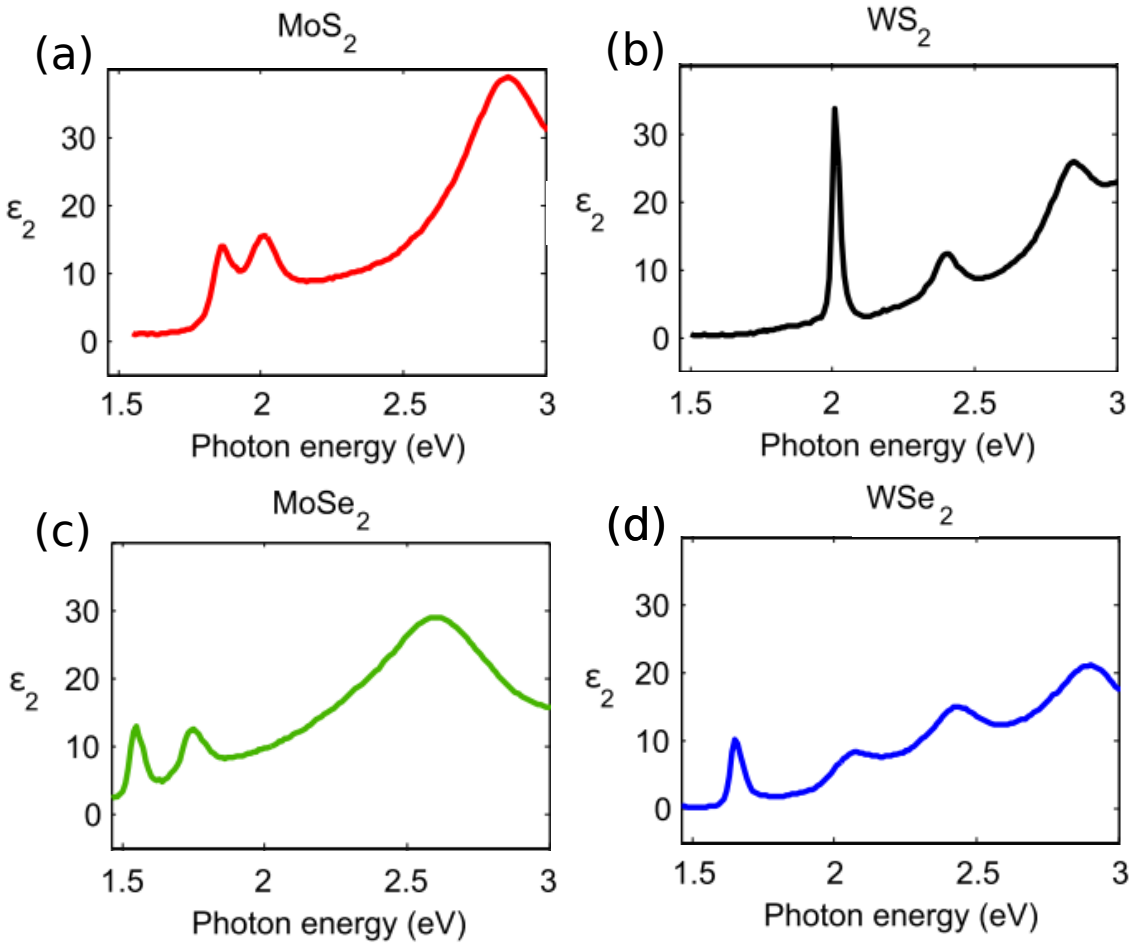



Figure 2.10: Imaginary dielectric function obtained from optical reflectance experiments by Li *et al.* [11] for (a) $MoS_2$, (b) $WS_2$, (c) $MoSe_2$, and (d) $WSe_2$ on silica substrate. Reprinted with permission from [11], Copyright 2014 by the American Physical Society.

a short-range interaction [104].

The weaker dielectric screening effect that is present in monolayer TMDCs, compared to in 3D bulk semiconductors, results in a stronger Coulomb interaction between electrons and holes which leads to large exciton binding energies [104, 105]. This has been shown in work by Li *et al.* [11], by extracting the imaginary part of the dielectric function through optical reflectance measurements for a handful of monolayer TMDCs ($MoS_2$, $WS_2$, $MoSe_2$, $WSe_2$) on fused silica substrates. This demonstrated that for these TMDCs, peaks appear at photon energies several hundreds of meV below the value of the quasi-particle band gap, which for $MoS_2$ on fused silica is found to be approximately 2.5 eV, and approximately 2.7 eV for $WS_2$ on fused silica [104]. The lowest of the peaks corresponds to the optical band gap. The energy peaks in the imaginary part of the dielectric function appear to come in a pairs, more closely spaced in the case of the

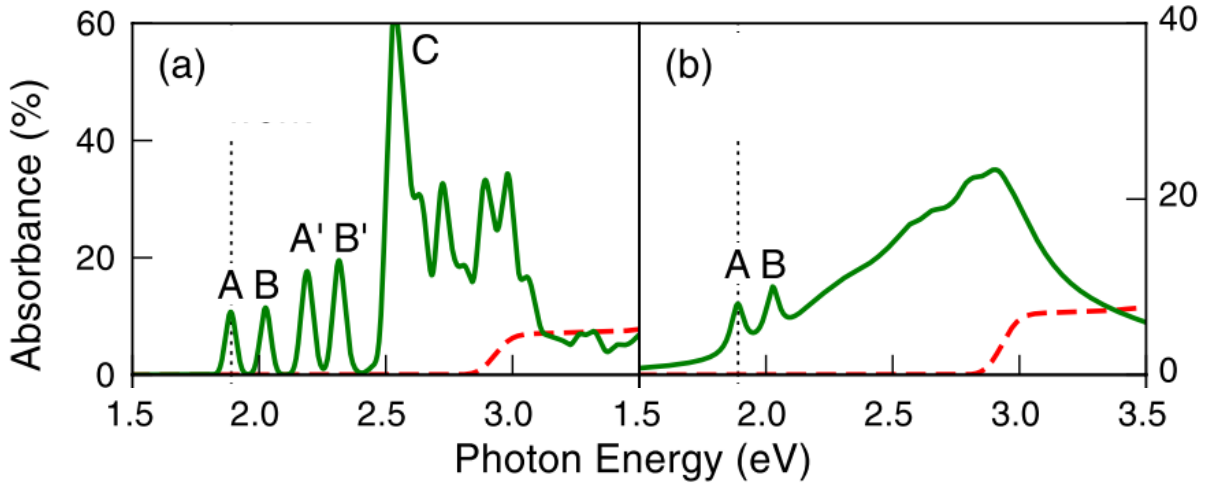



Figure 2.11: Absorbance for $MoS_2$ using ab initio $GW$ calculations for (a) without and (b) with the inclusion of broadening from the quasi-particle lifetimes [12]. Reprinted with permission from [12], Copyright 2013 by the American Physical Society.

Mo-based TMDCs. These are referred to as the $A$ and $B$ excitons, and arise because of the strong spin-orbit splitting in the monolayer valence bands. This is known by comparing the separation between the $A$ and $B$ exciton to the spin-orbit splitting present in ab initio models or from ARPES [11, 104]. This double peaked feature in the reflectance has also been observed in other work [106]. The presence of two excitons with sizeable binding energy is also found when performing ab initio calculations. Calculations of the absorption spectrum and exciton resonances using the $GW$ method demonstrate how the weak screening in the material gives rise to larger binding energies [12]. These calculations are shown in Fig. 2.11(a), where as well as the $A$ and $B$ exciton peaks of monolayer $MoS_2$, additional peaks are found in the band gap region that were not observed in experiment. This discrepancy is resolved when the broadening from quasi-particle lifetimes is included in the absorption spectrum, as seen in Fig. 2.11(b).

In TMDCs, the extent of the exciton wavefunction is on the order of several nanometres, with binding energy significantly less than that of a hydrogen atom, which is known as being within the Wannier-Mott regime [104]. This is as opposed to the case of Frenkel excitons which have extents on the scale of the lattice parameter. Another unconventional property of TMDCs with respect to bulk semiconductors that manifests itself in the optical properties, is the large effective mass of the valley extrema ($\sim 0.5m_0$, where $m_0$ is the free electron mass). In a simple positronium model (electron + positron in free space) model for excitons in 2D,

the lowest energy is proportional to the reduced mass $m_+m_-/(m_+ + m_-)$, where $m_\pm$ is the electron/hole mass (which for positronium, has $m_\pm = m_0$). This reduced mass in TMDCs, which evaluates to about $0.25m_0$, contributes to the unusually large binding energies of excitons. In the ab initio study of the optical properties of TMDCs by Qiu *et al.* [12], the character of the excitons is analysed and were compared to the bound states of the screened two-dimensional hydrogen model. The excitons corresponding to $A$ and $B$ resonances exhibited similar localised wavefunctions with a root mean square radius of 1 nanometre [12]. The $A$ and $B$ excitons were found to be doubly degenerate, because of the spin-valley locking present in the Brillouin zone, such that transitions for spin up electrons at $K$ are identical to spin down electrons at $K'$ [104]. Additional exciton states were observed between the $B$ exciton and the quasi-particle band gap energy, which are labelled in Fig. 2.11(a) as $A'$ and $B'$. These were found to be six-fold degenerate, and corresponded to $2s/2p$ states at the $K/K'$ points in the BZ [12].

In addition to ab initio efforts to calculate properties of the excitons in monolayer TMDCs, tight-binding models can provide a quick and efficient means of describing the behaviour of excitons. In work by MacDonald *et al.* [107], the Bethe-Salpeter equation was solved for a simple $4d$-orbital tight-binding model to obtain exciton binding energies of $MoS_2$ on $SiO_2$ substrate, which agree with experimentally obtained values. In contrast to Qiu *et al.* [12], in which the *GW* calculations provided an accurate picture of the screening through the dielectric matrix of $MoS_2$, the screening was modelled using the Keldysh function. The inability of the two-dimensional Keldysh-screened Coulomb potential $V_{\mathbf{R}}$, given as a function of position $\mathbf{R}$, to accurately capture the electron-hole interaction at sub-nanometre scales was avoided through the truncation of the interaction. For $\mathbf{R} = 0$, MacDonald sets the value of the interaction to be $UV_{\mathbf{R}=a}$ where $a$ is the lattice parameter and $U$ is an adjustable parameter that accounts for the screening of on-site potentials by remote bands, which takes unit value for the calculation (despite an uncertainty on its actual value). The optical conductivity from this approach exhibits similar features to the absorption obtained from both *GW* calculations and reflectance experiments, namely a strongly bound exciton with binding energy on the order of a few hundred meV, and two dominant peaks at the lowest part of the spectrum corresponding to the $A$ and $B$ excitons [107]. Overall, it can be seen that such a technique is capable of modelling optical properties of monolayer TMDC

systems with significantly less computational cost than ab initio *GW* calculations.

### 2.5.2 Defect-induced Optical Properties of Monolayer TMDCs

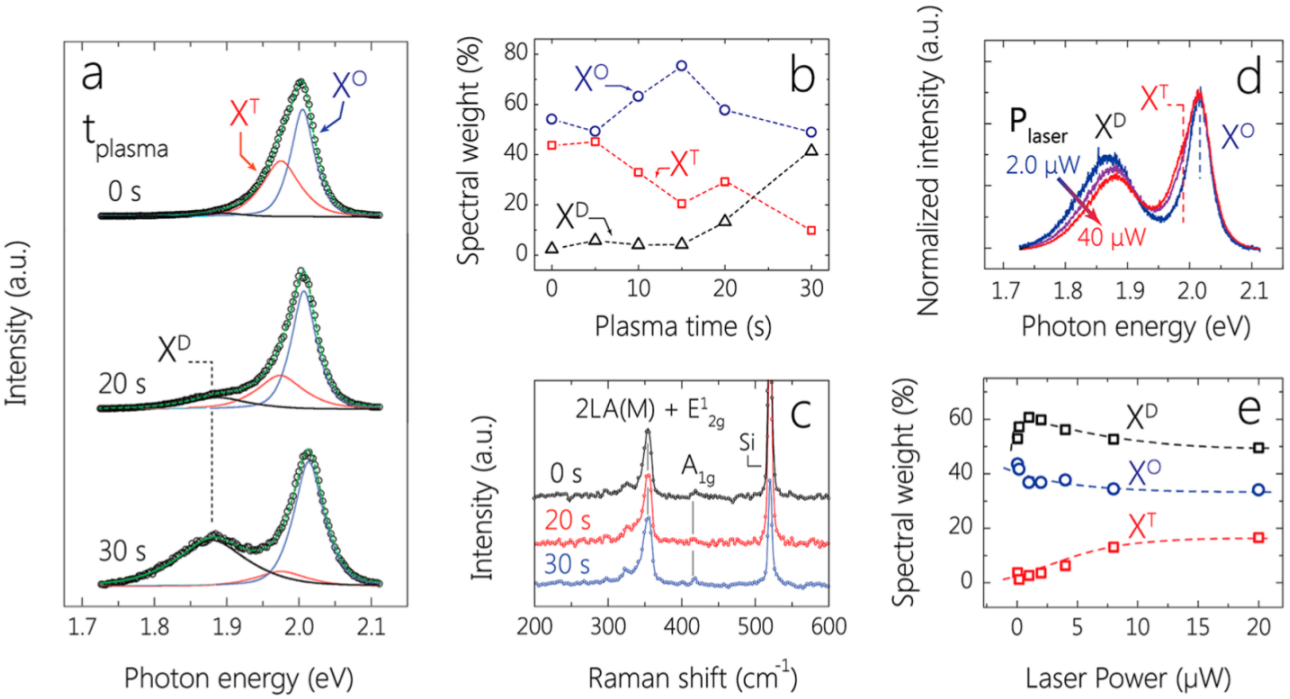



Figure 2.12: (a) PL intensity at 0, 20 and 30 seconds of plasma argon bombardment. (b) Spectral weight of the defect bound excitons $X_D$, neutral excitons $X_O$ and charged excitons $X_T$ as a function of exposure time. (c) PL intensity as a function of Raman shift. (d) Normalised PL as a function of photon energy absorbed. (e) Spectral weight of the defect bound excitons $X_D$, neutral excitons $X_O$ and charged excitons $X_T$, as a function of laser power [13]. Reprinted with permission from [13], Copyright 2015 by the American Chemical Society.

Point defects in the TMDC crystal can act as traps for excitons, which lead to light emission at energies lower than the optical band gap [72]. In work by Chow *et al.* [13], monolayer $MoS_2$ and $WS_2$ were bombarded via argon plasma treatment over time, and the photoluminescence (PL) of the sample was measured. The bombardment caused vacancy defects which resulted in doping when exposed to air, causing a rise in the defect population over time. The PL exhibits a very strong peak occurring at time $t = 0$ s corresponding to the first excited state of neutral excitons that occur in the pristine system, labelled at $X_O$. Additionally at $t = 0$ s, a peak (labelled as $X_T$) forms that corresponds to charged excitons, known as trions, that are known to occur in heavily excited systems and doped systems. Over time (Figure 2.12(b)) during the plasma treatment, there is a period where the spectral weight of the $X_D$ peak is

minimal, while a conversion occurs from trions ($X_T$) to neutral excitons ($X_O$) [13]. After 15 seconds of bombardment, the weight of the $X_D$ peak rises, while $X_T$ continues to fall, and $X_O$ drops significantly more. This indicates a regime in which conversion occurs from neutral excitons (and possible charged excitons) to the defect bound excitons that arise because the hole is heavily localised to the defect atom. It was deduced from comparison to studies of the defect free sample, that the $X_D$ peak arises from the bombardment of TMDCs causing radiative defect states that trap excitons [13].

In the work of Tongay *et al.* [72], $MoS_2$, $MoSe_2$ and $WSe_2$ were irradiated with alpha-particles ($He^{2+}$) to attain desired concentrations of point defects at $5\times10^{13}$ $cm^{-2}$ and $8\times10^{13}$ $cm^{-2}$, in the presence of $N_2$ gas. Similarly, they observe transitions from charged excitons to neutral excitons, which is explained as resulting from the charge depletion associated with the irradiation. The interaction of $N_2$ with the defect sites causes this charge depletion, which stabilises the neutral excitons and destabilises the trions [72]. As the defect concentration is enhanced by irradiation, the authors observe that a peak occurs with lower energy than both the charged and the neutral excitonic resonances, attributed to the radiative recombination of excitons that are bound to the created defects. The origin of these defects is inferred to be the interaction of defect sites with the $N_2$ gas because the observed bound excitonic resonances vanish upon purging of the $N_2$ gas [72]. The $N_2$, inert in the absence of vacancies in the TMDC, interacts with the chalcogen vacancies caused by irradiation, resulting in a small charge transfer from the TMDC to the $N_2$. The discrete defect states that arise from this interaction (which the authors have determined using supplementary first-principles calculations), are believed to be the source of multiple transitions to/from the conduction and valence bands near the band gap of the TMDC [72].

In these experiments, different conclusions have arose when deducing the origin of the low-energy excitonic resonances that occur in the PL spectra. While the work of Tongay *et al.* (vacuum + $N_2$) suggests possible transitions between defect states, Chow *et al.* (ambient air: $O_2$, $N_2$, $H_2O$ etc) suggest that such transitions are not occurring in their experiments, while the strong defect potential traps the excitons. Both observe the conversion between charged and neutral excitons, indicating that the interaction with surrounding gas acts to dope the system, depleting charge. Although these two effects could arise from different sources of point defects,

the effects of the nature of the charged defect may prove to be interesting in the discussion. With different interacting chemicals, the charge transfer may differ between defect species, resulting in transitions to/from defect states that play roles of different importance in the optical spectrum. Thus, a greater understanding of how charged defects interplay with the excitonic features will provide insight to groups that observe such phenomena in PL experiments. This motivates study of how the optical absorption and binding energy of the excitons are modified by the external field caused by a charged defect.

# Chapter 3

# Methods: Monolayer TMDCs

In this chapter, I will discuss the techniques used in my work to gain a deeper and clearer understanding of the electronic and optical properties of charged defects in monolayer transition metal dichalcogenides, briefly outlining relevant theory beforehand. This work has heavily utilised the efficiency and accuracy that tight-binding models provide, and combines them with suitable electrostatic potentials, derived from first-principles, that capture the dielectric screening present in TMDC monolayers. The application of tight-binding theory was selected because of its computational feasibility in modelling periodic systems large enough so that the bound states of a charged defect, placed in the centre of the supercell, are fully captured. This prevents interaction between periodic defect images and thus treats the charged defect as if it were completely isolated in an infinite semiconducting medium. To complement this, first-principles calculations are chosen to determine the electrostatic screening of the defect taking place in the monolayer, producing an accurate defect potential that reflects the short-range behaviour of electrons which is typically overlooked in continuum models.

Firstly, I will provide an overview of the first-principles calculations that were necessary to model the dielectric screening of TMDC monolayers, and the incorporation of this screening into a defect potential. This will cover the density-functional theory (DFT) calculations, the *GW* calculations within the random-phase approximation (RPA) which yielded the dielectric matrix, and the representation of the screening as a continuous, integrable function. Secondly,

I will outline the basics of tight-binding theory, and the orbital structure of the model chosen for this work. This part will then detail how the periodic supercell was constructed in a way to match the Bravais lattice of the unit cell model, and the means by which commonly understood electronic properties were extracted from the solution of this atomistic model. Following this, I will detail the variational approach within the effective mass approximation, used to compare to the results of the atomistic model, as a means to establish similarities to a continuum treatment of defects in 2D semiconductors. In the final section, I will outline the techniques used to calculate the optical conductivity of TMDCs with a charged defect, and derive the tight-binding formulation of the well-known Bethe-Salpeter equation.

## 3.1 Density Functional Theory

### 3.1.1 Theoretical Concept

In this work, the description of how the monolayer TMDC system screens external potentials, from charged defects or otherwise, is reliant on solving the Schrödinger equation and obtaining a large number of electronic bands in the crystal. To do this, the many-body Schrödinger equation is approximated through a technique known as density-functional theory (DFT). This widely used method relies on the theorem by Hohenberg and Kohn [108], that states that the electronic ground state density $n_0(\mathbf{r})$ and ground state energy $E_0$ are uniquely determine by the total crystal potential $V_{\text{crys}}(\mathbf{r})$ acting on the system of electrons. The density $n_0(\mathbf{r})$ is directly obtainable from the many-body ground state wavefunction $\Psi_0(\{\mathbf{r}\})$, where $\{\mathbf{r}\} = \{\mathbf{r}_0, \mathbf{r}_1, \cdots\}$ is the set of coordinates $\mathbf{r}_i$ $(i = 0, 1, \cdots, N-1)$ for all $N$ electrons in the system, and is found by minimising the ground state energy functional $E_0[\Psi_0(\{\mathbf{r}\})]$:

$$E_0[\Psi_0] = \left\langle \Psi_0 \left| \sum_i \left( \frac{-\hbar^2 \nabla^2_{\mathbf{r}_i}}{2m_{\text{e}}} + V_{\text{crys}}(\mathbf{r}_i) \right) + \frac{1}{2} \sum_{i,j \neq i} \frac{e^2}{4\pi\varepsilon_0 |\mathbf{r}_i - \mathbf{r}_j|} \right| \Psi_0 \right\rangle, \tag{3.1}$$

with respect to $\Psi_0(\{\mathbf{r}\})$. Here, $m_{\text{e}}$ is the free electron mass, and $\varepsilon_0$ is the permittivity of free space. To solve this many-body problem, the kinetic energy of the system was expressed

as the sum of single-particle kinetic energies, and the electron-electron interactions expressed as a Hartree integral. The differences between the many-body problem and this simplified representation are accumulated into a functional $E_{\mathrm{xc}}[n_0]$ that accounts for both the exchange and correlation of the electrons. This maps the many-body problem onto a single-particle problem which needs only $E_{\mathrm{xc}}[n_0]$ to be estimated in order to solve. Kohn and Sham showed that by choosing this extra contribution wisely, one can effectively approximate the energy functional as [109]:

$$E_{\mathrm{KS}}[n_0] = \frac{-\hbar^2}{2m_{\mathrm{e}}} \sum_i \langle \psi_i | \nabla^2_{\mathbf{r}_i} | \psi_i \rangle + \int \mathrm{d}\mathbf{r}\; n_0(\mathbf{r}) V_{\mathrm{crys}}(\mathbf{r}) + \int \mathrm{d}\mathbf{r}\; n_0(\mathbf{r}) V_{\mathrm{H}}(\mathbf{r}) + E_{\mathrm{xc}}[n_0], \tag{3.2}$$

where $|\psi_i\rangle$ are single-particle states and $V_{\mathrm{H}}(\mathbf{r})$ is the Hartree potential given by

$$V_{\mathrm{H}}(\mathbf{r}) = \frac{e^2}{4\pi\varepsilon_0} \int \mathrm{d}\mathbf{r}' \frac{n_0(\mathbf{r}')}{|\mathbf{r} - \mathbf{r}'|}, \tag{3.3}$$

and describes the mean-field interaction that arises from the electron density itself. The functional derivative of Eq. (3.2) with respect to the ground-state density, under the constraints of orthonormality for each state, yields a series of single-particle Schrödinger equations for each electron in the system that takes the form [110]:

$$\frac{\delta E_{\mathrm{KS}}[n_0]}{\delta \psi^*(\mathbf{r}_i)} = \frac{-\hbar^2}{2m_{\mathrm{e}}} \nabla^2_{\mathbf{r}_i} \psi_i(\mathbf{r}_i) + v_{\mathrm{eff}}(\mathbf{r}_i)\psi_i(\mathbf{r}_i) - E_i \psi_i(\mathbf{r}_i) = 0 \tag{3.4}$$

$$v_{\mathrm{eff}}(\mathbf{r}_i) = V_{\mathrm{crys}}(\mathbf{r}_i) + V_{\mathrm{H}}(\mathbf{r}_i) + \frac{\delta E_{\mathrm{xc}}[n_0]}{\delta n_0(\mathbf{r}_i)}, \tag{3.5}$$

where $E_i$ is the Lagrange multiplier for the orthonormality condition $\langle \psi_i | \psi_i \rangle = 1$. Eq. (3.4) is solved to obtain *Kohn-Sham* energies $E_i$ and *Kohn-Sham* single-particle states $\psi_i(\mathbf{r})$, that are used to form the ground-state density via [110]:

$$n_0(\mathbf{r}) = \sum_i |\psi_i(\mathbf{r})|^2. \tag{3.6}$$

The procedure to arrive at Eq. (3.6) requires an initial guess of the single-particle states $\psi_i$, typically randomised, which is inserted into Eq. (3.6) to obtain $n_0$, which in turn is inserted

into Eq. (3.2) to obtain a new set of single-particle states. This procedure is iterated until the ground state energy has converged. The accuracy of Eq. (3.2) in representing the true many-body system with an auxiliary system of non-interacting electrons, lies in the careful selection of the exchange-correlation functional $E_{\mathrm{xc}}$.

### 3.1.2 Functionals, Pseudo-potentials and Convergence Parameters

In this work, the Generalised Gradient Approximation (GGA) is used to approximate $E_{\mathrm{xc}}$, which itself is a function of both the ground-state density and its derivative $\nabla n_0$ [111]. This goes beyond the local density approximation (LDA), another commonly used approximation that assumes the system of electrons has a form of $E_{\mathrm{xc}}$ identical to that of a homogeneous electron gas, but is susceptible to overbinding [110]. The GGA allows for a small gradient expansion of $E_{\mathrm{xc}}$, that makes it more suitable for describing systems with greater inhomogeneity. It is found in many crystalline cases to give a significantly better agreement with experiments that determine electronic properties, including ionisation energies and structural energy differences [73]. There exist several formulations of this approximation, and this work primarily utilizes the formulation by Perdew, Burke and Ernzerhof (PBE) [73].

While the selection of an exchange-correlation functional and the continuous iteration of the Kohn-Sham equations are the fundamental concepts for its estimation of the electronic ground state, there are several further simplifications that can be used to improve the efficiency of calculations performed in this framework. It is widely known that, in a material with several multi-shell atoms, the electrons that predominantly participate in inter-atomic bonding are in the outer-most shells of these constituent atoms. Hence, in the iterative procedure, a large proportion of the calculation involves solving Eq. (3.4) for states that do not contribute to any of the interesting features of the material. A solution to this is to repackage what is known as the *core* electron states of atoms that do not participate in bonding nor vary greatly between the materials the atoms are in, into an effective potential that describes the positive nucleus and the core electrons. These are known as *pseudo-potentials*, and act to both greatly simply the number of states to solve Eq. (3.4) for, and to soften the strong divergent Coulomb potential

near the ionic centres. For this work, the choice of pseudo-potential scheme for studying TMDCs is to use so called optimized norm-conserving Vanderbilt (ONCV) pseudo-potentials [112].

For the study of periodic systems, Bloch's theorem states that the wavefunction $\psi_{n\mathbf{k}}(\mathbf{r})$ of an electron in a crystal is the product of a plane-wave and a function $u_{n\mathbf{k}}$ that has the periodicity of the unit cell of the crystal. This periodicity of the plane-wave part, and thus the wavefunction, corresponds to that of a fictitious periodic box of with an arbitrary but large length $L$. This is given formally as:

$$\psi_{n\mathbf{k}}(\mathbf{r}) = e^{i\mathbf{k}\cdot\mathbf{r}} u_{n\mathbf{k}}(\mathbf{r}), \tag{3.7}$$

where $n$ is a band index and $\mathbf{k}$ is the wavevector defined the choice of periodic box and size $L$. In first-principles calculations, it is common to choose a basis that reflects this periodicity, achieved through the use of plane waves. The wavefunction $\psi_i(\mathbf{r})$ can be expanded into Fourier components $\mathbf{q}$ corresponding to plane waves on the grid that includes $\mathbf{k}$, taking the form [110]

$$\psi_i(\mathbf{r}) = \frac{1}{\sqrt{N_q \Omega_{\text{uc}}}} \sum_{\mathbf{q}} c_{i,\mathbf{q}} e^{i\mathbf{q}\cdot\mathbf{r}}, \tag{3.8}$$

where $\Omega_{\text{uc}}$ is the volume of the unit cell, $N_q$ is the total number of plane waves used, and $c_{i,\mathbf{q}}$ are coefficients to be solved for. The effective crystal potential that the electrons experience can be expanded in terms of plane waves corresponding to reciprocal lattice vectors of the crystal:

$$v_{\text{eff}}(\mathbf{r}) = \sum_{\mathbf{G}} v_{\text{eff}}(\mathbf{G}) e^{i\mathbf{G}\cdot\mathbf{r}} \tag{3.9}$$

Inserting this into Eq. (3.4) yields a set of linear equations for the coefficients :

$$\frac{\hbar^2 |\mathbf{k}-\mathbf{G}|^2}{2m_e} c_{i,\mathbf{k}-\mathbf{G}} + \sum_{\mathbf{G}'} v_{\text{eff}}(\mathbf{G}') c_{i,\mathbf{k}-\mathbf{G}-\mathbf{G}'} = E_{i,\mathbf{k}} c_{i,\mathbf{k}-\mathbf{G}}, \tag{3.10}$$

which can be solved to obtain $c_{i,\mathbf{k}-\mathbf{G}}$. It can be seen in Eq. (3.10) that only coefficients with the same value of $\mathbf{k} = \mathbf{q} + \mathbf{G}$ are coupled via a seemingly infinite set of $\{\mathbf{G}\}$ vectors. This produces a unique set of eigenvalue solutions to the Kohn-Sham equations for each wavevector $\mathbf{k}$, which represents continuous bands in reciprocal-space. For computational reasons, the number

of reciprocal lattice vectors $\mathbf{G}$ must be finite, and it is typically the case that the Fourier components $v_{\text{eff}}(\mathbf{G})$ of the potential become small for large enough $\mathbf{G}$. This is due to the relatively smooth and slow variation of the crystal potential of the lattice on scales comparable to the atomic radii. Hence, the smaller wavelength reciprocal lattice vectors can be cut off by introducing an energy $E_{\text{cut}}$ such that the calculation only includes reciprocal lattice vectors that satisfy:

$$\frac{\hbar^2|\mathbf{G}|^2}{2m_0} < E_{\text{cut}}. \tag{3.11}$$

This cut-off, along with the size of the $\mathbf{k}$-point grid $N_k^{(\text{DFT})}$ (corresponding to an $N_k^{(\text{DFT})} \times N_k^{(\text{DFT})}$ periodic supercell), are convergence parameters of the calculation that must be both adjusted up such that the total energy ceases to vary upon further increase, within an acceptable tolerance. It should be noted that the potential and charge density is typically represented on a much finer grid and with a larger cutoff (4 times larger in Quantum Espresso), which avoids aliasing.

Another key convergence parameter in the DFT calculations of quasi-two-dimensional TMDC monolayers, addresses the inability of plane-wave DFT in modelling systems with no periodicity in the out-of-plane direction. To represent features in the out-of-plane direction with plane waves, the monolayer system must also be repeated in this direction. To prevent spurious interaction between consecutive monolayers, the *supercell approximation* is employed, in which isolated systems are approximated with periodic systems with a large period. The periodic images are separated by a length $L_z$ that is large enough to prevent inadvertent bonding to occur in the calculation. However, large values of $L_z$ increase the size of the real-space grid and thus increase the number of $\mathbf{G}_z \propto \frac{1}{L_z}$ plane waves in the out-of-plane direction that would satisfy the condition in Eq. (3.11). This is undesirable because it limits both the computational efficiency of the calculation and the accuracy with which in-plane features can be represented. Hence, a suitable medium is required for an accurate but computationally feasible DFT calculation to be performed. I will specify the values of convergence parameters $E_{\text{cut}}$, $N_k^{(\text{DFT})}$ and $L_z$ in the sections that they are required for.

## 3.2 Defect Potentials

### 3.2.1 Linear Response and the Random-Phase Approximation

The density-density response of a periodic solid to external potentials can be determined by considering a small perturbation in a system in which the electrons only interact through a mean-field potential, known as a *Hartree* potential. This is known as the *random-phase approximation* (RPA) [113]. In this approximation, the total potential $V(\mathbf{r})$ experienced by electrons in the solid can be written as a sum of the external potential $V_{\text{ext}}$ and the mean-field Hartree interaction with the induced density $n_{\text{ind}}(\mathbf{r}', t)$ as a result of $V_{\text{ext}}$:

$$V(\mathbf{r}, t) = V_{\text{ext}}(\mathbf{r}, t) + \int \mathrm{d}\mathbf{r}' \, \frac{e^2 n_{\text{ind}}(\mathbf{r}', t)}{4\pi\varepsilon_0 |\mathbf{r}' - \mathbf{r}|}, \tag{3.12}$$

where $n_{\text{ind}}$ itself can be written in terms of $V_{\text{ext}}$ and a response function $\chi$:

$$n_{\text{ind}}(\mathbf{r}, t) = \int \mathrm{d}\mathbf{r}' \, \chi(\mathbf{r}, \mathbf{r}', t) V_{\text{ext}}(\mathbf{r}', t). \tag{3.13}$$

The response function contains all necessary information for predicting the change in electron density, given an external perturbation. It is possible to estimate $\chi$ by considering a small perturbation and working in the linear regime.

In the presence of small perturbations to the system, linear response theory (LRT) can be adopted to determine the changes to observable quantities as a function of these perturbations. Given a perturbation of the form $V_{\text{pert}}(t) = -F(t)\hat{B}$, where $\hat{B}$ is an operator and $F(t)$ is some time-dependent envelope function, one can determine changes to an observable quantity $\hat{A}$, through the Fourier-space susceptibility [103] [Chapter II]:

$$\chi_{AB}(\omega) = \frac{i}{\hbar} \int_0^\infty \mathrm{d}\tau \, e^{i\tau\omega} \langle \left[ \hat{A}(\tau), \hat{B}(0) \right] \rangle_0, \tag{3.14}$$

where $\left[\hat{A}, \hat{B}\right] = \hat{A}\hat{B} - \hat{B}\hat{A}$ is the operator commutator, $\hat{A}(t) = e^{-i\hat{H}t/\hbar}\hat{A}e^{i\hat{H}t/\hbar}$ gives the operator $\hat{A}$ in the Heisenberg representation, and $\langle \cdots \rangle_0$ denotes the expectation value in the ground

state of the many-body system. The susceptibility describes the *linear* relationship $\Delta A(\omega) = \chi_{AB}(\omega)F(\omega)$ in Fourier-space, between the perturbation and the affected observable. In the context of perturbing electrostatic potentials, LRT can be used to determine the induced density $n_{\text{ind}}(\mathbf{r})$, which itself is the change in the observable quantity that is the total electronic density before and after the perturbation is applied. Typically, this is done in Fourier-space, and calculates the change in components $\hat{n}_{\mathbf{q}}$ of the induced density. The perturbation can be described formally in Fourier-space as a Coulombic Hartree interaction between the electronic density and the charge density $n_{\text{ext}}(\mathbf{q}, t)$ associated with the external potential, taking the form $V(\mathbf{q}, t) = -v_{\mathbf{q}}\hat{n}_{-\mathbf{q}}n_{\text{ext}}(\mathbf{q}, t)$, where $v_{\mathbf{q}}$ is the Fourier transform of the bare Coulomb potential and $\hat{n}_{\mathbf{k}}$ is the charge density operator that can be expressed in terms of the fermionic ladder operators as $\sum_{n\mathbf{k}'} c^{\dagger}_{n\mathbf{k}+\mathbf{k}'}c_{n\mathbf{k}'}$. If the perturbation $\Delta A(\omega)$ of interest is the Fourier-transform of the induced density $n_{\text{ind}}(\mathbf{q}, \omega)$, then Eq. (3.14) can be used by identifying $\hat{n}_{\mathbf{q}}(t)$ as $\hat{A}$ and $-v_{\mathbf{q}}n_{\text{ext}}(\mathbf{q}, t)$ as $F(t)$, and $\hat{n}_{-\mathbf{q}}(t)$ as the operator $\hat{B}$ [103] [Chapter II]. This allows the expression for ratio of the total density to external density to be written as:

$$\frac{n_{\text{ind}}(\mathbf{q}, \omega) + n_{\text{ext}}(\mathbf{q}, \omega)}{n_{\text{ext}}(\mathbf{q}, \omega)} = \frac{1}{\varepsilon(\mathbf{q}, \omega)} = 1 + \lim_{\Gamma \to 0} \frac{iv_{\mathbf{q}}}{\hbar} \int_0^{\infty} \mathrm{d}\tau \; e^{i\tau(\omega + i\Gamma)} \langle [\hat{n}_{\mathbf{q}}(\tau), \hat{n}_{-\mathbf{q}}(0)] \rangle_0, \tag{3.15}$$

where $\Gamma \to 0$ is a damping factor used to regularise the integral [103]. The quantity $\varepsilon(\mathbf{q}, \omega)$ is the dielectric function, and describes the response of electrons in a system to external potentials, mathematically formulating the redistribution of bound charge in a periodic system to screen electric fields.

After first Fourier-transforming in time, we can insert $n_{\text{ind}}$ into the total potential to obtain [114]:

$$V(\mathbf{r}, \omega) = V_{\text{ext}}(\mathbf{r}, \omega) + \int\int \mathrm{d}\mathbf{r}' \mathrm{d}\mathbf{r}'' \; \frac{e^2 \chi(\mathbf{r}', \mathbf{r}'', \omega) V_{\text{ext}}(\mathbf{r}'', \omega)}{4\pi\varepsilon_0 |\mathbf{r}' - \mathbf{r}|} \tag{3.16}$$

$$= \int \mathrm{d}\mathbf{r}'' \left[ \delta(\mathbf{r} - \mathbf{r}'') + \int \mathrm{d}\mathbf{r}' \; \frac{e^2}{4\pi\varepsilon_0 |\mathbf{r}' - \mathbf{r}|} \chi(\mathbf{r}', \mathbf{r}'', \omega) \right] V_{\text{ext}}(\mathbf{r}'', \omega) \tag{3.17}$$

$$= \int \mathrm{d}\mathbf{r}' \; \varepsilon^{-1}(\mathbf{r}, \mathbf{r}', \omega) V_{\text{ext}}(\mathbf{r}', \omega), \tag{3.18}$$

where $\varepsilon^{-1}(\mathbf{r}, \mathbf{r}', \omega)$ is the inverse dielectric function of the system. For the case of a homogeneous

material, this becomes a convolution, such that $\varepsilon^{-1}(\mathbf{r},\mathbf{r}',\omega)=\varepsilon^{-1}(\mathbf{r}-\mathbf{r}',\omega)$. This means that in Fourier-space the dielectric function becomes [114]:

$$\varepsilon^{-1}(\mathbf{q},\omega)=\frac{V(\mathbf{q},\omega)}{V_{\text{ext}}(\mathbf{q},\omega)}. \tag{3.19}$$

For the case of a semiconductor whose electronic structure is represented by a set of single-particle Bloch states $\{\psi_{n\mathbf{k}}(\mathbf{r})\}$ with energies $\{E_{n\mathbf{k}}\}$, the dielectric function takes the Adler-Wiser form [115, 116]:

$$\varepsilon(\mathbf{q},\omega)=1-\frac{v_{\mathbf{q}}}{\Omega}\sum_{\mathbf{k}nn'\sigma}(f_{n\mathbf{k}\sigma}-f_{n'\mathbf{k}+\mathbf{q}\sigma})\frac{\left|\langle\psi_{n'\mathbf{k}+\mathbf{q}\sigma}|e^{i\mathbf{q}\cdot\mathbf{r}}|\psi_{n\mathbf{k}\sigma}\rangle\right|^2}{\hbar\omega-E_{n'\mathbf{k}+\mathbf{q}\sigma}+E_{n\mathbf{k}\sigma}+i\delta}, \tag{3.20}$$

where $\Omega$ is the total volume of the periodic supercell, $f_{n\mathbf{k}}$ is the occupation function of the Bloch state, and $\delta$ is a small positive number that obviates the pole at $\omega=(E_{n'\mathbf{k}+\mathbf{q}}-E_{n\mathbf{k}})/\hbar$. For the case of electrostatic ($\omega=0$) fields applied to an undoped semiconductor, Eq. (3.20) simplifies to

$$\varepsilon(\mathbf{q})=1+\frac{v_{\mathbf{q}}}{\Omega}\sum_{\mathbf{k}cv\sigma}\frac{\left|\langle\psi_{c\mathbf{k}+\mathbf{q}\sigma}|e^{i\mathbf{q}\cdot\mathbf{r}}|\psi_{v\mathbf{k}\sigma}\rangle\right|^2}{E_{c\mathbf{k}+\mathbf{q}\sigma}-E_{v\mathbf{k}\sigma}}, \tag{3.21}$$

where the sum is now over valence band (occupied) states labelled by $v$ and conduction band (unoccupied) states labelled by $c$. We can see how this formalism provides the electronic response of the system to external potentials, as Eq. (3.21) equates to a sum of scattering amplitudes from one state to another by a plane wave, which can be used linearly to construct any potential, where each amplitude is normalised more for scatterings that entail a larger change in the energy. It can also be seen that the denominator of each term decays inverse-linearly with the transition energy, and thus a large number of bands are required to converge this quantity. In this work, a DFT calculation is performed for $MoS_2$ and $WS_2$, in order to obtain the Kohn-Sham states $\psi_{n\mathbf{k}\sigma}$ and eigenvalues $E_{n\mathbf{k}\sigma}$ for a large number of bands in the system, where the eigenstates are labelled by the band index $n$, the wavevector $\mathbf{k}$, and the spin index $\sigma$. These are used to construct the inverse dielectric matrix $\varepsilon^{-1}_{\mathbf{G}\mathbf{G}'}(\mathbf{q})$, where $\mathbf{G}$ are the reciprocal lattice vectors of the crystal that obey Eq. (3.11), and $\mathbf{q}$ is a Fourier component.

This takes the form

$$\varepsilon^{-1}_{\mathbf{G}\mathbf{G}'}(\mathbf{q}) = \delta_{\mathbf{G}\mathbf{G}'} - v_{\text{trunc}}(\mathbf{q}+\mathbf{G}) \sum_{cv\mathbf{k}\sigma} \frac{\langle \psi_{v\mathbf{k}\sigma} | e^{-i(\mathbf{q}+\mathbf{G})\cdot\mathbf{r}} | \psi_{c\mathbf{k}+\mathbf{q}\sigma} \rangle \langle \psi_{c\mathbf{k}+\mathbf{q}\sigma} | e^{-i(\mathbf{q}+\mathbf{G}')\cdot\mathbf{r}} | \psi_{v\mathbf{k}\sigma} \rangle}{E_{c\mathbf{k}+\mathbf{q}\sigma} - E_{v\mathbf{k}\sigma}}, \quad (3.22)$$

where $v_{\text{trunc}}(\mathbf{q})$ is the truncated Coulomb interaction that prevents interaction between periodic monolayers in the out-of-plane direction [102]. This takes the form of

$$v_{\text{trunc}}(\mathbf{q}) = \frac{4\pi}{q_{xy}^2} \left[ 1 - e^{-\frac{q_{xy} L_z}{2}} \cos\left( \frac{q_z L_z}{2} \right) \right], \quad (3.23)$$

where $q_{xy} = \sqrt{q_x^2 + q_y^2}$ is the in-plane wavevector.

### 3.2.2 Calculating the Dielectric Function

In chapter 2, I described the necessary calculations that Qiu *et al.* [12] performed to extract the two-dimensional dielectric function of monolayer $MoS_2$. In this work, the same techniques were adopted to obtain the defect potential, and in this short section of the methods chapter, I will detail the density-functional theory (DFT) parameters necessary for studying charged defects on monolayer TMDCs. Before the dielectric matrix was calculated, a geometry relaxation was performed to determine the crystal structure of $MoS_2$ and $WS_2$.

The workflow began with a geometry relaxation of each TMDC, using a plane-wave DFT code, (`pw.x` in the QUANTUM ESPRESSO 6.1 software package), converging the forces to within $10^{-4}$ eV/Å per atom. This was done within the generalised gradient approximation (GGA), using the Perdew-Burke-Ernzerhof (PBE) exchange-correlation functional and optimized norm-conserving Vanderbilt pseudo-potentials [112]. The chosen unit cell was spanned by lattice vectors $\mathbf{a}_1 = a_m \hat{\mathbf{x}}$ and $\mathbf{a}_2 = \frac{a_m}{2}\left(-\hat{\mathbf{x}} + \sqrt{3}\hat{\mathbf{y}}\right)$, where $a_m$ is the lattice parameter for material $m$, which was found to be [1] $a_{MoS_2} = 3.17$ Å and $a_{WS_2} = 3.189$ Å for $MoS_2$ and $WS_2$, respec-

[1] In the density-functional theory (DFT) calculations of monolayer $MoS_2$ that were used to obtain the Kohn-Sham eigenstates and eigenvalues necessary to insert into the Adler-Wiser formula for $\varepsilon^{-1}_{\mathbf{G}\mathbf{G}'}(\mathbf{q})$, the geometry relaxation resulted in an unconverged lattice parameter $a_{MoS_2} = 3.17$ Å which was 0.47% smaller than the expected value of 3.185 Å. However, using another calculation of the $MoS_2$ effective two-dimensional dielectric function $\varepsilon_{2D}(q)$ (with 25 Ry cutoff) which had been performed with the expected lattice parameter, it was found that this did not significantly change the results in this thesis, as the binding energies only changed by up to 1%.

tively. In these calculations, $E_{\text{cut}}$ and $N_k^{(\text{DFT})}$ were chosen superfluously high at 100 Ry and 15, respectively, while the interlayer separation $L_z$ was chosen at $\approx 18$ Å. This provided the lattice parameter and the optimal geometry for the material. Following this, the optimal values of $E_{\text{cut}}$ and $N_k^{(\text{DFT})}$ were determined by performing a self-consistent field calculation of the ground state for a grid of parameters. The combination of $E_{\text{cut}}$ and $N_k^{(\text{DFT})}$ for which the total energy of the ground state converged within 0.1%, was chosen for that system. Then for the converged values of $E_{\text{cut}}$, $N_k^{(\text{DFT})}$ and $a_m$, the Kohn-Sham wavefunction $\psi_{n\mathbf{k}}$ and eigenvalues $E_{n\mathbf{k}}$ were found for the occupied states in the ground state, along with a large number $N_{\text{bands}}$ of unoccupied states above the band gap. The set of $\psi_{n\mathbf{k}}$ and $E_{n\mathbf{k}}$ were combined in Eq. (3.22) to obtain the inverse dielectric matrix $\varepsilon^{-1}_{\mathbf{GG'}}(\mathbf{q})$ as a function of wavevector difference $\mathbf{q}$. For this, a cutoff for the reciprocal lattice vectors $\mathbf{G}$ was chosen for the system, enough to converge the dielectric matrix. This was chosen as 30 Ry and 25 Ry for $MoS_2$ and $WS_2$, respectively, which then determined the value of $N_{\text{bands}}$ used, which were 2587 and 2543, respectively. As performed for the work of Qiu *et al.* [10], a 2D dielectric function was extracted from $\varepsilon^{-1}_{\mathbf{GG'}}(\mathbf{q})$, according to:

$$\varepsilon^{-1}_{2D}(q) = \frac{q}{2\pi e^2 L_z} \sum_{\mathbf{G}_z\mathbf{G'}_z} \varepsilon^{-1}_{\mathbf{G}_z\mathbf{G'}_z}(\mathbf{q}) v_{\text{trunc}}(\mathbf{q} + \mathbf{G'}_z). \tag{3.24}$$

While $\varepsilon^{-1}_{\mathbf{G_z}\mathbf{G'_z}}(\mathbf{q})$ is sampled on a 2D reciprocal-space grid, the left hand side of Eq. (3.24) is independent of the direction of $\mathbf{q}$ due to the assumption of isotropy which allows for this expression to be derived [10].

### 3.2.3 Screened Defect Potentials

Once the expression $\varepsilon^{-1}_{2D}(q)$ for the effective 2D screening of a charge in a TMDC monolayer was calculated from first-principles, it was integrated in the following formula to obtain the screened potential [14]:

$$V(r; Z, d) = \frac{Ze^2}{4\pi\varepsilon_0} \int \mathrm{d}q \; \varepsilon^{-1}_{2D}(q) J_0(qr) e^{-qd}, \tag{3.25}$$

where $J_0$ is the zeroth order Bessel function of the second kind. The calculated form of $\varepsilon_{2D}^{-1}(q)$ is sampled at the points in the $N_k^{(\mathrm{DFT})} \times N_k^{(\mathrm{DFT})}$ reciprocal-space grid. Hence, to obtain a continuous function that can be integrated in inverse Fourier transforms, the sampled dielectric function needed to be interpolated. At smaller $q \lesssim 1$ Å$^{-1}$, the dielectric function was interpolated via a cubic spline with the `interp1d` functionality of the `scipy.interpolate` library. At larger $q \gtrsim 1$ Å$^{-1}$, reaching beyond the domain of the calculated data, the tail portion of the dielectric function was fitted to a linear sum of inverse power terms, of the form:

$$\tilde{F}(x; A_1, A_2) = 1 + A_1 x^{-1} + A_2 x^{-2}. \tag{3.26}$$

where $A_{1,2}$ are parameters. To improve the accuracy of the fitting, the tail region of the dielectric function was also interpolated. Once interpolated and converted into a functional form, $\varepsilon_{2D}^{-1}(q)$ is inserted into Eq. (3.25). This integral is performed on a log-radial grid, by changing to variable $x$ defined by $q = -q_0 \ln x$, with $q_0 = 1$ Å$^{-1}$.

### 3.2.4 Substrate Screening: Doped Graphene and the Image Effect

In this work, a charged defect in a sheet of monolayer $WS_2$ that rests on a substrate of doped graphene, which itself lies on top of a silicon carbide (SiC) substrate, was studied and compared to scanning tunnelling experiments. To model the specific screening of this system, the dielectric function used to determine the defect potential was modified to account for this setup. The dielectric function for the $WS_2$ monolayer on a doped graphene + SiC substrate takes the form

$$\varepsilon_{\mathrm{RPA}}(q) = -v(q)\chi_{\mathrm{TMD}}(q) - v(q)\chi_{\mathrm{Gr}}(q)e^{-z_{\mathrm{g}}q} + \eta(q), \tag{3.27}$$

where $v(q) = e^2/2\varepsilon_0 q$ denotes the 2D Fourier transform of the Coulomb interaction, $\chi_{\mathrm{Gr}}$ is the polarisability of the doped graphene monolayer, $z_{\mathrm{g}}$ is the separation between the graphene and the $WS_2$, $\eta(q)$ is the contribution from the SiC substrate which accounts for the image charge effect that occurs due to its surface charge density, and $\chi_{\mathrm{TMD}}(q)$ is the polarisability of $WS_2$. The form of $-v(q)\chi_{\mathrm{TMD}}(q) = \varepsilon_{\mathrm{TMD}}(q) - 1$ is extracted from the 2D dielectric function calculated

in Eq. (3.24) from first-principles. The second term in Eq. (3.27) captures the screening from the doped graphene monolayer that sits a distance $z_g = 4.9$ Å beneath the TMD (measured from the plane of the transition metal atoms). The value of $z_g$ was obtained from density-functional theory (DFT) calculations including van der Waals interactions. Specifically, $\chi_{Gr}(q)$ is the RPA polarisability of doped graphene given by [117]:

$$\chi_{Gr}(q) = -\frac{2k_F}{\pi\hbar v_F}\left[1 - \Theta(q - 2k_F)\Lambda(q)\right], \tag{3.28}$$

$$\Lambda(q) = \frac{1}{2}\sqrt{1 - \left(\frac{2k_F}{q}\right)^2} - \frac{q}{4k_F}\cos^{-1}\left(\frac{2k_F}{q}\right), \tag{3.29}$$

where $k_F$ and $v_F$ denote the Fermi wavevector and Fermi velocity of the doped graphene, respectively. From experiment, the values $v_F = 1.15 \times 10^6$ ms$^{-1}$ [118] and $k_F = 0.059$ Å$^{-1}$ [119] were used in this model. The last term $\eta(q)$ in Eq. (3.27) describes the screening by the SiC substrate located a distance $z_s = 1.7$ Å beneath the graphene layer [120]. Due to the spatial gap between the $WS_2$ and the SiC substrate supporting it, the substrate can result in significant change to the screening, which goes beyond the simple average dielectric constant of the substrate and the vacuum above [121]. When a charge is placed on the $WS_2$, there exists a contribution to the total potential from both the induced density of the $WS_2$ by this charge, and the induced response to a second, generally weaker *image* charge that arises from the surface charge density on the surface of the substrate. This additional charge would have an unscreened Coulomb potential of:

$$\Delta W(\mathbf{r}) = -\frac{\varepsilon_{SiC} - 1}{\varepsilon_{SiC} + 1}\frac{e^2}{4\pi\varepsilon_0\sqrt{r^2 + (2h)^2}}, \tag{3.30}$$

where $\varepsilon_{SiC}$ is the dielectric constant of the SiC substrate, and $h$ is the distance separating the substrate from the $WS_2$ layer. Taking the two-dimensional Fourier transform and adding this to the Fourier transform of the unscreened interaction in the layer, one obtains

$$W(q) + \Delta W(q) = \frac{e^2}{2\varepsilon_0 q} - \frac{\varepsilon_{SiC} - 1}{\varepsilon_{SiC} + 1}\frac{e^2}{2\varepsilon_0 q}e^{-2hq} \tag{3.31}$$

$$= \frac{e^2}{2\varepsilon_0 q}\left[\frac{\varepsilon_{SiC}(1 - e^{-2hq}) + (1 + e^{-2hq})}{\varepsilon_{SiC} + 1}\right] \tag{3.32}$$

$$= \frac{e^2}{2\varepsilon_0 q}\frac{2}{\varepsilon_{\mathrm{SiC}}+1}\left[\frac{\varepsilon_{\mathrm{SiC}}\sinh(hq)+\cosh(hq)}{e^{hq}}\right] \tag{3.33}$$

$$= \frac{e^2}{2\varepsilon_0 q}\frac{2}{\varepsilon_{\mathrm{sub}}+1}\left[\frac{\varepsilon_{\mathrm{SiC}}+\coth(hq)}{1+\coth(hq)}\right] = \frac{e^2}{2\varepsilon_0 q\varepsilon_{\mathrm{bg}}(q)}, \tag{3.34}$$

where the relation $e^x \sinh^{-1}(x) = 1 + \coth(x)$ was used, and

$$\varepsilon_{\mathrm{bg}}(q) = \frac{\varepsilon_{\mathrm{SiC}}+1}{2}\frac{1+\coth(hq)}{\varepsilon_{\mathrm{SiC}}+\coth(hq)}. \tag{3.35}$$

It can be seen that as the separation between the $WS_2$ and the substrate tends to $h = 0$, one obtains the commonly used $\varepsilon_{\mathrm{bg}}(q) = \frac{\varepsilon_{\mathrm{sub}}+1}{2}$. In the opposite limit, as $h \to \infty$, it can be seen that $\varepsilon_{\mathrm{bg}}(q) = 1$ and the effects of the substrate predictably vanish, leaving nothing but the vacuum. By setting setting $h = z_{\mathrm{g}} + z_{\mathrm{s}}$ and writing $\varepsilon_{\mathrm{bg}} = \eta$, an image charge model for the SiC substrate yields

$$\eta(q) = \frac{\varepsilon_{\mathrm{SiC}}+1}{2}\frac{e^{q(z_{\mathrm{s}}+z_{\mathrm{g}})} - e^{-q(z_{\mathrm{s}}+z_{\mathrm{g}})} + e^{q(z_{\mathrm{s}}+z_{\mathrm{g}})} + e^{-q(z_{\mathrm{s}}+z_{\mathrm{g}})}}{\varepsilon_{\mathrm{SiC}}\left(e^{q(z_{\mathrm{s}}+z_{\mathrm{g}})} - e^{-q(z_{\mathrm{s}}+z_{\mathrm{g}})}\right) + e^{q(z_{\mathrm{s}}+z_{\mathrm{g}})} + e^{-q(z_{\mathrm{s}}+z_{\mathrm{g}})}} \tag{3.36}$$

$$= \frac{\varepsilon_{\mathrm{SiC}}+1}{2}\frac{2e^{q(z_{\mathrm{s}}+z_{\mathrm{g}})}}{e^{q(z_{\mathrm{s}}+z_{\mathrm{g}})}\left[\varepsilon_{\mathrm{SiC}}\left(1-e^{-2q(z_{\mathrm{s}}+z_{\mathrm{g}})}\right)+1+e^{-2q(z_{\mathrm{s}}+z_{\mathrm{g}})}\right]} \tag{3.37}$$

$$= \frac{\varepsilon_{\mathrm{SiC}}+1}{\varepsilon_{\mathrm{SiC}}+1-(\varepsilon_{\mathrm{SiC}}-1)e^{-2q(z_{\mathrm{s}}+z_{\mathrm{g}})}}, \tag{3.38}$$

with $\varepsilon_{\mathrm{SiC}} = 9.7$ denoting the bulk dielectric constant of SiC [122].

## 3.3 Variational Effective Mass Model

To identify possible conditions and cases in which commonly used continuum theories for charged defects in semiconductors can be applied to monolayer TMDC materials, a variational model within the effective mass approximation (EMA) was implemented. The EMA begins with the expansion of the energy $E_{\mathrm{extrem}}(\mathbf{k})$ of the conduction band minimum or valence band maximum at wavevector as $\mathbf{k}_0$, in terms of the wavevector $\mathbf{k}$ [123]:

$$E_{\mathrm{extrem}}(\mathbf{k}) = E_{\mathrm{extrem}}(\mathbf{k}_0+\delta\mathbf{k}) = E_{\mathrm{extrem}}(\mathbf{k}_0) + \frac{1}{2}\sum_{\alpha,\beta}\frac{\partial^2 E_{\mathrm{extrem}}}{\partial k_\alpha \partial k_\beta}\delta k_\alpha \delta k_\beta + \cdots, \tag{3.39}$$

where $\delta\mathbf{k} = \mathbf{k} - \mathbf{k}_0$ is the deviation of the wavevector from that of the extremum. If Eq. (3.39) is terminated at the quadratic terms, then charge carriers can be described by an effective mass $m^*$ that is independent of $\mathbf{k}$ [123]. While $m^*$ is constant in $\mathbf{k}$, it can be direction-dependent due to anisotropy of the bands [29]. However, if $m^*$ is isotropic and an external potential $V_{\text{ext}}(r)$ is applied to a semiconductor, a carrier in the vicinity of the extremum at $\mathbf{k}_0$ will behave as a free particle with charge $\pm e$ and mass $m^*$ [123]. The wavefunction of an electron in the vicinity of this extremum can be written as an expansion of Bloch functions

$$\psi(\mathbf{r}) = \sum_n \int \mathrm{d}\mathbf{k}\ \phi_n(\mathbf{k})\psi_n(\mathbf{k},\mathbf{r}), \tag{3.40}$$

where $\phi_n(\mathbf{k})$ is the coefficient of the Bloch state $\psi_n(\mathbf{k},\mathbf{r})$ for band $n$ at wavevector $\mathbf{k}$. The wavefunction $\psi$ obeys the time-independent Schrödinger equation:

$$\left[-\frac{\hbar^2\nabla^2}{2m_0} + V_{\text{lat}}(\mathbf{r}) + V_{\text{ext}}(\mathbf{r})\right]\psi(\mathbf{r}) = E\psi(\mathbf{r}) \tag{3.41}$$

$$\sum_n \int \mathrm{d}\mathbf{k}\ \phi_n(\mathbf{k})\left[E_n(\mathbf{k}) + V_{\text{ext}}(\mathbf{r}) - E\right]\psi_n(\mathbf{k},\mathbf{r}) = 0, \tag{3.42}$$

where $m_0$ is the free electron mass, $V_{\text{lat}}(\mathbf{r})$ is the lattice potential of the crystal, and $E$ is energy eigenvalue associated with $\psi$. By multiplying by Bloch state $\psi^*_{n'}(\mathbf{k},\mathbf{r})$ and integrating over $\mathbf{r}$, one obtains a reciprocal-space impurity equation [29]:

$$\left[E_n(\mathbf{k}) - E\right]\phi_n(\mathbf{k}) + \sum_n \phi_{n'}(\mathbf{k})U_{nn'}(\mathbf{k},\mathbf{k}') = 0 \tag{3.43}$$

$$U_{nn'}(\mathbf{k},\mathbf{k}') = \int \mathrm{d}\mathbf{r}\ \psi^*_{n'}(\mathbf{k},\mathbf{r})V_{\text{ext}}(\mathbf{r})\psi_n(\mathbf{k},\mathbf{r}). \tag{3.44}$$

The behaviour of the states at the extremum of conduction or valence bands are particularly interesting in the presence of a potential $V_{\text{ext}}(r)$. For a functional form $V_{\text{ext}}(r)$, such as one that describes a screened Coulomb potential, the EMA assumes that $V_{\text{ext}}(r)$ is slow-varying over space, such that only small wavevector deviations $\delta\mathbf{k}$ from the extremum at $\mathbf{k}_0$ are required to construct solutions $\psi(\mathbf{r})$ using Bloch functions [29]. It is also assumed to be shallow enough such that interband transitions can be neglected to remove the band index $n$ from the summation in

Eq. (3.40). With these assumptions, the Bloch functions used in the expansion in Eq. (3.40) and the wavefunction itself can be approximated by [29]:

$$\psi_{n_0\mathbf{k}}(\mathbf{r}) \approx u_{n_0\mathbf{k}_0}(\mathbf{r})e^{i\mathbf{k}\cdot\mathbf{r}} \tag{3.45}$$

$$\psi(\mathbf{r}) = \left[\int \mathrm{d}\mathbf{k}\; f_{n_0}(\mathbf{k}-\mathbf{k}_0)e^{i(\mathbf{k}-\mathbf{k}_0)\cdot\mathbf{r}}\right] u_{n_0\mathbf{k}_0}(\mathbf{r})e^{i\mathbf{k}_0\cdots\mathbf{r}} = F_{n_0}(\mathbf{r})\psi_{n_0\mathbf{k}_0}(\mathbf{r}), \tag{3.46}$$

where the wavefunction is simply the product of the Bloch function at the extremum and an envelope function $F_{n_0}$. This envelope function can be shown to be the solution to the single-particle Schrödinger equation [123]:

$$\left[-\frac{\hbar^2\nabla^2}{2m^*} + V_{\mathrm{ext}}(\mathbf{r})\right] F_{n_0}(\mathbf{r}) = EF_{n_0}(\mathbf{r}). \tag{3.47}$$

The variational calculations began by defining a Hamiltonian $H_{\mathrm{va}}$ of a single-particle with effective mass $m^*$, confined to a two-dimensional plane, experiencing a potential $V_{\mathrm{ext}} = V_{\mathrm{Keld}}$, which in polar coordinates takes the form:

$$H_{\mathrm{va}} = -\frac{\hbar^2}{2m^*}\left(\frac{\partial^2}{\partial r^2} + \frac{1}{r}\frac{\partial}{\partial r} + \frac{1}{r^2}\frac{\partial^2}{\partial\theta^2}\right) + V_{\mathrm{Keld}}(r). \tag{3.48}$$

In this variational approach to studying charged defects in TMDCs, a defect with charge strength $Z$ and height $d$ above the plane is considered. The Keldysh potential shown in Eq. (2.1) was chosen as the continuum potential for this model, due to its efficiency and its success in modelling such materials at long-range. For the most strongly bound state of this defect potential, a reasonable ansatz is an exponential decay from the defect, identical to that of the $1s$ state in the hydrogenic series. In this work, a modified version of the exponential decay $\propto e^{-\alpha\sqrt{r^2+d^2}}$ with inverse decay scale $\alpha$ is used, such that the softening of the potential due to $d$ is incorporated into the ansatz, which is normalised to give:

$$\psi_{\mathrm{va}}(r;\alpha) = \langle r|\psi_{\mathrm{va}}(\alpha)\rangle = \frac{2\alpha e^{\alpha d}}{\sqrt{2\pi(2\alpha d+1)}}e^{-\alpha\sqrt{r^2+d^2}}. \tag{3.49}$$

To estimate the ground state of $H_{\mathrm{va}}$, the expectation value of $H_{\mathrm{va}}$ is taken in the state $|\psi_{\mathrm{va}}(\alpha)\rangle$ and is minimised with respect to the parameter $\alpha$:

$$E_{\mathrm{va}} = \min_{\alpha} \left\{ \langle \psi_{\mathrm{va}}(\alpha) | H_{\mathrm{va}} | \psi_{\mathrm{va}}(\alpha) \rangle \right\}. \tag{3.50}$$

The energy integral in Eq. (3.50) can be split up into a kinetic component which can be performed analytically, and a potential component that must be calculated numerically. Using the fact that this ansatz is isotropic and thus independent of the azimuthal variable $\theta$, the kinetic energy as a function $\alpha$ is found to be:

$$\begin{aligned}
T_{\mathrm{va}}(\alpha) &= \langle \psi_{\mathrm{va}}(\alpha) | H_{\mathrm{va}} - V_{\mathrm{va}} | \psi_{\mathrm{va}}(\alpha) \rangle && (3.51)\\
&= -\frac{\hbar^2}{2m^*} \int_0^\infty \mathrm{d}r\, 2\pi r \psi_{\mathrm{va}}(r;\alpha) \left( \frac{\partial^2}{\partial r^2} + \frac{1}{r}\frac{\partial}{\partial r} \right) \psi_{\mathrm{va}}(r;\alpha) && (3.52)\\
&= -\frac{\hbar^2}{2m^*} \frac{(2\alpha)^2 e^{2\alpha d}}{(2\alpha d + 1)} \int_0^\infty \mathrm{d}r\, r e^{-2\alpha\sqrt{r^2+d^2}} \left( \frac{-\alpha d^2}{(r^2+d^2)^{\frac{3}{2}}} + \frac{\alpha^2 r^2}{r^2+d^2} + \frac{-\alpha}{\sqrt{r^2+d^2}} \right) && (3.53)\\
&= \frac{\hbar^2}{2m^*} \frac{4\alpha^3 e^{2\alpha d}}{(2\alpha d + 1)} \int_d^\infty \mathrm{d}u\, u e^{-2\alpha u} \left( \frac{d^2}{u^3} + \frac{\alpha(d^2-u^2)}{u^2} + \frac{1}{u} \right) && (3.54)\\
&= \frac{\hbar^2}{2m^*} \frac{4\alpha^3 e^{2\alpha d}}{(2\alpha d + 1)} \left( d^2 \int_d^\infty \mathrm{d}u e^{-2\alpha u} \left[ \frac{1}{u^2} + \frac{\alpha}{u} \right] + \int_d^\infty \mathrm{d}u\, e^{-2\alpha u}(1-\alpha u) \right) && (3.55)\\
&= \frac{\hbar^2}{2m^*} \frac{4\alpha^3 e^{2\alpha d}}{(2\alpha d + 1)} \left( d^2 \left[ \frac{e^{-2\alpha d}}{d} - \alpha\Gamma(0, 2\alpha d) \right] + e^{-2\alpha d} \left( \frac{1}{2\alpha} - \frac{d}{2} - \frac{1}{4\alpha} \right) \right) && (3.56)\\
&= \frac{\hbar^2}{2m^*} \frac{4\alpha^2}{(2\alpha d + 1)} \left( \alpha d \left[ \frac{1}{2} - \alpha d e^{2\alpha d} \Gamma(0, 2\alpha d) \right] + \frac{1}{4} \right), && (3.57)
\end{aligned}$$

where $\Gamma(n, x)$ is the incomplete gamma function defined by

$$\Gamma(n, x) = \int_x^\infty \mathrm{d}t\; t^{n-1} e^{-t}. \tag{3.58}$$

The integral for the potential component is found by evaluating:

$$V_{\mathrm{va}}(\alpha) = \langle \psi_{\mathrm{va}}(\alpha) | V_{\mathrm{Keld}} | \psi_{\mathrm{va}}(\alpha) \rangle = \frac{(2\alpha)^2 e^{2\alpha d}}{(2\alpha d + 1)} \int_0^\infty \mathrm{d}r\; e^{-2\alpha\sqrt{r^2+d^2}} V_{\mathrm{Keld}}(r). \tag{3.59}$$

This uses a log-radial grid akin to the calculation of the defect potential, by converting to a variable $x$ such that $r = -r_0 \ln(x)$, where $r_0 = 1$ Å. The sum of both the kinetic and potential

components is minimzed with respect to $\alpha$ using a Nelder-Mead simplex algorithm that is implemented in the function `fmin` within the `scipy.optimize` library, which provides both the inverse scale length $\alpha_{\min}$ that minimizes $E_{\text{va}}$ and binding energy $E_{\text{va}}(\alpha_{\min})$.

## 3.4 Tight-Binding Calculations

### 3.4.1 Fundamental Concept

The problem of calculating the electronic ground state of a many-body system exactly, entails in theory an immense level of computational power, which is often unattainable by today's standards. It is possible for systems such as the hydrogen and helium atomic systems, which involve only one or two electrons. In large solids with tens of thousands of atoms, each with an orbital structure much more intricate than hydrogen, this becomes interminable without proper means of approximation. There exist a plurality of possible approximations one can make in order to ensure a much quicker calculation time without a significant loss in accuracy, one of which is commonly used in electronic structure and known as tight-binding theory. Tight-binding relies on the concept that the Hilbert space of the wavefunction of states in the system can be spanned by atomic orbitals situated on each of the atoms, and by linearly combining them in the correct way, one can accurately portray the band structure of the system. To determine how the orbitals are combined, one of several methods can be chosen, utilising interactions between an arbitrary number of spatial neighbours for each atomic site. Tight-binding has continued to demonstrate its efficacy for providing very good representations of the band structure of semiconductors in particular, with only a few valence states and nearest neighbour interactions alone needed to converge to the true band structure [124].

Initially, the tight-binding method begins with a commonly used approximation that the many-body wavefunction $|\Psi\rangle$ is separable into single-particle states. This allows the problem to be massively reduced in complexity. The wavefunction of the single-particle state in band $n$ at $\mathbf{k}$

in the Brillouin zone (BZ), is represented by a linear combination of basis states $|\chi_{\mathbf{k}li}\rangle$:

$$|\psi_{n\mathbf{k}}\rangle = \sum_{li} c_{n\mathbf{k}li}|\chi_{\mathbf{k}li}\rangle, \quad \text{where} \quad |\chi_{\mathbf{k}li}\rangle = \frac{1}{N_R}\sum_{\mathbf{R}} e^{i\mathbf{k}\cdot\mathbf{R}}|\phi_{li\mathbf{R}}\rangle, \tag{3.60}$$

where $\langle\mathbf{r}|\phi_{li\mathbf{R}}\rangle = \phi_l(\mathbf{r}-\boldsymbol{\tau}_i-\mathbf{R})$, is the atomic state of orbital $l$ situated on an atom at vector $\boldsymbol{\tau}_i$ in the unit cell, which itself is situated at real-space lattice vector $\mathbf{R}$. The points $\mathbf{R}$ lie on an $N_R \times N_R$ grid, which in turn defines the $N_R \times N_R$ $k$-point grid. It should be noted that the basis chosen for tight-binding models can be done so in specific conventions that determine the phase of the state $|\phi_{li\mathbf{R}}\rangle$ in Eq. (3.60). Another alternative choice of basis to Eq. (3.60) is the inclusion of the vector $\boldsymbol{\tau}_i$ of the atom in the cell, such that

$$|\tilde{\chi}_{\mathbf{k}li}\rangle = \frac{1}{N_R}\sum_{\mathbf{R}} e^{i\mathbf{k}\cdot(\mathbf{R}+\boldsymbol{\tau}_i)}|\phi_{li\mathbf{R}}\rangle. \tag{3.61}$$

The basis states $|\chi_{\mathbf{k}li}\rangle$ are linear combinations of these atomic orbitals chosen in a way to obey Bloch's theorem. The single-particle states are eigenstates of the Hamiltonian $\hat{H}$, obeying the eigenvalue problem

$$\hat{H}|\psi_{n\mathbf{k}}\rangle = E_{n\mathbf{k}}|\psi_{n\mathbf{k}}\rangle \tag{3.62}$$

$$\langle\chi_{\mathbf{k}li}|\hat{H}|\psi_{n\mathbf{k}}\rangle = \langle\chi_{\mathbf{k}li}|E_{n\mathbf{k}}|\psi_{n\mathbf{k}}\rangle \tag{3.63}$$

$$\sum_{mj} H^{\mathbf{k}}_{li,mj} c_{n\mathbf{k}mj} = E_{n\mathbf{k}} c_{n\mathbf{k}li}. \tag{3.64}$$

where the matrix element $H^{\mathbf{k}}_{li,mj}$ obtained for each $k$-point is:

$$H^{\mathbf{k}}_{li,mj} = \langle\chi_{\mathbf{k}li}|\hat{H}|\chi_{\mathbf{k}mj}\rangle = \sum_{\mathbf{R}\mathbf{R}'} \frac{e^{-i\mathbf{k}\cdot(\mathbf{R}-\mathbf{R}')}}{N_R^2}\langle\phi_{li\mathbf{R}}|\hat{H}|\phi_{mj\mathbf{R}'}\rangle = \sum_{\Delta\mathbf{R}} e^{-i\mathbf{k}\cdot\Delta\mathbf{R}}\langle\phi_{li\Delta\mathbf{R}}|\hat{H}|\phi_{mj\mathbf{0}}\rangle \tag{3.65}$$

$$= \sum_{\Delta\mathbf{R}} e^{-i\mathbf{k}\cdot\Delta\mathbf{R}}\left[\delta_{lm}\delta_{ij}\delta_{\Delta\mathbf{R},\mathbf{0}}E_{li} + \sum_{\mathbf{d}_{j\to i}} \delta_{\boldsymbol{\tau}_i+\Delta\mathbf{R}-\boldsymbol{\tau}_j,\mathbf{d}_{j\to i}} V_{li,mj}(\mathbf{d}_{j\to i})\right] \tag{3.66}$$

$$= \delta_{lm}\delta_{ij}E_{li} + \sum_{\mathbf{d}_{j\to i}} V_{li,mj}(\mathbf{d}_{j\to i}) e^{-i\mathbf{k}\cdot(\mathbf{d}_{j\to i}-\boldsymbol{\tau}_i+\boldsymbol{\tau}_j)} \tag{3.67}$$

where $E_{li}$ is the on-site energy of the orbital $l$ on an atom at location $\boldsymbol{\tau}_i$ in the unit cell, $\mathbf{d}_{j\to i}$

is the vector that points from site $\boldsymbol{\tau}_j$ to $\boldsymbol{\tau}_i$, and $V_{li,mj}(\mathbf{d}_{j\to i})$ is known as the hopping integral which represents the scattering energy of the potential between atomic states $|\phi_{li}\rangle$ and $|\phi_{mj}\rangle$.

While the construction of the model with the correct valence atomic orbitals and directional interaction is pertinent to its success in reproducing the desired band structure, the more difficult task that determines its success lies primarily in determining the parameters for the Hamiltonian. For this task there are several, well-documented and tested methods which originate from a variety of quantum mechanical approaches. One of the most common means of obtaining the tight-binding parameters is by analytically or numerically determining the energies that result from the model, and adjusting the parameters until such energies match those obtained from more chemically descriptive calculations, predominantly density-functional theory (DFT). This has the potential to provide accurate results for chemical trends, treatment of alloys as well as semiconductors with defects [125].

### 3.4.2 Constructing a Supercell

To model an isolated charged defect on a two-dimensional semiconductor, a periodic supercell was used, which is large enough to contain the bound states resulting from shallow defects whilst remaining computationally feasible. Typical bound states of shallow defects on the surfaces of semiconductors can extend on the order of tens of nanometres, which means that for a monolayer TMDC, a supercell of about 50 unit cells in length would be adequate. Several tight-binding models have been formulated by different groups to represent the band structure of monolayer TMDCs, with different levels of complexity and accuracy for different regions of the Brillouin zone (BZ) and energy ranges. In this work, the predetermined parameters of one such model by Liu *et al.* are utilised to construct a Hamiltonian for a $51 \times 51$ supercell of monolayer $MoS_2$ and monolayer $WS_2$.

For the purpose of modelling the electronic behaviour of charged defects in semiconductors, both three-dimensional and quasi-two-dimensional, the most important region of the band structure to accurately describe lies close to the band gap and the extrema in both the conduction and valence bands, commonly known as the *low energy* region of the band structure. Throughout

the Brillouin zone (BZ), it is in this region where the most interesting defect-related phenomena occur. This means that it is also a region in which the most significant optical properties of the material manifest themselves, especially for semiconductors whose band gap lies within the visible range of the electromagnetic spectrum. To describe the electronic behaviour of transition metal dichalcogenides (TMDCs) well in the low energy region of the band structure, whilst having a small enough basis set of orbitals to allow efficient calculations over tens of nanometres, the three-band model by Liu *et al.* [1] with a basis of $\{d_{z^2}, d_{xy}, d_{x^2-y^2}\}$ was chosen (the merits of which have been discussed in chapter 2). While lacking in its description of the chalcogen atoms, it can be seen that from the orbital characterisation of the band structure that the $p_{x,y,z}$ orbitals associated with both the top and bottom chalcogens bear minimal importance in the electronic structure of the primary and secondary band extrema at $K/K'$, $\Gamma$ and $Q$. The success of this model's agreement with the ab initio results is mainly due to the large number of parameters included in this model, using first, second and third nearest neighbour interactions. These parameters are optimised such that the model reproduces the low-energy band structure found from a DFT (GGA-PBE) calculation.

The model itself was one of a periodic unit-cell, with lattice parameter $a$ (3.19 Å for $MoS_2$), with a single atomic site in its motif. To adapt this for modelling charged defects, the tight-binding parameters contained within the model by Liu *et al.* were used to construct a supercell for an $N \times N$ periodic slab of monolayer TMDC with supercell lattice parameter $Na$. The unit-cell Hamiltonian of this model, with spin-orbit coupling, was adapted for the purpose of a supercell by expanding the sines and cosines for each of its elements, which was then grouped into terms of common complex exponentials. The coefficient $T_{i,j}^{(\nu)}$ of each complex exponential, written in terms of the hopping parameters of the model, corresponds to the overall hopping parameter in a particular direction, labelled by $\nu$, from orbital $i$ to orbital $j$. These single-hop terms were individually used to formulate the supercell Hamiltonian, which itself does not have terms corresponding to first, second and third nearest neighbours in the same element.

To understand this, consider the unspinned $3 \times 3$ Hamiltonian

$$H_0(\mathbf{k}) = \begin{pmatrix} h_{00}(\mathbf{k}) & h_{01}(\mathbf{k}) & h_{02}(\mathbf{k}) \\ h_{01}^*(\mathbf{k}) & h_{11}(\mathbf{k}) & h_{12}(\mathbf{k}) \\ h_{02}^*(\mathbf{k}) & h_{12}^*(\mathbf{k}) & h_{22}(\mathbf{k}) \end{pmatrix}, \tag{3.68}$$

where $\mathbf{k} = (k_x, k_y)$ is the wavevector of interest. The terms from this Hamiltonian are expanded into their component plane-waves and grouped together to obtain the parameter $T_{i,j}^{(\nu)}$ associated with an electron hopping from one site to another. For the case of $h_{11}(\mathbf{k})$, this results in:

$$\begin{aligned} h_{11}(\mathbf{k}) &= \epsilon_2 + (t_{11} + 3t_{22})\cos(\alpha)\cos(\beta) + 2t_{11}\cos(2\alpha) + 4r_{11}\cos(3\alpha)\cos(\beta) \\ &\quad + 2(r_{11} + \sqrt{3}r_{12})\cos(2\beta) + (u_{11} + u_{22})\cos(2\alpha)\cos(2\beta) + 2u_{11}\cos(4\alpha) \\ &= \epsilon_2 + \frac{(t_{11} + 3t_{22})}{2}\left[\cos(\alpha+\beta) + \cos(\alpha-\beta)\right] + 2t_{11}\cos(2\alpha) + 2r_{11}\left[\cos(3\alpha+\beta) + \cos(3\alpha-\beta)\right] \\ &\quad + 2(r_{11} + \sqrt{3}r_{12})\cos(2\beta) + \frac{(u_{11} + u_{22})}{2}\left[\cos(2\alpha+2\beta) + \cos(2\alpha-2\beta)\right] + 2u_{11}\cos(4\alpha) \\ &= \epsilon_2 + \frac{(t_{11} + 3t_{22})}{4}\left[e^{i(\alpha+\beta)} + e^{i(\alpha-\beta)} + \text{c.c.}\right] + t_{11}\left[e^{2i\alpha} + \text{c.c.}\right] + r_{11}\left[e^{i(3\alpha+\beta)} + e^{i(3\alpha-\beta)} + \text{c.c.}\right] \\ &\quad + (r_{11} + \sqrt{3}r_{12})\left[e^{2i\beta} + \text{c.c.}\right] + \frac{(u_{11} + u_{22})}{4}\left[e^{i(2\alpha+2\beta)} + e^{i(2\alpha-2\beta)} + \text{c.c.}\right] + u_{11}\left[e^{4i\alpha} + \text{c.c.}\right] \end{aligned}$$

where $\alpha = k_x a/2$, $\beta = \sqrt{3}k_y a/2$, $\epsilon_2$ is the on-site energy for the $d_{xy}/d_{x^2-y^2}$ orbitals, while the parameters $t_{11}$, $t_{22}$, $r_{11}$, $r_{12}$, $u_{11}$, and $u_{22}$ are the $d_{xy}-d_{xy}$ hopping integrals, given in reference [1] along with the other hopping parameters $t_0$, $t_1$, $t_2$, $u_0$, $u_1$, $u_2$, $r_0$, $r_\pm$. In this formalism, the directional orbital-orbital hopping integral for each first, second and third nearest neighbour hop, becomes the prefactor of the phase $e^{i\mathbf{k}\cdot\mathbf{v}}$, where $\mathbf{v}$ is the vector associated with the inter-orbital hop. The decomposition of the other Hamiltonian elements into hopping parameters associated with each hop between any two orbitals at neighbouring lattice sites, is given in Table 3.1. While in the unit cell Hamiltonian, the terms in each column of Table 3.1 are multiplied by the appropriate phase $e^{i\mathbf{k}\cdot\mathbf{v}}$ and summed (accounting for both directions) to get a particular element corresponding to a hop between periodic images of the same orbital in neighbouring sites. However, in a supercell Hamiltonian, these individual terms are spread out across different matrix elements corresponding to the atomic sites contained within it, which

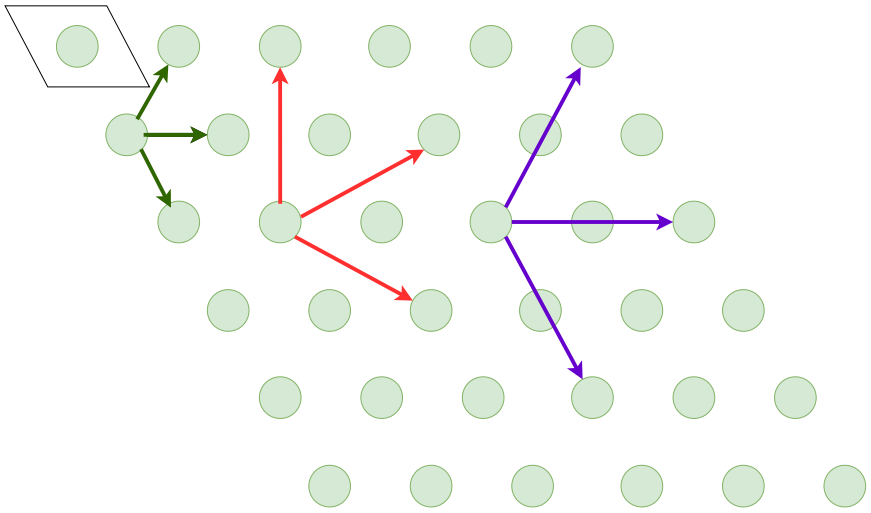


Figure 3.1: $6 \times 6$ supercell of monolayer TMDC shown with just $M$ atoms (green circles) representing the sites in the three-band tight-binding model. The unit cell of the $MoS_2$ is shown as a black rhombus, and the first, second and third nearest neighbour hopping vectors (positive directions only) are shown in green, red and magenta, respectively.

can include the first, second and third nearest neighbours of a particular atomic site. The supercell for this system was constructed as shown in Fig. 3.1, which illustrates the positive form (signs in Table 3.1) of the first, second and third nearest neighbour hopping directions in green, red and magenta, respectively. To construct the Hamiltonian efficiently, *positive* directions were defined such that for a single direction, all hops between all orbitals from site $i \rightarrow j$ can be inputted, and then the hops in opposite direction can be addressed by adding the complex conjugate of the hopping term to the corresponding transpose element of the Hamiltonian. This ensured that the Hamiltonian was Hermitian in its construction. The phase that multiplied the elements in Table 3.1 corresponded to the interatomic displacement between the two atoms. For hops that are completely contained within the supercell, this cancels out the phase $e^{i\mathbf{k}\cdot\mathbf{t}}$, while for terms for which the electron hops out of the supercell into a periodic image, this converts the phase into $e^{i\mathbf{k}\cdot(\zeta_1\mathbf{A}_1+\zeta_2\mathbf{A}_2)}$, where $\zeta_i$ are integers and $\mathbf{A}_{1,2} = N\mathbf{a}_{1,2}$ are the lattice parameters for an $N \times N$ supercell. As a result, all terms added to the Hamiltonian are periodic in $k$-space.

| $\nu$ | $\mathbf{v}$ | $T^{(\nu)}_{z^2,z^2}$ | $T^{(\nu)}_{z^2,xy}$ | $T^{(\nu)}_{z^2,x^2-y^2}$ | $T^{(\nu)}_{xy,xy}$ | $T^{(\nu)}_{xy,x^2-y^2}$ | $T^{(\nu)}_{x^2-y^2,x^2-y^2}$ |
|---|---|---|---|---|---|---|---|
| 1 | $\pm a\left(\frac{\mathbf{x}+\sqrt{3}\mathbf{y}}{2}\right)$ | $t_0$ | $\frac{\mp t_1+\sqrt{3}t_2}{2}$ | $\frac{\mp\sqrt{3}t_1-t_2}{2}$ | $\frac{t_{11}+3t_{22}}{4}$ | $\frac{\sqrt{3}(t_{11}-t_{22})}{4}\pm t_{12}$ | $\frac{3t_{11}+t_{22}}{4}$ |
| 1 | $\pm a\mathbf{x}$ | $t_0$ | $\mp t_1$ | $t_2$ | $t_{11}$ | $\mp t_{12}$ | $t_{22}$ |
| 1 | $\pm a\left(\frac{\mathbf{x}-\sqrt{3}\mathbf{y}}{2}\right)$ | $t_0$ | $\frac{\mp t_1-\sqrt{3}t_2}{2}$ | $\frac{\pm\sqrt{3}t_1-t_2}{2}$ | $\frac{t_{11}+3t_{22}}{4}$ | $\frac{\sqrt{3}(-t_{11}+t_{22})}{4}\pm t_{12}$ | $\frac{3t_{11}+t_{22}}{4}$ |
| 2 | $\pm\sqrt{3}a\mathbf{y}$ | $r_0$ | $0$ | $\frac{2r_{\mp}}{\sqrt{3}}$ | $r_{11}+\sqrt{3}r_{12}$ | $0$ | $r_{11}-\frac{r_{12}}{\sqrt{3}}$ |
| 2 | $\pm a\left(\frac{3\mathbf{x}+\sqrt{3}\mathbf{y}}{2}\right)$ | $r_0$ | $-r_{\pm}$ | $\frac{-r_{\pm}}{\sqrt{3}}$ | $r_{11}$ | $-r_{12}$ | $r_{11}+\frac{2r_{12}}{\sqrt{3}}$ |
| 2 | $\pm a\left(\frac{3\mathbf{x}-\sqrt{3}\mathbf{y}}{2}\right)$ | $r_0$ | $r_{\mp}$ | $\frac{-r_{\mp}}{\sqrt{3}}$ | $r_{11}$ | $r_{12}$ | $r_{11}+\frac{2r_{12}}{\sqrt{3}}$ |
| 3 | $\pm a(\mathbf{x}+\sqrt{3}\mathbf{y})$ | $u_0$ | $\frac{\mp u_1+\sqrt{3}u_2}{2}$ | $\frac{\mp\sqrt{3}u_1-u_2}{2}$ | $\frac{u_{11}+3u_{22}}{4}$ | $\frac{\sqrt{3}(u_{11}-u_{22})}{4}\pm u_{12}$ | $\frac{3u_{11}+u_{22}}{4}$ |
| 3 | $\pm 2a\mathbf{x}$ | $u_0$ | $\mp u_1$ | $u_2$ | $u_{11}$ | $\mp u_{12}$ | $u_{22}$ |
| 3 | $\pm a(\mathbf{x}-\sqrt{3}\mathbf{y})$ | $u_0$ | $\frac{\mp u_1-\sqrt{3}u_2}{2}$ | $\frac{\pm\sqrt{3}u_1-u_2}{2}$ | $\frac{u_{11}+3u_{22}}{4}$ | $\frac{\sqrt{3}(-u_{11}+u_{22})}{4}\pm u_{12}$ | $\frac{3u_{11}+u_{22}}{4}$ |

Table 3.1: Hopping integral $T^{(\nu)}_{i,j}$ from orbitals $i$ to $j$ at different neighbouring sites connected by inter-orbital vector $\mathbf{v}$, in the monolayer $MoS_2$ model by Liu *et al.* [1], in terms of the hopping parameters of the model.

### 3.4.3 Applying Defect Potentials

To model charged adsorbate defects with this TB framework, the presence of such a defect is emulated through the electrostatic potential that is associated with its charge distribution, as well as the screening properties of the medium it resides in. For an arbitrary defect potential $V_{\text{def}}(\mathbf{r})$ as a function of distance from the defect $\mathbf{r}$, associated with a charged impurity, an extra term is added to the diagonal elements $H_{i,i}(\mathbf{k})$ of the $\mathbf{k}$-dependent Hamiltonian for the supercell. This term is equal to the defect potential evaluated at the displacement from the defect site of the atomic site associated with element $i$ in the Hamiltonian basis. Like in the case of the effective mass approach, which is a widely accepted framework for defects in semiconductors [29], the same assumptions of a slow-varying potential that isn't strong enough to induce transitions between bands are applied. Unlike in the effective mass approximation, in which the band structure is assumed to be a perfect parabola, potentially differing in effective mass between directions, the tight-binding model offers the full band structure shape which may vary in effective mass in the vicinity of critical points such as $K$ or $\Gamma$. Just as the effective mass in the EMA is not modified by the presence of the defect, the tight-binding parameters of the model are not modified by the presence of the defect. This is an approximation used in various studies as a means of understanding defects in large tight-binding models, where it becomes unfeasible to recalculate parameters for crystal supercells with an extra defect included [91, 126]. This

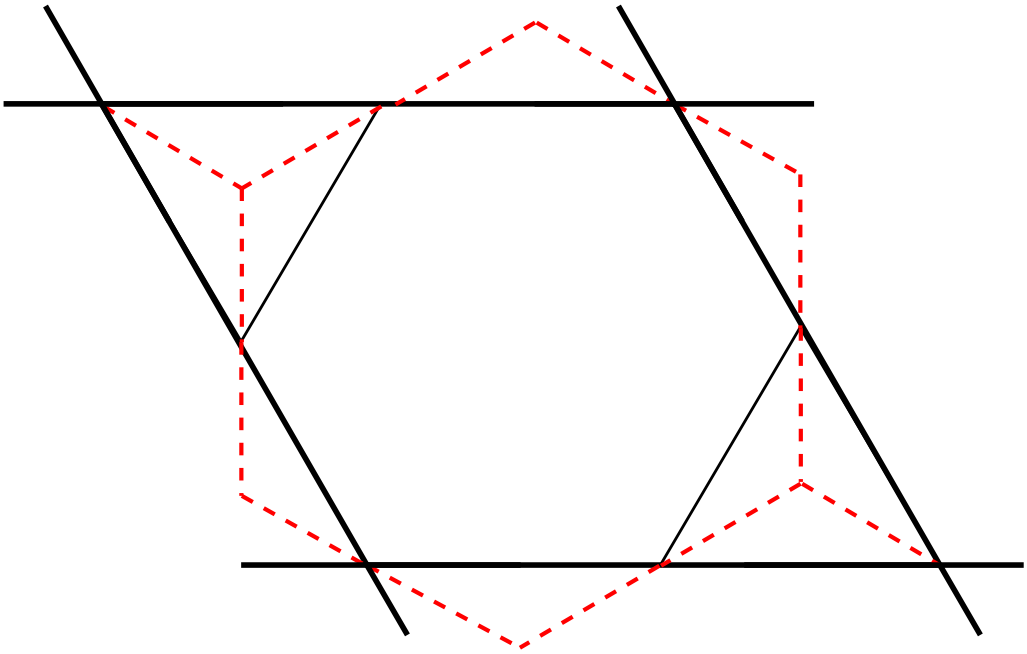


Figure 3.2: Schematic of the rhombic supercell (black) shown along with the lines (red dashed) across which the defect potential is reflected within the triangular corners.

approach has also been used to understand the properties of zinc-blende semiconductors [127]. In this framework the chemical nature of the defect is not important for understanding charged defects in the system, as electrostatic bound states can be treated separately to chemical defect states. It is important to note that the chemical nature of the defect does in many cases result in in-gap defect states that are observable in experiment in the same way that in-gap states bound by the electrostatic defect potential can be observed, and their exclusion in this approach is not dismissive of their importance in deciding the performance of monolayer TMDCs with such defects in transport or optoelectronic devices. However, chemical defect states, such as those associated with adsorbate-substrate bonding, are typically highly localised to the defect site within a few Ångstroms, and thus should not generally alter predictions of electronic phenomena on scales of nanometres, and can be treated independently to the defect states that would arise from the binding nature of the electrostatic defect potential. Additionally, little structural change is made to the lattice in the vicinity of the defect site, such that the unrelaxed TB parameters are a good approximation to the relaxed ones. A large majority of charged defects, typically adsorbates which are a strong focus in this work, tend to distort the lattice minimally, found to be the case in previous works [88, 128].

Due to the rhombic shape of the supercell in the calculation, the application of a potential $V(r)$ where $r$ is simply the distance from the defect in the centre of the supercell (See Fig. 3.2), will result in value discontinuities of the potential energy at the edges of the supercell when the hop of an electron takes it to a site of the supercell's periodic neighbour. The defect potential in the triangular corners of the rhombic supercell in Fig. 3.2 was reflected in the red dashed lines. This was chosen so that the calculation of the continuous potential function $V(r)$ can be adapted to the periodic nature of the rhombus supercells used in the calculations.

### 3.4.4 Calculating the Electronic Properties of the Supercell Model

Solving the TB model is as simple as performing a diagonalisation of the Hamiltonian $H(\mathbf{k})$ in an eigenvalue problem described by Eq. (3.63). From these two components of the solution to the TB model, several observable quantities can be extracted and used to predict the electronic signatures of charged defects in monolayer TMDCs. Firstly, the probability density of the state, or the *modulus square* of the wavefunction of the state, gives the approximated probability of an electron in that state to exist on a particular orbital of a particular atom in the system. Given an eigenvector solution $\mathbf{c}_{n\mathbf{k}}$ to Eq. (3.63), the modulus square wavefunction is

$$|\psi_{n\mathbf{k}i}|^2 = \sum_{ls} |c_{n\mathbf{k}lsi}|^2 \tag{3.69}$$

where the sum is over all orbitals $l$ and both spin states $s$ associated with atomic site $i$. To understand the composition and orbital character of the resulting states associated with the charged defect + supercell model, it is useful to determine how they project onto the states $|\psi^0_{n\mathbf{k}}\rangle$ of the pristine system. This first requires a knowledge of how the bands of the pristine unit cell system fold when the supercell is created. Upon a simple extension of the unit cell to a supercell, keeping the lattice vectors proportional to those of the unit cell model, a diagonalisation of the Hamiltonian at point $\mathbf{k}$ in the supercell BZ will produce an eigensystem containing the set of eigenvalue solutions for all points $\mathbf{k} + \mathbf{g}$, where $\{\mathbf{g}\}$ is the set of all supercell reciprocal lattice vectors that are uniquely contained within the BZ of the unit cell. Hence by constructing these pristine supercell states (i.e. without the defect potential) by manually folding pristine unit

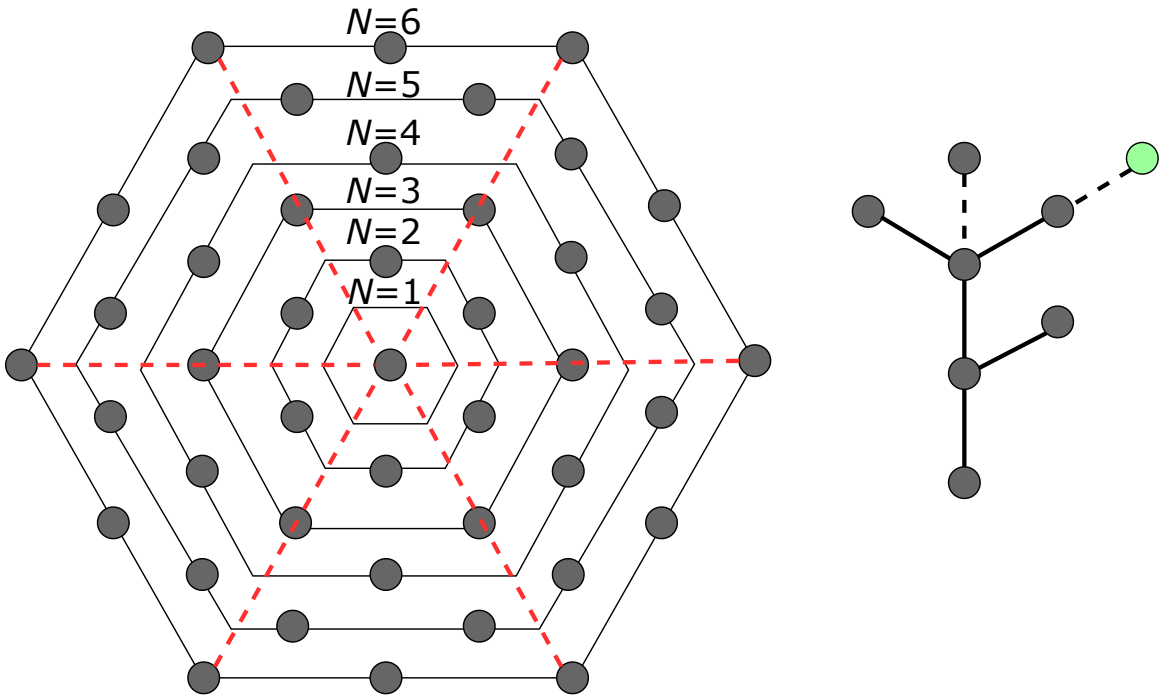



Figure 3.3: (left) Schematic of the band folding of reciprocal lattice vectors (grey circles), with the central circle representing the Γ point and the red dashed lines are the sectants of the hexagon. Each hexagon labelled by supercell size $N$, corresponds to the relative size of the unit cell BZ when the smallest hexagon is the supercell BZ. (right) Example of tree algorithm to determine folding points for $N = 6$, where the dashed lines are only counted for the first three sectants of the hexagonal BZ and the green circle indicates the $K/K'$ which should only be counted in two neighbouring sectants.

cell eigenstates onto the supercell Brillouin zone, such that they have the same atomic and orbital basis as the supercell Hamiltonian with a charged defect, the origin and composition of the states associated with the system with a charged defect can be identified and studied with respect to the unperturbed states of the pristine system. To construct a state for an $N \times N$ supercell at point $\mathbf{k}$ in the supercell BZ, the set of lattice vectors that fold onto $\mathbf{k}$ are found for the particular value of $N$ as depicted in Fig. 3.3 (left). In this schematic, for a given $N$, each hexagon represents the relative size of the unit cell BZ when the smallest ($N = 1$) hexagon is the supercell BZ, and the points that lie within this hexagon, excluding duplicates on the edge, are considered for folding. While an exhaustive search can be performed for this task, the lattice points are found instead using an in-house hexagonal tree algorithm, which determines all points in a given sectant that do not overlap with neighbouring sectants. This also avoids including duplicates at the edges of the BZ, by only counting the BZ edges for three consecutive

sectants and prevents duplicates of the $K$ and $K'$ points by only counting the right corner points for the first two of them. The TB Hamiltonian was solved at these points to determine the pristine unit cell states $|\psi^0_{n\mathbf{k}+\mathbf{g}}\rangle$. Bloch's theorem dictates that the translation of a quantum state at wavevector $\mathbf{k}$ in a periodic crystal by an integer number of lattice vectors $\mathbf{t}$, simply results in multiplying the state by a phase $e^{i\mathbf{k}\cdot\mathbf{v}}$. As such, the construction of pristine supercell states involves the concatenation of copies of a particular unit cell state each translated by a unit cell lattice vector within the supercell, which takes the form:

$$|\psi_{\tilde{n}\mathbf{k}}\rangle = \frac{1}{N}\begin{pmatrix} e^{i\mathbf{k}\cdot\boldsymbol{\tau}_0} \\ e^{i\mathbf{k}\cdot\boldsymbol{\tau}_1} \\ \vdots \\ e^{i\mathbf{k}\cdot\boldsymbol{\tau}_{N^2-1}} \end{pmatrix} \bigotimes |\psi^0_{n\mathbf{k}+\mathbf{g}}\rangle, \tag{3.70}$$

where $\bigotimes$ is the tensor product operator, and $\tilde{n} \equiv (n, \mathbf{g})$ is the band index of the supercell model, which can be bijectively mapped to a combination of a supercell reciprocal lattice vector $\mathbf{g}$ and the band index of the unit cell model. The prefactor $\frac{1}{N}$ is for normalisation, accounting for the increased size of the basis by $N^2$. The projection of an eigenstate $|\psi'_{\tilde{m}\mathbf{k}}\rangle$ of the supercell Hamiltonian for an arbitrary defect potential, onto the $n$th band at $\mathbf{k}+\mathbf{g}$ in the BZ is determined through

$$\Pi_{\tilde{m}\mathbf{k},n}(\mathbf{k}+\mathbf{g}) = |\langle\psi_{\tilde{n}\mathbf{k}}|\psi'_{\tilde{m}\mathbf{k}}\rangle|^2. \tag{3.71}$$

Typically, many of the supercell wavefunctions calculated in this work are calculated at $\Gamma$ for a supercell size $N = 3n$ such that $n \in \mathbb{N}$ so that the $K/K'$ points fold onto the $\Gamma$ point.

In this work, the effective mass of band extrema plays an important role in interpreting the results of placing a charged defect in the system. Due to this, the formula for the effective mass at high-symmetry point $P$ along $k$-space axis $j = x, y$ is approximated via a finite difference expression of the form:

$$\frac{m^*_{P,j}}{m_0} = \frac{\hbar^2}{m_0}\left(\frac{\partial^2 E_{v,\mathbf{k}_P}}{\partial k_j^2}\right)^{-1} \tag{3.72}$$

$$= 7.639 \text{ eVÅ}^{-2} \left( \frac{-(E_{\upsilon,\mathbf{k}_P-\delta\mathbf{k}_j} + E_{\upsilon,\mathbf{k}_P+\delta\mathbf{k}_j}) + 16(E_{\upsilon,\mathbf{k}_P-2\delta\mathbf{k}_j} + E_{\upsilon,\mathbf{k}_P+2\delta\mathbf{k}_j}) - 30E_{\upsilon,\mathbf{k}_P}}{12|\delta\mathbf{k}_j|^2} \right)^{-1}, \tag{3.73}$$

where $\upsilon$ is the band of interest, $\mathbf{k}_P$ is the $k$-space vector corresponding to $P$, $E_{\upsilon,\mathbf{k}}$ is the energy of the band $\upsilon$ at $\mathbf{k}$ in the BZ, and $\delta\mathbf{k} = \bar{\epsilon}\frac{4\pi}{3a}\hat{\mathbf{j}}$ is a small increment vector along the direction $\hat{\mathbf{j}}$, proportional to the $K/K'$ separation, with $\bar{\epsilon} = 10^{-6}$. This approximation is accurate up to fourth order in $|\delta\mathbf{k}_j|$, and the expression is dimensionless because the band energy and wavevectors are given in eV and $\text{Å}^{-1}$, respectively.

The local density of states (LDOS) is an important quantity that is directly proportional to an observable experimental signature that a charged defect has on a monolayer TMDC sample. As mentioned in chapter 2, the LDOS is proportional to the derivative of the tunnelling current in scanning tunnelling spectroscopy (STS) experiments. To calculated this from the TB model, the Hamiltonian is solved on a grid of points $\{\mathbf{k}\}$ and corresponding weights $w_\mathbf{k}$ that span a reduced BZ of the monolayer TMDC. For this honeycomb lattice structure, a choice of reduced BZ is shown as a triangle whose vertices lie on $\Gamma$, $K$ and $K'$ in Fig. 2.4(f). The resulting eigenvectors $\mathbf{c}_{n\mathbf{k}}$ and eigenvalues $E_{n\mathbf{k}}$ on this grid are combined with a Gaussian broadening function $G(E; E_{n\mathbf{k}}, W)$ with broadening width $W$ to get a term that depends on lattice site in the crystal $i$ and the energy the LDOS is being measured at, namely:

$$\rho_{\text{LDOS}}(\mathbf{r}_i, E; W) = \frac{1}{N_k^2 \Omega} \sum_{\mathbf{k}} \sum_{\{l\}\in\mathbf{r}_i} w_\mathbf{k} |c_{\mathbf{n}\mathbf{k}li}|^2 G(E; E_{n\mathbf{k}}, W), \tag{3.74}$$

where $\Omega$ is the crystal area and $N_k^2$ is the sum of all weights in the $k$-grid. The broadening was chosen at $W = 0.02$ eV both because it was close to the thermal energy scale at room temperature, and to smooth the LDOS while retaining the structure of the peaks corresponding to defect resonances.

## 3.5 Optical Properties and the Bethe-Salpeter Equation

### 3.5.1 Velocity Matrix Element and Optical Conductivity

To determine the optical properties of the monolayer TMDC system, the strength with which transitions between occupied and unoccupied electronic states couple to the illuminating radiation is determined predominantly by their matrix elements of the velocity operator. In the tight-binding formulation, the velocity matrix element takes the form [129]:

$$v_{cv}(\mathbf{k}) = \langle \psi_{c\mathbf{k}} | \nabla_{\mathbf{k}} H(\mathbf{k}) | \psi_{v\mathbf{k}} \rangle = \sum_{limj} c^*_{c\mathbf{k}li} c_{v\mathbf{k}mj} \langle \chi_{\mathbf{k}li} | \nabla_{\mathbf{k}} H(\mathbf{k}) | \chi_{\mathbf{k}mj} \rangle. \tag{3.75}$$

To determine the value of the derivative, the convention of tight-binding model must be considered, as this can modify the form of the momentum matrix element. This makes use of the tight-binding basis:

$$\chi_{\mathbf{k}li}(\mathbf{r}) = \frac{1}{N_k} \sum_{\mathbf{R}} e^{i\mathbf{k}\cdot\mathbf{R}} \phi_l(\mathbf{r} - \mathbf{R} - \boldsymbol{\tau}_i), \tag{3.76}$$

where $N_k$ is the size of the $N_k \times N_k$ grid of $k$-points the Schrödinger equation is solved on. The velocity matrix element then takes the form:

$$\nabla_{\mathbf{k}} H(\mathbf{k}) = \sum_{limj} \left[ \nabla_{\mathbf{k}} H_{limj}(\mathbf{k}) |\chi_{\mathbf{k}li}\rangle\langle\chi_{\mathbf{k}mj}| + H_{limj}(\mathbf{k}) \nabla_{\mathbf{k}} \left( |\chi_{\mathbf{k}li}\rangle\langle\chi_{\mathbf{k}mj}| \right) \right] \tag{3.77}$$

$$\nabla_{\mathbf{k}} \left( |\chi_{\mathbf{k}li}\rangle\langle\chi_{\mathbf{k}mj}| \right) = \frac{i}{N_k^2} \sum_{\mathbf{R}\mathbf{R}'} (\mathbf{R} - \mathbf{R}') e^{i\mathbf{k}\cdot(\mathbf{R}-\mathbf{R}')} |\phi^{\mathbf{R}}_{l\boldsymbol{\tau}_i}\rangle\langle\phi^{\mathbf{R}'}_{m\boldsymbol{\tau}_j}| \tag{3.78}$$

$$\langle \chi_{\mathbf{k}li} | \nabla_{\mathbf{k}} H(\mathbf{k}) | \chi_{\mathbf{k}mj} \rangle = \nabla_{\mathbf{k}} H_{limj}(\mathbf{k}) + i H_{limj}(\mathbf{k}) \frac{1}{N_k^4} \sum_{\mathbf{R}\mathbf{R}'} (\mathbf{R} - \mathbf{R}') = \nabla_{\mathbf{k}} H_{limj}(\mathbf{k}) \tag{3.79}$$

$$\langle \psi_{c\mathbf{k}} | \nabla_{\mathbf{k}} H(\mathbf{k}) | \psi_{v\mathbf{k}} \rangle = \sum_{limj} c^*_{c\mathbf{k}li} c_{v\mathbf{k}mj} \nabla_{\mathbf{k}} H_{limj}(\mathbf{k}). \tag{3.80}$$

There are several ways to determine the matrix element of $\nabla_{\mathbf{k}} \hat{H}_{limj}(\mathbf{k})$. The first is via a finite difference for the first derivative, which can be used for the case of specific directions, for example, $\partial_{k_x}$. A second way is to use the generic form of a tight-binding term in this model, $B_i e^{i\mathbf{k}\cdot\mathbf{a_i}}$. Hopping between different unit cells is achieved through the use of complex

exponentials, therefore given a direction $\mathbf{e}$, the derivative of these individual terms is

$$\mathbf{e} \cdot \nabla_{\mathbf{k}} (B e^{i\mathbf{k}\cdot\mathbf{d}}) = i(\mathbf{e}\cdot\mathbf{d}) B e^{i\mathbf{k}\cdot\mathbf{d}}, \tag{3.81}$$

which can be used to build the gradient of the Hamiltonian analytically. This means that the imaginary part of the dielectric function and thus the optical conductivity, are calculated through the formulae [130]:

$$\varepsilon_2(\omega) = \frac{e^2}{\varepsilon_0 \Omega} \sum_{c,v,\mathbf{k}} \frac{|\mathbf{e}\cdot\langle\psi_{c\mathbf{k}}|\nabla_{\mathbf{k}}\hat{H}(\mathbf{k})|\psi_{v\mathbf{k}}\rangle|^2}{(E_{c\mathbf{k}} - E_{v\mathbf{k}})^2} \delta(\hbar\omega - E_{c\mathbf{k}} + E_{c\mathbf{k}}) \tag{3.82}$$

$$\sigma(\omega) = \frac{e^2}{\hbar \Omega} \sum_{c,v,\mathbf{k}} \frac{|\mathbf{e}\cdot\langle\psi_{c\mathbf{k}}|\nabla_{\mathbf{k}}\hat{H}(\mathbf{k})|\psi_{v\mathbf{k}}\rangle|^2}{E_{c\mathbf{k}} - E_{v\mathbf{k}}} \delta(\hbar\omega - E_{c\mathbf{k}} + E_{c\mathbf{k}}), \tag{3.83}$$

where $\Omega$ is the total area of the fictitious periodic box used to model the two-dimensional crystal. Note that for TMDCs, rank 2 tensors are in-plane isotropic because of the $D_{3h}$ point group [130]. To check units, the prefactor of the sum is $\mathrm{eV\AA}^{-1}$, as $e^2/\varepsilon_0 = 4\pi r V_{\mathrm{Coul}}(r)$ has units of eVÅ, while each term in the sum has $\mathrm{eV}^{-1}$ from the dirac delta, $\mathrm{eV}^{-2}$ from the energies, and $\mathrm{eV}^2\mathrm{\AA}^2$ from the matrix element. This means that overall, the imaginary part of the dielectric function is dimensionless as expected.

### 3.5.2 Bethe-Salpeter Equation

Excitons are the bound state of an electron and a hole, and the inclusion of such states into the optical conductivity requires the solution to the two-particle problem of the attractive interaction between a valence hole and a conduction electron [107]. Exciton states can be constructed from single electron-hole states:

$$|\chi_Q\rangle = \sum_{vc\mathbf{k}} \psi_Q(\mathbf{k}, c, v) b^\dagger_{(\mathbf{k}+Q)c} b_{\mathbf{k}v} |0\rangle \tag{3.84}$$

where $Q$ is the centre-of-mass momentum of the electron-hole pair, $b_{\mathbf{k}n}(b^\dagger_{\mathbf{k}n})$ are the annihilation (creation) operators for fermions, and $|0\rangle$ is the many-body ground state. The summation

over non-interacting transitions runs over indices $c$ and $v$, referring to the conduction and valence band, respectively, between which the transition takes place, as well as running over the wavevector $\mathbf{k}$. In the work of MacDonald [107], the coefficients $\psi_Q(\mathbf{k}, c, v)$, which also constitutes the exciton wavefunction, are obtained from the Bethe-Salpeter Equation (BSE). The BSE is an eigenvalue equation for the matrix defined by [107]:

$$\langle \mathbf{k}, c, v, Q | H_{\mathrm{BSE}} | \mathbf{k}', c', v', Q \rangle = \delta_{vv'}\delta_{cc'}\delta_{\mathbf{k}\mathbf{k}'}(E_{(\mathbf{k}+Q)c} - E_{\mathbf{k}v}) - (D - X)^{cc'}_{vv'}(\mathbf{k}, \mathbf{k}', Q), \tag{3.85}$$

where $D$ and $X$ are the direct and exchange integrals, respectively. These originate from the Fourier transforms of the two-body integrals between states at different $k$ points involving transitions between conduction bands and valence bands:

$$D^{cc'}_{vv'}(\mathbf{k}, \mathbf{k}', Q) = \int \mathrm{d}^3 r \mathrm{d}^3 r' \psi_{v\mathbf{k}}(\mathbf{r}) \psi^*_{c\mathbf{k}+\mathbf{Q}}(\mathbf{r}') V_{\mathrm{int}}(\mathbf{r}, \mathbf{r}') \psi^*_{v'\mathbf{k}'}(\mathbf{r}) \psi_{c'\mathbf{k}'+\mathbf{Q}}(\mathbf{r}') \tag{3.86}$$

$$X^{cc'}_{vv'}(\mathbf{k}, \mathbf{k}', Q) = \int \mathrm{d}^3 r \mathrm{d}^3 r' \psi_{v\mathbf{k}}(\mathbf{r}) \psi^*_{c\mathbf{k}+\mathbf{Q}}(\mathbf{r}) \tilde{V}_{\mathrm{int}}(\mathbf{r}, \mathbf{r}') \psi^*_{v'\mathbf{k}'}(\mathbf{r}') \psi_{c'\mathbf{k}'+\mathbf{Q}}(\mathbf{r}'), \tag{3.87}$$

where $V_{\mathrm{int}}$ and $\tilde{V}_{\mathrm{int}}$ are the screened and unscreened interaction, respectively. The expression for the TB basis of a three-band unit cell model is inserted into this equation, to prove the form in MacDonald's paper is appropriate. For the direct term in the chosen tight-binding basis, the equation evaluates to:

$$D^{cc'}_{vv'}(\mathbf{k}, \mathbf{k}', \mathbf{Q}) = \sum_{\substack{lmij \\ l'm'i'j'}} c^*_{c\mathbf{k}+\mathbf{Q}li} c_{v\mathbf{k}mj} c_{c'\mathbf{k}'+\mathbf{Q}l'i'} c^*_{v'\mathbf{k}'m'j'} I^{lmij}_{l'm'i'j'}(\mathbf{k}, \mathbf{k}', \mathbf{Q}) \tag{3.88}$$

$$I^{lmij}_{l'm'i'j'}(\mathbf{k}, \mathbf{k}', \mathbf{Q}) = \int \mathrm{d}\mathbf{r} \mathrm{d}\mathbf{r}' \chi^*_{\mathbf{k}+\mathbf{Q}li}(\mathbf{r}) \chi_{\mathbf{k}mj}(\mathbf{r}') V_{\mathrm{int}}(\mathbf{r}, \mathbf{r}') \chi_{\mathbf{k}'+\mathbf{Q}l'i'}(\mathbf{r}) \chi^*_{\mathbf{k}'m'j'}(\mathbf{r}') \tag{3.89}$$

$$= \sum_{\substack{\mathbf{R_1}\mathbf{R_2} \\ \mathbf{R_3}\mathbf{R_4}}} \frac{e^{-i(\mathbf{k}+\mathbf{Q})\cdot\mathbf{R}_1 + i\mathbf{k}\cdot\mathbf{R}_2 + i(\mathbf{k}'+\mathbf{Q})\cdot\mathbf{R}_3 - i\mathbf{k}'\cdot\mathbf{R}_4}}{N_k^4} K^{lmij}_{l'm'i'j'}(\mathbf{R}_1, \mathbf{R}_2, \mathbf{R}_3, \mathbf{R}_4) \tag{3.90}$$

$$K^{lmij}_{l'm'i'j'}(\{\mathbf{R}_i\}) = \int \mathrm{d}\mathbf{r} \phi_{li\mathbf{R}_1}(\mathbf{r}) \phi_{l'i'\mathbf{R}_3}(\mathbf{r}) \int \mathrm{d}\mathbf{r}' V_{\mathrm{int}}(\mathbf{r} - \mathbf{r}') \phi_{mj\mathbf{R}_2}(\mathbf{r}') \phi_{m'j'\mathbf{R}_4}(\mathbf{r}') \tag{3.91}$$

$$\approx \delta_{\mathbf{R_2}\mathbf{R_4}} \delta_{mm'} \delta_{jj'} \delta_{\mathbf{R_1}\mathbf{R_3}} \delta_{ll'} \delta_{ii'} V_{\mathrm{int}}(\mathbf{R}_1 - \mathbf{R}_2 + \boldsymbol{\tau}_i - \boldsymbol{\tau}_j) \tag{3.92}$$

$$I^{lmij}_{l'm'i'j'}(\mathbf{k}, \mathbf{k}', \mathbf{Q}) = \delta_{mm'}\delta_{ll'}\delta_{ii'}\delta_{jj'} \sum_{\mathbf{R}} \frac{e^{-i(\mathbf{k}-\mathbf{k}')\cdot\mathbf{R}}}{N_k^2} V_{\mathrm{int}}(\mathbf{R} + \boldsymbol{\tau}_i - \boldsymbol{\tau}_j) = \delta_{mm'}\delta_{ll'}\delta_{ii'}\delta_{jj'} V_{ij}(\mathbf{k} - \mathbf{k}') \tag{3.93}$$

$$D^{cc'}_{vv'}(\mathbf{k},\mathbf{k},Q) = \sum_{ij}\left(\sum_{l} c^{*}_{c\mathbf{k}+\mathbf{Q}li}c_{c'\mathbf{k}'+\mathbf{Q}li}\right)V_{ij}(\mathbf{k}-\mathbf{k}')\left(\sum_{m} c_{v\mathbf{k}mj}c^{*}_{v'\mathbf{k}'mj}\right), \tag{3.94}$$

where it is approximated that the states $\phi_{li\mathbf{R}}(\mathbf{r}) = \phi_l(\mathbf{r}-\mathbf{R}-\boldsymbol{\tau}_i)$ are highly localised delta functions centred on $\mathbf{R}+\boldsymbol{\tau}_i$. Proceeding similarly for the exchange term,

$$X^{cc'}_{vv'}(\mathbf{k},\mathbf{k},\mathbf{Q}) = \sum_{ij}\left(\sum_{l} c^{*}_{c\mathbf{k}+\mathbf{Q}li}c_{c'\mathbf{k}'+\mathbf{Q}li}\right)\tilde{V}_{ij}(\mathbf{Q})\left(\sum_{m} c_{v\mathbf{k}mj}c^{*}_{v'\mathbf{k}'mj}\right). \tag{3.95}$$

In the case of the unit cell for the three-band monolayer TMDC model, there is no index for atoms in the basis, and thus the equations reduce to a simplified form [107]:

$$\begin{aligned} D^{cc'}_{vv'}(\mathbf{k},\mathbf{k}',\mathbf{Q}) &= \frac{1}{N_k^2}V_{\mathbf{k}-\mathbf{k}'}(\mathcal{U}^{\dagger}_{\mathbf{k}+\mathbf{Q}}\mathcal{U}_{\mathbf{k}'+\mathbf{Q}})_{cc'}(\mathcal{U}^{\dagger}_{\mathbf{k}'}\mathcal{U}_{\mathbf{k}})_{v'v}, \\ X^{cc'}_{vv'}(\mathbf{k},\mathbf{k}',\mathbf{Q}) &= \frac{1}{N_k^2}\tilde{V}_{\mathbf{Q}}(\mathcal{U}^{\dagger}_{\mathbf{k}+\mathbf{Q}}\mathcal{U}_{\mathbf{k}})_{cv}(\mathcal{U}^{\dagger}_{\mathbf{k}'}\mathcal{U}_{\mathbf{k}'+\mathbf{Q}})_{v'c'}, \end{aligned}$$

where $V_{\mathbf{k}} = \sum_{\mathbf{R}} e^{-i\mathbf{k}\cdot\mathbf{R}}V_{\text{int}}(\mathbf{R})$, $\tilde{V}_{\mathbf{k}} = \sum_{\mathbf{R}} e^{-i\mathbf{k}\cdot\mathbf{R}}\tilde{V}_{\text{int}}(\mathbf{R})$, and $\mathcal{U}_{\mathbf{k}}$ is the matrix of eigenvectors for the TB Hamiltonian. For the case of direct transitions, where $Q=0$, the exchange integral is zero.

In work by MacDonald *et al.* [107], the Keldysh interaction is used to represent the interaction potential between the electron excited into the conduction band, and the hole in the valence band left behind. Typically, samples of TMDC in experiments are examined on a substrate which incurs a level of screening of the electron-hole charge. The screening included in the Keldysh interaction is the average of a silicon dioxide ($SiO_2$) substrate and air, $\varepsilon = 2.4-2.5$. In this work, the interaction between the electron and the hole was modelled using the screening developed earlier in the random-phase approximation, using the Hankel transform in Eq. (3.25). The calculations are done for two different substrates corresponding to $SiO_2$ and diamond (which has a dielectric constant of 5.7). The lattice Fourier transform $V_{\mathbf{q}}$ is represented on a grid spanned by vectors $\mathbf{R}_1 = a\hat{\mathbf{x}}$ and $\mathbf{R}_2 = (a/2)\hat{\mathbf{x}} + (\sqrt{3}a/2)\hat{\mathbf{y}}$, and has a size of $N_k \times N_k$. This is directly related to the $\mathbf{k}$ grid used to calculate the BSE Hamiltonian. At $\mathbf{R}=0$, the potential of the electron-hole interaction diverges, and thus must be truncated to regularise the interaction. In this work, for the RPA potential, the height $d$ in Eq. (3.25) is treated as a

| Species | $\varepsilon_{\text{sub}}$ | $E_{\text{cut}}^{\text{BSE}}$ (eV) |
|---|---|---|
| Acceptor | 3.8 | 2.125 |
| Donor | 3.8 | 2.075 |
| Acceptor | 5.7 | 2.15 |
| Donor | 5.7 | 2.1 |

Table 3.2: Values of the energy cutoff $E_{\text{cut}}^{\text{BSE}}$ used for the donor and acceptor defect calculations for the two substrates considered in the section of this work that looks at the optical properties of charged defects on monolayer $MoS_2$.

phenomenological parameter and tuned for the pristine optical conductivity to similarly match the lowest exciton binding energy obtained in experiment, which was found to be 1.2 Å.

A technique to reduce calculation time while retaining accuracy in the energy ranges of interest, involves limiting the number of transitions considered in the calculation between higher bands whose exciton energies are not greatly affected by the presence of charged defects. This is performed by introducing an energy cutoff $E_{\text{cut}}^{\text{BSE}}$, which determines the highest conduction band and lowest valence band considered in the calculation. The maximum conduction band $c_{\max}(\mathbf{k})$ is the index of the highest energy conduction band at wavevector $\mathbf{k}$ for which the energy obeys $E_{c\mathbf{k}} \leq E_{v\mathbf{k}}^{\max} + E_{\text{cut}}^{\text{BSE}}$, where $E_{v\mathbf{k}}^{\max}$ is the energy of highest valence band state at $\mathbf{k}$. The minimum valence band $v_{\min}(\mathbf{k})$ is the index of the lowest valence band at wavevector $\mathbf{k}$ for which the energy obeys $E_{v\mathbf{k}} \geq E_{c\mathbf{k}}^{\min} - E_{\text{cut}}^{\text{BSE}}$, where $E_{c\mathbf{k}}^{\min}$ is the energy of lowest conduction band state at $\mathbf{k}$. The BSE Hamiltonian is then constructed for direct transitions between conduction bands $c \leq c_{\max}(\mathbf{k})$ and valence bands $v \geq v_{\min}(\mathbf{k})$ at each $\mathbf{k}$. This limits the size of the basis, which increases in proportion to $N_k^2 N_c^4$. The energy cutoff for calculations for an $18 \times 18$ supercell with a $\Gamma$ point sampling ($N_k = 1$), was increased until the calculation required an amount of memory that was too large for the resources available, which are shown in Table. 3.2 for the calculations performed in this work.

The BSE Hamiltonian for direct transitions ($Q = 0$) in Eq. (3.85) is diagonalised through the eigenvalue equation:

$$\sum_{c'v'\mathbf{k}'} \langle \mathbf{k}, c, v, Q = 0 | H_{\text{BSE}} | \mathbf{k}', c', v', Q = 0 \rangle A_{\mathbf{k}'c'v'}^{M} = E^{M} A_{\mathbf{k}cv}^{M} \tag{3.96}$$

to obtain exciton eigenvectors $\mathbf{A}^{M}$ and exciton transition energy $E_M$. The binding energy

$E^M_{\text{bind}} = E_M - E_g$ of exciton $M$ is calculated by subtracting the free-particle band gap $E_g$ from the exciton eigenvalue. The inclusion of electron-hole interactions into the optical conductivity of the TMDC monolayer changes its form to

$$\sigma(\omega) = \frac{e^2}{\hbar\Omega} \sum_M \frac{\left| \sum_{\mathbf{k},c,v} (A^M_{\mathbf{k}cv})^* \langle \psi_{c\mathbf{k}} | \mathbf{e} \cdot \nabla_{\mathbf{k}} \hat{H}(\mathbf{k}) | \psi_{v\mathbf{k}} \rangle \right|}{E_M} \delta(\hbar\omega - E_M), \tag{3.97}$$

where $\Omega$ is the area of the periodic supercell system. To approximate the delta function in Eq. (3.97), a normalised Lorentzian function is used with constant broadening of $W = 0.02$ eV to match the value used in Refs. [10, 107].

# Chapter 4

# Defects in Monolayer $MoS_2$

In this chapter, I will first analyse the wavefunctions and binding energies of defect states arising from a charged defect in monolayer $MoS_2$, comparing the electronic behaviour of donor and acceptor defects. I will discuss how the shape of the conduction and valence band structure influences the properties of defect states. Unlike graphene, the low-energy shape of the conduction and valence bands of $MoS_2$ exhibits strong asymmetry, with secondary conduction and valence band extrema that are at different regions in the Brillouin zone (BZ) to the primary extrema and to each other. The secondary extrema also have effective masses that are significantly larger than those of the primary ones. These differences seen between the conduction and valence band suggests significantly different behaviour between donor and acceptor defect states. To begin this section, I will first discuss the inherent properties of monolayer $MoS_2$ from this model. This will be followed by a discussion of the form of the screened potential for an adsorbate defect in monolayer $MoS_2$, calculated from first-principles, which is a crucial aspect of this work. Then, the binding energies of in-gap defect states are studied with respect to a small set of parameters. These parameters include the height of the defect above the transition metal layer and its effective charge, as well as the dielectric constant of the substrate that the $MoS_2$ can sit on in experiment. I will predict experimental signatures of specific parameter sets, such as the LDOS which can be measured in scanning tunnelling spectroscopy, identifying observed defect states in the spectrum. Finally, I will explain how the properties of acceptor

and donor defect states manifest in the optical conductivity of monolayer $MoS_2$ in the presence of a charged defect.

## 4.1 Electronic Structure of $MoS_2$

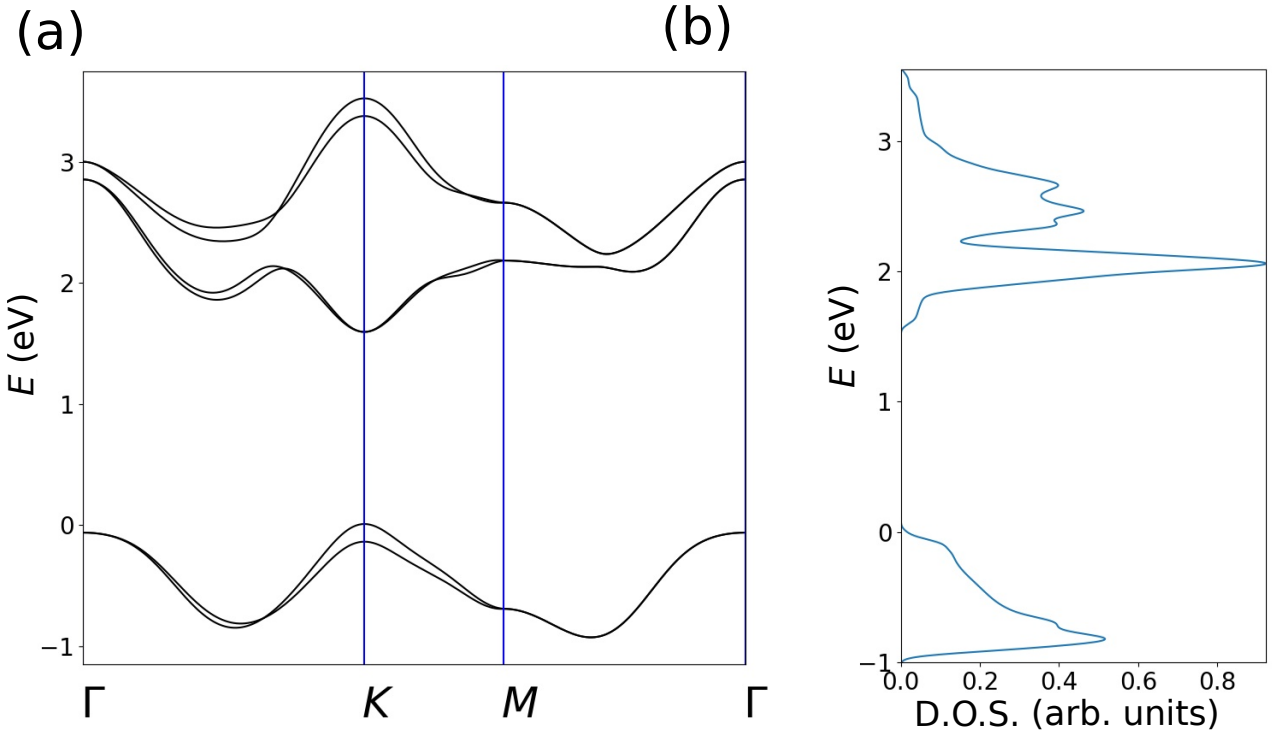



Figure 4.1: (a) Band structure along the $\Gamma KM\Gamma$ line in the $MoS_2$ Brillouin zone, along with the (b) corresponding density of states (DOS).

The band structure for monolayer $MoS_2$ is shown in Fig. 4.1(a), with complementing density of states (DOS) in (b). Here, the VBM at $K/K'$ and $\Gamma$ are shown to be at very similar energies, separated by 0.071 eV. They also show very different effective masses. These are compared in Table 4.1, with the VBM at $\Gamma$ being an order of magnitude larger than the VBM at $K/K'$. It should also be noted that the strong spin-splitting in the VBM at $K/K'$ is not matched

| | $K_v$ | $\Gamma_v$ | $K_c$ | $Q_c$ |
|---|---|---|---|---|
| $m_x^*/m_0$ | 0.479 | 2.65 | 0.448 | 0.806 |
| $m_y^*/m_0$ | 0.479 | 2.65 | 0.448 | 2.21 |

Table 4.1: Effective masses $m_x^*$ and $m_y^*$ (in units of the free electron mass $m_0$) along the $k_x$ and $k_y$ reciprocal-space directions, respectively, for $MoS_2$, shown for the valence band (subscript $v$) and conduction band (subscript $c$), at valence band maxima and conduction band minima.

anywhere else in the valence band; The VBM at the Γ point is spin-degenerate. In fact, along the $\Gamma - M$ line, the spins are also degenerate. The spin-splitting of the VBM at $K/K'$ is seen in the DOS in Fig. 4.1(b) as a double shoulder close to 0 eV (defined to be the VBM). In the conduction band, it can be seen that the CBM at $K/K'$ is spin-degenerate. This is not consistent with first principles calculations which show a small spin-orbit interaction on the order of 1 meV, and is a limitation of the simplified model for this work. The secondary CBM at $Q$ demonstrates both a significant spin-splitting and a strong asymmetry along the $\Gamma - K$ line. The conduction band shows a high density of states at energies close to the gap, with a large peak just above the small shoulder of the CBM at $K/K'$ (See Fig. 4.1(b)).

## 4.2 Screened Defect Potentials in Monolayer $MoS_2$

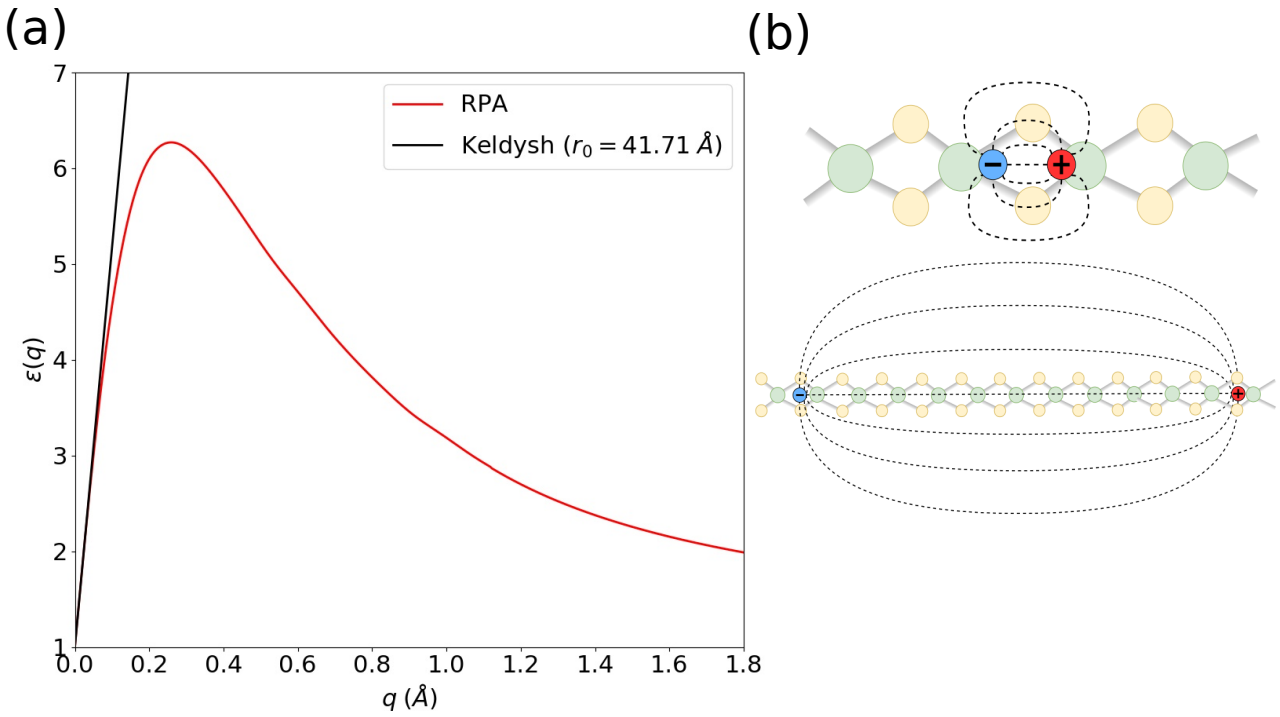



Figure 4.2: (a) Dielectric function obtained from the random-phase approximation, compared to screening in the Keldysh model. (b) Schematic for screening at different length scales.

The dielectric function $\varepsilon$ for monolayer $MoS_2$, obtained from first-principles and calculated within the random-phase approximation (RPA), is shown in Fig. 4.2(a) in red, as a function of wavevector magnitude $q$. It can be seen that the dielectric function is always greater than unity in this system, since the screening semiconducting medium cannot increase the magnitude of a

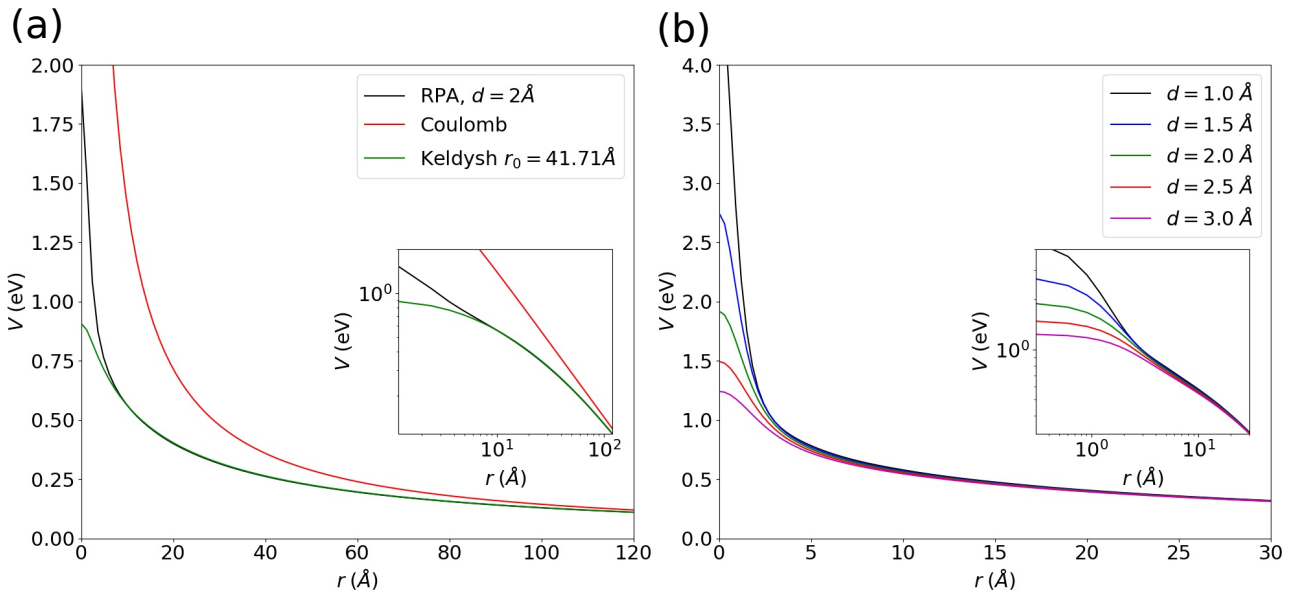



Figure 4.3: Defect potential of monolayer $MoS_2$ for a $1e$ charge, derived from first principles within the random-phase approximation (a) for $d = 2$ Å compared to both the Keldysh model and the unscreened Coulomb potential (both with $d = 2$ Å), as well as (b) for multiple values of the defect height $d$. Insets show the log-log form of the potentials in the main plot.

Fourier component $V(q)$ of the bare electrostatic potential. The variation of $\varepsilon$ with $q$ strongly reflects the behaviour of electric field lines permeating over different length-scales within the monolayer system. Firstly, the most notable feature is a peak that occurs on the order of an inverse lattice parameter $\sim 1/a$, which indicates that the strongest screening between charges occurs on the length-scale of a few atoms. On smaller scales than this, corresponding to large values of $q$, the screening slowly decreases with increasing $q$ from the peak. This arises from the reduced presence of bound electrons between two charges whose separation is smaller than typical bond length in $MoS_2$, resulting in less medium between the charges to contribute to screening. Due to the non-zero tails of quasi-particle probability distributions within the system, the screening converges slowly to unity as $q \to \infty$, a limit that corresponds to the charges being superimposed on one another. At long range, corresponding to small values of $q$, the screening becomes almost linear, reaching unity as $q \to 0$. As the distance between the two charges in the quasi-two-dimensional semiconductor increases, the out-of-plane thickness of screening medium becomes increasingly negligible relative to the in-plane separation of the charges, which can be seen in Fig. 4.2(b). As a result, field lines between two charges separated by a larger distance pass through less of the medium and further avoid the screening charge

within it, such that no screening of the interaction is present when the charges are infinitely separated in the quasi-2D material. The gradient of the linear segment of the dielectric function in Fig. 4.2(a) is found to be $r_0 = 41.71$ Å, and is proportional to the polarisability of monolayer $MoS_2$ [131]. In the form of $1+r_0q$, the resulting defect potential when integrated takes the form of the Keldysh model, which is frequently applied to thin-film semiconductors and semimetals in a classical electrostatic context [99]. This linear form has been shown in Fig. 4.2(a) in black, and is reasonably congruent with the RPA dielectric function until about $q = 0.1$ Å$^{-1}$ which in real-space corresponds to an agreement between the two screening models on the nanometre scale and beyond. This validates that while the Keldysh function presents an effective model of the screening in quasi-2D materials for long-range behaviour, it fails to capture the atomic nature of the short-range screening in the system, significantly overestimating it.

The dielectric function in Fig. 4.2(a) was used to obtain the screened defect potential as a function of position, parameterised by a defect height $d$ and prefactor $Z$ corresponding to an effective charge of $Ze$. In Fig. 4.3(a), the defect potential for $d = 2$ Å and charge $e$ ($Z = 1$) is shown as a function of position, compared to both the unscreened Coulomb potential, and Keldysh function for the value of $r_0 = 41.71$ Å estimated from Fig. 4.2(a). It is observed that, in comparison to the unscreened Coulomb potential, the RPA potential obtained from first-principles calculations screens more heavily at short range, and the gradient of the potential is generally less steep, as can be seen more clearly in the inset of Fig. 4.3(a) where the plot is shown in log-log format. However, as the distance from the defect increases, the screening becomes weaker and the RPA defect potential converges towards the unscreened case.

This convergence can be seen to occur at approximately $r = 100$ Å in Fig. 4.3(a), and demonstrates that the screened defect potential in two-dimensional semiconductors like monolayer $MoS_2$ is highly long range. This is in stark contrast to a three-dimensional semiconductor, where the screened Coulomb potential between two charges at long range can be associated with a bulk dielectric constant. This is because an increasing distance between charges in a true 3D semiconductor entails more screening medium between them, while maintaining zero free space through which electric field lines can permeate. In addition, Fig. 4.3(a) compares the screened potential found from using the RPA dielectric function to one in which the di-

electric function is substituted with the Keldysh model $\varepsilon_{\text{Keld}}(q) = 1 + r_0 q$, where $r_0 = 41.71$ Å. This shows that beyond approximately 8-10 Å, the Keldysh potential acts as an effective approximation to the screened potential within the RPA, provided that the value of $r_0$ used in the calculation of the Keldysh potential is matched to the gradient of the RPA dielectric function. The agreement in this part of real-space corresponds to the long-wavelength segment of the reciprocal-space dielectric function in 4.3(b) which is approximately linear. At shorter distances than 8-10 Å, the Keldysh potential is a poor representation of the screened potential in the monolayer, substantially overestimating the screening by up to 50%. This indicates that for states strongly bound to the defect, the potential energy associated with the defect state can be vastly inaccurate. This disagreement of the Keldysh potential with the one obtained from first principles is due to the assumptions in the original work by Keldysh and Rytova when constructing the model [99,100]. In this work, they assume a uniform medium occupying a thin region of thickness $h$, such that the expression for the dielectric function $\varepsilon_{\text{Keld}}(q)$ is arrived at after only considering the reciprocal-space region where $qh \ll 1$, corresponding in real-space to $r \gg h$ where $r$ is the in-plane separation of the charges [99]. Thus, for continuum models, the Keldysh potential could provide a quick and effective means of calculating quantities within the effective mass approximation for monolayer $MoS_2$, and potentially other TMDCs.

The height of the defect above the system plays an important role for the strength of the potential energy that bound states experience in the material, and can vary substantially between different species of adatom defects, due to both the size and chemical valence of the defect atom. In Fig. 4.3(b), the RPA defect potential for a charge of $e$ is shown for a variety of defect heights $d$ above the Mo layer in monolayer $MoS_2$. Firstly, it can be seen that defects closer to the Mo atom result in larger defect potentials in the vicinity of the defect, whereas larger defect heights soften the gradient of the potential near $r = 0$. This is understood even in the absence of screening, as the form of the unscreened potential $V_{\text{Coul}}(r; d) \propto 1/\sqrt{r^2 + d^2}$ has its maximum value proportional to $1/d$. Similarly, in the screened case shown in Fig. 4.3(b), it can be seen that subsequent increases of $d$ result in smaller reductions to the maximum value of the defect potential. As the distance from the defect charge increases such that $d \ll r$, the significance of this extra out-of-plane distance reduces greatly, causing potentials corresponding

to defects at different heights from the Mo layer to converge. In monolayer $MoS_2$, this occurs at approximately 15-20 Å, within reasonable precision. The large quantitative short-range change to the defect potential associated with an increase in $d$, highlights $d$ as a useful parameter in this study of charged defects. It should be noted that while the variation of defect height controls the form of the defect potential close to the adatom defect, the size of the charge $Ze$ is a prefactor that does not change the overall shape of the potential (not shown in Fig. 4.3).

## 4.3 Wavefunctions of Defect States

Once the defect potential, as in Fig. 4.3(a), was applied to the three-band tight-binding (TB) model for monolayer $MoS_2$, diagonalisation of the Hamiltonian, evaluated at the $\Gamma$ point in the Brillouin zone (BZ), resulted in a series of levels appearing in what would otherwise be the band gap in the pristine system. These states are localised to the defect, and exhibit strong similarity to the bound states of the two-dimensional (2D) hydrogenic model, and will be referred to as bound defect states. Fig. 4.4(a) shows the six most strongly bound defect states for an acceptor adsorbate with partial charge $-0.3e$ and situated a distance 2 Å above the Mo layer, with their binding energies, referenced from the valence band maximum (VBM), shown in the top left corner. It can be seen that the defect states are localised to the defect site, and possess nodal structure which allow them to be labelled as states in the 2D hydrogen series. The most strongly bound defect state ($n_{\mathrm{def}} = 1$ in Fig. 4.4(a)) corresponds to a localised $1s$ state, whose probability density is described mathematically by an exponential decay of inverse scale length $\alpha$. The scale length of this most strongly bound state is $\alpha^{-1}$ =12.6 Å [14], which is on the order of the lattice parameter. The second most strongly bound state for this value of the defect charge ($-0.3e$), also takes on the form of a $1s$ exponential decay but with a smaller scale length of $\alpha^{-1} = 5.1$ Å. The binding energy of this second state is within 2 meV of the most bound $1s$ state, whereas in the linearly screened 2D hydrogen model, states with a larger value of $\alpha$ typically correspond to a much greater binding energy. Following these two $1s$-like states, are a series of bound states with lower binding energy as measured from the VBM, that exhibit nodes along their radial cross-section. In descending order of binding

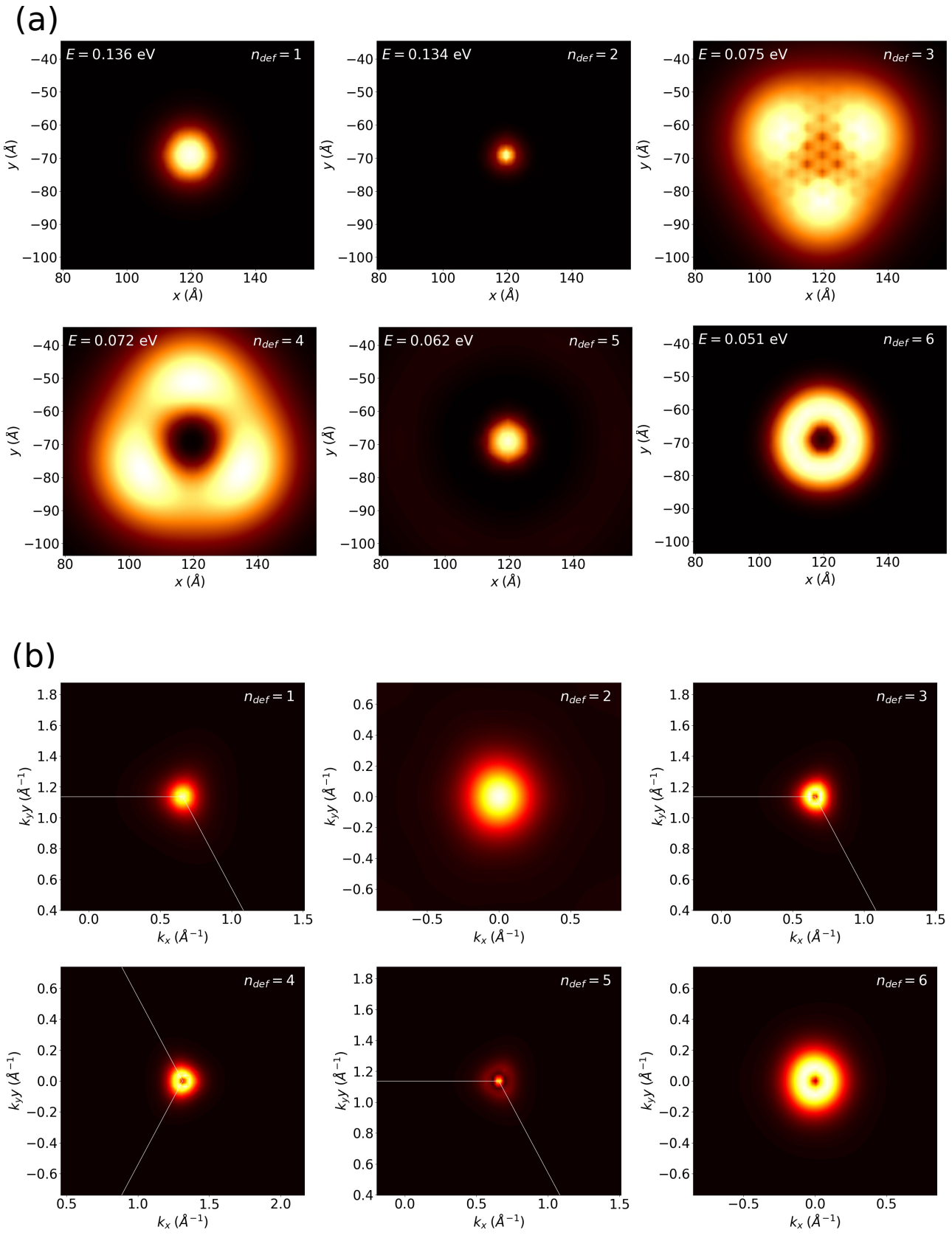



Figure 4.4: (a) Defect state wavefunctions (modulus square) and (b) corresponding defect state projections for an acceptor defect on monolayer $MoS_2$ for a charge of $-0.3e$ and a defect height of $d = 2$ Å . States are labelled by their order $n_{\text{def}}$ in the defect series, with $n_{\text{def}} = 1$ being the most strongly bound. Each unique $n_{\text{def}}$ corresponds to a spin-degenerate pair of states.

energy, these non-1$s$ states include two 2$p$-like states, a 2$s$-like state, and a more localised and more isotropic 2$p$-like state. This is an interesting parallel to the pair of 1$s$ states, in which a more localised form of a bound defect state with the same nodal structure appears at a lower binding energy.

To understand exactly why this small difference in binding energy between these two 1$s$-like states is observed with such a large change in the localisation of the state, it is useful to determine the region in the Brillouin zone (BZ) of the pristine monolayer $MoS_2$ system from which each member of the series of in-gap states overlaps most strongly with. This is referred to in this work as the *projection* of the defect state onto the pristine BZ. By calculating the projection of the defect state from this supercell calculation onto a state from a pristine monolayer $MoS_2$ (that in a supercell of the same size, would have folded onto the $\Gamma$ point from some point $\mathbf{k}$ of the BZ of the unit cell), the contribution of that region of the BZ to the construction of the defect state can be quantitatively described. The calculation of this quantity was simplified in the context of this TB+RPA framework, as the representation of the defect through the defect potential alone means that the Hilbert space of the pristine supercell is identical to that of the supercell with a charged defect. Hence, the projections identify a unitary matrix that relates the two eigenbases of these two systems. Physically, the projections represent the overlap of the states within the pristine band structure with the defect state, and the importance of particular regions of the BZ in describing how particular defect states behave with regards to effective mass and orbital characterisation. Fig. 4.4(b) shows the projections of each of the defect states in Fig. 4.4(a), with the hexagonal BZ marked in white. A reciprocity can be observed, where the states that are more strongly localised in real-space demonstrate a more delocalised projection in the BZ. It can be seen that these projections are centred on different symmetry points in the BZ where a valence band maximum is present. The most strongly bound state is constructed primarily from states near the $K$ point, and its spin-degenerate pair is constructed primarily from states near $K'$ due to spin-valley locking. Conversely, the second most strongly bound state is constructed primarily from pristine system states near the spin-degenerate $\Gamma$ point, a secondary valence band maximum with a large isotropic effective mass ($2.65m_0$) compared to that of the $K/K'$ points ($0.48m_0$). This reveals a possible explanation for the highly localised

nature of this state despite being of lower binding energy than the less localised state originating from $K/K'$. In the framework of the effective mass approximation in which the band structure is described as a single parabolic extremum, an impurity state $|\phi_i\rangle$ can be treated as a linear combination of band states [29]:

$$|\phi_i\rangle = \int \mathrm{d}\mathbf{k}\ \tilde{\phi}_i(\mathbf{k})|\psi_\mathbf{k}\rangle, \tag{4.1}$$

where $\tilde{\phi}_i(\mathbf{k})$ is a function that determines the contribution of that band state to the linear combination of $|\phi_i\rangle$. Inserting $|\phi_i\rangle$ into the Schrödinger equation for a particle of mass $m^*$ experiencing an external potential $U(\mathbf{r})$, which corresponds to the impurity potential, one obtains [29]:

$$(E(\mathbf{k}) - E_i)\tilde{\phi}_i(\mathbf{k}) + \int \mathrm{d}\mathbf{k}'\ U(\mathbf{k},\mathbf{k}')\tilde{\phi}_i(\mathbf{k}') = 0, \tag{4.2}$$

$$U(\mathbf{k},\mathbf{k}') = \langle\psi_\mathbf{k}|U|\psi_{\mathbf{k}'}\rangle, \tag{4.3}$$

where $E(\mathbf{k})$ is the band energy and $E_i$ is the binding energy of the impurity state labelled by $i$. However, in the case of the band structure in real non-metallic materials, there are generally multiple extrema within the BZ, with potentially different effective masses. In this case, the BZ can be split up into subzones $\Omega_j$, that each contain an extremum or "critical point", as outlined by Bassani [29]. By splitting up $\tilde{\phi}_i(\mathbf{k})$ into a piece-wise function across the different subzones, such that $\tilde{\phi}_i(\mathbf{k}) = \tilde{\phi}_i^{(j)}(\mathbf{k})$ for $\mathbf{k} \in \Omega_j$, the impurity equation in Eq. (4.2) becomes:

$$(E(\mathbf{k}) - E_i)\tilde{\phi}_i^{(j)}(\mathbf{k}) + \sum_{j'} \int_{\Omega_{j'}} \mathrm{d}\mathbf{k}'\ U^{jj'}(\mathbf{k},\mathbf{k}')\tilde{\phi}_i^{(j')}(\mathbf{k}') = 0, \tag{4.4}$$

where $U^{jj'}(\mathbf{k},\mathbf{k}')$ takes the same value as $U(\mathbf{k},\mathbf{k}')$ so long as $\mathbf{k} \in \Omega_j$ and $\mathbf{k}' \in \Omega_{j'}$, otherwise it is zero. In the case of acceptor defects in $MoS_2$, the critical points associated with individual subzones would be the $K$, $K'$ and $\Gamma$ points, since these subzones can individually be approximated as isolated parabolas. A zeroth order approximation to Eq. (4.5) is to recognise that the value of $U^{jj'}(\mathbf{k},\mathbf{k}')$ is much smaller for the case of $j \neq j'$ than it is for $j = j'$, and neglect

off diagonal terms [29], which leads to:

$$(E(\mathbf{k}) - E_{i,0}^{(j)})\tilde{\phi}_{i,0}^{(j)}(\mathbf{k}) + \int_{\Omega_{j'}} \mathrm{d}\mathbf{k}'\, U^{jj}(\mathbf{k},\mathbf{k}')\tilde{\phi}_{i,0}^{(j)}(\mathbf{k}') = 0, \tag{4.5}$$

where $E_{i,0}^{(j)}$ and $\tilde{\phi}_{i,0}^{(j)}(\mathbf{k})$ are the zeroth order energy and Bloch transform of the impurity wavefunction, respectively. At this order, effective mass theory produces an independent Schrödinger equation for each subzone, and thus a set of impurity states for each critical point in the band structure. Eq. (4.5) also implies that in subzone $j$, the defect binding energy is referenced to the extremum apex in that subzone. The wavefunctions and projections of those wavefunctions, seen in Fig. 4.4(a) and (b), respectively, demonstrate that localised bound states are observed in the gap, which when examined draw contribution primarily from one of the extrema in the BZ. In the case of the acceptor defect, a 1$s$-like defect state is seen for each extremum in the valence band, namely the $\Gamma$ point and the $K/K'$ points.

To understand why the vastly different effective mass of $K/K'$ and $\Gamma$ points are important for understanding the energetic and spatial differences in the 1$s$-like states from each, the real-space form of Eq. (4.5) can be considered. The Fourier transform $F_i^{(j)}(\mathbf{r})$ of $f_i^{(j)}(\mathbf{q})$ such that $f_i^{(j)}(\mathbf{k}-\mathbf{k}_{j,0}) = \tilde{\phi}_i^{(j)}(\mathbf{k})$ for an extremum at $\mathbf{k}_{j,0}$ in the BZ, is an envelope function of the impurity state that obeys a Schrödinger equation of the form:

$$\left(-\frac{\hbar^2\nabla^2}{2m_j^*} + (E_{j,0} - E) + U(\mathbf{r})\right) F_i^{(j)}(\mathbf{r}) = 0, \tag{4.6}$$

where $m_j^*$ and $E_{j,0}$ are the effective mass and energy of the extrema in subzone $j$, respectively [29]. The impurity state in real-space is approximately the envelope function multiplied by the Bloch state at the VBM:

$$\phi(\mathbf{r}) \approx F_i^{(j)}(\mathbf{r})\psi(\mathbf{k}_{j,0},\mathbf{r}). \tag{4.7}$$

In the absence of non-linear screening, $U(\mathbf{r})$ reduces to a $\frac{1}{r}$ form, and the binding energies $E_n$ and radii $\alpha_n^{-1}$ of the impurity states follow the solutions to the two-dimensional hydrogen model [132]

$$E_n = -\frac{Z^2 m_j^* e^4}{2\hbar^2(n-\frac{1}{2})^2}, \quad \alpha_n^{-1} = \frac{2|Z|m_j^* e^2}{\hbar^2(n-\frac{1}{2})}, \tag{4.8}$$

where $Z$ is the effective charge of the defect in the linearly screened model, and $n \in \mathbb{N}^+$. In this, the binding energy and the inverse scale length of the $1s$ election are proportional to the effective mass of the electron. The screening of the impurity potential means that such formulaic relations as in Eq. (4.8) will not apply exactly. However, it would still be expected that the most strongly bound solution is a localised decaying distribution centred on the defect. Similarly, the monotonic increase with increasing effective mass of both the binding energy of this state and the inverse scale length, will also apply in the non-linear case because of the denominator in the kinetic energy operator. This can be used to explain the differing localisation of the $1s$-like state from the $K/K'$ points and $\Gamma$ points, despite their similar binding energy in Fig. 4.4(a). The higher effective mass of the $\Gamma$ maximum in the valence band results in a highly localised $1s$ state as the most strongly bound defect state from the extremum. However, its binding energy is smaller than the less localised $1s$ state at $K/K'$ because it is referenced from the global VBM at $K/K'$, rather than the VBM energy at $\Gamma$ as it is in Eq. (4.5). The binding energies of the states in Fig. 4.4(a) do not share the same correspondence to the binding energy as seen in the 2D hydrogen model, as in Eq. (4.8). This can be attributed to the non-linear screening that occurs in this material, which prevents both the binding energy and wavefunction from taking an analytic form, while significantly screening the potential in the vicinity of the defect where this state is seen to be most abundantly distributed.

Looking at the non-$1s$ states in Fig. 4.4(a), trigonally lobed states are found following the $1s$-like states in binding energy. These appear to be of $2p$-nature, with a node located at the defect. In the 2D hydrogen model, the probability density of either of the $2p$ states appears as an isotropic ring, which differs from the $2p$-like states in this defect spectrum. One possible cause for this is the well known trigonal warping of the conduction and valence bands at $K/K'$ [74]. This non-parabolic shape of the bands results in an angular variation of contribution from some pristine Bloch states near the maximum at $K/K'$ to the impurity state than Bloch states for a fixed wave vector magnitude, which can be explained by the degree of trigonal warping the bands experience close to the VBM at $K/K'$. To understand this, one can make use of an

expansion of the impurity state by Bassani *et al.* [133]:

$$\phi(\mathbf{r}) = \int \mathrm{d}\mathbf{k}\, \frac{\left(\sum_n a_n f_n^*(\mathbf{k})\right)\psi(\mathbf{k},\mathbf{r})}{E(\mathbf{k}) - E}\psi(\mathbf{k},\mathbf{r}) = \int \mathrm{d}\mathbf{k}\, \tilde{\phi}(\mathbf{k})\psi(\mathbf{k},\mathbf{r}), \tag{4.9}$$

where $a_n$ are linear coefficients and the functions $f_n(\mathbf{k})$ are defined as

$$f_n(\mathbf{k}) = \int \mathrm{d}\mathbf{r}\, \psi(\mathbf{k},\mathbf{r})\sqrt{|U(\mathbf{r})|}g_n(\mathbf{r}), \tag{4.10}$$

with the arbitrary functions defined by $g_n(\mathbf{r})$ forming a complete basis [133]. Inserting Eq. (4.10) into Eq. (4.9) and extracting the form of the projection $\tilde{\phi}(\mathbf{k})$, one obtains

$$\tilde{\phi}(\mathbf{k}) = \frac{\int \mathrm{d}\mathbf{r}\, \left[\left(\sum_n a_n g_n^*(\mathbf{r})\right)\sqrt{|U(\mathbf{r})|}\psi(\mathbf{k},\mathbf{r})\right]}{E(\mathbf{k}) - E}. \tag{4.11}$$

It can be seen in the denominator of Eq. (4.11) that states with a smaller energy separation from the defect level will have a larger contribution to the impurity state. In the presence of a trigonal warping, $\tilde{\phi}(\mathbf{k})$ itself will demonstrate a trigonal warping that matches those of the bands, which can clearly be seen in Fig. 4.4(b) for the $2p$-like states. For the $2p$-like state at 0.075 eV ($n_{\mathrm{def}} = 3$ in Fig. 4.4(a)), there exists some modulation of the wavefunction in the vicinity of the central node at the defect site. This state has non-zero projections onto the $\Gamma$ point, which means that oscillatory terms proportional to $\cos\left(\zeta\frac{4\pi}{3a}\right)$ are seen in the linear combination of Bloch states, where $\zeta$ is approximately unity. While the effect is small, hybridisation between impurity states at different extrema can occur in the effective mass treatment of impurity states. Following the $2p$ states, a $2s$ like state is seen, with a very strong peak in the centre, surrounded by a concentric node. Unlike in the 2D hydrogen model, the $n = 2$ bound states of the non-linear screening in the impurity potential in $MoS_2$ are not *accidentally* degenerate. The final wavefunction shown in Fig. 4.4(a) is a $2p$-like ring state, whose corresponding projection in Fig. 4.4(b) identifies it as being primarily constructed from states near the secondary VBM at the $\Gamma$ point in the BZ. Compared to the $2p$-like states from the $K/K'$, there are no significantly pronounced trigonal lobes present in the one from $\Gamma$, nor in the projections in Fig. 4.4(b), which is due to the lack of trigonal warping found at its secondary VBM.

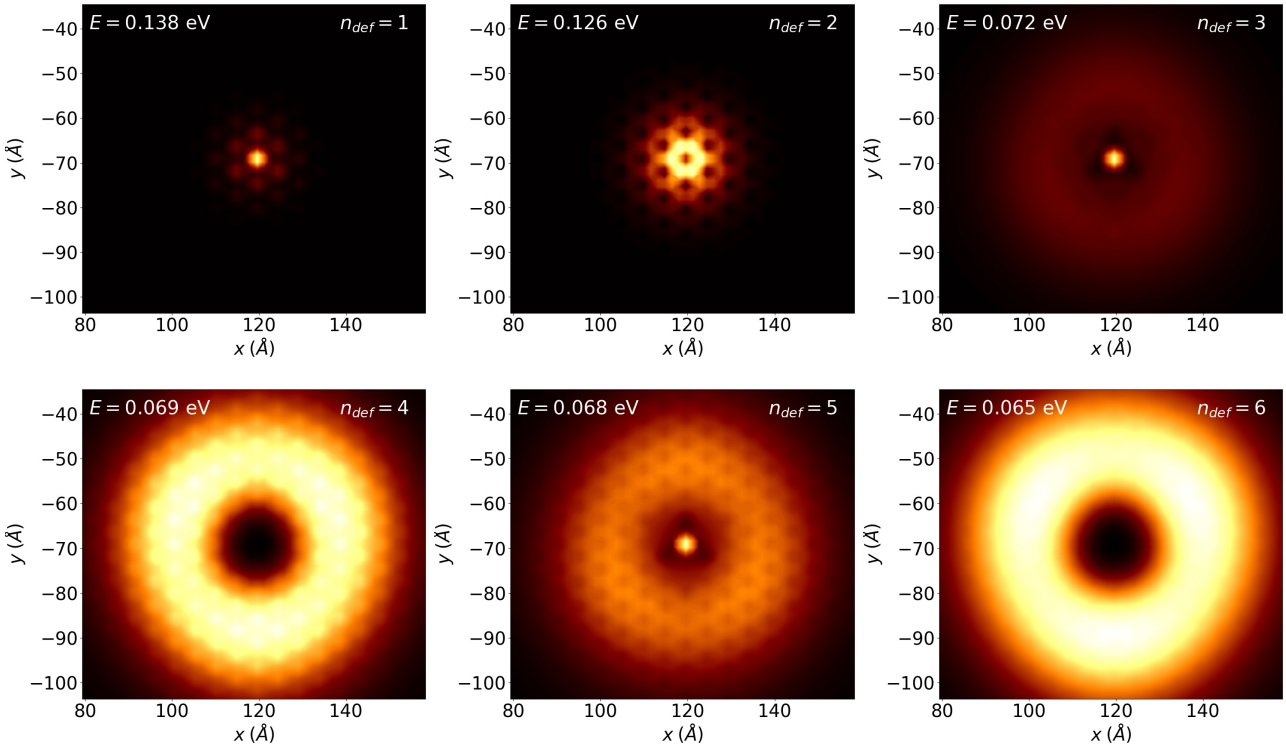



Figure 4.5: Defect state wavefunctions (modulus square) and for a donor defect on monolayer $MoS_2$ for a charge of $0.3e$ and a defect height of $d = 2$ Å . States are labelled by their order $n_{\text{def}}$ in the defect series, with $n_{\text{def}} = 1$ being the most strongly bound. Each unique $n_{\text{def}}$ corresponds to a spin-degenerate pair of states.

In Fig. 4.5, the first six (spin-degenerate) most strongly bound states in the band gap are shown for the case of a donor atom with the same height ($d = 2$ Å) and effective charge magnitude ($Z = +0.3$). Despite the binding energies of these states being on a very similar energy scale to the $Z = -0.3$ case, their wavefunctions exhibit very different features compared to their acceptor counterparts. The projections for these states all show that the wavefunctions in Fig. 4.5 are constructed primarily from Bloch states near the $K/K'$ conduction band minima (CBM). Firstly, in Fig. 4.5, a pair of modulated $1s$-like states are observed as the two most strongly bound states in the donor defect spectrum with noticeably different binding energies and different spatial extents. While in the case of the acceptor, the presence of two $1s$ states originated from two band extrema with vastly different effective masses, these $1s$-like donor defect states originate from the $K/K'$ points. However, it was determined that hybridisation takes place between the impurity states of the subzone containing the CBM at the $K$ point and those of the subzone containing the $K'$ point, due to the lack of spin-orbit splitting present in the conduction band of the three-band model [14]. To understand this, consider the folding

of the unit cell band structure when creating a supercell. The Γ point is sampled for the wavefunctions in this section, because in the infinite supercell limit, all possible **k**-points in the BZ fold onto it. While sufficiently large supercells would provide a good enough approximation to the isolated system, in this calculation, the size of the supercell is chosen to be both large enough to sufficiently capture the defect states and to be of size $3n \times 3n$ s.t. $n \in \mathbb{N}^+$, so that the $K/K'$ points fold directly onto the Γ point. In addition to the impurity potential coupling these folded band states, this choice of supercell size results in four-fold degeneracy at the energy of the CBM in $MoS_2$. This is shown schematically in Fig. 4.6. Were it the case that only the CBM at the $K$ point is present in the band structure, the presence of a defect potential would result in a spectrum of spin-up defect states from the CBM with effective mass $0.44m_0$ and a spectrum of spin-down defect states arising from the CBM with effective mass of $0.39m_0$ (vice versa for $K'$). However, the folding of the CBMs at $K$ and $K'$ onto one another means that similarly spinned CBMs of differing effective mass form a degenerate subspace, and the presence of a defect potential creates a coupling between the two. This hybridisation also explains the strong modulation in the wavefunctions, since it results in a linear combination of Bloch-waves from $K$ ($\sim e^{i\mathbf{K}\cdot\mathbf{r}}$) and $K'$ ($\sim e^{-i\mathbf{K}\cdot\mathbf{r}}$) being present in the non-envelope part of the defect state. This approximately gives rise to densities possessing sinusoidal contributions $\sim \cos(\mathbf{K}\cdot\mathbf{r})$ that repeat every three unit-cells, which is confirmed in the troughs and peaks of the $1s$-like states in Fig. 4.5. This modulation is still present in the four $2p$ states (shown in Fig. 4.5) to a lesser degree, which do not take contributions directly from the $K/K'$ points, despite the fact that the four-fold degeneracy only occurs at the minima at $K/K'$ and not in its reciprocal-space neighbourhood. In the vicinity of the $K/K'$ points, the two conduction bands are very close in energy, which is sufficient for the hybridisation of the $2p$ states to occur. This suggests that, despite the non-zero spin-splitting of the conduction band minima of $\sim 1$ meV present in the real system, this modulation effect is not necessarily an artifice of the tight-binding model.

In the $2p$ states, the trigonal lobes are less pronounced, meaning that they appear to take a more circular density. This is further evidence that the trigonal warping is responsible for the trigonal lobes observed in these calculations, as the lesser degree to which the conduction bands are warped compared the valence band has been previously shown by other groups [74].

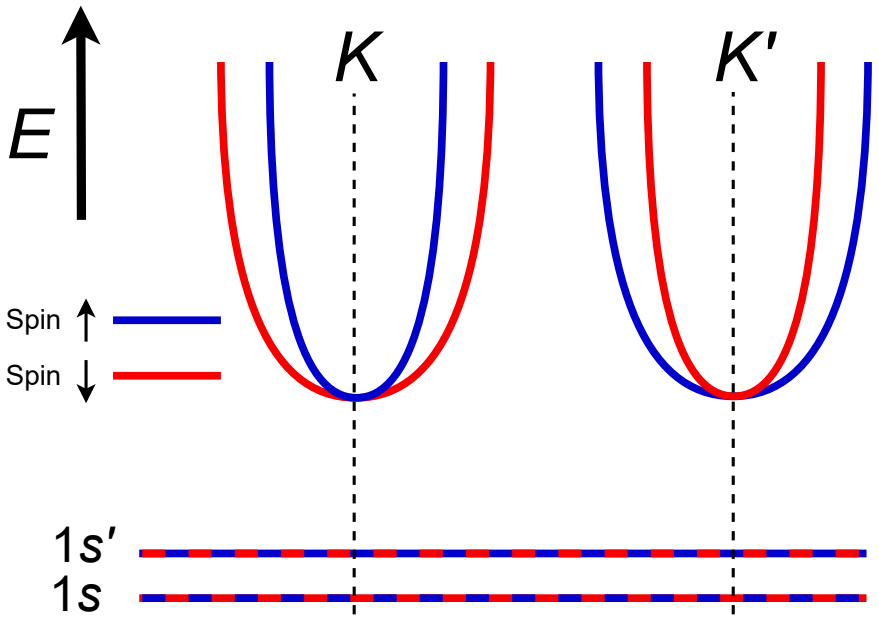



Figure 4.6: Schematic of the hybridisation present in the conduction band of $MoS_2$ in the presence of an impurity potential. Shows a sketch of the conduction band structure at $K$ and $K'$, with zero spin-orbit coupling at the $K/K'$ points. The positive energy axis $E$ is shown in the top left. This is only shown for the $1s$ and $1s'$ states.

Additionally, the binding energies of the donor states from $K/K'$ measured from the CBM are on the same energy scale as the acceptor states from $K/K'$ measured from the VBM. This can be understood as resulting from the similar effective masses of the conduction band ($0.448m_0$) and valence band ($0.478m_0$) at $K/K'$.

## 4.4 Theory of Defect State Binding Energies

| Label in Fig. 4.7(a) | VBM | Hydrogenic label |
|---|---|---|
| A | $\Gamma$ | $1s$ |
| B | $K/K'$ Upper | $1s$ |
| C | $K/K'$ Lower | $1s$ |
| D | $\Gamma$ | $2s$, $2p$ and $2p'$ |
| E | $K/K'$ Upper | $2s$, $2p$ and $2p'$ |

Table 4.2: Identity of the labelled states in Fig. 4.7(a), showing the VBM in the BZ from which the state is most strongly constructed from, and the hydrogenic label of the state relating to its nodal structure. In the middle column, "Upper" and "Lower" refer to the upper and lower energy valence band in the spin-split region near $K/K'$.

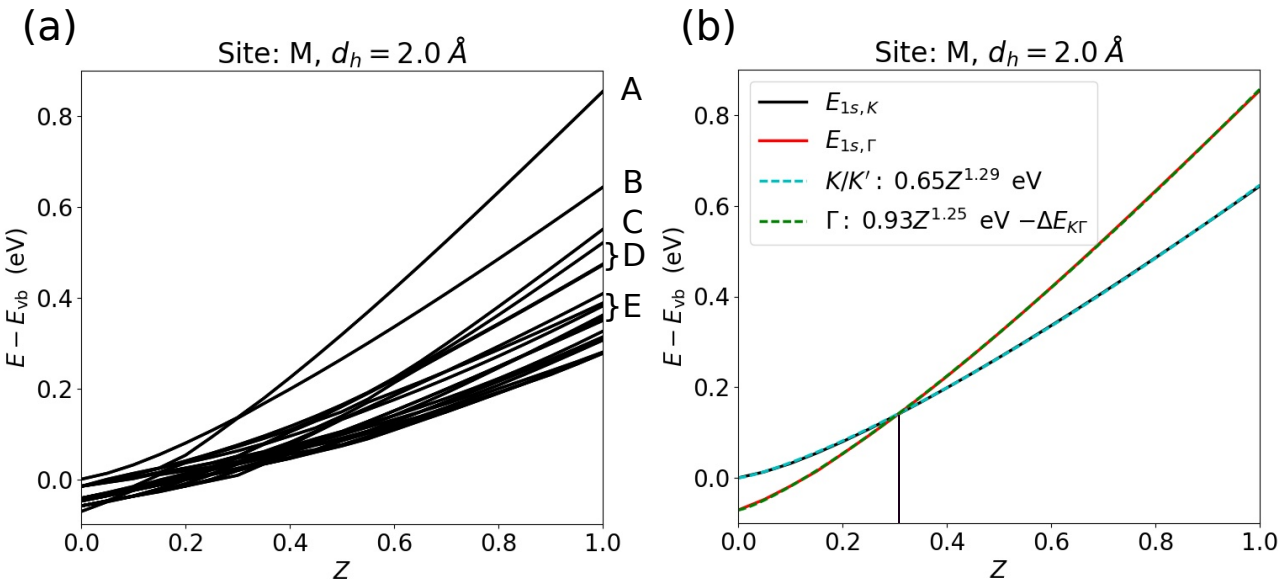



Figure 4.7: (a) Acceptor binding energies in $MoS_2$ as a function of charge size $Z$ for a defect at 2 Å above the $M$ site. The identity of the states is given in Table 4.2. (b) Acceptor binding energies of the $1s$ states from $K/K'$ and $\Gamma$ as a function of $Z$ for the same height and defect site, with power law fittings shown in the legend. All energies are referenced from the valence band maximum at $K/K'$, and $\Delta_{K\Gamma} = 0.0711$ eV is the energy difference between the valence band maxima at $\Gamma$ and $K/K'$.

### 4.4.1 Acceptor State Binding Energies with Defect Charge

In the two-dimensional (2D) hydrogen model, where the screening is absent in the potential, it is known that the binding energy of the electron increases as $\propto Z^2$. Hence, probing the sensitivity of the binding energy of charged defects in monolayer $MoS_2$ can reveal how the inherent screening of the Coulomb potential changes this proportionality with $Z$. To understand how the size of the charge changes the structure of the defect levels in monolayer $MoS_2$, the binding energy of the donor and acceptor defect levels was studied. This is shown for acceptor defects in Fig. 4.7(a) as a function of the charge magnitude $Z$, with the defects labelled by their hydrogenic state. This shows that the binding energies increase with $Z$, which is expected since a stronger charge results in a deeper potential that binds free carriers to a greater extent. However, it is also noticed that with the increase of charge, different defect levels increase by different amounts, leading to various order changes of defect states shown by the crossovers in Fig. 4.7(a). By looking at the projections of these states as performed for the $Z = -0.3$ in Fig. 4.4(b), both the hydrogenic label and associated subzone of origin within the effective mass approach can be ascribed. As such, lines and groups of lines at the $Z = 1$ position in Fig. 4.7(a)

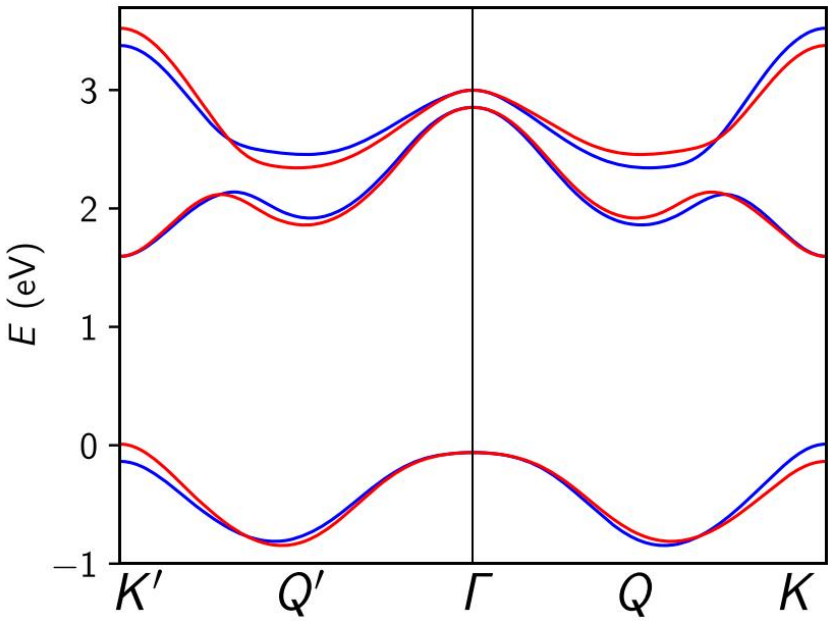



Figure 4.8: Tight-binding band structure, where bands with spin-up (spin-down) character are in red (blue) [14]. From [14] (own) under the Creative Commons License (subfig. (a) removed).

are labelled by their hydrogenic state analogue and the extrema most strongly constructing the state in the projections. It can be seen that for charge strengths greater than around 0.2, the most strongly bound states are $1s$ type defect states, which are spin-degenerate and constructed exclusively from $K/K'$ and from $\Gamma$. At $Z \approx 0.3$, the $1s$ state from $\Gamma$ point has the same energy as the $1s$ state from the $K/K'$ points, and beyond this at $Z \gtrapprox 0.3$, the $\Gamma$ point defect state remains the most strongly bound. Following this at large values of $Z > 0.7$, a third $1s$ state can be seen in the spectrum which arises from the lower spin-split valence band at the $K/K'$ points. Additional to these $1s$ states, there is a collection of $2p$, $2s$ and higher order states from both the $K/K'$ and $\Gamma$ points. At $Z = 1$, it can be see that the most strongly bound defect states that are not of $1s$ type, are $2p$-like defect states constructed from Bloch states near the $\Gamma$ point, whereas below $Z \approx 0.6$, a $2p$-state constructed from the $K/K'$ points is the most dominant non-$1s$ state. The crossovers of binding energy curves with increasing $Z$ would not arise in the 2D hydrogen model, as they are all proportional to the Rydberg with decreasing constants of proportionality for higher order states. They arise due to the multi-valley nature of the valence band structure in $MoS_2$, and the fact that binding energies of defect states constructed from different valleys respond differently to the defect charge.

At $Z = 0$, the energies in Fig. 4.7(a) match those of the unperturbed supercell with size

$51 \times 51$, with the top state being the VBM at $K/K'$ and the bottom state being the VBM at $\Gamma$ at -0.0711 eV below it. In between these two maxima, Fig. 4.7(a) shows the energies of the sampled points near the VBM at $K/K'$ that fold onto the $\Gamma$ point in the creation of the supercell. Hence, at small values of the defect charge, the *auxiliary* defect states ($2p$, $2s$ etc.) appear to be resonant with valence band continuum, as their binding energy curves continue smoothly from the sampled points at the $K/K'$. It should be noted that this would not be the case for a truly isolated defect in an infinite system, as all defect states constructed from the $K/K'$ points would increase in binding energy from 0 as $Z$ is increased. This discrepancy between the supercell calculation and what would be expected in the ideal case can be explained with use of the supercell size $N_c$. As $N_c \to \infty$, the sampled points at $Z = 0$ from which the binding energy curves of the auxiliary defect states continue from as $Z$ is increased, would converge towards the VBM at $K/K'$. However, at larger values of $Z$ e.g. $Z = 1$, the auxiliary defect states for $N_c = 51$ are completely captured by the supercell, such that their energy is independent of $N_c$. This suggests that there is a value of $Z$, above which the binding energies of the auxiliary states are converged. Below this value, the weak defect potential results in auxiliary states that are too delocalised such that the supercell is not a sufficiently large enough window to capture them.

To understand how each set of defect states respond to a change in the defect's strength, it can be useful to isolate the binding energy curves for the $1s$ states alone, which is shown in Fig. 4.7(b). Here, the binding energy curve of the $1s$ state from $K/K'$ increases from the global valence band maximum at $K/K'$ with increasing $Z$. This is not the case for the binding energy curve of the $1s$ state which was found by projections to originate strongly from the $\Gamma$ point. It was found that as $Z$ is gradually increased, this state increases in energy from -0.0711 eV below the global VBM corresponding to the energy of the secondary VBM at $\Gamma$. Hence, it is appropriate to reference this defect level from the $\Gamma$ point energy, which means that for charge sizes $Z \lessapprox 0.2$, the state is resonant with the valence band continuum. It is important to observe that $E_{1s,K/K'}$ increases less with $Z$ than $E_{1s,\Gamma}$. Given the fact that all the orbitals taken into consideration in the model are $d$-orbitals on the Mo atoms, and that the Coulomb potential is indifferent to orbital character, the distinct orbital character of the two types of

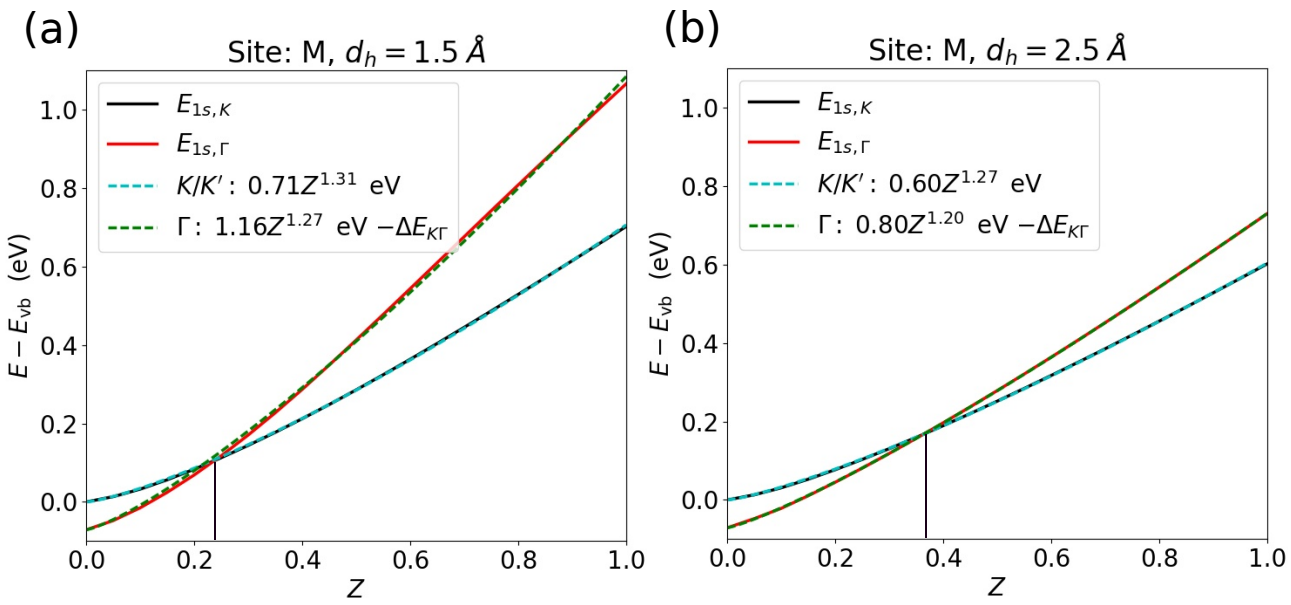



Figure 4.9: Variation of binding energy of the two most strongly bound 1$s$ states with defect charge $Z$, referenced to the valence band, for a defect height of (a) $d$ =1.5 Å and (b) $d$ =2.5 Å above the Mo atom. $\Delta_{K\Gamma} = 0.0711$ eV is the energy difference between the valence band maxima at $\Gamma$ and $K/K'$.

VBM cannot justify this difference in sensitivity to $Z$. Within the effective mass approximation, the only difference between the two types of VBM in $MoS_2$ is between the distinct effective masses of $K/K'$ and $\Gamma$ as shown in Table 6.1. This significant difference in sensitivity of the binding energy to changes in $Z$, can be quantified by fitting the two binding energy curves in Fig. 4.7(b) to a power law of the form $AZ^{\eta}$, where $A$ and $\eta$ are parameters. The power law demonstrates an excellent fit to the binding energy, with parameters for each shown in the legend of Fig. 4.7(b) which includes the difference between the $K/K'$ and $\Gamma$ VBM. The parameters demonstrate that while there is not a large difference between the exponents of the power law, the coefficients $A$ of the binding energy fits for the 1$s$ state of $K/K'$ and $\Gamma$ differ by approximately 43%. Since the effective mass of $\Gamma$ is roughly 5 times the size of the mass at $K/K'$, this behaviour is significantly different to the case of the 2D hydrogen model, where the binding energy is linear in the electron mass. However, the difference between the power law fittings of the binding energies, almost entirely in the coefficient, indicates a monotonic increase of the binding energy with effective mass. This also contributes to the explanation to why the two 1$s$ states have similar binding energy referenced from the $K/K'$ VBM for $Z = -0.3$, despite having completely different spatial extent.

### 4.4.2 Acceptor State Binding Energy with Defect Height

If the defect height is varied, it is expected that the binding energies of the $1s$ states from both the $K/K'$ and $\Gamma$ points would be significantly affected. This is because changes to the defect potential, upon tuning the defect height, are highly local to the defect site, which is where the $1s$ states are mostly distributed. As can be seen in Fig. 4.3(b), the effect on the defect potential of changing the defect height is negligible at in-plane distances from the defect beyond 10-15 Å. In the case of $d = 1.5$ Å, Fig. 4.9(a) shows that the binding energies of the two $1s$ states are generally larger for all values of $Z$, with the binding energy of the most strongly bound $1s$ state at $Z = 1$ being around 0.15 eV larger than in the case of $d = 2$ Å shown in Fig. 4.7(b). More significantly, compared to Fig. 4.7(b), 4.9(a) shows a larger difference in the gradients of the binding energy with $Z$, or a larger difference in their sensitivities to $Z$, between the state from $\Gamma$ and the one from $K/K'$. This is observed in 4.9(a) firstly through the increased size of the separation between the curves associated with these two $1s$ states, relative to the binding energy, as for $Z = 1$ the separation is almost double that for the case of $d = 2$ Å. This higher sensitivity to $Z$ of the binding energy of the $1s(\Gamma)$ can also be noticed in the lower value of $Z_c(d)$ for which the two $1s$ states are degenerate. This is marked in Fig. 4.9(a) with a vertical line at $Z_c(d = 1.5 \text{ Å}) = 0.235$, which is lower than in Fig. 4.7(b) where $Z_c(d = 2 \text{ Å}) = 0.305$. This correlates with the much stronger localisation to the defect of the $1s(\Gamma)$ defect state, as this means it has a higher probability density in the regions where there is a stronger increase in potential energy due to the smaller value of $d$. Fittings to the same power law are also shown in Fig. 4.9(a), for both the $1s(K/K')$ and $1s(\Gamma)$ states. For the $1s(K/K')$ state, the most significant change is a 10% increase in the coefficient, with the power law still presenting a good fit to the binding energy curve. However, for the $1s(\Gamma)$ defect state, the errors in the power law fitting to the binding energy are higher, which can be seen by crossovers between the calculated and fitted curves. This arises because of the poor quality of fit to the data at larger $Z$, where the defect state is highly localised to the defect site such that in reciprocal-space, the set of Bloch states required to construct it extend significantly enough beyond the parabolic region of the VBM at $\Gamma$. It is at this point where the effective mass pertaining most strongly to the defect state becomes ambiguous, causing the lack of conformity of the binding energy

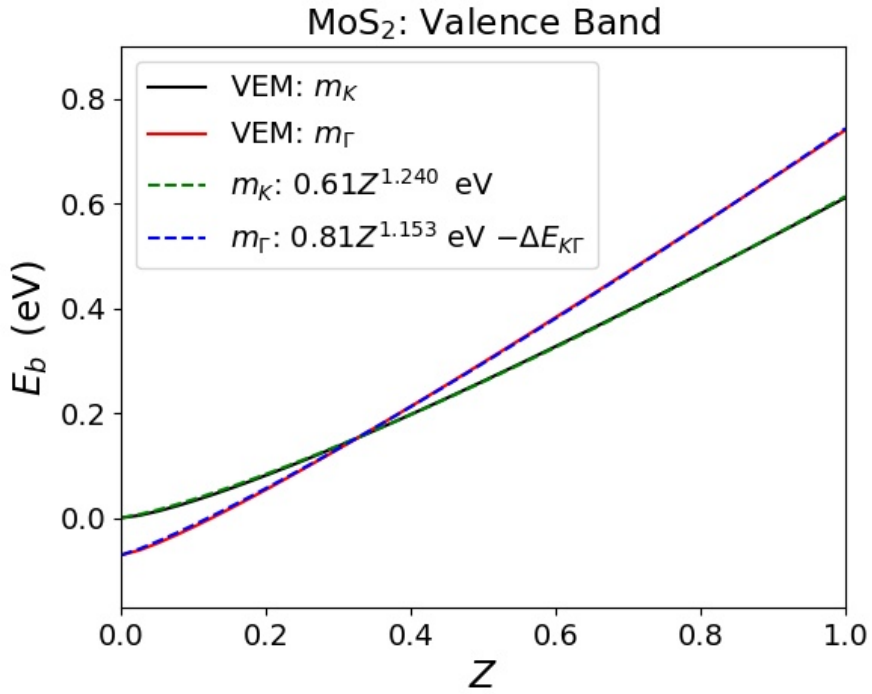



Figure 4.10: Binding energies as a function of charge $Z$, calculated from the variational effective mass (VEM) model. This is done for a particle in a potential $V(r)$ of a charged defect a height $d$ above the Mo atom, screened by Keldysh dielectric function $1 + r_0 q$ with $r_0 = 41.71$ Å. The particle has either a mass $m_K^*$ of the VBM at $K/K'$ or mass $m_\Gamma^*$ of the VBM at $\Gamma$. Fitting parameters to the power law $AZ^\gamma$ are also shown, with the energy difference between the $\Gamma$ and $K/K'$ maxima given as $\Delta E_{K\Gamma}$.

to a power law in which the effective mass is fixed throughout the curve. Conversely, when the value of $d$ is slightly increased to 2.5 Å as seen in Fig. 4.9(b), the binding energies of both the $1s(K/K')$ and $1s(\Gamma)$ defect states are generally smaller in value, their crossover occurs at a higher value of $Z_c(d = 2.5\ \text{Å}) = 0.36$, and they both conform well to the simple power-law fitting. This final point reinforces the idea that extreme localisation results in defect states whose binding energy is not entirely determined by one value of the effective mass, resulting in a poorer fit of a power law to the binding energy with charge strength.

### 4.4.3 Variational Effective Mass Model for Acceptor States

The behaviour exhibited in the tight-binding (TB) calculations presented here can be further compared to the effective mass approximation, using a variational approach. In Fig. 4.10, the binding energies as a function of $Z$ are shown for the variational effective mass (VEM) model

in which the total energy of a particle of effective mass $m^*$ in a potential $V_{\text{def}}(r)$ of the form:

$$V_{\text{def}}(r) = -\frac{Ze^2}{4\pi\varepsilon_0}\int \mathrm{d}q\, \frac{J_0(qr)e^{-qd}}{1+r_0 q}, \tag{4.12}$$

where $J_0$ is the zeroth Bessel function of the second kind, $d = 2$ Å is the defect height, and $r_0$ is the linear coefficient of the Keldysh dielectric function fitted to the ab initio dielectric function obtained from Eq. (3.24). The binding energy is shown for the effective masses of the VBM at the $K/K'$ and $\Gamma$ points separately, which are the only differing parameters in the VEM calculation besides the reference energy. This shows good agreement with the binding energies obtained from the TB supercell calculations, with a crossover of the two binding energy curves occurring at a charge strength of $Z \approx 0.35$. The VEM binding energy curves were also fit to the same power law form as for the TB model, shown in Fig. 4.10. This shows that generally, while the fitting parameters are similar to those of the TB model, the binding energies in the VEM model are less than the TB. It can be seen that the coefficient of the power law differs by about 26% between the two values of the effective mass in the VEM model. At $Z = 1$, the similarity between the VEM and TB binding energies is not as clear, owing to the fact that the Keldysh screening implemented in the continuum VEM model describes the system poorly at short range where it results in a weaker potential. This means that the highly localised $1s$ states experience a potential energy which differs substantially between the two formulations of the defect potential. Nevertheless, this indicates that by simply increasing the effective mass of the VBM in consideration, the in-gap defect states built from pristine Bloch states of that VBM have larger binding energies. This further corroborates the conclusion above that the difference in binding energy dependence on $Z$ between defect states from the $K/K'$ and the $\Gamma$ point, is primarily attributed to the differences in their effective mass.

### 4.4.4 Donor State Binding Energies with Defect Charge

In the case of donor defects, the behaviour of the in-gap defect state binding energies is notably different. While in the conduction band there are six secondary conduction band minima (CBM) at the $Q$ points, their energy relative to the primary CBM at $K/K'$ is larger than the

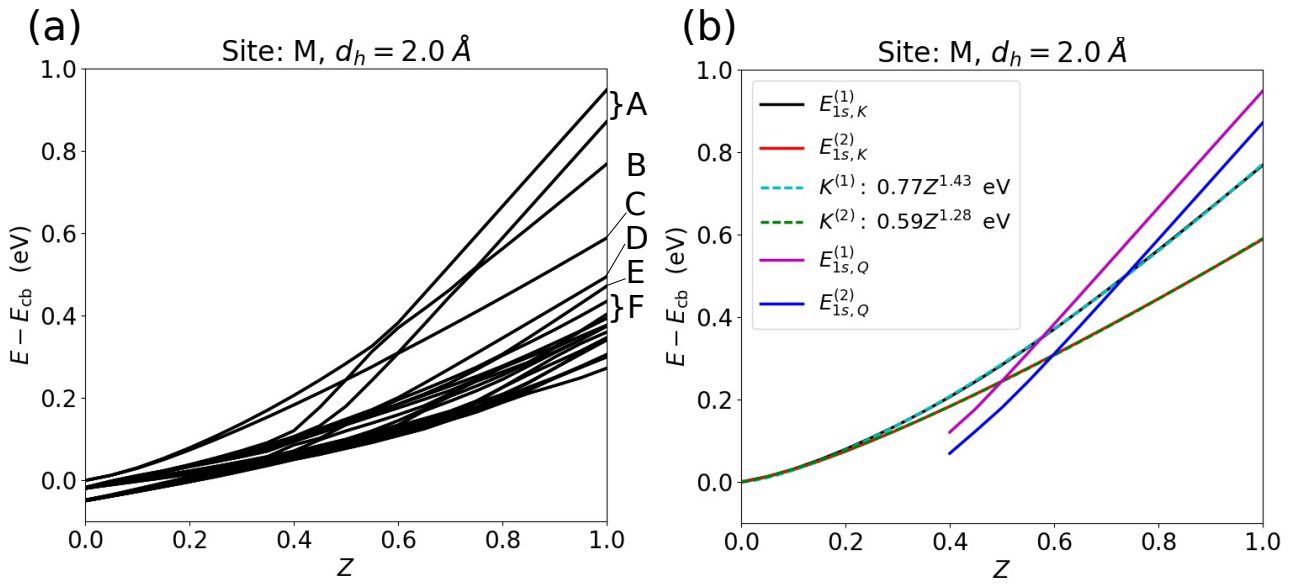



Figure 4.11: (a) Donor binding energies in $MoS_2$ as a function of charge size $Z$ for a defect at 2 Å above the $M$ site. The identity of the states is given in Table 4.3. (b) Donor binding energies of the $1s$ states from $K/K'$ and $Q$ as a function of $Z$ for the same height and defect site, with power law fittings for the $1s$ states shown in the legend. All energies are referenced from the conduction band minimum at $K/K'$.

| Label in Fig. 4.11(a) | CBM | Hydrogenic label |
|---|---|---|
| A | $Q$ Upper & Lower | $1s$ and $1s'$ |
| B | $K/K'$ | $1s$ |
| C | $K/K'$ | $1s'$ |
| D | $K/K'$ | $2s$ |
| E | $Q$ Lower | $1s''$ |
| F | $K/K'$ | $2s$, $2p$ and $2p'$ |

Table 4.3: Identity of the labelled states in Fig. 4.11(a), showing the CBM in the BZ from which the state is most strongly constructed from, and the hydrogenic label of the state relating to its nodal structure. In the middle column, "Upper" and "Lower" refer to the upper and lower energy conduction band in the spin-split region near the six $Q$ points.

difference between the VBM at $\Gamma$ and $K/K'$. Additionally, these secondary conduction band minima are anisotropic, meaning that simple applications of the effective mass approximation are less likely to be satisfactory. Due to the lack of spin-orbit coupling in the primary CBM at $K/K'$, same-spin CBMs from the $K$ and $K'$ have the same energy and can be strongly coupled by a potential, creating pairs of hybrid states. The binding energy of the donor states with reference to the CBM at $K/K'$ is shown in Fig. 4.11(a), with labels which map to the hydrogenic series and are related to the nodal structure of the state. For donor charge strengths between $Z = 0$ and 0.5, the most strongly bound donor states are a pair of $1s$ like states whose energy

monotonically increases from the CBM at $K/K'$ with increasing $Z$. There is a splitting between them that increases with $Z$, up to a maximum of 0.2 eV at $Z = 1$, which is attributed to the same mechanism as depicted in Fig. 4.6. Interestingly, between $Z = 0.5$ and 0.7, the pair of hybridised donor $1s$ states are crossed by a second pair of states. This is similar to the acceptor case, since as $Z \to 0$ the binding energy curves of this second pair converge to an energy above the CBM, such that the states they represent are resonant with the conduction band continuum for small $Z$. This means that their increase in binding energy with $Z$ is stronger than that of either of the hybridised $1s$ states from $K/K'$. By observing the projections of these states, they arise primarily from a hybridised combination of the six $Q$ states that exist approximately halfway along the $\Gamma - K$ lines in the BZ of the pristine system. In Fig. 4.7(b), the two $1s$ states from $K/K'$ and the two from $\{Q\}$ are shown, isolated from the other bands. The splitting exhibited by these two $Q$ states appears to be indifferent to the size of the charge $Z$. This suggests that alone they are not hybridised with each other, but are instead states from two separate hybridised sets of defect states from the six $\{Q\}$ points. As can be seen in Fig. 4.8, the CBM at the $\{Q\}$ points (shown as $Q$ and $Q'$) are not spin degenerate, and are furthermore spin-valley locked. In a large supercell scheme, these six $Q$ points fold onto one another to give two sets of CBM, each containing three spin up CBMs and three spin down CBM at the same energy. Hence in the presence of the defect potential, for each spin there will be a two sets of three-way hybridised states associated with the spin-split $\{Q\}$ CBM. This is also supported by considering the spin-splitting between the bands, which varies between approximately 65-75 meV in the vicinity of the $Q$ CBM. This compares well to the 77 meV separation between the two $1s$ states from $\{Q\}$ in the defect spectrum.

### 4.4.5 Variational Effective Mass Model for Donor States

As for the case of the acceptor, the VEM model can be applied to the $1s$ states built up from the $K/K'$ points, by inserting the effective mass of the CBM at $K/K'$. The effective masses for the upper and lower CBM are almost identical, and thus the splitting between the two $1s$ states in the tight-binding model is not replicated. To model this hybridisation, the interaction between

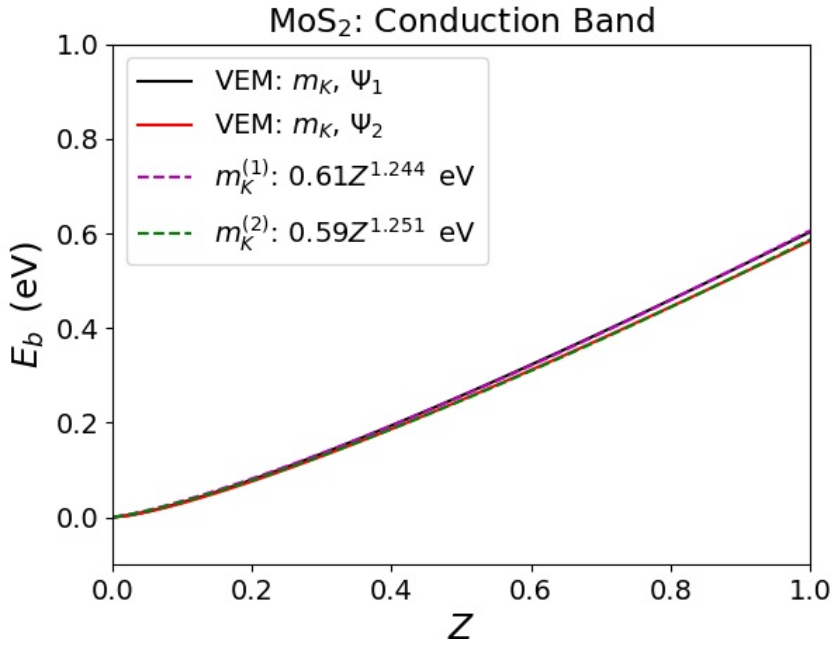



Figure 4.12: Donor binding energies as a function of charge $Z$, calculated from the variational effective mass model. This is done for a particle in a potential $V(r)$ of a charged defect a height $d$ above the Mo atom, screened by Keldysh dielectric function $1 + r_0 q$ with $r_0 = 41.71$ Å. The particle has either a mass $m_K^{*(1)}$ and $m_K^{*(2)}$ of the CBM at $K/K'$. Fitting parameters to the power law $AZ^\gamma$ are also shown.

these two states was considered within the framework of the effective mass approximation [29]. Using this approach, the hybridisation between two $1s$ states from Brillouin subzones $\Omega_K$ and $\Omega_{K'}$ takes the form:

$$\Delta_{1s,\Omega_K,1s,\Omega_{K'}} = \int \mathrm{d}\mathbf{k} \int \mathrm{d}\mathbf{k}' \; \phi^*_{1s,\Omega_K}(\mathbf{k}) V_{\Omega_K\Omega_{K'}}(\mathbf{k},\mathbf{k}') \phi_{1s,\Omega_{K'}}(\mathbf{k}'), \tag{4.13}$$

where $\phi_{1s,\Omega_K}(\mathbf{k})$ is the Bloch transform of the $1s$ defect state and

$$V_{\Omega_K\Omega_{K'}}(\mathbf{k},\mathbf{k}') = \int \mathrm{d}\mathbf{r} \; \psi^*_{\mathbf{k}}(\mathbf{r}) V(\mathbf{r}) \psi_{\mathbf{k}'}(\mathbf{r}), \quad \mathbf{k} \in \Omega_K, \;\; \mathbf{k}' \in \Omega_{K'}. \tag{4.14}$$

Using an expansion in reciprocal lattice vectors $\mathbf{G}$, $V_{\Omega_K\Omega_{K'}}(\mathbf{k},\mathbf{k}')$ can be approximated as:

$$V_{\Omega_K\Omega_{K'}}(\mathbf{k},\mathbf{k}') = \sum_{\mathbf{G}} C_{\mathbf{G}}(\mathbf{k},\mathbf{k}') V(\mathbf{k}-\mathbf{k}'+\mathbf{G}) \approx V(\mathbf{k}-\mathbf{k}'), \tag{4.15}$$

where $C_{\mathbf{G}}(\mathbf{k}, \mathbf{k}')$ are parameters and $V(\mathbf{k} - \mathbf{k}')$ is the Fourier transform of the defect potential. This is because in Eq. (4.15), the dominant term is for $\mathbf{G} = 0$ for which $C_{\mathbf{G}}(\mathbf{k}, \mathbf{k}') = 1$. For shallow to moderate impurities, the forms of $\phi_{1s,\Omega_K}(\mathbf{k})$ are localised to the vicinity of the VBM at $K/K'$, meaning that the integral for splitting $\Delta_{1s,\Omega_K,1s,\Omega_{K'}}$ can be approximated by [29]:

$$\Delta_{1s,\Omega_K,1s,\Omega_{K'}} \approx F_{1s,\Omega_K}(r=0)F_{1s,\Omega_{K'}}(r=0)V(\mathbf{K} - \mathbf{K}'), \tag{4.16}$$

where $F_{1s,\Omega_K}$ is the envelope function of the impurity state and $\mathbf{K}/\mathbf{K}'$ is the wavevector corresponding to $K/K'$. Due to the usage of the Keldysh dielectric function in the VEM model, $V(\mathbf{K} - \mathbf{K}')$ is expressed as:

$$V(\mathbf{K} - \mathbf{K}') = \frac{Ze^2}{2\varepsilon_0|\mathbf{K} - \mathbf{K}'|(1 + r_0|\mathbf{K} - \mathbf{K}'|)} e^{-|\mathbf{K}-\mathbf{K}'|d}. \tag{4.17}$$

When this is applied to the variational model to emulate the splitting seen in the tight-binding calculations, as shown in Fig. 4.12, the curves appear very close together. While the small difference in effective mass between the $K$ and $K'$ minima for a single spin results in non-degenerate binding energy curves, the hybridisation as calculated from Eq. (4.16) is negligible. This discrepancy is caused by the inaccurate behaviour of the predominantly long-range Keldysh model at large wave vectors, which has an unreasonably large dielectric function at the wavevector magnitude $|\mathbf{K} - \mathbf{K}'|$.

### 4.4.6 Variation of Defect Binding Energy with Substrate

In this discussion, the primary parameter used to explore the behaviour of donor and acceptor states has been the effective charge $Z$ of the defect. For specific defects, the value of this parameter can be surmised using, for example, techniques like Bader charge analysis. For a phenomenological understanding of deep donor and acceptor defects, the charge of the defect can be set to an integer number of the electron charge. The substrate of $MoS_2$ is an important factor to consider when comparing results from models to those obtained from experiments, since the dielectric constant of the substrate can immensely affect the strength of the defect

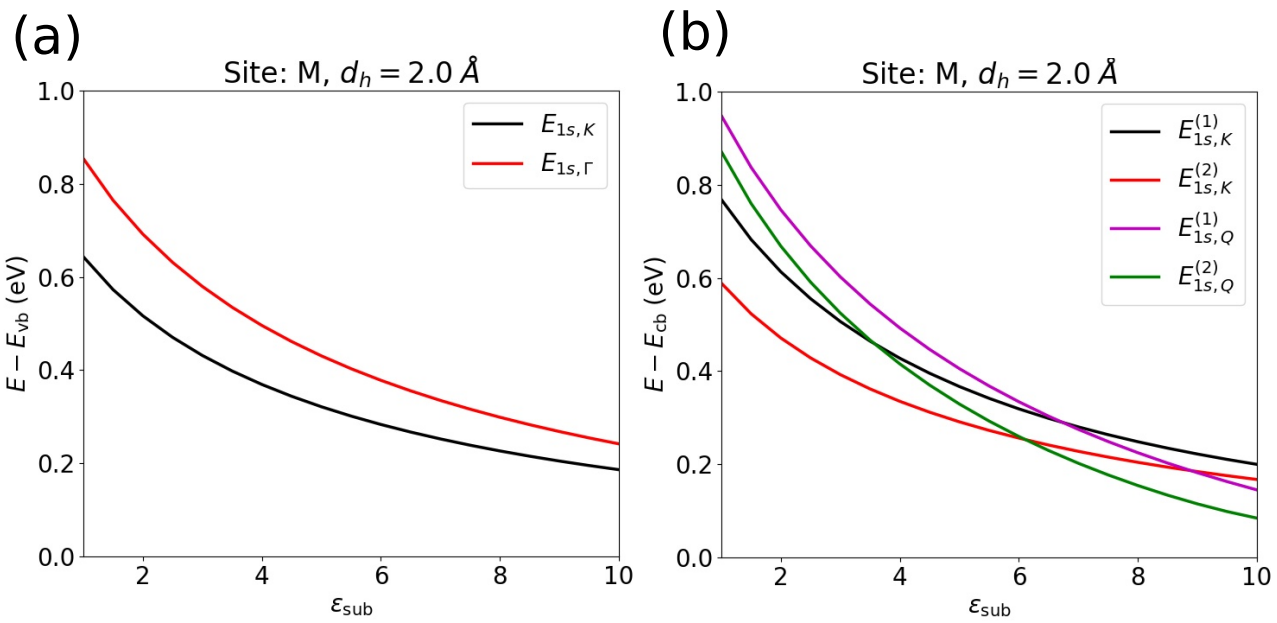



Figure 4.13: Variation of the defect state binding energy with substrate dielectric constant $\varepsilon_{\text{sub}}$, for (a) the $1s(K)$ and $1s(\Gamma)$ states for an acceptor defect with unit charge, and (b) the hybridised $1s$ states from $K/K'$ and $Q$ for a donor defect with unit charge. The defects in both (a) and (b) are placed 2.0 Å above the Mo atom layer.

potential. Hence, it is crucial to the validity of the understanding gained from previous subsections, to explore the variation of the binding energies when the dielectric constant of the environment is continuously changed.

Figs. 4.13(a) and (b) show the binding energies of $1s$ in-gap defect states for a defect of unit charge placed 2 Å from the Mo atom layer for a donor and acceptor defect, respectively, (with respect to the conduction band minima and the valence band maxima at $K/K'$, respectively). In Fig. 4.13(a) it can be seen that for an acceptor charge of $e$, within the range of dielectric constants between 1 and 10, the crossover of binding energy curves that was seen in Fig. 4.7, corresponding to the $1s$ states constructed from $\Gamma$ and $K/K'$, is not observed. Instead, the curves approach each other as $\varepsilon_{\text{sub}}$ is increased. However, it is expected that $E_{1s,\Gamma}$ and $E_{1s,K/K'}$ will switch order as $\varepsilon_{\text{sub}}$ is increased further beyond 10. The lack of such a crossover arises due to the strength of the defect potential when $Z = -1$ and the strong effective mass of the $\Gamma$ point causing $E_{1s,\Gamma}$ to remain above $E_{1s,K/K'}$ for a significant range of $\varepsilon_{\text{sub}}$. The variation of the hybridised $1s$ donor state binding energies with substrate dielectric constant exhibits different behaviour to the acceptor case. In particular, within the range $1 - 10$ for $\varepsilon_{\text{sub}}$, the same crossovers seen in Fig. 4.11 with increasing $Z$, are seen with decreasing $\varepsilon_{\text{sub}}$. Since the

crossovers of binding energy occur at a larger $Z$ for donor states, crossovers between the bound states as $\varepsilon_{\text{sub}}$ is varied will generally occur at a smaller value of $\varepsilon_{\text{sub}}$. The effect of increasing the dielectric constant of the substrate is akin to the reduction of the effective charge of a defect. However, it is not exactly reciprocal due to the form of the dielectric function when including the static screening from a substrate.

## 4.5 Local Density of States

The local density of states (LDOS) is an important quantity that can be directly compared to measurements in scanning tunnelling spectroscopy (STS) experiments. The value of $\mathrm{d}I/\mathrm{d}V$, which is the rate of change of the tunnelling current as the bias voltage of the sample is tuned, is directly proportional to the LDOS, and provides a signature of the particular defect being studied. The LDOS was calculated for two different adsorbates with partial charges of $Z_{\text{C}} = -0.58$ and $Z_{\text{Li}} = 0.63$ and defect heights of $d_{\text{C}} = 1.58$ Å and $d_{\text{Li}} = 3.1$ Å above the Mo layer, corresponding to carbon and lithium, respectively, adsorbed to monolayer $MoS_2$ on a $SiO_2$ substrate with a dielectric constant of $\varepsilon_{\text{SiO}_2} = 3.7 - 3.9$ [14]. The values of the partial charges are rough estimates obtained from Bader charge analysis of the DFT charge density [89, 90], which still provide a useful qualitative insight into the nature of the adatoms in $MoS_2$. The LDOS for a carbon atom (C), which is predicted in $MoS_2$ to behave as an acceptor, is shown near the valence band in Fig. 4.14(a) and near the conduction band in (b) for several distances away from the defect between 9.57 Å and 70.18 Å, with the DOS of the pristine system given as black dashed lines. Since the potential does not vanish at the supercell edge, acting as a finite size effect, the application of the potential shifts the VB up in energy compared to the pristine case. Hence, in Fig. 4.14(a-b), the pristine LDOS is plotted such that the VB maxima aligns with the value of the LDOS far away from the impurity. It can be see that above the valence band maximum (VBM), several strong peaks arise that are localised to the vicinity of the defect. Among them, two prominent peaks at 0.15 eV and 0.22 eV above the VBM were shown through the projections to correspond to the $1s$ defect states constructed from the $K/K'$ and $\Gamma$, respectively (labelled in Fig. 4.14(a)) [14]. The smaller size of the $\Gamma$ peak compared to the

$K/K'$ peak at the distance 9.57 Å , beyond which the peak vanishes, is indicative of a greater localisation to the defect. Closer to the VBM at approximately 0.05 eV into the gap, a large conglomerate peak of the $2s/2p$ states composed of states near the $K/K'$ VBM is seen, whose separation in energy is on the order of the Gaussian broadening (0.02 eV) used for calculating the LDOS. This peak exhibits a more extended electron distribution, with noticeable values of the LDOS at over 25 Å. At a distance of $\approx 66$ Å from the adatom, the LDOS of the perturbed system has converged to the form of the LDOS of pristine $MoS_2$. There are also a number of other peaks below the VB minima, which correspond to impurity states that are *resonant* with the band continuum, and have applications in transport experiments [2, 29]. The behaviour of the conduction band for this system is shown in Fig. 4.14(b), near which no defect states are observed. However, the screened potential associated with the defect leads to a shift and flattening of the LDOS, which is flatter when closer to the impurity. This is not a rigid shift in LDOS due to the fact that CB states are not localised to the impurity and have wavefunctions which are delocalised across the supercell. The spatial variation of the density of Bloch states in the CB results in a higher potential experienced by some states over others. This leads to a spreading-out effect in energy of the conduction band states upon the application of the defect potential, an effect which vanishes as the LDOS is calculated further away from the impurity. This can be interpreted as the electrons, that would otherwise occupy these CB states upon excitation, experiencing a repulsive energy from the negative acceptor potential. This is commonly seen in STS experiments as dark patches in tunnelling spectra in the vicinity of charged defects, when Coulomb potentials cause local band-bending. Importantly, as the distance away from the defect increases, the LDOS converges quickly to the pristine conduction band at about 70 Å, which is approximately 10 Å from the edge of the supercell and validates the choice of its size.

Fig. 4.14(c) and (d) show the tight-binding LDOS for a Li adsorbate on $MoS_2$ in the vicinity of VB maximum and the CB minimum, respectively. The peaks near the CB minima (Fig. 4.14(d)) in the vicinity of the defect originate from bound donor states and can be observed up to a distance of $\approx 25$ Å from the adatom. Note that the splitting of the two impurity states from the $K$ and $K'$ points is too small to be resolved into individual peaks for each donor state.

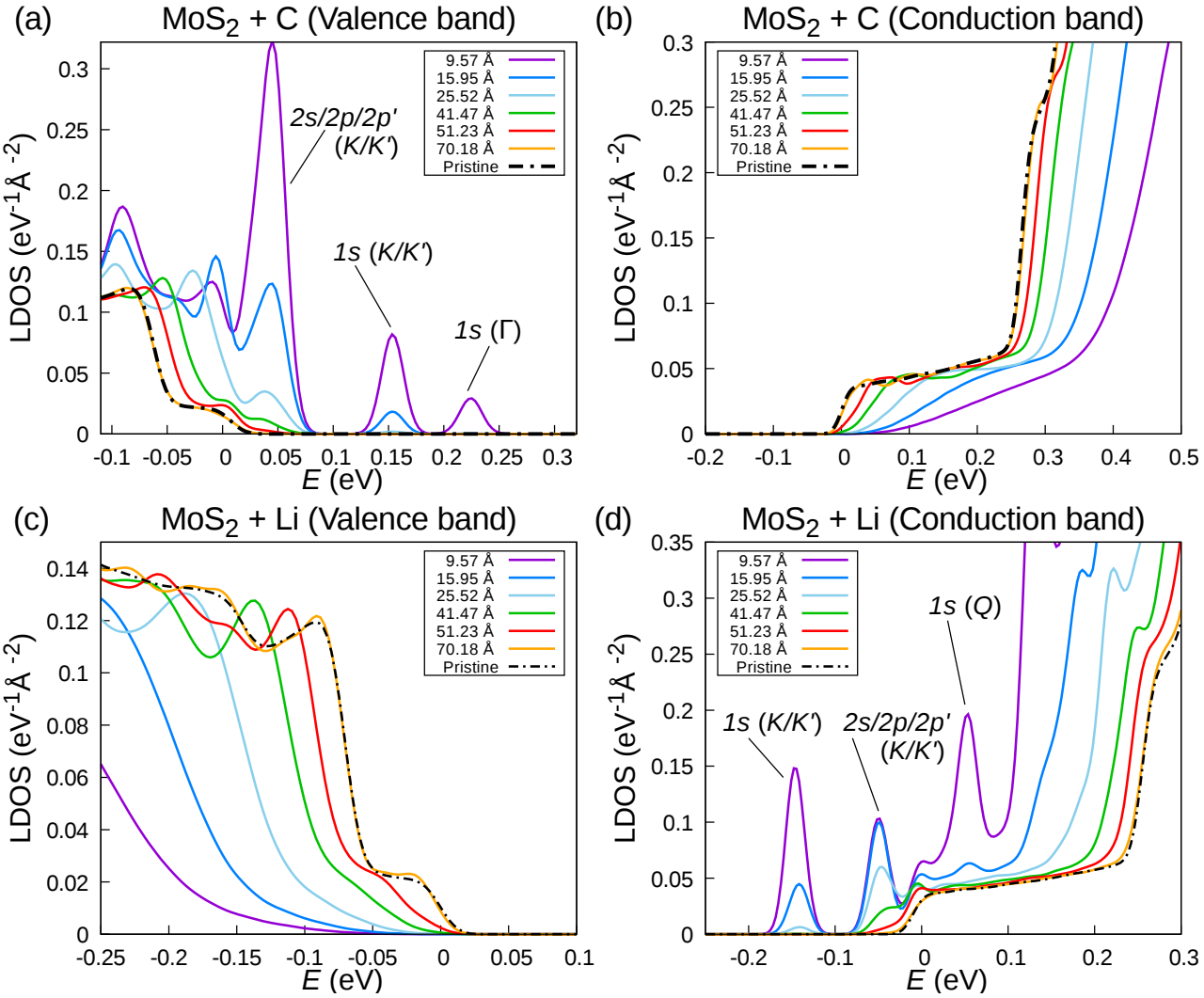



Figure 4.14: (a,b) LDOS of a carbon (C) adatom on $MoS_2$ ($+SiO_2$ substrate) near the (a) valence band and (b) conduction band edge. (c,d) LDOS of a lithium (Li) adatom on $MoS_2$ ($+SiO_2$ substrate) near the (c) valence band and (d) conduction band edge. Results are shown for several distances from the impurity. In each graph, the zero of energy is set to the band edge of the unperturbed $MoS_2$ [14]. From [14] (own) under the Creative Commons License.

However, the noticeable misalignment of the LDOS of the $1s$ peak at 9.57 Å with its value at 15.95 Å is indicative of a superposition of non-degenerate defect states that possess slightly different degrees of localisation. Just below the CB, lie states of $2s$, $2p$ and $2p'$ character which have larger extent and can be observed up to $\approx$ 50 Å from the impurity. The states originating from the $Q$ point in the BZ are resonant with the CB continuum. As with the case for C atoms, the LDOS converges to the form of the pristine LDOS as the distance from the defect increases, while the LDOS of the VB in Fig. 4.14(c) shifts down in energy and is flattened more at smaller distances from the defect, with no defect states being observed.

## 4.6 Optical Properties of Charged Defects on $MoS_2$

In this section, I aim to use some of the intuition and understanding gained from studying the static electronic properties of charged defects on monolayer TMDCs to probe the optical properties of these systems. The presence of defect levels in the band gap indicates that, in absorption and photoluminescence experiments, it is possible to detect resonances at low energies corresponding to *defect excitons*, arising from transitions between these levels. To model this, the tight-binding+RPA formalism was combined with the Bethe-Salpeter equation to determine the excitons that arise in monolayer $MoS_2$ in the presence of a charged defect. This was performed for monolayer $MoS_2$ on typical substrates of $SiO_2$ and diamond with dielectric constants of $\varepsilon_{\text{sub}} = 3.8$ and $\varepsilon_{\text{sub}} = 5.7$, respectively, to highlight the sensitivity of the results to the environment. I will first compare the pristine optical conductivity of monolayer $MoS_2$ systems on these two choices of dielectric substrate. Following this, the optical conductivity of $MoS_2$ with a charged defect will be compared to the pristine case, looking at both acceptor and donor defects. Analysing this in terms of transitions between the continuum bands and the defect states, I will attempt to explain both the origin of the observed bright optical resonances, and the differences seen between donor and acceptor defects.

### 4.6.1 Pristine System Calculations

In the pristine undoped system, electronic transitions will occur between the valence and conduction bands of the system, inducing an attractive interaction between the excited electrons and the holes they leave behind. This binding energy between the oppositely charged carriers reduces the photonic energy required for the excitation, and is known as the *exciton binding energy*. For $MoS_2$, the pristine optical conductivity is shown in Fig. 4.15 for the case of a $SiO_2$ substrate ($\varepsilon_{\text{sub}} = 3.8$) and a diamond substrate ($\varepsilon_{\text{sub}} = 5.7$). Firstly, it can be seen that the optical conductivity exhibits two strong peaks at low excitation energies. These correspond to the $A$ and $B$ peaks of monolayer $MoS_2$, which arise from transitions at $K/K'$ between the conduction band and the two spin-split valence bands.

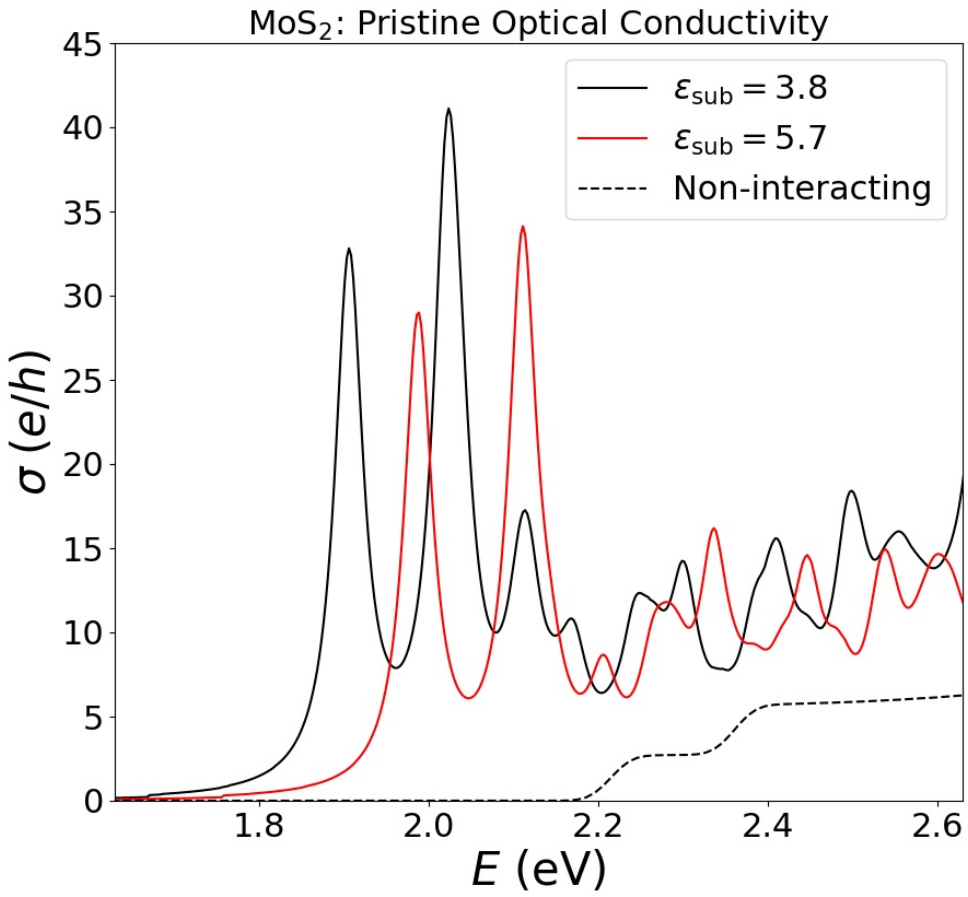



Figure 4.15: Optical conductivity of the pristine $MoS_2$ monolayer on a $SiO_2$ substrate (black) and a diamond substrate (red), using an interaction potential determined from the random-phase approximation. The optical conductivity found from exclusion of the electron-hole interaction is shown as a black dashed line.

Similar to the treatment given in previous work [107], the energy axis in Fig. 4.15 is shifted to align the $A$ peak for $\varepsilon_{\text{sub}} = 3.8$ with the experimental value of 1.93 eV [104]. The $A$ and $B$ peaks are separated by 118 meV, similar to the spin-splitting in the valence band of 146 meV. The difference between these two values arises from the slight differences in effective mass between the top and bottom spin-split valence band, which will result in a different reduced mass of the exciton. Between the $B$ peak and the second shoulder of the non-interacting conductivity at about 2.4 eV, there lies a set of peaks which arise from the excitonic states built from transitions between the lower lying valence bands and the higher lying conduction bands at $K/K'$. The non-interacting conductivity in Fig. 4.15, which neglects the binding energy resulting from the electron-hole interaction, takes the shape of a double step, which is also a consequence of the

valence band spin-splitting. Fig. 4.15 also shows that, for a diamond substrate ($\varepsilon_{\text{sub}} = 5.7$), the pristine optical conductivity appears very similar in shape to that of monolayer $MoS_2$ on the $SiO_2$. The $A$ and $B$ peaks are separated by a slightly larger amount (123 meV), which is unexpected given that the increase of the dielectric constant should weaken the electron-hole interaction and thus generally reduce the separation between binding energies for excitons. A possible explanation for this is the difference in the reduced mass of the $A$ and $B$ exciton, with values of $0.215m_0$ and $0.257m_0$, respectively. Theoretically, the exciton binding energy behaves similarly to that of a defect, since it arises from the screened Coulomb interaction in the material. As was seen in the case of the two $1s$ defect states originating from the $K/K'$ and $\Gamma$ valleys of the BZ, the larger effective mass results in a higher sensitivity of the binding energy to changes in the general strength of the binding potential. This means that the sensitivity of the $B$ exciton binding energy to changes in the dielectric environment is larger. Indeed, the $B$ exciton binding energy decreases more than the $A$ exciton. Consequently, the separation between the $A$ and the $B$ exciton will increase slightly upon the reduction of $\varepsilon_{\text{sub}}$. The dependence of exciton energy on the effective masses of the bands involved in the transition also partially explains why the other resonances between the $B$ exciton and the free-particle band gap do not shift rigidly either, as different excitons in that part of the spectrum are constructed from transitions between different bands. Additionally, since these states extend further in real-space, they will experience a different shift in local potential compared to the localised $A/B$ excitons, due to the change in dielectric screening when $\varepsilon_{\text{sub}}$ is varied.

| Label | State in Fig. 4.16(b, d) | State in Fig.4.17(b, d) |
|---|---|---|
| A | $1s$, $\Gamma$ | $1s$, $Q$ Lower |
| B | $1s$, $K/K'$ Upper | $1s$, $K/K'$ |
| C | $1s$, $K/K'$ Lower | $1s$, $Q$ Upper |
| D | $2p$, $K/K'$ Upper | $1s'$, $K/K'$ |

Table 4.4: Identity of the labelled states in Fig. Fig. 4.16(b, d) and Fig.4.17(b, d), in the form of the hydrogenic label and the band extremum/extrema from which the state is most strongly constructed from. "Upper" and "Lower" refer to the upper and lower energy in regions of the band structure where spin-splitting is significant.

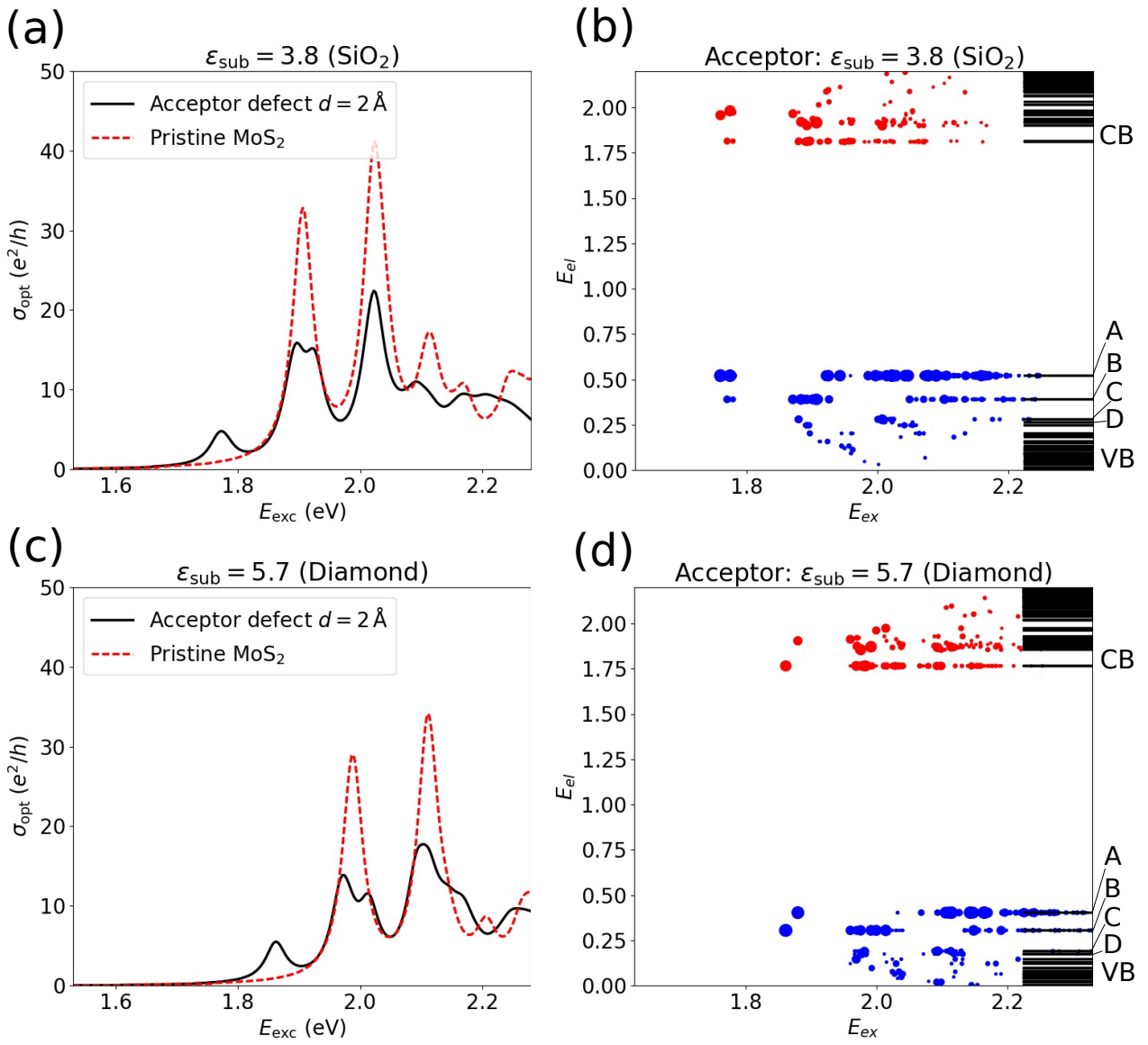



Figure 4.16: (a) Optical conductivity and (b) exciton projections of monolayer $MoS_2$ on a $SiO_2$ ($\varepsilon_{sub} = 3.8$) substrate in the presence of an acceptor defect of unit charge situated $d = 2$ Å above the transition metal atom. (c) Optical conductivity and (d) exciton projections for the same setup but on a diamond ($\varepsilon_{sub} = 5.7$) substrate. The size of the blue (valence band) and red dots (conduction band) in (b, d) indicate the relative strength of the projection.

### 4.6.2 Defect Cell Calculations

For an $18 \times 18$ supercell, the optical conductivity of monolayer $MoS_2$ on a $SiO_2$ substrate in the presence of an acceptor defect of unit charge is shown in Fig. 4.16(a) and compared to the conductivity of the pristine case. The excitons of the defect supercell have been shifted by 40 meV to align the peaks of the $A$ and $B$ excitons. It can be seen that the $A$ exciton peak is split into two overlapping peaks, while the groups of peaks corresponding to both the $A$ and

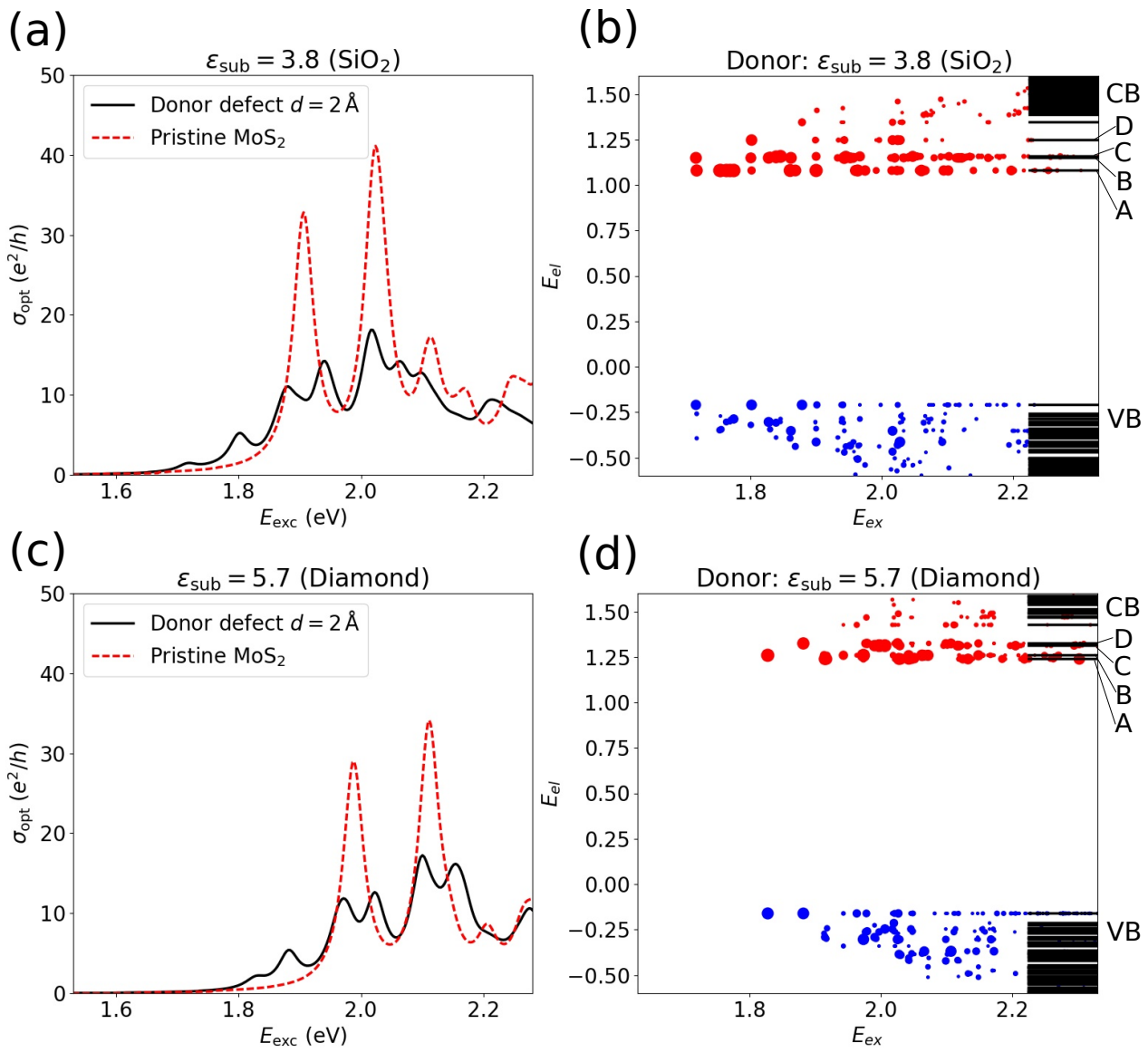



Figure 4.17: (a) Optical conductivity and (b) exciton projections of monolayer $MoS_2$ on a $SiO_2$ ($\varepsilon_{sub} = 3.8$) substrate in the presence of a donor defect of unit charge situated $d = 2$ Å above the transition metal atom. (c) Optical conductivity and (d) exciton projections for the same setup but on a diamond ($\varepsilon_{sub} = 5.7$) substrate. The size of the blue (valence band) and red dots (conduction band) in (b, d) indicate the relative strength of the projection.

$B$ excitons are reduced in their height. The projections of the exciton wavefunction on the single-particle states found from diagonalising the defect supercell at the Γ point are shown in Fig. 4.16(b). The identity of the defect states, labelled by A-E, are detailed in Table 4.4. This shows that the excitonic resonances at approximately 1.9 eV and 2.02 eV, while still being composed of some transitions from the deeper valence band states at $K/K'$, are now mixed with transitions from the $1s$ state at $K/K'$ to the conduction band. This is due to the fact that in the case of the charged defects many of the in-gap states are constructed from the valence band

of the pristine system. Hence, excitons associated with transitions between the conduction band and valence bands of the pristine system will be in part constructed from transitions to/from the defect levels in the presence of the defect potential. This can be seen near 1.9 eV in Fig. 4.16(b) where the excitonic resonances associated with the $A$ exciton contain significant contributions from a distribution of the defect states at $K/K'$. Just below 1.8 eV in Fig. 4.16(a) is a smaller peak, consisting purely of transitions between the conduction band states and the $1s$ states from $\Gamma$ and $K/K'$. Fig. 4.16(b) shows that this peak is comprised solely of defect excitons, with the lowest energy peak being associated with a transition from the $1s$ state from $\Gamma$. Just next to this is a defect exciton that appears to mix between the transitions from the most strongly bound $1s$ state at $\Gamma$ and the $1s$ state at $K/K'$. It can also be seen in this graph that transitions from the $1s$ acceptor states from $\Gamma$ and $K/K'$ contribute to a large section of the optical conductivity between the $B$ exciton and the quasi-particle band gap of the model. When the substrate dielectric constant is slightly increased from 3.8 to 5.7 (corresponding to diamond), the optical conductivity in Fig. 4.17(c) shows that, similar to the pristine case, there is almost a rigid shift of the conductivity towards higher energies. The defect exciton just below 1.9 eV is composed two defect excitons, one from each of the $1s$ acceptor states ($K/K'$ and $\Gamma$) to the conduction band, as seen in the projections of these excitons in Fig. 4.16(d).

In the case of a charged donor defect, the conductivity (Fig. 4.17(a)) shows multiple peaks in the vicinity of where the $A$ and $B$ peak reside in the pristine case (applying the same 40 meV shift as for Fig. 4.16). This occurs due to the splitting and hybridisation present between the two conduction band minima (CBM) at $K/K'$ when coupled by the defect potential. Since the $A$ and $B$ excitons are constructed from these minima, the interaction of states from $K/K'$ drives the separation of the peaks. At the lower end of the spectrum, several peaks are observed between 1.7 eV and 1.9 eV. The projections of these excitons, shown in Fig. 4.17(b), demonstrate the presence of several low-energy defect excitons. The lowest energy excitonic resonance has contributions from both the transitions to the $1s$ defect state from $K/K'$ and the $1s$ defect state from the hybridised $Q$ points. A possible explanation of this is the strong localisation of the defect states which corresponds to a more delocalised projection in reciprocal-space, and mediates an interaction between the $K/K'$ and $Q$ valley. Directly above this are a set of excitons

that can be seen to arise purely from transitions from the valence band to the $1s$ donor states at $Q$. Also due to the hybridisation, the transitions to the $1s$ donor states from $K/K'$ appear as a pair of defect excitons. The optical conductivity for a donor defect on monolayer $MoS_2$ on a diamond substrate is shown in Fig. 4.17(c). When the dielectric constant of the substrate is increased, as for the acceptor case, there is an upward shift in energy of the conductivity from the weakened electron-hole interaction. Furthermore, the reduced strength of the defect potential means that the defect excitons are not as low in energy compared to that of the $SiO_2$ substrate. In Fig. 4.17(d), projections show that the low-energy excitons are constructed from defect states exclusively from $K/K'$ or from the hybridised $Q$ points. In both Fig. 4.16 and Fig. 4.17, it can be seen that increasing the substrate dielectric function refines the low-energy defect excitons to being predominantly composed of transitions exclusively from a single defect state to the opposite band continuum.

### 4.6.3 Inclusion of Exchange

When calculating the excitons of the pristine system for exciton momentum $Q = |\mathbf{Q}| = 0$ (not to be confused with the $Q$ point in the BZ), the exchange component of the Bethe-Salpeter equation (BSE) is not necessary for determining the optical conductivity, as finite-momentum states are dark. In the presence of the defect potential, the band states near the valleys of the pristine system are coupled to form the defect states. This coupling means that transitions between the defect states and the continuum band states involves transitions between occupied and unoccupied states that are in different locations of the pristine unit cell BZ when mapped back. Due to the simplicity of the three-band model used in this work, the Hamiltonians corresponding to either spin can be decoupled from one another, meaning that if only the bright exciton states are required, the BSE can also be decoupled into same-spin transitions between either spin. However, the inclusion of exchange interactions will act to couple spin-up and spin-down transitions, such that the BSE can no longer be solved separately for each spin. The BSE already scales with supercell size $N_c$ to the fourth power, since it is proportional to the product of the number of conduction and valence bands. To check how the results would

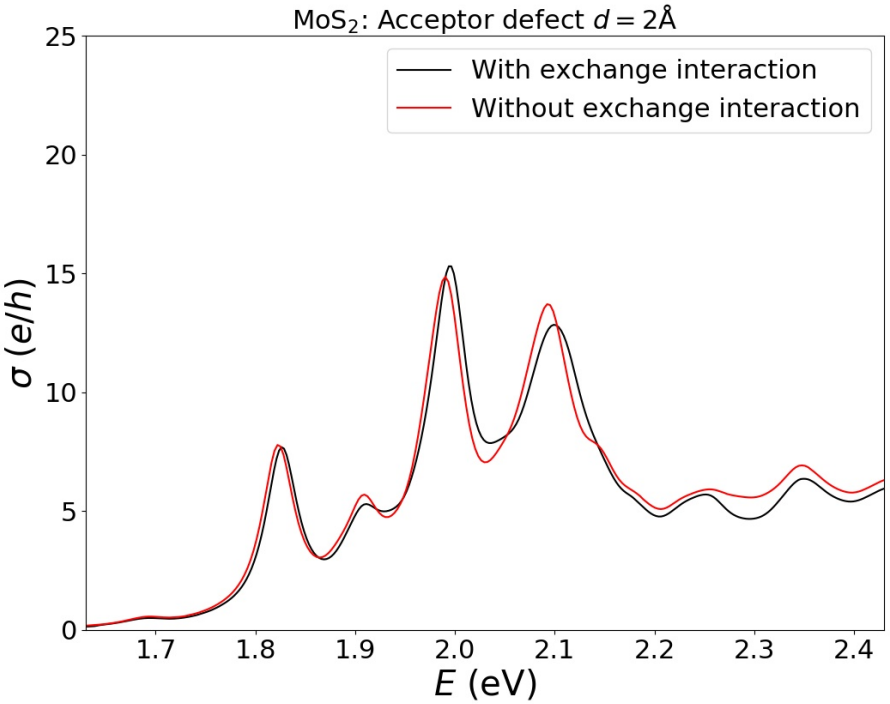



Figure 4.18: Optical conductivity for a $12 \times 12$ supercell of $MoS_2$ on an $SiO_2$ substrate, in the presence of a charged acceptor defect with unit charge situated 2 Å above a Mo site, comparing the calculation with the inclusion of the exchange (black) and without exchange (red). The conductivity has not been rigidly shifted to align with the pristine case.

change in the presence of exchange, the exchange interaction was included in the model and the optical calculation for a smaller $12 \times 12$ supercell with a donor defect was performed both with and without the exchange interaction. This is shown in Fig. 4.18, and demonstrates firstly that the changes to the lower energy excitons are negligible in terms of binding energy, and minimal in terms of the momentum coupling of the exciton to the electromagnetic field (indicated by the height of the peak). It can be seen that for higher energy excitons, the shape and positions of $\sigma$ are more strongly altered.

# Chapter 5

# Bound and Resonant States of Charged Defects on $WS_2$

The concepts discussed and explored in the Chapter 4 with regards to the electronic properties of charged defects on $MoS_2$, can also be applied to the other group 6 TMDCs, such as monolayer $WS_2$, which has identical symmetry and a qualitatively similar band structure. Similarly to $MoS_2$, it has a direct gap at the $K$ point in the Brillouin zone, and a secondary valence band maxima (VBM) at the $\Gamma$ point with an effective mass significantly larger than that of the $K/K'$ points. However, compared to monolayer $MoS_2$, the energy difference between the secondary VBM at $\Gamma$ and the primary VBM at $K/K'$ is larger in $WS_2$ [134]. It was found in the case of $MoS_2$ that, for shallow defects, there is a region of charge strength in which the bound defect state constructed from the pristine Bloch states near $\Gamma$ point, is below the primary VBM, otherwise known as a resonant state. It was also shown that for a given charge, the difference in binding energy of the acceptor $1s$ states constructed from pristine Bloch states at $K/K'$ or $\Gamma$, referenced from their respective VBM, can be explained primarily by the difference in effective mass. Thus, with a larger difference in energy and a smaller difference in effective mass between the $K/K'$ and $\Gamma$ in $WS_2$, resonant states of acceptor defects may be more detectable for larger ranges of defect heights and substrate dielectric constants, and would subsequently be observed more frequently in tunnelling experiments on various charged points defects. In

work performed in 2020 [2], collaborative efforts between experiment and theory sought to understand the electronic signatures of defects in $WS_2$ by comparing STS to results from this tight-binding + RPA framework.

Firstly, I will describe the experimental observations by researchers at UC Berkeley which are relevant to this discussion. Then, following a brief overview of basic electronic properties of this tight-binding model and defect potential, I will compare experiment to the electronic structure of the defect states from the tight-binding model, including their electronic signatures in the local density of states. This will require accounting for weaker tunnelling of holes from the scanning tip to the primary valence band maxima states, and subtracting continuum band contributions from resonant states. Lastly, I will show how this model can be combined with effective mass theory to obtain a resonant scattering time that is important for transport applications.

## 5.1 Properties of Monolayer $WS_2$

As for the case of $MoS_2$, the band structure and density of states of monolayer $WS_2$ is plotted and shown in Fig. 5.1(a) and (b), respectively. In the valence band, there are some noticeable differences compared to the $MoS_2$ band structure, despite the qualitative similarity in topography and spin-degeneracy at symmetry points. Firstly, it can be seen in Fig. 5.1(a) that $WS_2$ has a larger spin-orbit splitting of 0.43 eV between the valence bands at $K/K'$ seen in this tight-binding model compared to that of $MoS_2$ (0.138 eV) [1]. This is also noticeable in the density of states in Fig. 5.1(b), where the valence band shoulder is more elongated than in Fig. 4.1(b). Additionally, the energy difference between the VBM at $\Gamma$ and the VBM at $K/K'$

| | $K_v$ | $\Gamma_v$ | $K_c$ | $Q_c$ |
|---|---|---|---|---|
| $m_x^*/m_0$ | 0.296 | 2.15 | 0.35 | 0.753 |
| $m_y^*/m_0$ | 0.296 | 2.15 | 0.35 | 1.26 |

Table 5.1: Effective masses $m_x^*$ and $m_y^*$ (in units of the free electron mass $m_0$) along the $k_x$ and $k_y$ reciprocal-space directions, respectively, for $WS_2$, shown for the valence band (subscript $v$) and conduction band (subscript $c$), at valence band maxima and conduction band minima.

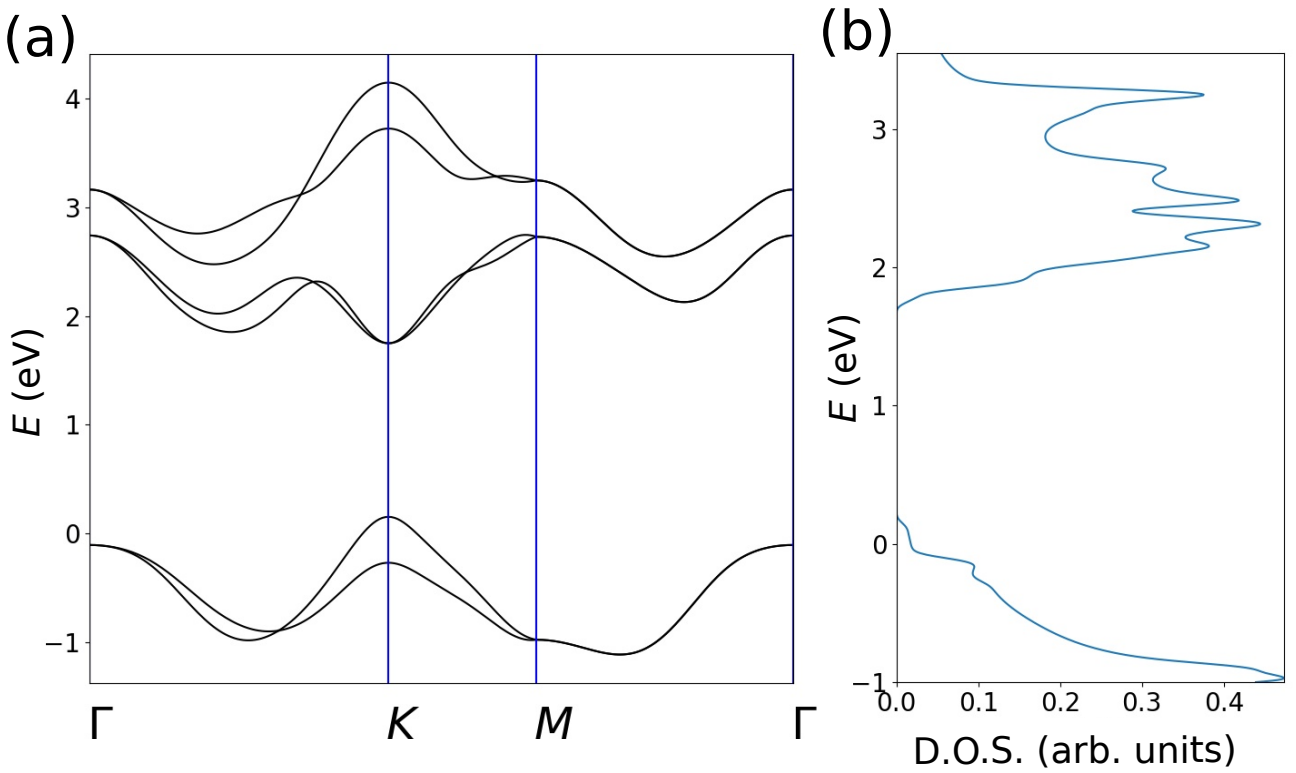



Figure 5.1: (a) Band structure along the $\Gamma - K - M - \Gamma$ line in the $WS_2$ Brillouin zone, along with the (b) corresponding density of states (DOS).

is 0.259 eV, over three times larger than in the case of $MoS_2$ (0.071 eV). Table 5.1 demonstrates that $WS_2$ generally has lower effective masses in both the conduction and valence band than $MoS_2$, including the $\Gamma$ point which has an isotropic effective mass of $2.14m_0$ for $WS_2$ compared to $2.65m_0$ for $MoS_2$. From the intuition developed in chapter 4, the lower effective mass means that the binding energy of defect states from the $\Gamma$ point will increase less with a stronger charge than for $MoS_2$. This, combined with the increased energy separation between $\Gamma$ and $K/K'$, suggests that there is a greater range of charge strength or substrate dielectric constant in which $WS_2$ exhibits resonant defect states.

In the experimental setup, the monolayer $WS_2$ is resting $z_g = 4.9$ Å above a multi-component substrate, consisting of a layer of doped graphene ($v_F = 1.15 \times 10^6$ ms$^{-1}$) which sits $z_s = 1.7$ Å above a SiC substrate ($\varepsilon_{SiC} = 9.7$). This is included in the dielectric function and shown in Fig. 5.2(a), showing that the inclusion of doped material below the $WS_2$ significantly changes the screening at long-range. While the screening of the freestanding monolayer $WS_2$ (shown in black) converges to unity at long range, the same cannot be said when the metallic nature of the doped graphene substrate is considered. The dielectric function of the composite

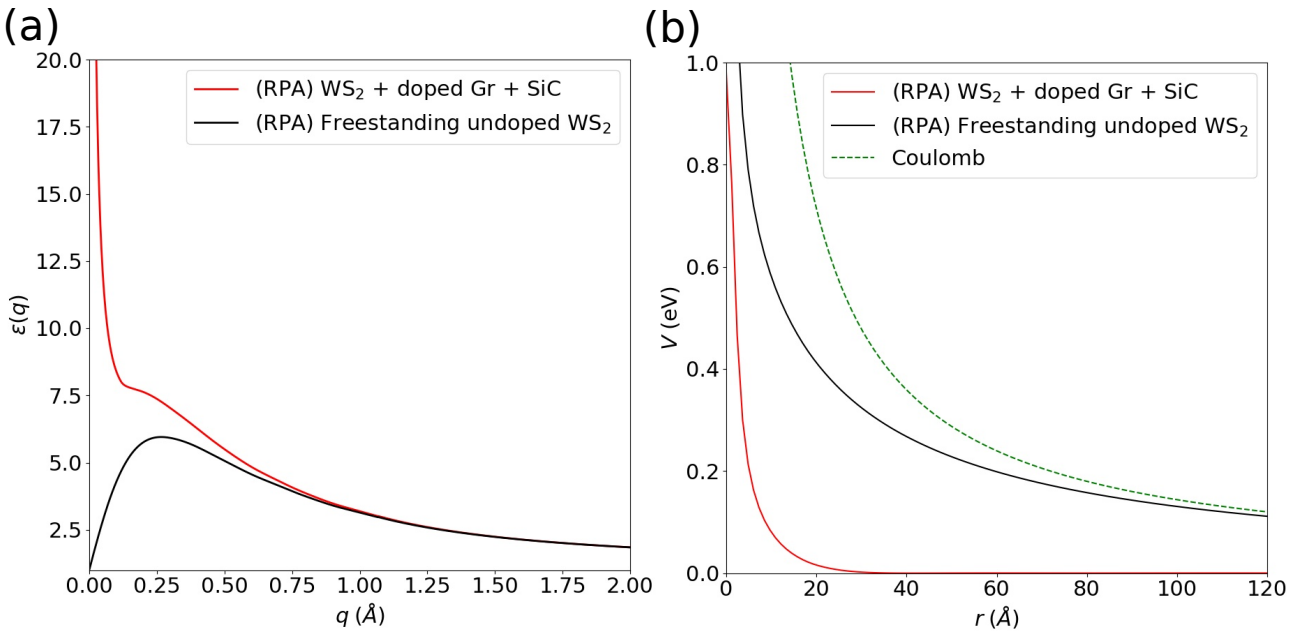



Figure 5.2: (a) Dielectric function for the combined system (red) of $WS_2$, which sits $z_g = 4.9$ Å above a layer of doped graphene ($v_F = 1.15 \times 10^6$ ms$^{-1}$) which itself lies $z_s = 1.7$ Å above a silicon carbide (SiC) substrate ($\varepsilon_{SiC} = 9.7$). This model takes into account the Lindhard screening present in the polarisation function of doped graphene and the image effect that occurs between the $WS_2$ and SiC. The dielectric function of a freestanding monolayer is also shown (black) for comparison. (b) Defect potential using the dielectric function in (a) of the combined system, for a charged defect of charge $1e$ sat $z_d = 2.4$ Å above the transition metal layer of $WS_2$ (red), compared to the freestanding monolayer case (black) and the unscreened Coulomb case (green dashed).

system diverges at small wavevectors $q$, which corresponds to exceptional screening at long-range. Due to the image effect caused by the substrate, weaker screening exists at short range (large wavevectors), such that the dielectric function of the composite system converges to the freestanding case at large $q$. The significance of the difference between the screening in the composite system versus the freestanding monolayer can be seen in Fig. 5.2(b). Here, the defect potential for a charge $1e$ placed $z_d = 2.4$ Å above the W layer of the $WS_2$ is shown in red, and compared to the freestanding case in black and the unscreened case in green. This demonstrates that beyond approximately 30 Å, the potential is almost completely screened, with a rapid decrease in defect potential with distance. The decay is more exponential in shape compared to the logarithmic decrease of freestanding case and unscreened case, due to the effective long-range screening capability of free carriers in the doped graphene.

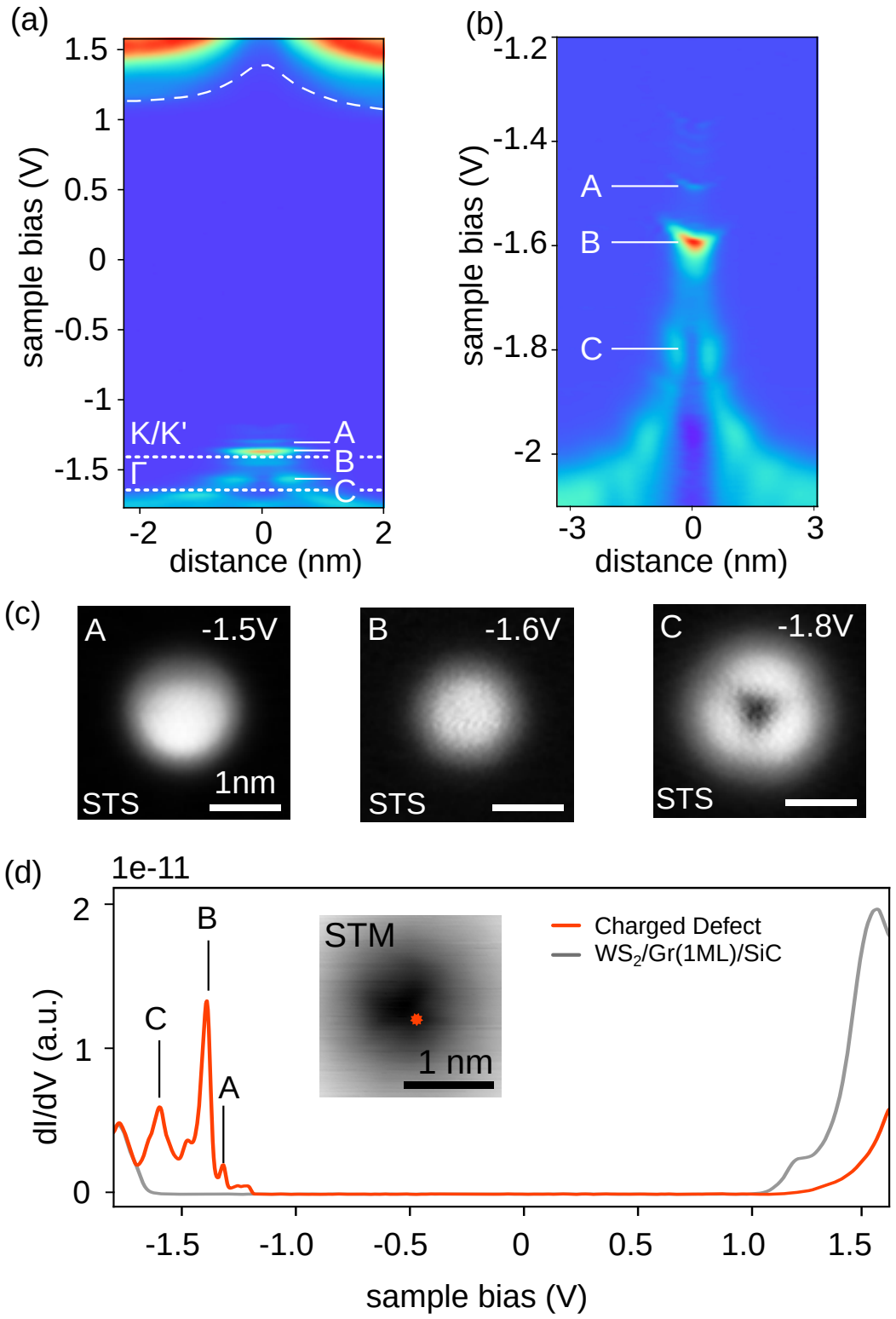



Figure 5.3: (a-b) STS spectra of a charged defect on $WS_2$, where upward bending of the conduction band due to the negatively charged defect is indicated with a dashed white line, and the onset of the $K/K'$ and $\Gamma$ valleys of pristine $WS_2$ are indicated with white dotted lines. Note that the spectra in (a) and (b) were taken on different defects. (c) STS of a CD. (d) Constant height $\mathrm{d}I/\mathrm{d}V$ of the defect corresponding to electronic states A, B, and C [2]. Reprinted with permission from [2] (own), Copyright 2020 by the American Physical Society.

## 5.2 Experimentally Observed Defect States

The experimental section of the work was performed by researchers at UC Berkeley, in a collaboration with Bruno Schuler, Katherine A. Cochrane, Jun-Ho Lee, Christoph Kastl, Jeffrey B. Neaton, and Alexander Weber-Bargioni of the Molecular Foundry at the Lawrence Berkeley National Laboratory, Berkeley, CA. In this work, STM measurements of the defect on the composite $WS_2$ + Gr + SiC system were carried out [2]. Fig. 5.3(a) shows measurements of the derivative $\mathrm{d}I/\mathrm{d}V$ of tunnelling current $I$ with respect to the bias voltage $V$, which is proportional to the local density of states. Here it can be seen that near a charged defect, electronic features can be seen in $\mathrm{d}I/\mathrm{d}V$ only within the vicinity of the defect. For positive biases, which causes electrons to tunnel from the tip into the conduction band of the semiconducting material, band-bending can be seen to increase as the tip scans closer to the defect. This is due to electrons in the conduction band experiencing a repulsive Coulomb force that increases their energy close to the defect, indicating that the defect is of an acceptor nature. For negative biases, in which electrons tunnel from the valence band into to the tip, a series of localised resonances arise in the $\mathrm{d}I/\mathrm{d}V$. These appear as a localised state (labelled A), a state with a much stronger LDOS signal (labelled B), both of which lie above the $K/K'$ VBM, and a lobed state (labelled C) between the $\Gamma$ and $K/K'$ VBM. It should be noted that because of their smaller effective mass and large crystal momentum, the tunnelling matrix elements of holes into $K/K'$ states are relatively weak compared to that of the states near the $\Gamma$ point, and thus cannot be seen well in the $\mathrm{d}I/\mathrm{d}V$ [2]. A closer look at this series of defect states above the valence band, for another defect of the same species, is shown in Fig. 5.3(b). Here the same pattern of states is observed as in 5.3(a), but with a set of fainter states visible above the A state, whose signature is less than a third the strength of the A peak as found in Fig. 5.3(d). The spatially resolved $\mathrm{d}I/\mathrm{d}V$ of the three most dominant states are shown in Fig. 5.3(c), and show highly isotropic signatures, indicative of non-chemical defect states. The STS of states A and B can be seen as localised $1s$ states of similar extent at $\approx 1$ nm, while C appears as a ring with a slight trigonal bias, similar to those seen in the case of $MoS_2$ [14]. This ring state extends further than either of the $1s$ states, which is consistent with the 2D hydrogenic

model in which states associates with higher principal quantum numbers are less localised to the atom.

## 5.3 Defect States Calculated from the Tight-binding Model

To better understand the experimental results, the electronic properties of the $WS_2$ composite system were modelled by applying the potential in Fig. 5.2(b) onto a supercell of the tight-binding model that produces the band structure in Fig. 5.1(a). Upon application of the defect potential, the local density of states (LDOS) of the supercell near the defect is shown in Fig. 5.4(a,b) on approximately the same energy scales and distances from the defect as in Fig. 5.3(a,b). The LDOS demonstrates a strong similarity with the observed tunnelling spectra, including both upward band bending in the conduction band and a series of localised bound states present above the valence band minima (VBM) at $K/K'$ and in between the VBM at $K/K'$ and $\Gamma$. The upward band bending itself arises from the negative potential of the acceptor defect raising the energy of the electrons with stronger distribution near the defect site. The spectrum of defect states near the valence band extend on the same order of magnitude as those seen in Fig. 5.3(a) with a radius between 1-2 nm, and include two dominant localised states above the $K/K'$ VBM. The spatial distributions of these states can be given a hydrogenic label that reflects its nodal structure. This is shown in Fig. 5.4(c), where the two localised states are labelled as $1s$. As in the case of $MoS_2$, the presence of two $1s$ states with generally different binding energies and spatial extent, arises from the existence of two different types of valleys in the TMDC valence band structure. As seen in Fig. 5.1, the energy and effective mass of the VBM at the $K/K'$ and $\Gamma$ points differ significantly. Hence, it can be inferred that these two $1s$ states are constructed from pristine Bloch states around the $K/K'$ points, or from around the $\Gamma$ point. The projections in Fig. 5.4(d) confirm this, demonstrating that the less localised $1s$ state from $K/K'$ projects onto the small regions in corners of the 1st BZ in the immediate vicinity of the $K$ (spin up) or $K'$ (spin down) points, whereas the more strongly localised but less strongly bound state projects onto a larger vicinity around the $\Gamma$ point. These occur at the same binding energy as state A and B in Fig. 5.3(a,b), within binding energies 95 meV and 25

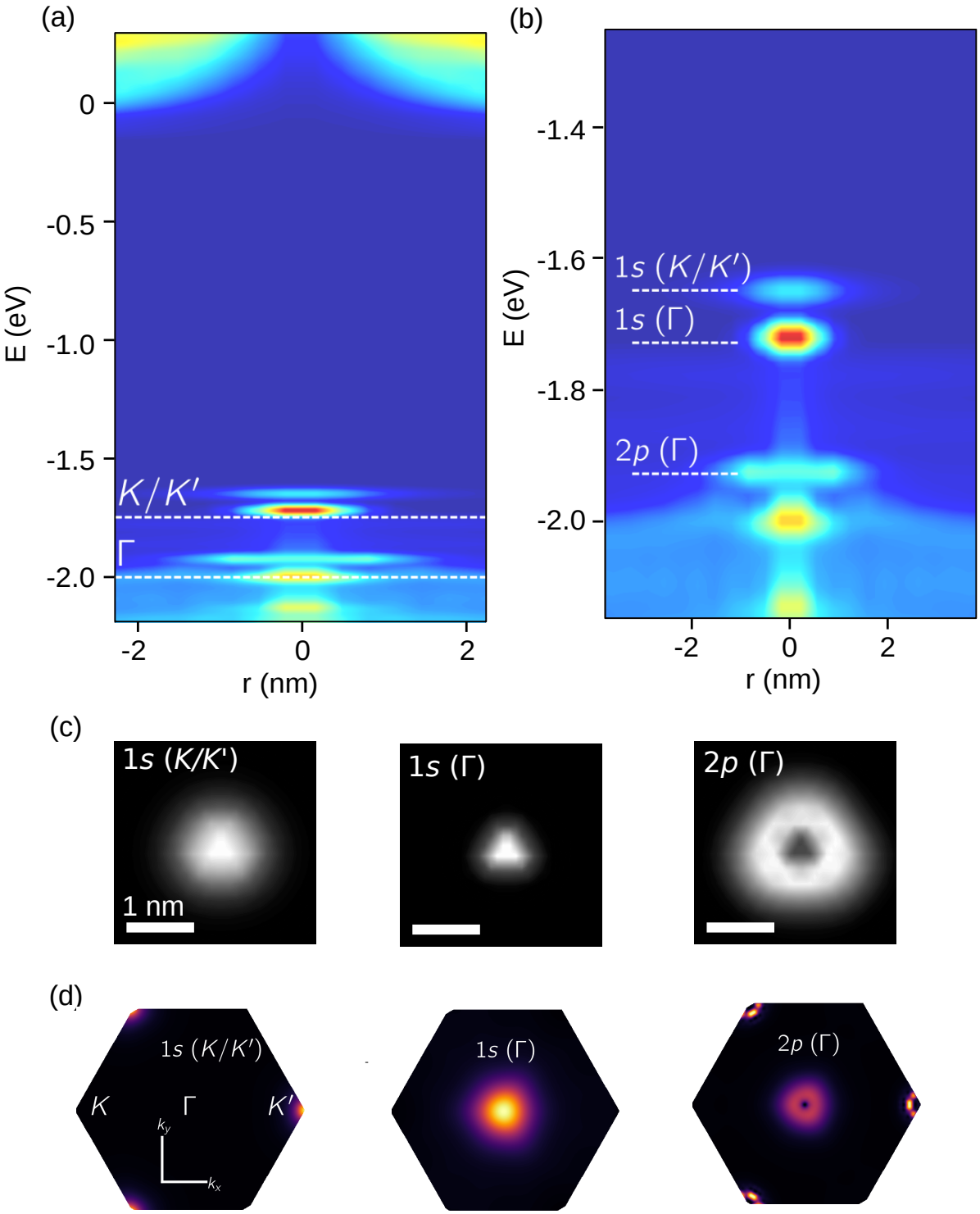



Figure 5.4: (a),(b) Calculated local density of states of a negatively charged defect in $WS_2$ on graphene/SiC substrate. In (a), the onset of the $K/K'$ and Γ valleys are indicated by dashed lines. In (b), the defect states are labelled by their hydrogenic quantum numbers and valley. (c) Simulated STS images of defect states. (d) Projections of defect wave functions onto unperturbed $WS_2$ states [2]. Reprinted with permission from [2] (own publication), Copyright 2020 by the American Physical Society.

meV, respectively, referenced from the VBM at $K/K'$ [2]. These are less than the binding energies extracted from tunnelling experiments, which are shown comparatively in Table 5.2. Since the $K/K'$ points register less strongly in the tunnelling experiment than the $\Gamma$, the referenced binding energies can be compared better between theory and experiment when the $\Gamma$ referenced energies are used. The energies of the two $1s$ states as calculated from the tight-binding model differ from the experimentally obtained values by about 50-60 meV, which is about a 15% difference [2]. Since the energy difference between theory and experiment is reasonably consistent for these states, their relative energy is also in agreement with experiment.

In addition to the bound defect states seen in Fig. 5.4(a,b) above the global VBM at $K/K'$, there exists a spectrum of defect states between the $\Gamma$ VBM and the $K/K'$ VBM, similar to that seen in Fig. 5.3(a,b). The majority of the states seen in this region are very faint and show negligible values of LDOS compared to the $1s$ peaks seen above the $K/K'$ VBM. However, at about $\approx -1.95$ eV in Fig. 5.4(b), there is an extended state that has a larger value of the LDOS and appears to have an almost constant value within 1 nm, and decaying with a different scale length beyond this radius. As this is more extended than the $1s$ states, this indicates that it is a higher order defect state. While its extent and energy relative to the $1s$ states suggest that it can be compared to state C in Fig. 5.3, it lacks the gap present in the STM results, which causes state C to appear as a ring in the spatially resolved tunnelling spectra. The wavefunctions of these states from a tight-binding supercell calculation are shown in Fig. 5.5(a), where there appear to be four different states (each doubly spin-degenerate) of the same spatial extent.

| | Experiment | | Theory | |
|---|---|---|---|---|
| | K | $\Gamma$ | K | $\Gamma$ |
| A [1s(K/K′)]/meV | +175 | +415 | +95 | +355 |
| B [1s($\Gamma$)]/meV | +95 | +335 | +25 | +285 |
| C [2p($\Gamma$)]/meV | −130 | +110 | −180 | +80 |

Table 5.2: Comparison of experimentally determined and theoretically calculated binding energies of three observed resonances: A, B, and C. Values are listed with respect to the K and $\Gamma$ valence band edges. Positive binding energies indicate a lower energy with respect to the band edge [2].

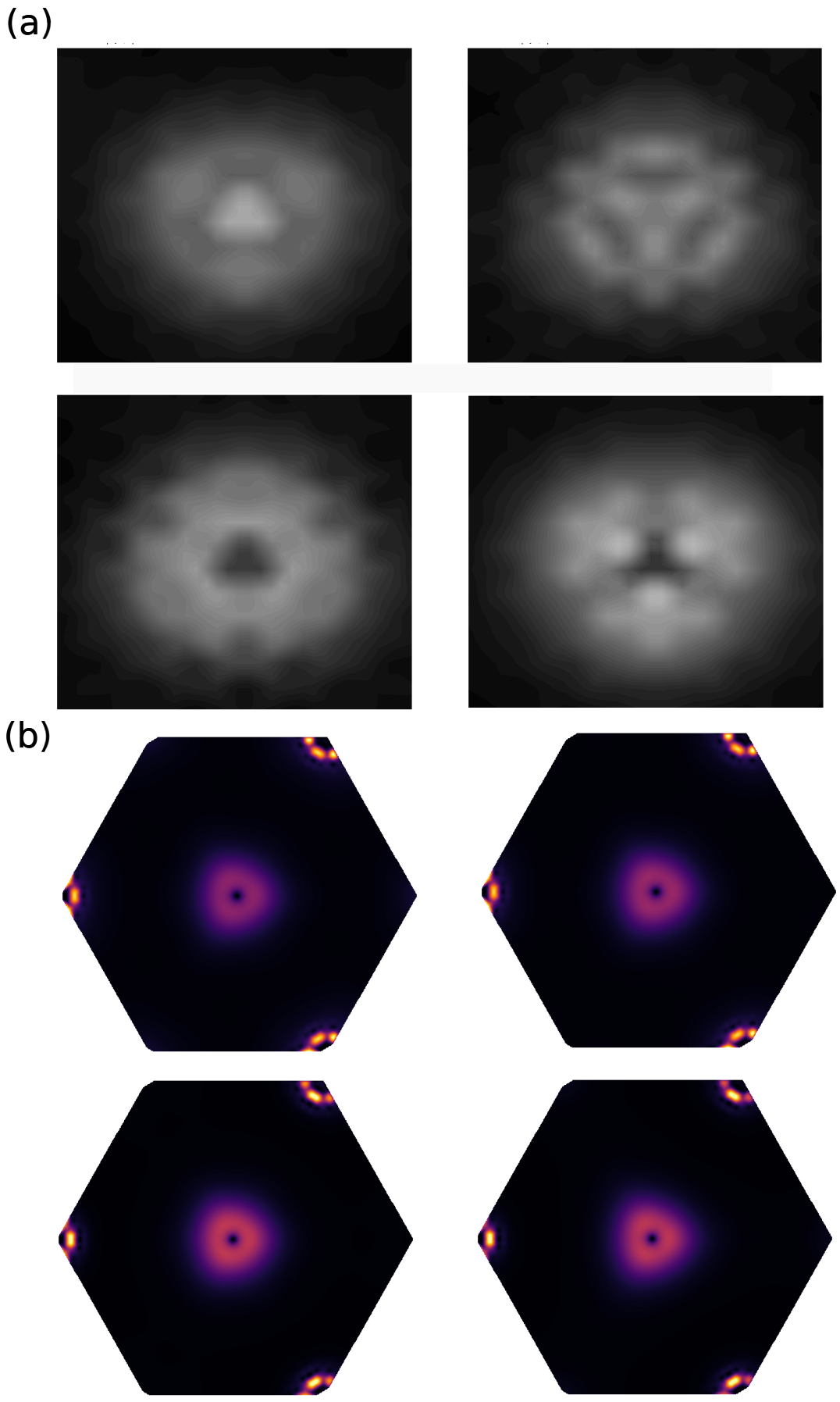



Figure 5.5: (a) Real-space wavefunctions and (b) reciprocal-space projections of the resonant defect states seen $\approx 80$ meV above the $\Gamma$ point.

While the top two of these in (a) exhibit a central distribution, the latter two demonstrate the presence of the ring seen the experimental results. These roughly resemble the $2p$ states seen in 4.4(a) for $MoS_2$, but with several differences in the structure. The projections of the states in Fig. 5.5(b) demonstrate that they are a hybridisation between the VBM at $\Gamma$ and $K/K'$. However, while the Bloch contribution from around the $\Gamma$ point appears as a $2p$-like ring with a small amount of trigonal warping, the contribution from the $K/K'$ points are at sampled $k$-points for which the energy at the band is equal to the energy of the defect state. The contributions from $K/K'$ do not appear as rings or any hydrogenic shape seen in the case of $MoS_2$, but as a segmented chain of resonances around the $K$ points. Additionally, these arise at much lower energy than the $K/K'$ VBM, indicating that the contributions from $K$ are not from defect states, but the valence band continuum. This suggests that the states seen in Fig. 5.5 are a hybridisation between the $2p$ states of the VBM at $\Gamma$ and the continuum of the valence band states near $K/K'$, as depicted in Fig. 5.6(a).

The valley hybridisation arises from the resonant nature of the $2p$ defect state and can be understood within the framework of effective mass theory [2,29]. In this approach, the coupling between different valleys is neglected, obtaining a set of bound defect states for each valley. The inclusion of the coupling between valleys means that bound states from the secondary VBM at $\Gamma$ which are degenerate with continuum states from the $K/K'$ valleys, can mix with the continuum states [2]. The resulting hybridised states can be written as

$$\psi_{2p(\Gamma)}(\mathbf{r}) = c_{2p(\Gamma)}\phi_{2p(\Gamma)}(\mathbf{r}) + \sum_{n\in\{K,K'\}} \int_{\Omega_n} \mathrm{d}\mathbf{k}\; c_n(\mathbf{k})\phi_{n\mathbf{k}}(\mathbf{r}), \tag{5.1}$$

where $\phi_{2p(\Gamma)}$ and $\phi_{n\mathbf{k}}$ denote the bound and continuum states obtained for decoupled valleys, respectively, (with $n$ labelling the valley), $c_{2p(\Gamma)}$ and $c_n(\mathbf{k})$ are complex coefficients, and $\Omega_n$ denotes the $k$-space region corresponding to the $n^{\text{th}}$ valley [2]. Since the continuum states at $K/K'$ do not provide a significant signal on account of their large crystal momentum, this component of the defect states is not observed in spatially resolved tunnelling spectra. To simulate this phenomenon, the defect states in Fig. 5.5(a) were reconstructed using only the Bloch components around the VBM at $\Gamma$ in Fig. 5.5(b) that correspond to the $2p$ defect state.

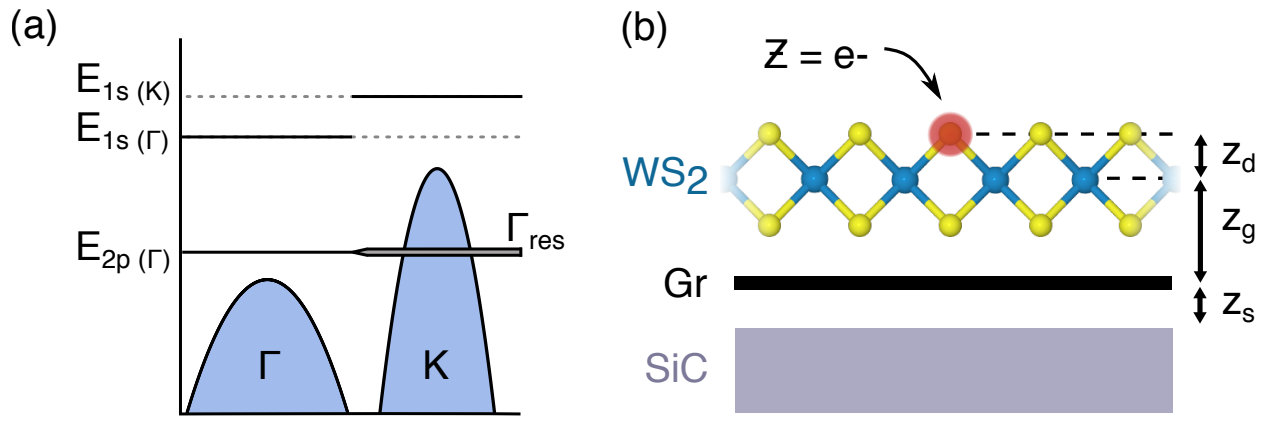



Figure 5.6: (a) Schematic of the electronic structure of a negatively charged defect in $WS_2$. Shown are the primary valence band maximum at $K$ (a second degenerate maximum exists at $K'$) and the secondary maximum at $\Gamma$ as well as the bound and resonant defect states. The states labelled 1s ($K$), 1s ($\Gamma$), and 2p ($K$) correspond to the experimental features A, B, and C, respectively. (b) Schematic of the system consisting of a $WS_2$ layer on graphene on a silicon carbide substrate with a substitutional impurity with charge $Z$ [2]. Reprinted with permission from [2] (own publication), Copyright 2020 by the American Physical Society.

Summing the four states with a suitable broadening gives the third wavefunction in Fig. 5.4(c). This shows a very good agreement with the distribution seen in the spatially resolved STM for defect state C in Fig. 5.3(c), in both extent and nodal structure. The trigonal symmetry seen in this state is more apparent in the theory than in experiment, which could be due to an overestimated warping in the $\Gamma$ point VBM in the tight-binding model, or due to the lower spatial sampling of the tight-binding model (one data point for every W atom).

### 5.3.1 Lifetimes of Resonant States

Due to the resonance of the defect state with the continuum, a carrier in the primary band extrema will not participate in conduction for a time $\tau_{\text{res}} = \hbar\Gamma_{\text{res}}$, upon the application of an external electric field. $\Gamma_{\text{res}}$ is the width of the resonant impurity level, indicating an energy range with which carriers in the band extrema can transition into the defect state. This quantity can be obtained using effective mass theory, through:

$$\Gamma_{\text{res}} = \pi \sum_{n\in\{K,K'\}} \int_{\Omega_n} d\mathbf{k} |V_{2p(\Gamma),n}(\mathbf{k})|^2 \delta(E_{2p(\Gamma)} - \epsilon_{n\mathbf{k}}), \tag{5.2}$$

where $\epsilon_{n\mathbf{k}}$ denotes the energy of a continuum state with crystal momentum $\mathbf{k}$ in valley $n$ and $V_{2p(\Gamma),n}(\mathbf{k})$ is the matrix element of the Bloch-transformed screened impurity potential between $\phi_{2p(\Gamma)}(\mathbf{r})$ and $\phi_{n\mathbf{k}}(\mathbf{r})$ [2, 29]. This quantity can be calculated by integrating around a ring of $k$-points at which the sampled state is closest in energy to the energy $E_{2p(\Gamma)}$ of the $2p$ state:

$$\begin{aligned}
\Gamma_{\text{res}} &= \pi \sum_{n\in\{K,K'\}} \int_{\Omega_n} \frac{\mathrm{d}k\mathrm{d}\theta}{(2\pi)^2} k |V_{2p(\Gamma),n}(\mathbf{K_n}+\mathbf{k})|^2 \delta\left(E - E(\mathbf{K}_n+\mathbf{k})\right), \\
&= \frac{1}{2}\int_{\Omega_n} \mathrm{d}k\; k\,\delta\left(E - \frac{\hbar^2 k^2}{2m^*_{K_n}}\right) \frac{1}{2\pi}\int \mathrm{d}\theta\; |V_{2p(\Gamma),n}(\mathbf{K}_n+\mathbf{k})|^2 \\
&= \frac{m^*_{K_n}}{2\hbar^2}\left\{\frac{1}{2\pi}\int \mathrm{d}\theta\; \left| V_{2p(\Gamma),n}\left(\mathbf{K}+\left(\frac{\sqrt{2m^*_K E}}{\hbar},\theta\right)\right)\right|^2\right\}
\end{aligned}$$

where the term in braces is the average of the coupling between the scattered Bloch states and the zeroth order impurity state (without the contribution from the valence band continuum). This coupling is calculated by expanding out the Bloch transform of the impurity potential.

$$\begin{aligned}
V_{2p(\Gamma),n}(\mathbf{k}) &= \int_{\Omega_\Gamma} \frac{\mathrm{d}\mathbf{k}'}{(2\pi)^2} \int_{\Omega_K} \frac{\mathrm{d}\mathbf{k}''}{(2\pi)^2} \phi^{0*}_\Gamma(\mathbf{k}') V_{\Gamma,K}(\mathbf{k}',\mathbf{k}'') \phi^0_{K,\mathbf{k}}(\mathbf{k}'') && (5.3)\\
&= \int_{\Omega_\Gamma} \frac{\mathrm{d}\mathbf{k}'}{(2\pi)^2} \int_{\Omega_K} \frac{\mathrm{d}\mathbf{k}''}{(2\pi)^2} \phi^{0*}_\Gamma(\mathbf{k}') \left(\int \mathrm{d}\mathbf{r}\psi^*(\mathbf{k}',\mathbf{r}) V(r) \psi(\mathbf{k}'',\mathbf{r})\right) \phi^0_{K,\mathbf{k}}(\mathbf{k}'') && (5.4)\\
&= \int \mathrm{d}\mathbf{r} \left(\int_{\Omega_\Gamma} \frac{\mathrm{d}\mathbf{k}'}{(2\pi)^2} \phi^{0*}_\Gamma(\mathbf{k}')\psi^*(\mathbf{k}',\mathbf{r})\right) V(r) \left(\int_{\Omega_K} \frac{\mathrm{d}\mathbf{k}''}{(2\pi)^2} \phi^0_{K,\mathbf{k}}(\mathbf{k}'')\psi(\mathbf{k}'',\mathbf{r})\right) && (5.5)\\
&= \int \mathrm{d}\mathbf{r}\; \phi^{0*}_\Gamma(\mathbf{r}) V(r) \phi^0_{K,\mathbf{k}}(\mathbf{r}) && (5.6)
\end{aligned}$$

where the impurity states are a linear superposition of the Bloch states with coefficient $\mathrm{d}\mathbf{k}'\phi^0_{K,\mathbf{k}}(\mathbf{k}')$. Expanding this into the tight-binding basis gives:

$$V_{2p(\Gamma),n}(\mathbf{k}) = \sum_{limj} c^*_{\Gamma li} c_{\Gamma(\mathbf{k})mj} \underbrace{\int \mathrm{d}\mathbf{r}\phi_l(\mathbf{r}-\boldsymbol{\tau}_i) U(r) \phi_m(\mathbf{r}-\boldsymbol{\tau}_j)}_{\approx \delta_{ij}\delta_{lm} V(\boldsymbol{\tau}_i)} \approx \sum_{li} c^*_{\Gamma li} c_{\Gamma(\mathbf{k})li} V(\boldsymbol{\tau}_i). \qquad (5.7)$$

This can further be simplified in terms of the Bloch states of the pristine tight-binding supercell, by using the fact that the $2p$ defect state at $\Gamma$ is a linear combination of supercell Bloch states with projection $d_{\Gamma,\mathbf{g}}$, and then writing the pristine supercell states in terms of unit cell states.

This gives:

$$\begin{aligned}\sum_{li} c^*_{\Gamma li} c_{\Gamma(\mathbf{k})li} V(\boldsymbol{\tau}_i) &= \sum_{li} \left( \sum_{\mathbf{g}} d_{\Gamma,\mathbf{g}} c^*_{\Gamma(\mathbf{g})li} \right) c_{\Gamma(\mathbf{k})li} V(\boldsymbol{\tau}_i) \\ &= \sum_{\mathbf{g}} d_{\Gamma,\mathbf{g}} \sum_{li} \left( \frac{e^{-i\mathbf{g}\cdot\boldsymbol{\tau}_i}}{\sqrt{N^2}} c^*_{v\mathbf{g}l} \right) \left( \frac{e^{i\mathbf{k}\cdot\boldsymbol{\tau}_i}}{\sqrt{N^2}} c_{v\mathbf{k}l} \right) V(\boldsymbol{\tau}_i) \\ &= \sum_{\mathbf{g}} d_{\Gamma,\mathbf{g}} \left( \sum_{l} c^*_{v\mathbf{g}l} c_{v\mathbf{k}l} \right) \frac{1}{N^2} \sum_{i} e^{i(\mathbf{k}-\mathbf{g})\cdot\boldsymbol{\tau}_i} V(\boldsymbol{\tau}_i) = \sum_{\mathbf{g}} d_{\Gamma,\mathbf{g}} \mathbf{c}^\dagger_{v\mathbf{g}} \cdot \mathbf{c}_{v\mathbf{k}} V_{\mathbf{k}-\mathbf{g}}\end{aligned}$$

where $V_{\mathbf{k}}$ is the lattice Fourier transform of the impurity potential. The width $\Gamma_{\text{res}}$ can then be written as:

$$\Gamma_{\text{res}} = \frac{m^*_K}{2\hbar^2} \frac{A}{N_{\mathcal{S}}} \sum_{\mathbf{k}\in\mathcal{S}} \left| \sum_{\mathbf{g}} d_{\Gamma,\mathbf{g}} \mathbf{c}^\dagger_{v\mathbf{g}} \cdot \mathbf{c}_{v\mathbf{k}} V_{\mathbf{k}-\mathbf{g}} \right|^2 , \tag{5.8}$$

where $N_{\mathcal{S}}$ denotes the size of the set $\mathcal{S}$, which contains all states in the rings around the $K/K'$ VBM with energy $E_{2p(\Gamma)}$, and $A$ is the area of the supercell. This was calculated for the $2p$ state built from states at $\Gamma$ and was found to be 20 meV, giving a lifetime $\tau_{\text{res}}$ of 30 ps. This result shows that resonant defect states exhibit relatively small linewidths which correspond to long trapping times, and suggests that resonant states should lead to a drastic reduction in conductivity when the Fermi level reaches the resonant impurity level [2]. Note that in a $WS_2$ transport device, graphene could not be used as a substrate as most carriers would propagate through the graphene. Without graphene, the screening of the impurity charge would be reduced, resulting in a resonant impurity level that lies closer to the VBM at $K/K'$. However, the trapping time would not change significantly because of the flat density of states of $WS_2$ near the VBM [2].

### 5.3.2 Sensitivity of the Binding Energies to Defect Height

The only parameter in this model not supplied directly by experiment was the height $z_d$ of the defect charge above the W layer. The value of $z_d$ used in this model was found by tuning within physically reasonable range ($1-2.5$ Å) to get the best comparison to experiment. The variation of the binding energy (referenced to the secondary VBM at $\Gamma$) of the defect states studied in this work, with this parameter is shown in Fig. 5.7, and demonstrates that the results seen in

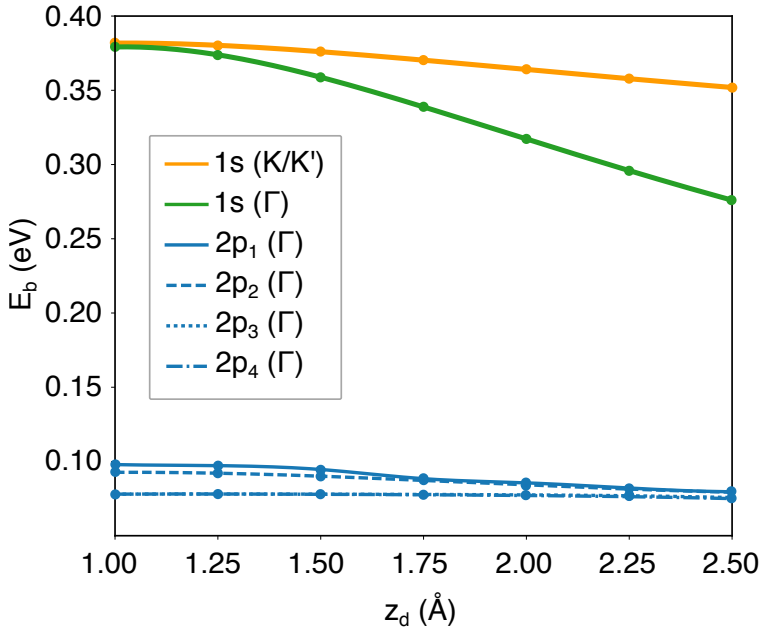



Figure 5.7: Dependence of the binding energy (measured with respect to the secondary valence band maximum at Γ) of various defect states on the parameter $z_d$ [2]. Reprinted with permission from [2] (own publication), Copyright 2020 by the American Physical Society.

Fig. 5.4 are not strongly dependent on this parameter to within 0.1 eV. A value of $z_d = 2.4$ Å was found to match the separation between the resonances in experimental work. It can be seen in Fig. 5.7 , that the $1s$ states are more sensitive to changes in $z_d$ than the $2p$ states as the most significant changes to the potential occur in the $WS_2$ region underneath the defect where the $2p$ states have a node. Note that the hybridisation of the localised $2p$ state from the Γ valley with the continuum states from the $K/K'$ valleys gives rise to multiple mixed states which are labelled by $2p_n(\Gamma)$ in Fig. 5.7. As a consequence of the larger effective mass of the Γ valley, the $1s(\Gamma)$ state is more localised than the $1s(K/K')$ state and therefore decreases more quickly as $z_d$ is increased.

### 5.3.3 Other Defect States in the Spectrum

In this work, only three defect states have been discussed in both the theory ($1s(K/K')$, $1s(\Gamma)$ and $2p(\Gamma)$) and experiment (A, B and C). However, in the study of defect states of $MoS_2$, several other states of different hydrogenically labelled nodal structure originating from both $K/K'$ and the Γ point arise in the defect spectrum. This also occurs in the case of $WS_2$, as can be seen in

the LDOS in Fig. 5.4 between the $2p(\Gamma)$ state and the $K/K'$ VBM, where there is a spectrum of states that appear to be mainly localised to the defect, but still faint in value. Due to the strong screening of the defect potential by both the $WS_2$ monolayer and the doped graphene sheet beneath it, secondary states constructed from pristine Bloch states near $(K/K')$ extend further into the supercell that those from the $\Gamma$ point. Hence, the normalisation requirement of the wavefunction means that the overall probability density of these spread-out defect states is significantly lower than the states seen in Fig. 5.4(c). The states that do faintly appear in the LDOS of Fig. 5.4(a,b) are those with a $2s$, and $3s$ nature which have non-negligible distribution at the defect site, where the localised potential is strongest. These are also seen in the $\mathrm{d}I/\mathrm{d}V$ in Fig. 5.3(b), but are not identified or further analysed in experiment.

# Chapter 6

# Defect States in Monolayer and Bilayer Black Phosphorus

## 6.1 Introduction to Monolayer and Bilayer Black Phosphorus

### 6.1.1 Electronic Properties and Applications

Bulk black phosphorus (BP) is a semiconductor with an orthorhombic crystal structure that consists of puckered layers, which are held together with weak van der Waals bonds as shown in Fig. 6.1(a). BP is the most stable allotrope of phosphorus at room temperature [135, 136]. As with graphite and TMDCs, individual monolayers or bilayers can be exfoliated from the bulk BP [137]. While micromechanical cleavage techniques are not suitable for mass production, many scalable fabrication methods such as chemical vapour deposition and epitaxial growth are difficult to apply to phosphorene on account of its highly reactive surface, which is prone to rapid oxidation [137]. Phosphorene has an alternating zig-zag pattern of phosphorus atoms arranged into two sublayers, as shown in Fig. 6.1(b). From a bird's-eye view, the structure appears to be that of a warped honeycomb, which is due to the three bonds forming $sp^3$ hybridised orbitals.

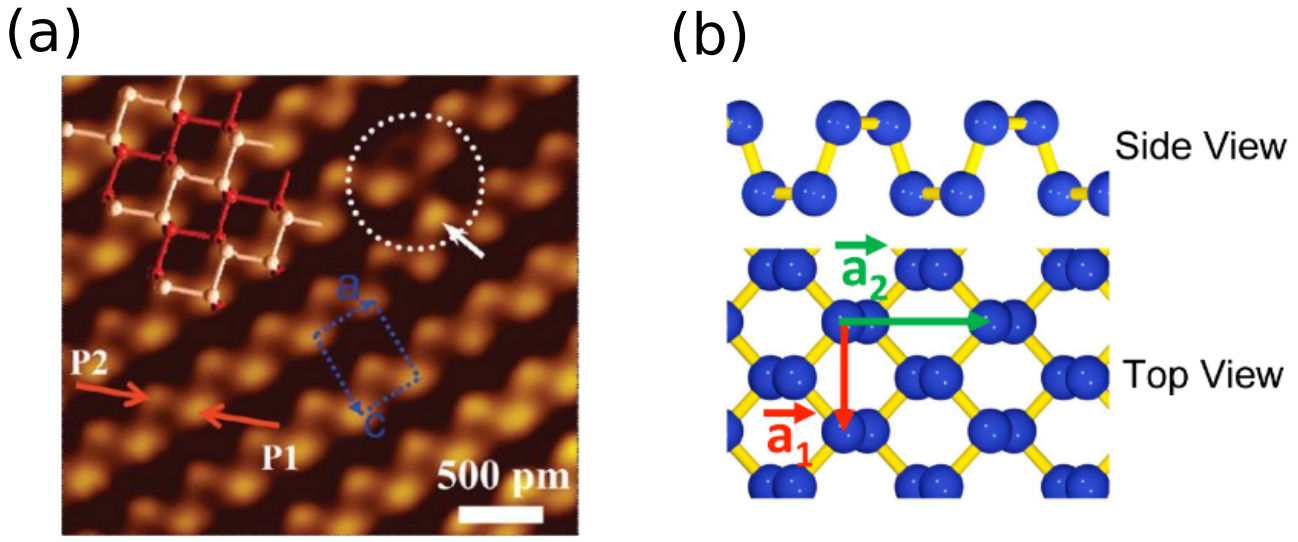



Figure 6.1: (a) Scanning tunnelling microscopy image of the upper atoms of the topmost sublayer of BP. From [15] under the Creative Commons License. (b, c) Crystal structure of bulk BP, shown for the side view and the top view [15]. Reprinted with permission from [16], Copyright 2014 by the American Chemical Society.

The two-dimensional Bravais lattice is square, spanned by primitive lattice vectors $\mathbf{a}_1 = a\hat{\mathbf{x}}$ and $\mathbf{a}_2 = -b\hat{\mathbf{y}}$ as seen in the top view in Fig. 6.1(c). In the bulk form, experimental values of $a$ and $b$ from powder diffraction methods are 4.38 Å and 3.31 Å, respectively [138]. This highly anisotropic crystal structure results in an anisotropic band structure, which is shown in Fig. 6.2(a) determined by Rudenko *et al.* [17] using first-principles *GW* calculations. Fig. 6.2(a) also highlights the contribution from the $3p_z$ orbitals, and shows the projected density of states onto the $3p_z$ manifold of the P atoms in the unit cell. The band structure shows the existence of a direct band gap of around 1.8 eV at the $\Gamma$ point, see Fig. 6.2(a). Furthermore the conduction and valence bands in the vicinity of $\Gamma$ are strongly composed of $p_z$ orbitals.

The valence band maximum at $\Gamma$ along the $\Gamma - Y$ line exhibits significantly less curvature than along the $\Gamma - X$ line, which translates into a larger effective mass. The large band gap seen in the *GW* band structure has been observed in scanning tunnelling spectra of the surface of BP, in measurements by Liang *et al.* [18]. In Fig. 6.2(b) the STS spectrum shows that despite *GW* calculations predicting a small band gap for bulk BP, probing the surface of BP results in a band gap of approximately 2 eV. Liang *et al.* suggested that this is because the STS measurements only detect the top monolayer of the surface [18]. To understand the shape of the valence band, angle-resolved photoemission spectroscopy (ARPES) experiments were conducted by Han *et*

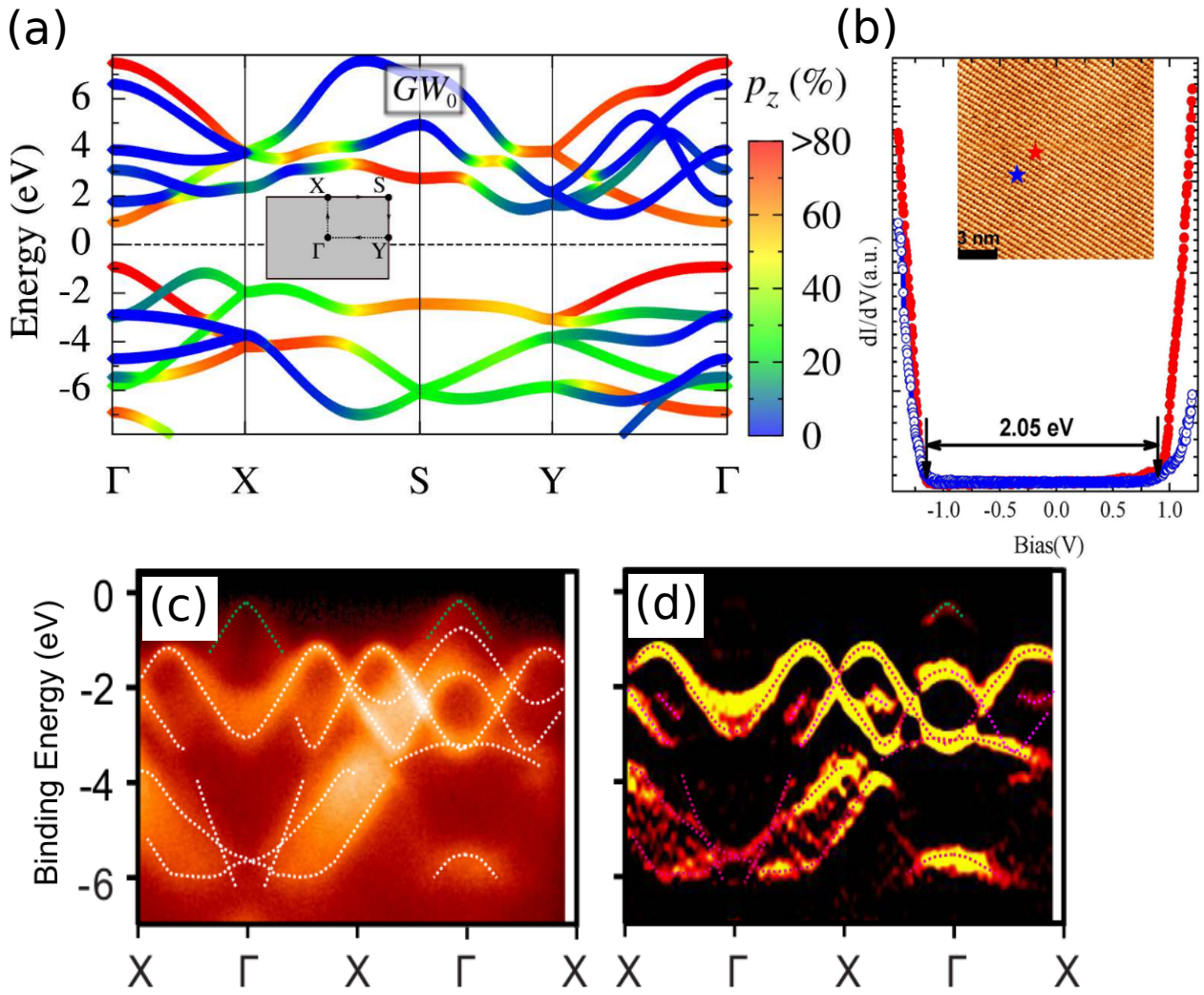



Figure 6.2: (a) Band structure and projected density of states (PDOS) for the $p_z$-orbitals calculated for monolayer BP by using $GW$, where the bands are coloured in accordance with their composition of $p_z$-orbitals [17]. Reprinted with permission from [17], Copyright 2016 by the American Physical Society. (b) Scanning tunnelling spectra of the black phosphorus surface, showing band gap at approximately 2 eV, with red and blue spectra found from different sublayers and marked in the STM image of the surface in the inset [18]. Reprinted with permission from [18], Copyright 2014 by the American Chemical Society. (c, d) Experimental band dispersions of bulk BP using ARPES with $s$-polarised light along the $X - \Gamma - X$ line in the BZ [19]. Reprinted with permission from [19], Copyright 2014 by the American Physical Society.

*al.* [19] on bulk black phosphorus, which is shown in Fig. 6.2(c) along the $X - \Gamma - X$ line. This shows a maximum of the dispersion at the $\Gamma$ point which agrees with *GW* calculations of the bulk band structure [17]. The band gap of BP decreases with increasing layer number as shown by Rudenko *et al.* [17] but calculations demonstrate that the gap remains at the $\Gamma$ point. Increasing the number of layers will result in a reduced quantum confinement effect in BP, which significantly decreases the band gap between conduction and valence band states [139].

In addition to its large band gap in the monolayer, which is a desirable property for photonic applications and transistors, monolayer BP (known as phosphorene) exhibits a high hole mobility [16]. High carrier mobility is essential for the operation of electronic devices, directly controlling the current in a transistor when in the ON state [140]. In work by He *et al.* [141], the carrier dynamics of multilayer BP were studied using transient absorption measurements, where a pump-probe laser is used to determine changes in the width of differential reflectance peaks. The changes in width are then fitted to a diffusion model from which the diffusion coefficient $D$ was extracted, hence obtaining carrier mobility $\mu$ through the Einstein relation $\mu = eD/k_{\mathrm{B}}T$ where $e$, $k_{\mathrm{B}}$ and $T$ are the electron charge, Boltzmann's constant and temperature, respectively [141]. The mobilities of electrons and holes found along the zigzag direction (along the $\Gamma - Y$ lines) were on the order of $10^4$ $\mathrm{cm^2V^{-1}s^{-1}}$ and on the order of $10^3$ $\mathrm{cm^2V^{-1}s^{-1}}$ along the armchair direction. Though the zigzag value is an order of magnitude smaller than in graphene, this value is still promising for its use in transport applications. Furthermore, simulations of the monolayer form have predicted that room-temperature hole mobilities can reach over $2 \times 10^5$ $\mathrm{cm^2V^{-1}s^{-1}}$ when a strain of 10% is applied along the zigzag direction [140]. For applications in transistors, another key property is the ratio $I_{\mathrm{ON}}/I_{\mathrm{OFF}}$ of the current $I_{\mathrm{ON}}$ when the gate voltage is turned on, and the current $I_{\mathrm{OFF}}$ when it is off. This has been found to be over $10^4$ for a field-effect transistor by Liu *et al.* [16]. On the other hand, BP undergoes substantial chemical degradation when exposed to ambient conditions, which remains a challenge for constructing stable electronic devices [142]. This is primarily due to oxidation of BP and humidity, but it has also been suggested that the presence of defects can accelerate this [142,143]. Compared to other 2D materials that have been considered as channel materials in transport devices, BP offers a compromise between graphene, which has an extremely high

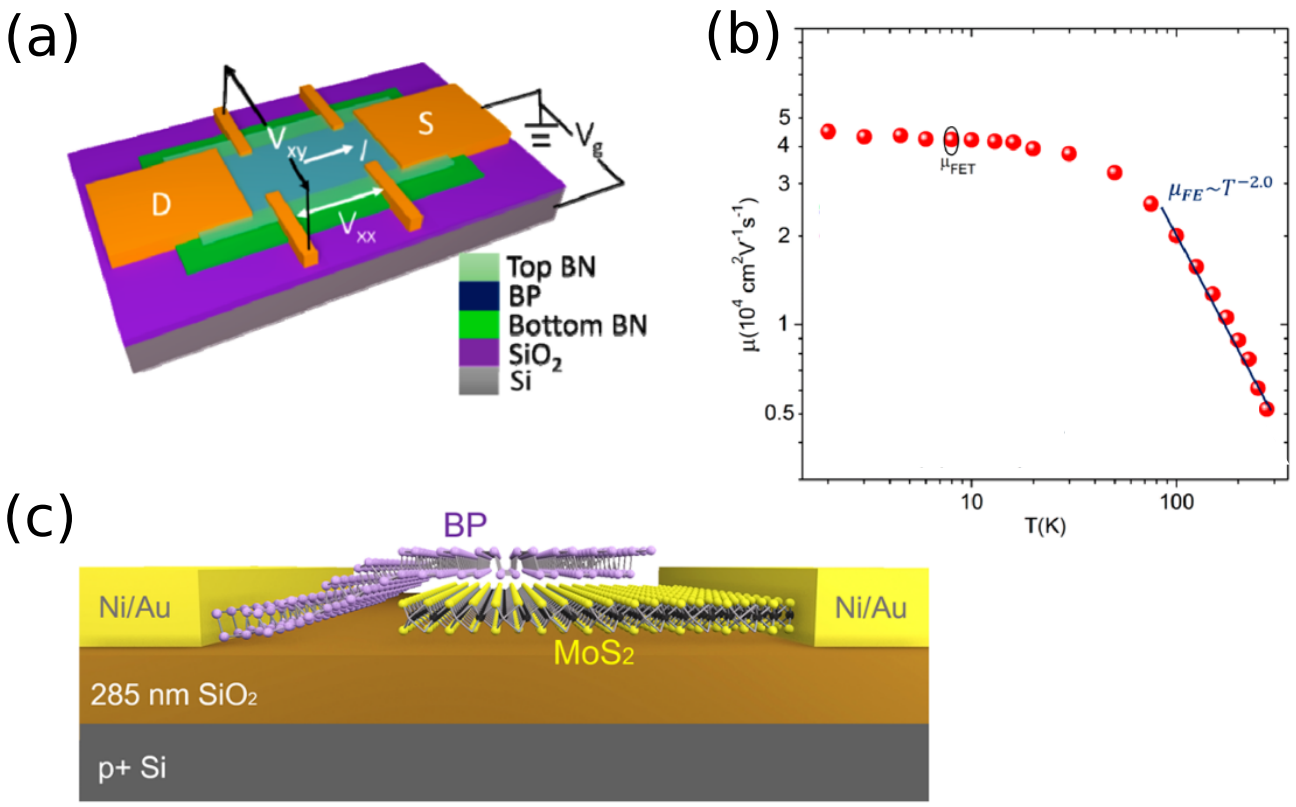



Figure 6.3: (a) Schematic of the BP field effect transistor and (b) field effect mobility as a function of temperature [20]. Reprinted with permission from [20], Copyright 2016 by the American Chemical Society. (b) has been adapted by removing the inset and curves corresponding to the hall mobility which are unrelated to this discussion. (c) Schematic of the BP-$MoS_2$ heterojunction $p-n$ diode, on $p+$ silicon wafer capped with $SiO_2$ as the global back gate and Ni/Au as contacts [21]. Reprinted with permission from [21], Copyright 2014 by the American Chemical Society.

mobility but zero band gap, and monolayer TMDCs, which have a large band gap but a lower carrier mobility [144].

The exceptional transport properties and sufficiently large band gap of black phosphorus in its few-layer and monolayer form make it a promising candidate for components in a variety of applications. Several groups have successfully constructed field-effect transistors from monolayer BP to utilise the high carrier mobility [11, 20, 144]. In work by Long *et al.* [20], few-layer BP was encapsulated in hexagonal boron nitride (HBN) in vaccuum, shown in Fig. 6.3(a). This demonstrated a high hole mobility on the order of $10^4$ $cm^2V^{-1}s^{-1}$ at 2 K, which is shown along with the mobility for other temperatures in Fig. 6.3(b). It can be seen that the mobility is lower by a factor of 10 at room temperature [11,20]. Additionally, the large band gap of few-layer BP means that it can perform reasonably well in a diode. This was attempted by Deng *et al.* [21],

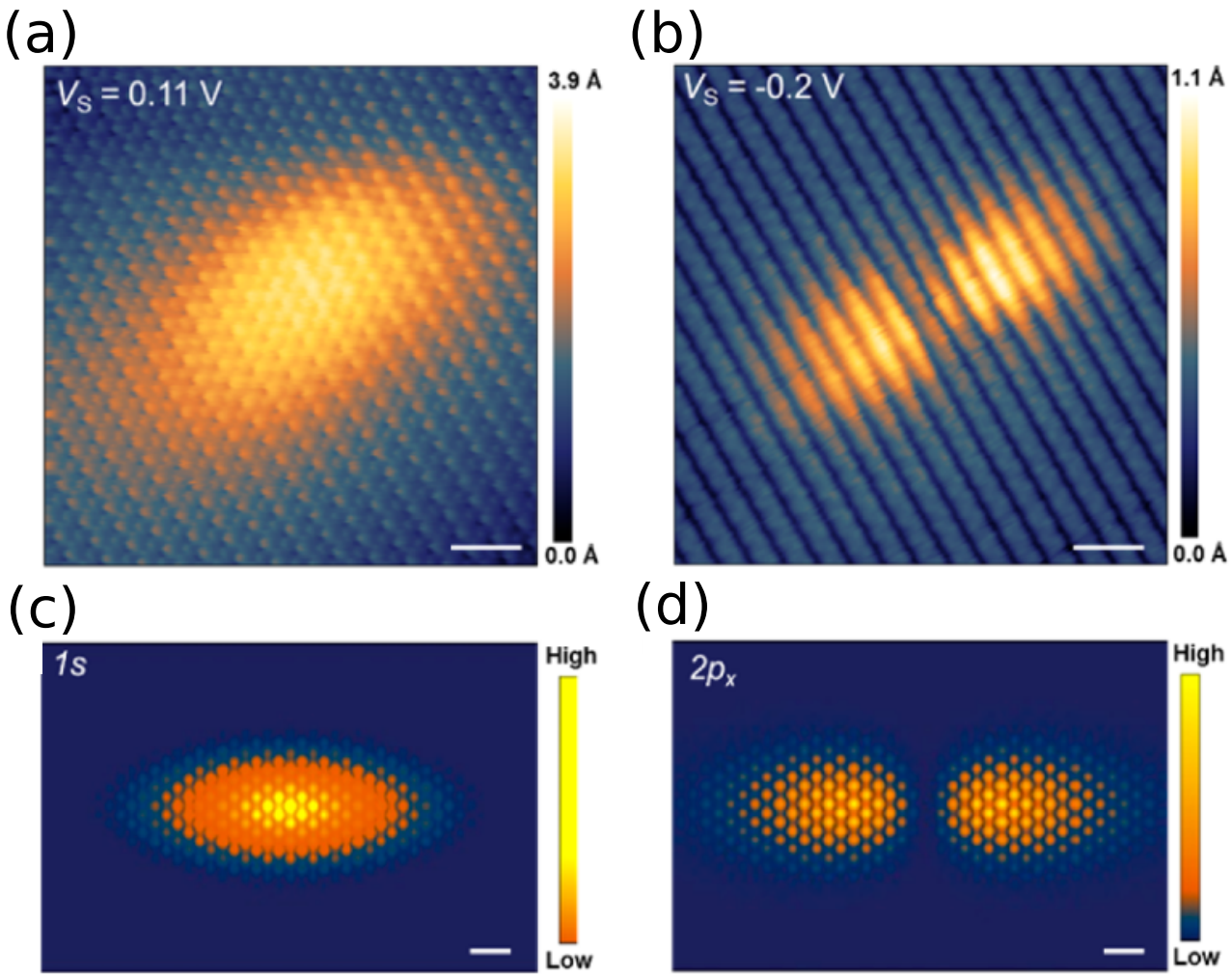



Figure 6.4: STM images of the spatial structures of the bound hole states showing (a) an ellipse shape for the ground state and (b) dumbbell shape. (c,d) Simulated top view of the squared wave function of $1s$ and $2p_x$ states calculated using an anisotropic hydrogen-like model [22]. Reprinted with permission from [22], Copyright 2017 by the American Chemical Society.

where monolayer BP and monolayer $MoS_2$ were combined in a $p-n$ diode heterojunction, as shown in Fig. 6.3(c), which demonstrated a high responsivity as a photodetector.

### 6.1.2 Defects Observed in Few-Layer BP

To explore the limits to which the properties of monolayer BP can be optimised for a variety of electronics applications, an understanding of the role defects play in the electronic properties of BP is needed. The defects present in BP can be probed experimentally with scanning tunnelling microscopy (STM), which is an important tool that several groups have used to observe them [22, 145, 146]. Single vacancies are a common defect in BP, and are suspected to

facilitate $p$-doping [145]. Kiraly *et al.* [145] investigated the extent of the changes by defects to the electronic structure, which were observed on the surface of bulk BP. They suggest that because the defect states observed in their experiments were present in samples that had undergone cleavage in vacuum, they are associated with native defects in black phosphorus, which in this case are believed to be single vacancies [145]. Kiraly *et al.* measured STM images of the surface for single vacancies at different sites in the top sublayer of the top monolayer in the sample. The bias voltage used to observe this resonance was -0.1 V, indicating that the defects observed were acceptors. These defect states were double-lobed and spanned several nanometres in width. Along the armchair direction, the resonances were still detectable as far as 5 nm from the defect, while only being observable as far as 2 nm from the defect in the zigzag direction [145]. The authors suggest that this anisotropy is likely linked to the strong anisotropy present in the electronic band structure of BP. While micromechanical cleavage results in fewer impurities being present at the surface, more scalable synthesis techniques will likely introduce atomic impurities as substitutional or interstitial defects [147]. Since atoms such as tin and sulfur are of a different valence to the phosphorus host, the defects could act as a dopant, possibly exhibiting electronic behaviour similar to that of intrinsic vacancies. This motivates investigation into the general concept of charged defects in BP.

In work by Carvalho *et al.* [22], surface defects were observed in BP using STM and it was shown that a tuning of the bias voltage resulted in the evolution of the spatial distribution of the hole bound state, between an ellipse ($1s$) and a double lobed state along the armchair ($2p_x$), similar to those observed in reference [145]. In Fig. 6.4(a) and (b), the STM images for the sample in the vicinity of the defect at bias voltages 0.11 V and -0.2 V are shown, respectively. Compared to the single-vacancy defect in reference [145], the double-lobed defect signature in Fig. 6.4(a,b) appears to extend less far away from the defect site. The source of these defects is suggested by the author in [22] to be impurities related to tin (Sn) atoms, such as substitutional defects, which arise during synthesis. The defects were determined to be shallow acceptors, since dark rings arise around the double-lobed states due to the repulsion of electrons tunnelling into empty states by a negatively charged acceptor [22]. The authors also approximated the STM images expected for a negative charge placed at the defect site

using a 2D anisotropic hydrogen model [148], shown in Fig. 6.4(c) and (d) corresponding to (a) and (b), respectively. The good agreement between the experimental results and simulations validates that the signatures seen in the STM are the bound states of a negatively charged acceptor defect. It is also noted that a positive bias, in which electrons tunnel into the sample, is needed to observe the $1s$ state in 6.4(a) while a negative bias, where holes tunnel into the sample, is required to observe the double-lobed state in Fig. 6.4(b). This can be explained by tip-induced band bending (TIBB), where the electric field originating from the point-like tip results in a local shift of the conduction and valence band that decreases with increasing height of the tip from the site. For a certain height of the tip above the sample, a positive bias would result in the TIBB pushing the acceptor states above a threshold which empties the acceptor state. This deionises the acceptor defect such that electrons from the tip can tunnel into it, offering some control to the charge states of individual acceptor states depending on the tip height [22].

### 6.1.3 Previous Defect Modelling Approaches for BP

A great deal of effort has gone into the simulation and study of defects in monolayer BP using first-principles calculations [88, 149, 150], in order to determine defect binding energies and geometric configurations. Such calculations were performed by Li *et al.* [149], both for single vacancies and for atomic dopants such as silicon (Si), sulfur (S) and aluminium (Al). However, they used a $4 \times 4$ supercell of BP, which includes 64 P atoms before defects are added and spans approximately 2 nm in width. In other work [88], even smaller $3 \times 3$ supercells are used to determine charge transfer of adsorbed atoms onto BP. In the previous subsection, single vacancies and Sn-defects were found in experiment to induce defect states that extended between 2-5 nm from the defect site, so the supercells used in these calculations are not large enough to sufficiently capture such states. While first-principles DFT calculations are practical and useful for determining geometry and stable defect configurations, their poor scaling with system size makes them less appropriate for trying to understand the electronic structure of individual defects in BP. On the other hand, the theoretical calculations accompanying the STM

in Fig. 6.4 were performed using continuum methods and numerically solving the Schrödinger equation for a $1s$ or $2p_x$ electron with effective masses $m_x^*$ and $m_y^*$ in the $x$ and $y$ direction, respectively, bound by the Keldysh potential [99]. Their agreement with the tunnelling images is primarily due to the capability of the method in capturing behaviour at long distances from the defect centre. However, their calculation assumes perfect parabolic bands, shallow defects and requires external parameterisation, making it unsuitable for developing a predictive and accurate model of the electronic behaviour across a wide range of parameter sets and defect potentials of varying depth. The STM data in reference [145] was accompanied by tight-binding calculations of a single vacancy in BP. The computational efficiency of the tight-binding model allowed large enough (tri-layer $16 \times 12$) supercells of BP to capture the defect states, while not simplifying the band structure as entirely parabolic. It should be noted that the vacancy defect in the study was not charged and thus did not require a supercell that was any larger. For electrically charged defects, particularly shallow ones, the supercell would need to be significantly larger [91].

### 6.1.4 Summary and Aims

Few-layer black phosphorus (BP) shows immense promise as a suitable and effective component in nanoscale electronics, on account of its several experimentally observed properties that are advantageous in transport and photodetection. Additionally, possibly charged intrinsic defects and defects introduced during synthesis have been shown to significantly change the local electronic structure of few-layer BP. This indicates that not only will the electronic structure be different depending on the method of fabrication, but that intentionally placed charged defects could be used to further engineer the electronic properties to great suitability for device applications. In order to achieve this, it is first important to understand and predict how charged defects modify the band structure of few-layer BP. This can be done through modelling the few-layer BP system with a single defect. However, because of the extended nature of the bound states as seen in tunnelling experiments, large enough samples of the system need to be simulated. This should sacrifice as little information about the electronic structure of the

pristine crystal or about the potential from the charged defect as possible. Similar to the monolayer TMDCs calculations in chapter 3, I have employed a tight-binding supercell of monolayer/bilayer BP with a defect potential determined from quantities extracted from ab initio calculations in the random-phase approximation (RPA).

In this chapter, I aim to study how the observed defect states in the system vary in both spatially-resolved electron distribution, binding energy, and local density of states for both donor and acceptor defects. This will look in particular at their tunability with respect to the height of the defect charge above the system and the dielectric constant of the substrate, the latter being particularly relevant for monolayer BP which is frequently encapsulated to prevent degradation in ambient conditions. With an understanding of how such a parameter space can be used to control the energy of defect levels in semiconductors, development of their applications in transport devices, transistors and optoelectronics can be pursued with greater efficiency. This work also aims to compare the binding energies of defect states from the monolayer tight-binding model with those obtained from a variational approach within the effective mass approximation, in order to assess the applicability of such continuum theories to the case of charged defects in phosphorene. This is designed to explore and understand the conditions in which the findings of this work can be primarily explained by such theories that do not require atomistic calculations. Finally, calculations of charged defects on bilayer phosphorene are performed and compared to the monolayer results, in attempts to outline fundamental similarities between their spectra, which result from the stark directional anisotropy in their electronic structure. This will look at charged defects both in the case of an adsorbate, and in the case of an intercalated defect, to understand how the location of the defect within the bilayer plays a role in its electronic signature.

## 6.2 Methods for Studying Few-layer Black Phosphorus

Here, I will briefly cover the methods used to study the effects of charged defects on monolayer and bilayer black phosphorus (BP), which include a supercell adaptation of a multi-layer tight-

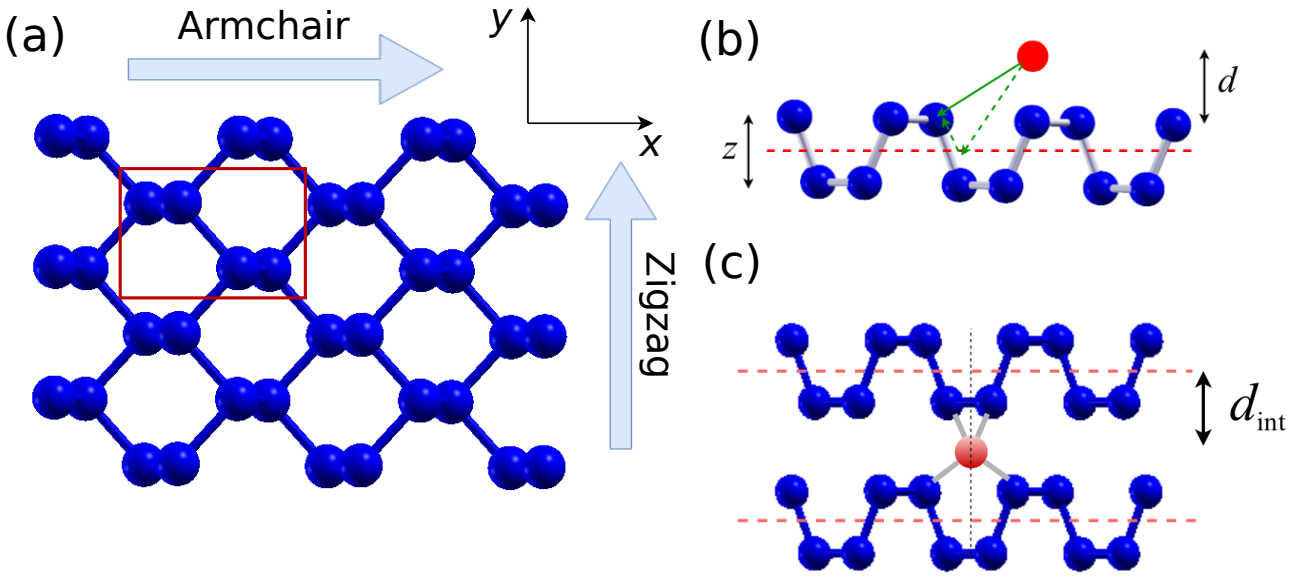



Figure 6.5: (a) Crystal structure of a black phosphorus monolayer, with armchair and zigzag directions labelled. The unit cell of the pristine crystal is outlined in red. (b) Schematic of the effective charge layer in the monolayer screening model, where $d$ is the defect height from the top sublayer. (c) Schematic of the placement of the intercalated defect in bilayer BP, where $d_{\text{int}} = 2.72$ Å is the out-of-plane distance of the defect below the effective charge sheet of the top layer (red dashed).

binding model and the development of an effective model for the screened potential that includes the material's puckered crystal structure. Finally, I outline an anisotropic variational model for studying how well the effective mass approximation applies to the case of charged defects in theses systems.

### 6.2.1 Screened Defect Potential

The method of calculating the defect potential for monolayer and bilayer black phosphorus (BP) was similarly performed to that of the monolayer transition metal dichalcogenides (TMDCs), with key differences pertaining to the puckered nature of the crystal structure of few-layer BP. The total defect potential $V^{\pm}_{\text{mono}}$ experienced by an electron localised in one of the sublayers (with $V^{+}_{\text{mono}}$ referring to the top sublayer and $V^{-}_{\text{mono}}$ referring to the bottom one) of monolayer black phosphorus (BP) can be expressed as the sum of the unscreened defect potential $V^{\pm}_{0}$ and

the induced potential $V_{\rm ind}^{\pm}$. The unscreened defect potential is given by

$$V_0^{\pm}(q) = \frac{v_q}{\varepsilon_{\rm bg}} e^{-q(d+\frac{z}{2}\mp\frac{z}{2})}, \tag{6.1}$$

where $v_q = e^2/2\varepsilon_0 q$ is the 2D Fourier transform of the Coulomb potential, $d$ is the defect height measured with respect to the top sublayer, and $z = 2.126$ Å is the thickness of the monolayer defined as the distance between the two sublayers. The parameter $\varepsilon_{\rm bg}$ is the background dielectric constant due the presence of the substrate.

The induced potential can be calculated from the induced electron density $\delta n_{\rm ind}(q)$ which is assumed to be confined to an effective 2D sheet located in the plane equidistant from the two sublayers, see Fig. 6.5(b). Then the induced potential is the same for both sublayers and given by

$$V_{\rm ind}^{\pm}(q) = \frac{v_q}{\varepsilon_{\rm bg}} e^{-qz/2} \delta n_{\rm ind}(q). \tag{6.2}$$

Within linear response theory, the induced density can be expressed as

$$\delta n_{\rm ind}(q) = \chi(q) V_0(q), \tag{6.3}$$

where $V_0(q) = v_q e^{-q(d+\frac{z}{2})}/\varepsilon_{\rm bg}$ is the value of the unscreened defect potential in the effective sheet and $\chi(q)$ denotes the interacting response function of the effective sheet. $\chi(q)$ can be expressed in terms of the non-interacting response function $\chi_0(q)$ as

$$\chi(q) = \frac{\chi_0(q)}{1 - v_q \chi_0/\varepsilon_{\rm bg}}, \tag{6.4}$$

where $\chi_0(q)$ is obtained from first-principles calculations (see discussion below). Note that the screening is assumed to be isotropic in the above. This is justified by our explicit first-principles calculations of the dielectric response (see below) and in agreement with recent experiments [151].

Combining the two contributions yields the total defect potential

$$V^{\pm}_{\mathrm{mono}}(q) = \left[1 - \frac{v_q \chi_0(q) e^{-q(\frac{z}{2}\pm\frac{z}{2})}}{\varepsilon_{\mathrm{bg}} - v_q \chi_0(q)(1 - e^{-q(\frac{z}{2}\pm\frac{z}{2})})}\right]^{-1} V^{\pm}_0(q). \tag{6.5}$$

Finally, an inverse Fourier transform yields the screened defect potential in real-space:

$$V^{\pm}_{\mathrm{mono}}(r) = \frac{1}{2\pi}\int \mathrm{d}q\, V^{\pm}_{\mathrm{mono}}(q) J_0(qr), \tag{6.6}$$

where $J_0$ is the zeroth Bessel function of the second kind.

To evaluate the screened defect potential, $\chi_0(q)$ is determined using the first-principles random-phase approximation (RPA). For this, the Kohn-Sham wavefunctions $\{|\phi_{n\mathbf{k}}\rangle\}$ and energies $\{E_{n\mathbf{k}}\}$ were first calculated, for all occupied states and 1490 unoccupied states on a $13 \times 13$ $k$-point mesh for a defect-free BP monolayer using plane-wave/pseudopotential density-functional theory (DFT) as implemented in the Quantum Espresso (6.5) software package. For these calculations, the PBE exchange-correlation functional [73], optimized norm-conserving Vanderbilt (ONCV) pseudopotentials [112] and a 120 Ry plane-wave cutoff were used. The inverse dielectric matrix $\varepsilon^{-1}_{\mathbf{G}\mathbf{G}'}(\mathbf{q})$ is then determined as a function of $\mathbf{q}$ in the first Brillouin zone (BZ), where $\mathbf{G}$ and $\mathbf{G}'$ are reciprocal lattice vectors. This is achieved by evaluating the Adler-Wiser formula [116, 152]

$$\varepsilon^{-1}_{\mathbf{G}\mathbf{G}'}(\mathbf{q}) = \delta_{\mathbf{G}\mathbf{G}'} + \frac{v_{\mathrm{tr}}(\mathbf{q}+\mathbf{G}')}{\Omega}\sum_{cv\mathbf{k}} \frac{M_{vc\mathbf{k}}(\mathbf{q},\mathbf{G}) M^*_{cv\mathbf{k}}(\mathbf{q},\mathbf{G}')}{E_{c\mathbf{k}+\mathbf{q}} - E_{v\mathbf{k}}}, \tag{6.7}$$

where $M^*_{nn'\mathbf{k}}(\mathbf{q},\mathbf{G}) = \langle \phi_{n\mathbf{k}+\mathbf{q}} | e^{i(\mathbf{q}+\mathbf{G})\cdot\mathbf{r}} | \phi_{n'\mathbf{k}} \rangle$, $\Omega$ is the crystal volume, and $v_{\mathrm{tr}}(\mathbf{q})$ is the 3D Fourier transform of the slab-truncated Coulomb interaction [102]. For the RPA calculation, a plane-wave cutoff of 15 Ry was used.

The anisotropic effective 2D inverse dielectric function and the anisotropic non-interacting response function $\chi^{\mathrm{ani}}_0(\mathbf{q})$ are then given by [10]

$$\varepsilon^{-1}_{\mathrm{2D}}(\mathbf{q}) = \frac{1}{1 - v_q \chi^{\mathrm{ani}}_0(\mathbf{q})} \tag{6.8}$$

$$= \frac{q}{2\pi e^2 L_z} \sum_{\mathbf{G}_z \mathbf{G'}_z} \varepsilon^{-1}_{\mathbf{G}_z \mathbf{G'}_z}(\mathbf{q}) v(\mathbf{q} + \mathbf{G'}_z), \tag{6.9}$$

where $L_z = 18$ Å is the distance between periodically repeated BP monolayers. It was found that $\chi_0^{\text{ani}}(\mathbf{q})$ only varies by less than three percent as function of the azimuthal angle justifying our assumption of isotropic screening above. Finally, the isotropic effective response function $\chi_0(q)$ which is used to calculate the screened defect potential is obtained as the angular average of the anisotropic response function.

Next, I discuss the calculation of the screened defect potential in the BP bilayer. As for the monolayer, the potential is expressed as the sum of an unscreened potential and an induced potential which is expressed in terms of the induced density $\delta n^{(l)}_{\text{ind}}(q)$ localised in two effective sheets (one for each monolayer and labelled by the superscript $l = 1, 2$). In terms of the non-interacting response function of the effective sheets $\tilde{\chi}_0(q)$ (note that this response function is not assumed to be the same as in the monolayer case), the induced densities are given by

$$\delta n^{(1)}_{\text{ind}}(q) = \frac{(\tilde{\chi}_0^{-1}(q) - v_q) V_0^{(1)}(q) + v_q e^{-qh} V_0^{(2)}(q)}{(\tilde{\chi}_0^{-1}(q) - v_q)^2 - v_q^2 e^{-2qh}}, \tag{6.10}$$

$$\delta n^{(2)}_{\text{ind}}(q) = \frac{(\tilde{\chi}_0^{-1}(q) - v_q) V_0^{(2)}(q) + v_q e^{-qh} V_0^{(1)}(q)}{(\tilde{\chi}_0^{-1}(q) - v_q)^2 - v_q^2 e^{-2qh}}, \tag{6.11}$$

where $h$ is the distance between the two effective sheets and $V_0^{(l)} = v_q e^{-qh(l-1)}$ is the unscreened defect potential experienced by the effective sheets.

The total potential is then given by

$$V^{(l),\pm}_{\text{bi}}(q) = V_0^{(l),\pm}(q) + \sum_{l'=1}^{2} v_q e^{-q|h_{l,\pm} - z_{l'}|} \delta n^{(l')}_{\text{ind}}(q), \tag{6.12}$$

where $V_0^{(l),\pm}(q)$ is the unscreened defect potentials in the sublayers of the each of the two monolayers, $z_l$ denotes the $z$-coordinate of effective sheet $l$ and $h_{l,\pm}$ is the $z$-coordinate of the top $(+)$ or bottom $(-)$ sublayer of monolayer $l$.

To determine $\tilde{\chi}_0(q)$, the screened potential between two charges located in the same effective sheet from this screening model, is compared to the result of a first-principles calculation.

According to Eq. (6.12), this potential is given by

$$V_{\mathrm{scr}}(q) = v_q \left[ \frac{\tilde{\chi}_0^{-2}(q) - \tilde{\chi}_0^{-1}(q) v_q (1 - e^{-2qh})}{\tilde{\chi}_0^{-2}(q) - 2\tilde{\chi}_0^{-1}(q) v_q + v_q^2 (1 - e^{-2qh})} \right]. \tag{6.13}$$

For the DFT calculations, ONCV pseudopotentials for phosphorus are used, but a plane-wave cutoff of 90 Ry, an out-of-plane periodicity of 20 Å, and a $13 \times 13$ $k$-grid is chosen instead. Then for Eq. (6.9), a cutoff of 11 Ry is used, including approximately 1200 states.

To calculate this potential from first principles, the same steps are followed as in the monolayer case to determine $\varepsilon_{\mathrm{2D}}^{-1}(q)$. Solving $\varepsilon_{\mathrm{2D}}^{-1}(q) v_q = V_{\mathrm{scr}}(q)$ for $\tilde{\chi}_0^{-1}(q)$ then yields

$$v_q^{-1} \tilde{\chi}_0^{-1}(q) = \frac{\varepsilon_{\mathrm{2D}}(q) - 2 - \sqrt{\varepsilon_{\mathrm{2D}}^2(q)(1 - e^{-2qh})^2 + 4e^{-2qh}}}{2(\varepsilon_{\mathrm{2D}}(q) - 1)}. \tag{6.14}$$

Inserting Eq. (6.14) into the expressions for $\delta n_{\mathrm{ind}}^{(l)}(q)$, one can obtain the bilayer Coulomb potential in Eq. (6.12) that can be integrated in a Hankel transform to obtain a defect potential for each sublayer in the system.

### 6.2.2 Tight-binding Model

The tight-binding model for phosphorene monolayers follows the implementation of Katsnelson *et al.* [153, 154], using a set of hopping parameters $t_{\|i}$ ($i = 1 \ldots 5$). For monolayer BP, the lattice constants are $a = 4.55$ Å and $b = 3.37$ Å which define and span the rectangular unit cell. The $4 \times 4$ unit cell tight-binding matrix, taken from the work of Katsnelson (2015) [154], is:

$$H_{00}(\mathbf{k}) = 2t_3 \cos(\mathbf{k} \cdot \mathbf{a}_2) + 2t_7 \cos(\mathbf{k} \cdot \mathbf{a}_1) + 2t_{10}(\cos(\mathbf{k} \cdot (\mathbf{a}_1 + \mathbf{a}_2)) + \cos(\mathbf{k} \cdot (\mathbf{a}_1 - \mathbf{a}_2)))$$

$$H_{11}(\mathbf{k}) = 2t_3 \cos(\mathbf{k} \cdot \mathbf{a}_2) + 2t_7 \cos(\mathbf{k} \cdot \mathbf{a}_1) + 2t_{10}(\cos(\mathbf{k} \cdot (\mathbf{a}_1 + \mathbf{a}_2)) + \cos(\mathbf{k} \cdot (\mathbf{a}_1 - \mathbf{a}_2)))$$

$$H_{22}(\mathbf{k}) = 2t_3 \cos(\mathbf{k} \cdot \mathbf{a}_2) + 2t_7 \cos(\mathbf{k} \cdot \mathbf{a}_1) + 2t_{10}(\cos(\mathbf{k} \cdot (\mathbf{a}_1 + \mathbf{a}_2)) + \cos(\mathbf{k} \cdot (\mathbf{a}_1 - \mathbf{a}_2)))$$

$$H_{33}(\mathbf{k}) = 2t_3 \cos(\mathbf{k} \cdot \mathbf{a}_2) + 2t_7 \cos(\mathbf{k} \cdot \mathbf{a}_1) + 2t_{10}(\cos(\mathbf{k} \cdot (\mathbf{a}_1 + \mathbf{a}_2)) + \cos(\mathbf{k} \cdot (\mathbf{a}_1 - \mathbf{a}_2)))$$

$$H_{01}(\mathbf{k}) = t_2 + t_6 e^{-i\mathbf{k}\cdot\mathbf{a}_1} + t_9(e^{-i\mathbf{k}\cdot(\mathbf{a}_1+\mathbf{a}_2)} + e^{-i\mathbf{k}\cdot(\mathbf{a}_1-\mathbf{a}_2)})$$

$$H_{02}(\mathbf{k}) = t_5(1 + e^{-i\mathbf{k}\cdot\mathbf{a}_1} + e^{-i\mathbf{k}\cdot(\mathbf{a}_1-\mathbf{a}_2)} + e^{i\mathbf{k}\cdot\mathbf{a}_2})$$

$$H_{03}(\mathbf{k}) = t_1 e^{-i\mathbf{k}\cdot\mathbf{a}_1}(1 + e^{i\mathbf{k}\cdot\mathbf{a}_2}) + t_4(1 + e^{i\mathbf{k}\cdot\mathbf{a}_2}) + t_8(e^{-i\mathbf{k}\cdot(\mathbf{a}_1+\mathbf{a}_2)} + e^{-i\mathbf{k}\cdot(\mathbf{a}_1-2\mathbf{a}_2)})$$

$$H_{12}(\mathbf{k}) = t_1(1 + e^{i\mathbf{k}\cdot\mathbf{a}_2}) + t_4 e^{-i\mathbf{k}\cdot\mathbf{a}_1}(1 + e^{i\mathbf{k}\cdot\mathbf{a}_2}) + t_8 e^{2i\mathbf{k}\cdot\mathbf{a}_2} + t_8 e^{-i\mathbf{k}\cdot\mathbf{a}_2}$$

$$H_{13}(\mathbf{k}) = t_5(1 + e^{-i\mathbf{k}\cdot\mathbf{a}_1} + e^{-i\mathbf{k}\cdot(\mathbf{a}_1-\mathbf{a}_2)} + e^{i\mathbf{k}\cdot\mathbf{a}_2})$$

$$H_{23}(\mathbf{k}) = t_2 + t_6 e^{-i\mathbf{k}\cdot\mathbf{a}_1} + t_9(e^{-i\mathbf{k}\cdot(\mathbf{a}_1+\mathbf{a}_2)} + e^{-i\mathbf{k}\cdot(\mathbf{a}_1-\mathbf{a}_2)})$$

where $\mathbf{a}_1 = a\mathbf{x}$ and $\mathbf{a}_2 = b\mathbf{y}$. This model is used to create an $N \times N$ rectangular supercell with length $aN$ and width $bN$. Using the same tight-binding model with additional interlayer hopping parameters, a supercell model was also constructed for obtaining defect state energies for AB-stacked bilayer BP. This follows the tight-binding parameterisation of Rudenko *et al.* [154]. In addition to two monolayer Hamiltonians $H_{\text{mono}}$ as defined previously, an interlayer Hamiltonian is also added, with the form:

$$H_{\text{bi}}(\mathbf{k}) = \begin{pmatrix} H_{\text{mono}}(\mathbf{k}) & H^{\dagger}_{\text{inter}}(\mathbf{k}) \\ H_{\text{inter}}(\mathbf{k}) & H_{\text{mono}}(\mathbf{k}) \end{pmatrix}$$

where the terms of $H_{\text{inter}}$ are:

$$(H_{\text{inter}}(\mathbf{k}))_{ii} = (H_{\text{inter}}(\mathbf{k}))_{13} = (H_{\text{inter}}(\mathbf{k}))_{20} = (H_{\text{inter}}(\mathbf{k}))_{23} = 0$$

$$(H_{\text{inter}}(\mathbf{k}))_{01} = t_1^{\perp}(1 + e^{-i\mathbf{k}\cdot\mathbf{a}_2}) + t_4^{\perp} e^{-i\mathbf{k}\cdot\mathbf{a}_1}(1 + e^{-i\mathbf{k}\cdot\mathbf{a}_2})$$

$$(H_{\text{inter}}(\mathbf{k}))_{02} = t_2^{\perp}(1 + e^{-i\mathbf{k}\cdot\mathbf{a}_1}) + t_3^{\perp}(e^{i\mathbf{k}\cdot\mathbf{a}_2} + e^{-i\mathbf{k}\cdot(\mathbf{a}_1-\mathbf{a}_2)} + e^{-i\mathbf{k}\cdot(\mathbf{a}_1+\mathbf{a}_2)} + e^{-i\mathbf{k}\cdot\mathbf{a}_2})$$

$$(H_{\text{inter}}(\mathbf{k}))_{03} = t_5^{\perp} e^{-i\mathbf{k}\cdot\mathbf{a}_1)}$$

$$(H_{\text{inter}}(\mathbf{k}))_{10} = t_4^{\perp} e^{-i\mathbf{k}\cdot\mathbf{a}_1}(1 + e^{-i\mathbf{k}\cdot\mathbf{a}_2})$$

$$(H_{\text{inter}}(\mathbf{k}))_{12} = t_5^{\perp}$$

$$(H_{\text{inter}}(\mathbf{k}))_{21} = t_5^{\perp} e^{-i\mathbf{k}\cdot\mathbf{a}_2}$$

$$(H_{\text{inter}}(\mathbf{k}))_{30} = t_5^{\perp} e^{i\mathbf{k}\cdot(\mathbf{a}_2-\mathbf{a}_1)}$$

$$(H_{\text{inter}}(\mathbf{k}))_{31} = t_2^{\perp} e^{-i\mathbf{k}\cdot\mathbf{a}_2}(1 + e^{i\mathbf{k}\cdot\mathbf{a}_1}) + t_3^{\perp}(1 + e^{i\mathbf{k}\cdot\mathbf{a}_1} + e^{-i\mathbf{k}\cdot(\mathbf{a}_2-\mathbf{a}_1)} + e^{-2i\mathbf{k}\cdot\mathbf{a}_2})$$

$$(H_{\text{inter}}(\mathbf{k}))_{32} = t_1^{\perp}(1 + e^{-i\mathbf{k}\cdot\mathbf{a}_2}) + t_4^{\perp}e^{i\mathbf{k}\cdot\mathbf{a}_1}(1 + e^{-i\mathbf{k}\cdot\mathbf{a}_2})$$

### 6.2.3 Anisotropic Variational Effective Mass Model

In a similar manner to the calculations performed for monolayer TMDCs in Chapter 3, a variational approach to the effective mass approximation was also carried out with monolayer BP, in an attempt to draw parallels of the atomistic results to concepts in continuum models. For monolayer BP, the anisotropy in the band structure meant that separate effective masses $m_x^*$ and $m_y^*$ in the respective armchair ($x$) and zigzag ($y$) directions were required. The Hamiltonian, whose expectation value will be minimised, is

$$H_{\text{va}} = -\frac{\hbar^2}{2m_x^*}\frac{\partial^2}{\partial x^2} - \frac{\hbar^2}{2m_y^*}\frac{\partial^2}{\partial y^2} + V_{\text{def}}(\sqrt{x^2 + y^2}), \tag{6.15}$$

where $V_{\text{def}}$ is the potential associated with the defect. The ansatz chosen to approximate the ground state wavefunction of a single particle trapped in $V_{\text{def}}$, is

$$\Psi_{1\text{s}}(\mathbf{r}; \alpha, \beta) = \sqrt{\frac{2\alpha\beta}{\pi}}e^{-\sqrt{(\alpha x)^2 + (\beta y)^2}}, \tag{6.16}$$

where $\mathbf{r} = (x, y)$, while $\alpha$ and $\beta$ are the inverse decay length scales in the armchair and zigzag directions, respectively. To enable a quantitative comparison between the binding energies of defect states obtained from the atomistic calculations and the effective mass approach, the position of the plane in which the wavefunction in Eq. (6.16) is localised must be chosen. As Fig. 6.7 shows that the screened defect potential has a significantly larger value in the top sublayer than in the other sublayers, it is assumed that the wavefunction of the most strongly bound 1$s$ state is primarily localised in the highest sublayer. The variational effective mass model shown here uses the same height $d$ as the height of the charge above the 2D plane, which itself approximates the quasi-2D surface of the monolayer. Due to the simple exponential nature of the ansatz chosen, the kinetic energy was determined analytically as:

$$T_{\text{va}}(\alpha, \beta) = \langle \Psi_{1\text{s}}(\alpha, \beta) | H_{\text{va}} - V_{\text{def}} | \Psi_{1\text{s}}(\alpha, \beta) \rangle$$

$$= \frac{2\alpha\beta}{\pi}\int\int \mathrm{d}x\mathrm{d}y\, e^{-\sqrt{(\alpha x)^2+(\beta y)^2}}\left(-\frac{\hbar^2}{2m_x^*}\frac{\partial^2}{\partial x^2}-\frac{\hbar^2}{2m_y^*}\frac{\partial^2}{\partial y^2}\right)e^{-\sqrt{(\alpha x)^2+(\beta y)^2}}$$
$$= -\frac{\hbar^2\alpha\beta}{\pi}\int\int \frac{\mathrm{d}x'}{\alpha}\frac{\mathrm{d}y'}{\beta}\, e^{-r'(x',y')}\left(\frac{\alpha^2}{m_x^*}\frac{\partial^2}{\partial(x')^2}+\frac{\beta^2}{m_y^*}\frac{\partial^2}{\partial(y')^2}\right)e^{-r'(x',y')}$$

where $r(x',y') = \sqrt{(x')^2+(y')^2}$

$$T_{\mathrm{va}}(\alpha,\beta) = -\frac{\hbar^2}{\pi}\int\int \mathrm{d}x'\mathrm{d}y'\,\frac{e^{-2r(x',y')}}{r^3(x',y')}\left(\frac{\alpha^2((x')^2r(x',y')-(y')^2)}{m_x^*}+\frac{\beta^2((y')^2r(x',y')-(x')^2)}{m_y^*}\right)$$
$$= -\frac{\hbar^2}{\pi}\int_0^\infty \mathrm{d}r\int_0^{2\pi}\mathrm{d}\theta\, e^{-2r}\left[\frac{\alpha^2}{m_x^*}(r\cos^2\theta-\sin^2\theta)+\frac{\beta^2}{m_y^*}(r\sin^2\theta-\cos^2\theta)\right]$$
$$= -\hbar^2\left(\frac{\alpha^2}{m_x^*}+\frac{\beta^2}{m_y^*}\right)\int_0^\infty \mathrm{d}r\mathrm{d}\theta\, e^{-2r}(r-1) = -\hbar^2\left(\frac{\alpha^2}{m_x^*}+\frac{\beta^2}{m_y^*}\right)\left(-\frac{1}{4}\right)$$
$$= \frac{\hbar^2}{4}\left(\frac{\alpha^2}{m_x^*}+\frac{\beta^2}{m_y^*}\right).$$

The potential energy component must be performed numerically which, in combination with the kinetic component, gives an expectation value of

$$\langle\Psi_{1\mathrm{s}}(\alpha,\beta)|H|\Psi_{1\mathrm{s}}(\alpha,\beta)\rangle = \frac{\hbar^2}{4}\left(\frac{\alpha^2}{m_x}+\frac{\beta^2}{m_y}\right)+V_{\alpha\beta}, \tag{6.17}$$
$$V_{\alpha\beta} = \frac{2}{\pi}\int \mathrm{d}r\; re^{-2r}\int \mathrm{d}\theta\; V_{\mathrm{def}}\left(\left|\left(\frac{r\cos\theta}{\alpha},\frac{r\sin\theta}{\beta}\right)\right|\right) \tag{6.18}$$
$$V_{\mathrm{def}}(r) = \frac{e^2}{4\pi\varepsilon_0}\int \mathrm{d}q\;\frac{J_0(qr)e^{-qd}}{\frac{\varepsilon_{\mathrm{sub}}-1}{2}+\varepsilon_{2\mathrm{D}}(q)}, \tag{6.19}$$

where $V_{\mathrm{def}}$ is the defect potential of the perfect 2D system. This is minimised using the same optimiser (`scipy.optimize.fmin`) as with the monolayer TMDC variational model.

## 6.3 Results and Discussion

### 6.3.1 Band Structure and Defect Potential

The band structure of the black phosphorus (BP) monolayer and bilayer tight-binding model is shown in Fig. 6.6(a) and 6.6(b), respectively. The monolayer band structure shows the direct band gap of approximately 1.8 eV present at the $\Gamma$ point in the BZ, with vastly different curvatures in the $\Gamma - X$ (armchair) and $\Gamma - Y$ (zigzag) directions, equating to immensely

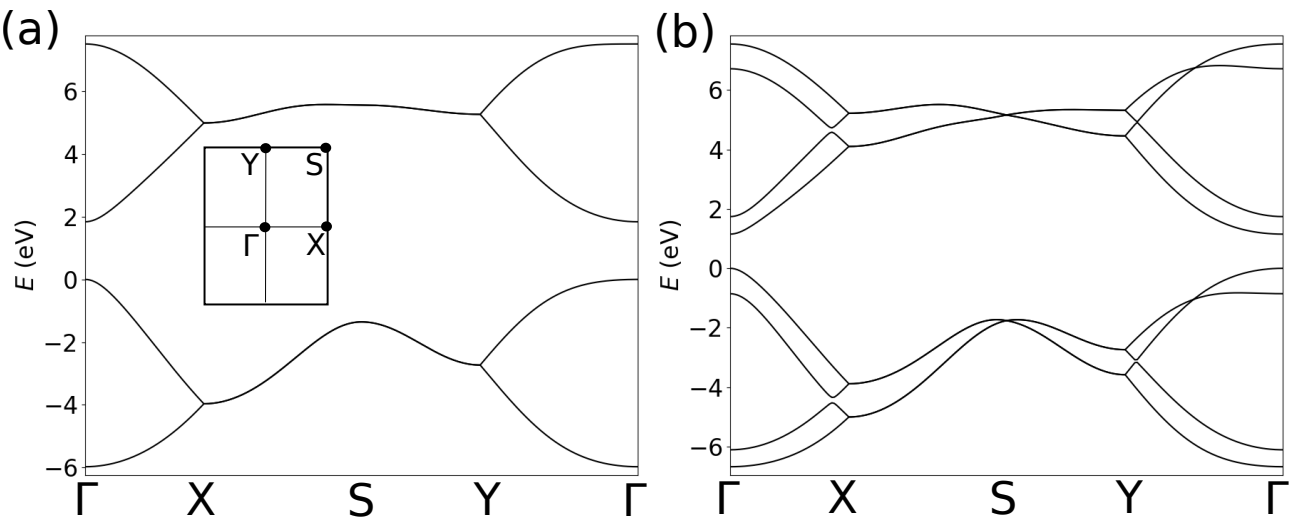



Figure 6.6: Tight-binding electronic band structure of black phosphorus in (a) the monolayer and (b) bilayer structure in the Brillouin zone (BZ). Inset of (a) depicts the high symmetry points of the BZ. All energies are referenced to the valence band maximum at Γ.

different effective masses. These effective masses are shown in Table 6.1, quantifying the large electronic anisotropy between the armchair and zigzag direction, both for the case of electrons and holes. In the case of the hole, the effective mass in the armchair direction is around 20 times the size than in the zigzag direction. In Fig. 6.6(a), a secondary valence band maximum (VBM) at $S$ is present, which appears over an electronvolt below the primary VBM. This indicates that unless the effective mass is comparable to that of the armchair effective mass at the Γ point, it is not in an energy range where acceptor charges of $-e$ will induce noticeable in-gap states constructed from the $S$ part of the pristine BZ. The bilayer band structure, shown in Fig. 6.6(b) along the same path $\Gamma - X - S - Y - \Gamma$, exhibits a split valence band and conduction band caused by the interlayer coupling. The band gap is reduce to approximately 1.2 eV, due to the inward energy shift of the CBM and VBM. The hole effective mass is significantly reduced along the armchair direction, whereas the electron effective mass is larger along the armchair direction. It can be seen that the lower split band of the valence band has a negative effective mass at Γ, meaning that there are two secondary VBM near Γ at either side along the armchair direction.

Fig. 6.7 and Fig. 6.8 show the sublayer-resolved screened defect potential for a charged adsorbate on monolayer and bilayer BP, respectively. As expected for 2D semiconductors, the screened potential in all sublayers approaches the unscreened potential at large distances from

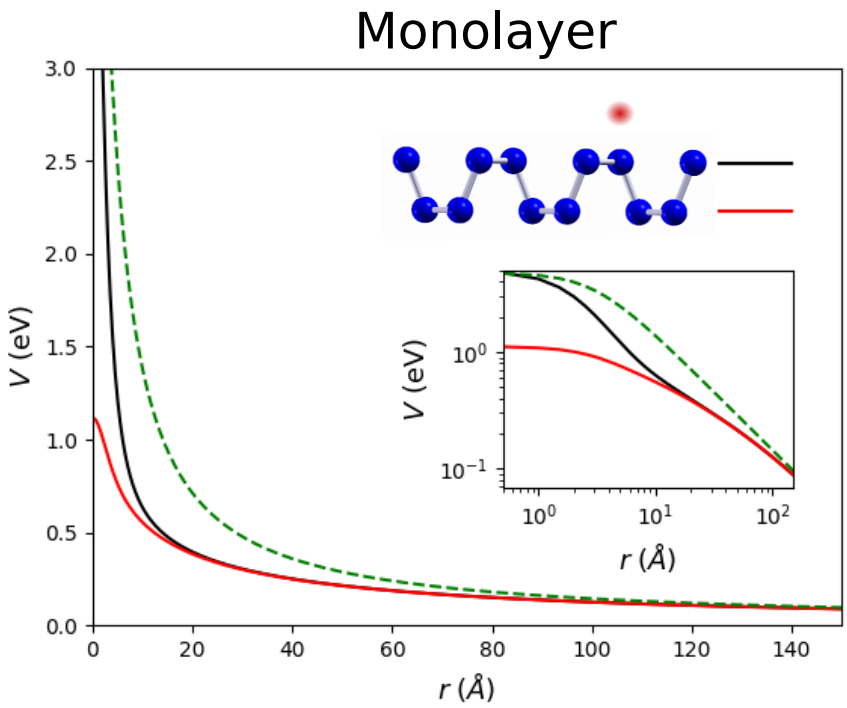



Figure 6.7: Defect potential for monolayer BP for a charged defect sitting $d = 2$ Å above the top sublayer, shown for the top sublayer (black) and the bottom sublayer (red), compared to the unscreened potential (green dashed). Inset displays the log-log form of this figure.

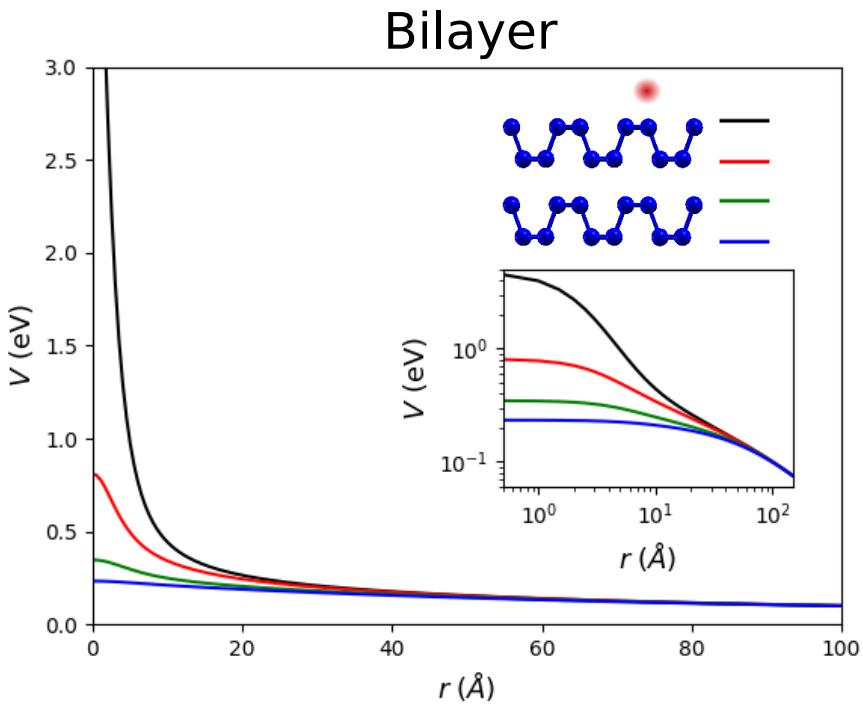



Figure 6.8: Defect potential for bilayer BP for a charged defect placed 2 Å above the top sublayer of the top layer, shown for all four sub-layers in the system. Inset displays the log-log form of this figure.

the adsorbate. However, at short distances the screened potential is reduced significantly. In bilayer BP, the screened potential in the top monolayer behaves qualitatively similar to the monolayer case, but is somewhat weaker as a consequence of screening from the additional BP layer. In the bottom monolayer the screened potential is an order of magnitude smaller than in the top layer and relatively flat indicating that bound defect states should reside in the top monolayer. Eq. (6.13) can also be applied to the case of an intercalated defect between the two layers of the bilayer. This is modelled by considering a charge placed between the layers, as shown in Fig. 6.5(c) where the defect is approximately equidistant from two P atoms in the top layer and two in the bottom, using a bond length of 2.2 Å, typical for a transition metal atom such as copper or nickel [147].

### 6.3.2 Monolayer BP Defect Wavefunctions

In the presence of a charged defect, the black phosphorus (BP) monolayer exhibits in-gap states that arise from the Coulombic electrostatic potential associated with the defect [26]. These in-gap states appear to be localised to the defect, and form a series with similar nodal structure to the 2D hydrogen model. The most strongly bound state exhibits a highly localised distribution with exponential decay characteristic for a Coulomb-like potential, labelled as $1s$. Fig. 6.9(i-vi) shows the wavefunctions of the bound defect states in monolayer BP on a substrate with $\varepsilon_{\text{sub}} = 2$, induced by a negatively charged adsorbate with a height of $d = 2\,\text{Å}$ above the top sublayer. As a consequence of the large difference of the effective masses in the armchair and zigzag direction, these wavefunctions resemble anisotropically distorted 2D hydrogenic orbitals and are therefore labelled as $1s$ (i), $2p_y$ (ii), $2s$ (iii), $3p_y$ (iv), $2p_x$ (v), and $3s$ (vi). Note that the ordering of the defect states is different than in the 2D hydrogen atom as a consequence of the

| | Monolayer | | Bilayer | |
|---|---|---|---|---|
| | Electron | Hole | Electron | Hole |
| $m^*_{\text{a}}/m_0$ | 0.196 | 0.166 | 0.180 | 0.152 |
| $m^*_{\text{z}}/m_0$ | 1.160 | 3.241 | 1.530 | 1.362 |

Table 6.1: Effective masses at the Γ point in the Brillouin zone for Monolayer and Bilayer BP, calculated from the tight-binding models using a 4th-order accurate finite difference approximation to the second derivative of the bands.

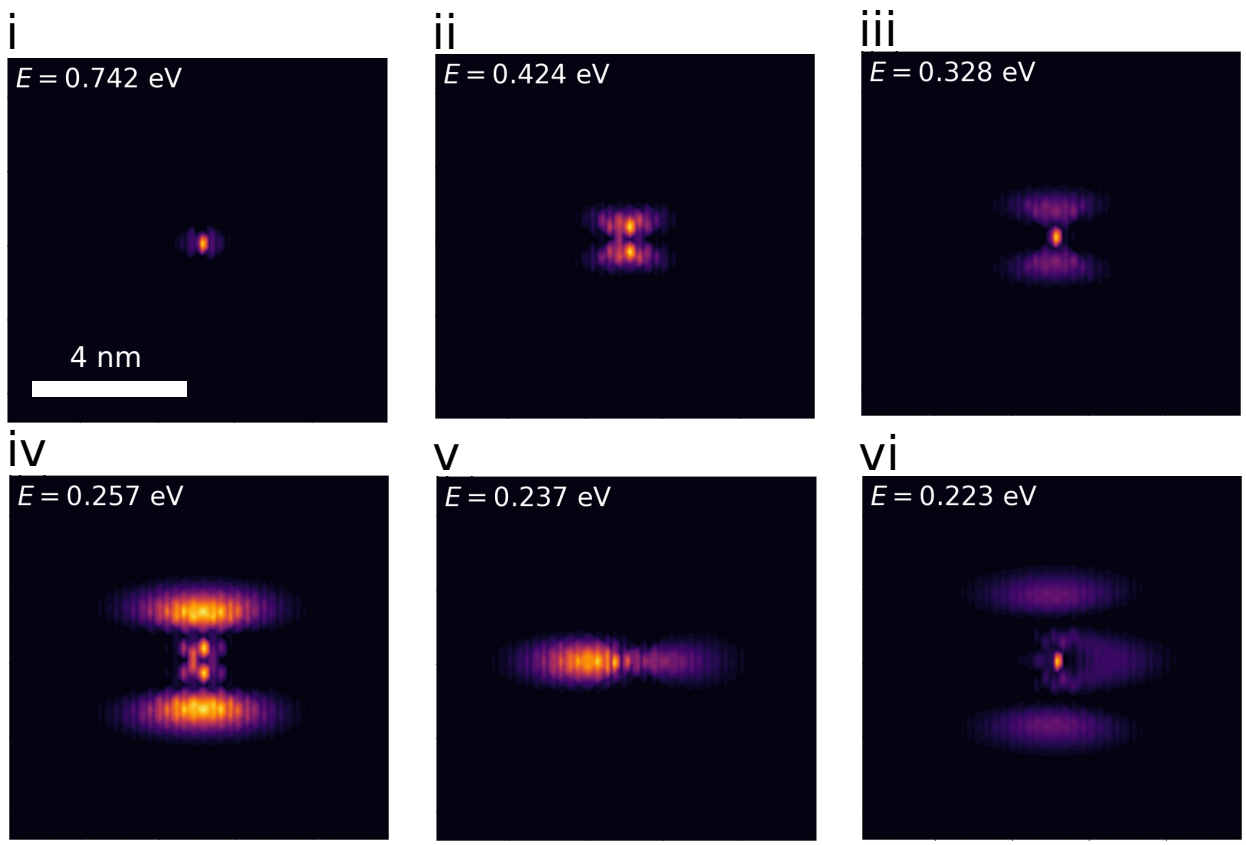



Figure 6.9: Wavefunctions of the six most bound acceptor defect states on monolayer black phosphorus, from (i) to (vi) in order of decreasing binding energy. This is shown for a defect height of $d = 2$ Å above the top sublayer and $\varepsilon_{\text{sub}} = 2$.

anisotropic dispersion which favours states that are oriented along the $y$-direction. For example, the $2p_x$ and the $2p_y$ orbitals are degenerate in the 2D hydrogen atom, but in monolayer BP the binding energy of the $2p_y$ state is almost 0.1 eV larger than that of the $2p_x$ state. Projecting the defect wavefunctions onto the unperturbed monolayer states, see Figs. 6.10(i-vi), reveals that they are predominantly constructed from bulk valence states near the valence band maximum at the $\Gamma$ point. Importantly, the shapes of the reciprocal-space projections are similar to those of their real-space counterparts. An inverse relationship can be seen between the exponential decay states of the real-space and reciprocal-space form of the defect state, along both the armchair and zigzag directions in the crystal, such that states with stronger localisation to the defect site in real-space are less localised in their reciprocal-space projections to the $\Gamma$ point. This relationship occurs independently for the armchair and zigzag directions, which in reciprocal-space corresponds to the $k_x$ and $k_y$ axes, respectively.

Upon increasing the substrate dielectric constant to $\varepsilon_{\text{sub}} = 8$, the defect states become more

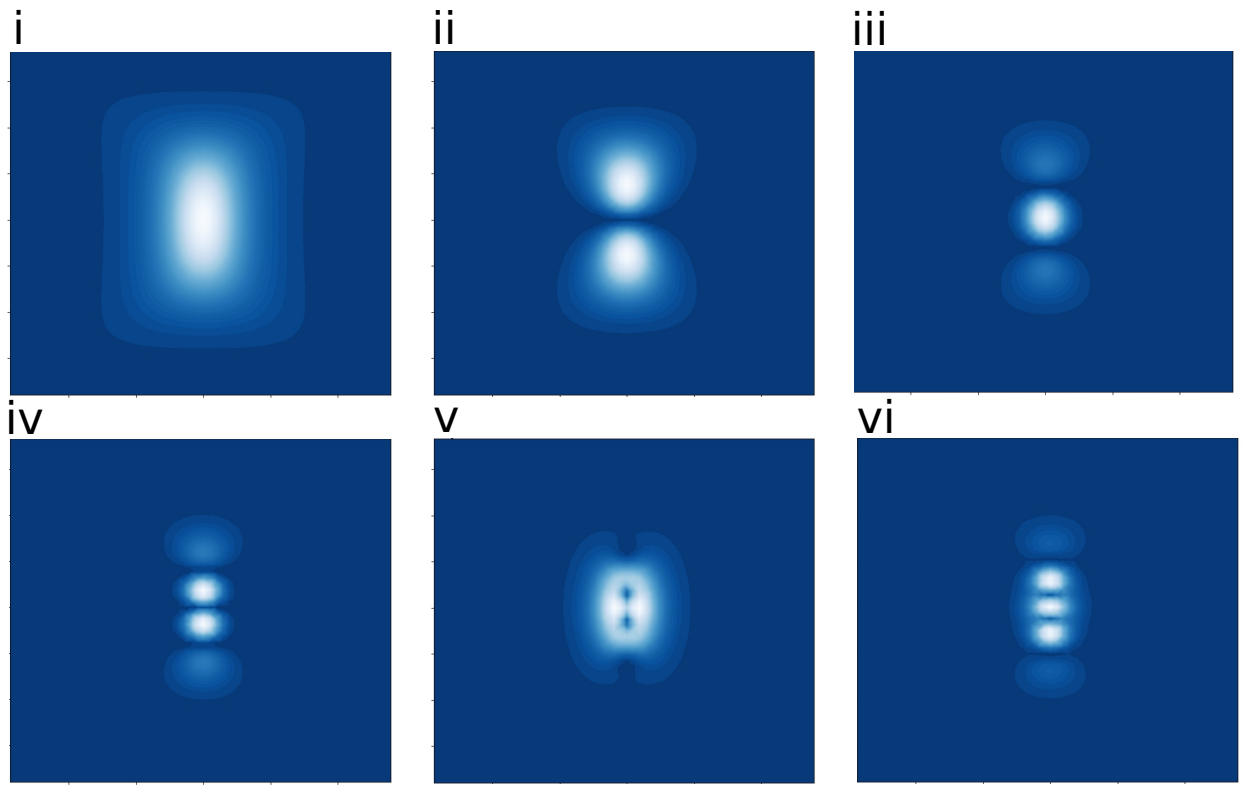



Figure 6.10: Projections of the six most bound acceptor defect states on monolayer black phosphorus, from (i) to (vi) in order of decreasing binding energy. This is shown for a defect height of $d = 2$ Å above the top sublayer and $\varepsilon_{\text{sub}} = 2$.

delocalised, see Figs. 6.11(i-vi), while their projections become more localised to the vicinity of the Γ point, see Figs. 6.12(i-vi). The ordering of the defect states changes with the fifth state exhibiting a different symmetry compared to the case of $\varepsilon_{\text{sub}} = 2$. As the dielectric constant of the substrate is modified, the fifth state is of a different spatial form, indicating that the $x$-directed lobed states can be modified in their relative binding energy to the $y$-directed lobed states using more polarisable substrates. For the $2s$ (iii) and $2p_x$ (iv) states, there exists a small change in the $x$-directed skew between $\varepsilon_{\text{sub}} = 2$ (a) to $\varepsilon_{\text{sub}} = 8$ (c), and the projections of these states in Fig. 6.12(i-v) increase in their reciprocal-space localisation. A significant comparison between both values of $\varepsilon_{\text{sub}}$ is through the projection of the $1s$ state, where it can be seen that compared to the case of $\varepsilon_{\text{sub}} = 8$, the extent of the reciprocal-space projection for the $1s$ state of $\varepsilon_{\text{sub}} = 2$ extends to regions of the band structure that deviate from the parabolic nature that is exhibited closer to the band maximum at Γ.

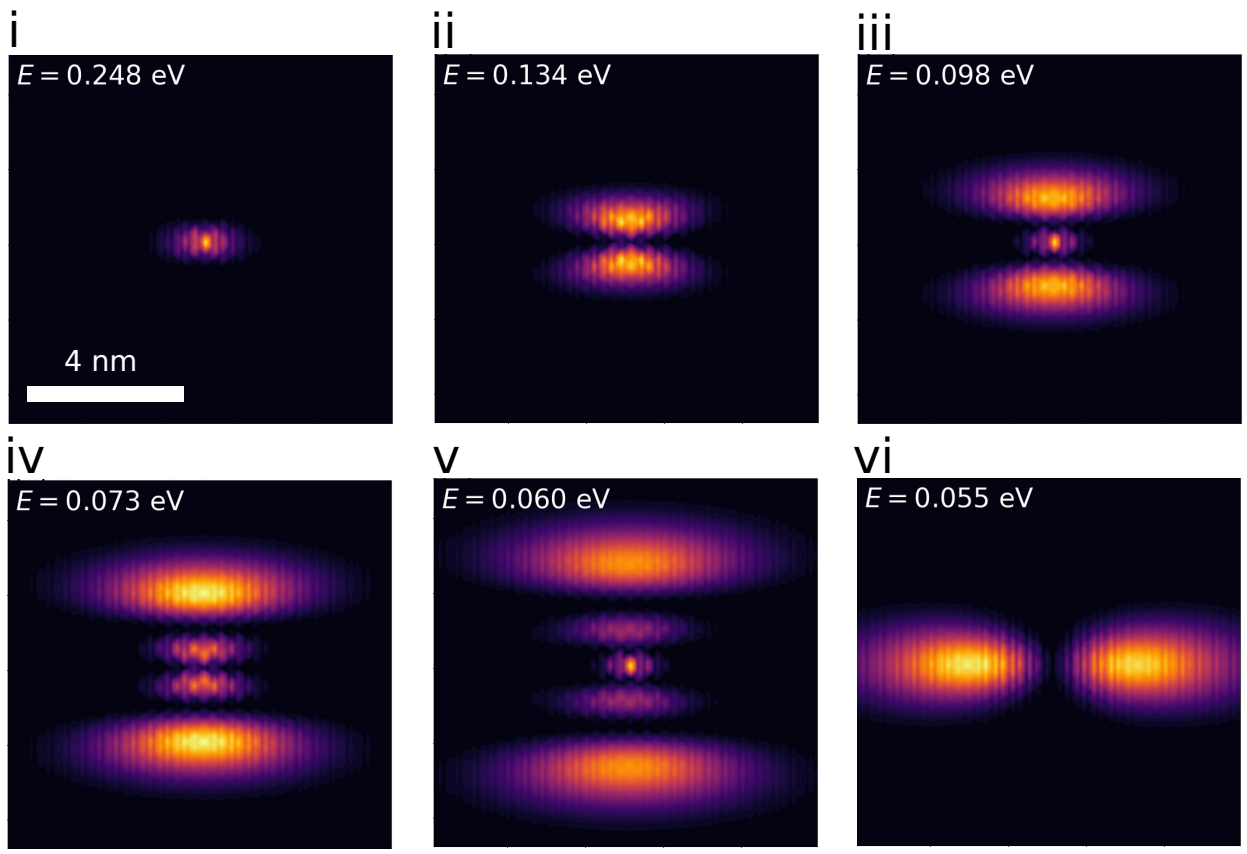



Figure 6.11: Wavefunctions of the six most bound acceptor defect states on monolayer black phosphorus, from (i) to (vi) in order of decreasing binding energy. This is shown for a defect height of $d = 2$ Å above the top sublayer and $\varepsilon_{\text{sub}} = 8$.

### 6.3.3 Monolayer BP Binding Energies

Figure 6.13 shows the binding energies of the 1s defect state as functions of the defect height $d$ and the substrate dielectric constant $\varepsilon_{\text{sub}}$. As expected, an increase in $\varepsilon_{\text{sub}}$ reduces the binding energies as the defect potential is weaker. Interestingly, for small defect heights ($d = 1.5$ Å) above the top sublayer and weakly screening substrates ($\varepsilon_{\text{sub}} < 3$), the binding energy of the acceptor state exceeds the size of the band gap, see Fig. 6.13(a). In this case, the defect state becomes resonant with the conduction band states. With the exception of these instances, the highly-localised $1s$ state is the most strongly bound of the defect state spectrum. Additionally, the sensitivity of the binding energy with $\varepsilon_{\text{sub}}$ increases with a smaller $d$, owing to the closer proximity of the charged defect to the system. The increase in binding energy from $d = 1$ Å to $d = 0.5$ Å maintains an approximately consistent size for the range of substrate dielectrics, indicating that because of both the large effective mass of the valence band and the close prox-

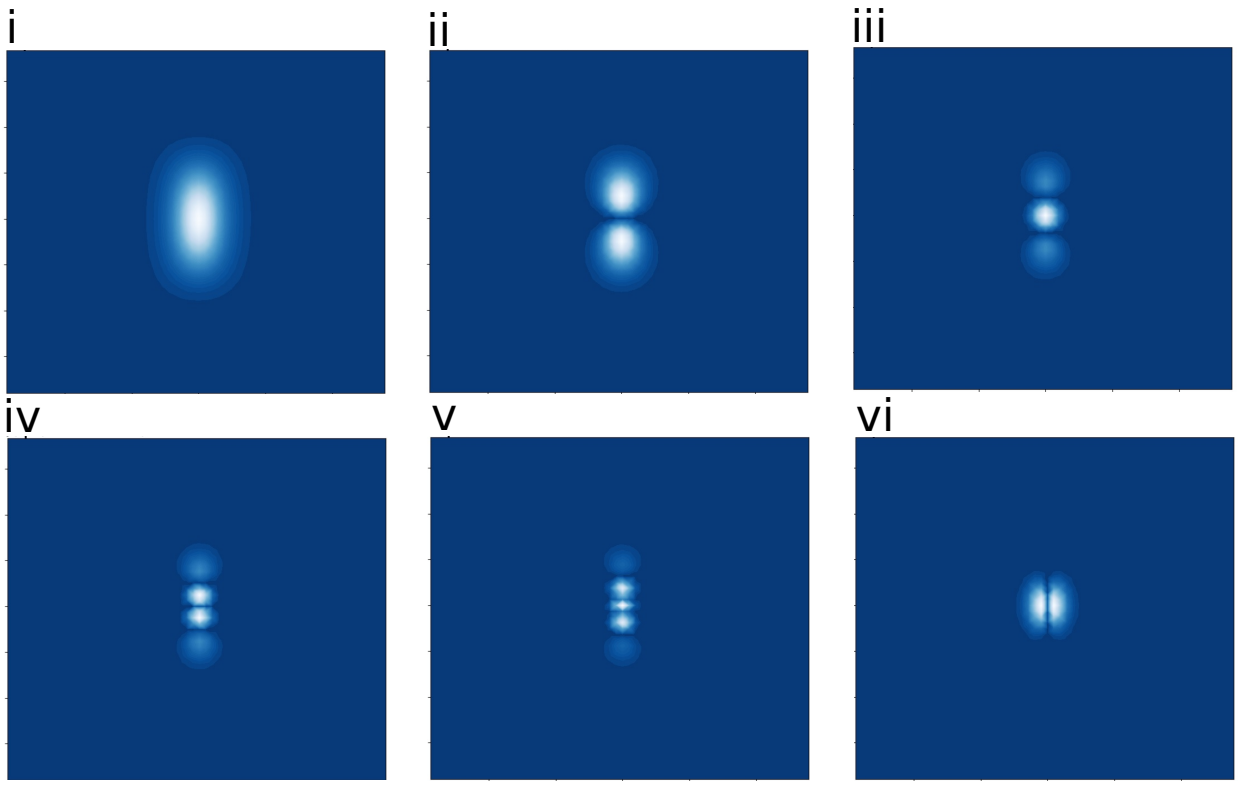



Figure 6.12: Projections of the six most bound acceptor defect states on monolayer black phosphorus, from (i) to (vi) in order of decreasing binding energy. This is shown for a defect height of $d = 2$ Å above the top sublayer and $\varepsilon_{\text{sub}} = 8$.

imity of the charge to the system, the $1s$ is almost entirely localised to within a few Ångstroms of the defect site. Hence, the local changes to the defect potential from varying $d$ will be experienced by the $1s$ state approximately as a linear shift in potential. The donor binding energies are displayed in Fig. 6.13(b), referenced from the conduction band. It can be seen that binding energies of acceptor and donor states are quite similar, which is a consequence of the strong similarity between the shapes of the conduction and valence band extrema. However, the donor binding energies are somewhat smaller due to the larger $m_y^*$ in the valence band maximum at $\Gamma$, dominating in influence over the binding energy. Similarly to the acceptor case, 6.13(b) shows that the donor states can also become resonant with valence band states for this parameter space.

Figures 6.13(c-d) show the binding energies obtained from the variational effective mass approach, see Eq. (6.16). The results from this approach are generally in good qualitative agreement with the atomistic calculations, but there are some important differences. In particular,

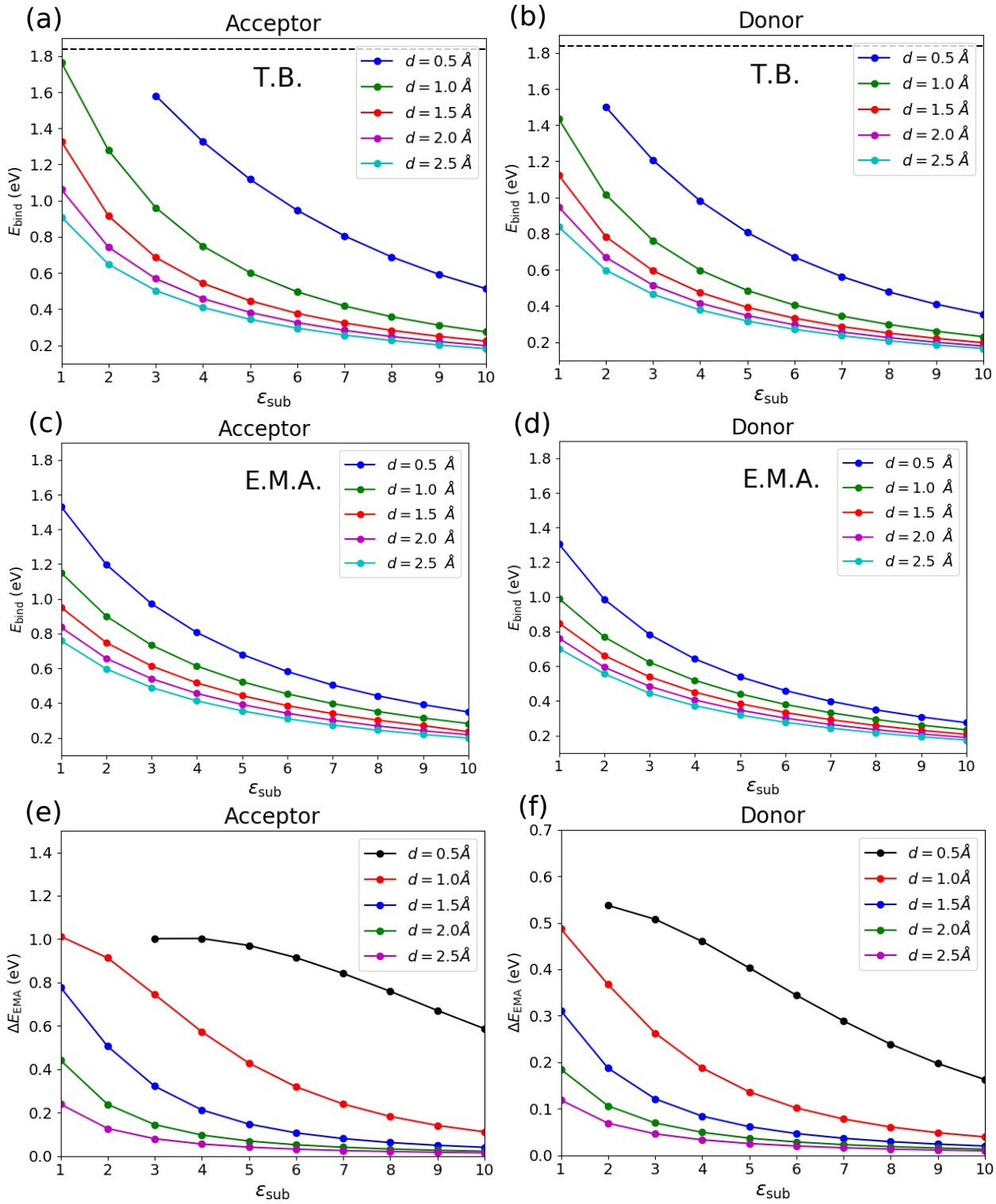



Figure 6.13: (a,b) Binding energy variation of (a) donor and (b) acceptor 1s defect states with $\varepsilon_{\text{sub}}$ and $d$, extracted from the tight-binding model with isotropic defect potential. (c,d) Variational 1s energy extracted from the effective mass model inserting the effective masses of (c) the conduction band minimum and (d) the valence band maximum. (e,f) Average parabolic energy deviation $\Delta E_{\text{EMA}}$ of the 1s state for the case of (e) acceptor and (f) donor, shown as a function of substrate dielectric constant for the same defect heights as (a-d).

the effective mass approximation underestimates binding energies when the defect is close to the monolayer and the substrate has a small dielectric constant. For larger substrate dielectric constants and defect heights, there is a good agreement between the two approaches, indicating that the error from the chosen wavefunction ansatz is small. Most importantly, the effective mass approximation does not reproduce the result that the most strongly bound defect state can cross the entire band gap and become resonant with bulk states. This failure of the effective mass approximation can be understood by analysing the projection of the defect state onto bulk monolayer states. As discussed above (see Fig. 6.10), the projections for the most strongly bound $1s$ states are delocalised over a larger part of the first Brillouin zone. However, the effective mass approximation is based on the assumption of an anisotropic parabolic dispersion which is only valid near the conduction and valence band edges.

The comparison between the tight-binding binding energies and those obtained through the variational effective mass approach, becomes better for values of $\varepsilon_{\text{sub}} > 1$ and defect heights $d > 1.5$ Å above the top sublayer. When the dielectric environment is highly polarisable, or the defect is further from the system, the defect potential is shallow enough to result in bound states that are not effectively confined to a single atom, and thus are delocalised over a region around the defect significantly greater in size than the lattice parameter. Hence the exact chemical description of the defect and the defect centre in the material becomes less important in characterising the electronic structure of the system, and relies more on electrostatic features of the charged defect on a larger scale, allowing it to be better compared to continuum theories such as the effective mass approximation. This can be understood by examining the projections for the defect states on the Brillouin zone of the unperturbed system, as plotted for $d = 2$ Å and $\varepsilon_{\text{sub}} = 2$ in Fig. 6.10(i). For deep potentials, the resulting defect states in the tight-binding model become highly localised, which conversely has a reciprocal-space projection that is significantly delocalised across the BZ. Since the highly localised defect state has non-negligible contributions from points in the BZ that are far from the central band extrema at $\Gamma$, for which the approximation of a parabolic band is not so suitably apparent, it is not expected that the application of a variational model within the effective mass approximation would result in a similar binding energy.

To quantitatively assess the validity of the effective mass approximation, a quantity $\Delta E_{\mathrm{EMA}}$ can be defined such that:

$$\Delta E_{\mathrm{EMA}} \equiv \sum_{\mathbf{k}} |\langle n\mathbf{k}|\Psi_{1s}\rangle|^2 \left| E_{n\mathbf{k}} - \frac{\hbar^2 k_x^2}{2m_x^*} - \frac{\hbar^2 k_y^2}{2m_y^*} \right|, \tag{6.20}$$

which measures the importance of deviations from a parabolic dispersion for the defect state binding energies. In this equation, $\langle n\mathbf{k}|\Psi_{1s}\rangle$ denotes the projection of the most strongly bound defect state (from the atomistic calculation) onto the bulk state $|n\mathbf{k}\rangle$ (where the band index $n$ refers to the highest valence band for acceptor states and to the lowest conduction band for donor states). Also, $\mathbf{k}$ denotes a crystal momentum and $E_{n\mathbf{k}}$ is the tight-binding band structure of the monolayer. Figures 6.13(e) and (f) show $\Delta E_{\mathrm{EMA}}$ for the most strongly bound acceptor and donor states. It is observed that $\Delta E_{\mathrm{EMA}}$ is large for small defect heights and small values of the substrate dielectric constant. Comparing donor and acceptor state, it can be seen that $\Delta E_{\mathrm{EMA}}$ is significantly larger for acceptor states (by up to a factor of 2). It can be easily seen that as the heights of the charged defects from the system or the dielectric constant of the substrate increase, the value of $\Delta E_{\mathrm{EMA}}$ for the $1s$ defect state converges to a small value. This indicates that in the vicinity of the $\Gamma$ point, the low-energy band structure conforms well to the approximation of a parabola, which is the region that $1s$ defect eigenstates of shallow potentials are most prominently constructed from. In the case of the donor, the energetic difference between the tight-binding and effective mass binding energies correlates very strongly with the corresponding value of $\Delta E_{\mathrm{EMA}}$, while for the acceptor case this correspondence is not as precise for all ($d$, $\varepsilon_{\mathrm{sub}}$) parameter sets but still applicable. Hence this provides a justification for the lack of congruence between the energies obtained through the tight-binding calculations and their variational counterparts as determined from effective mass theory, in the case of deep defect potentials. It can be concluded from this that, given the defect potential is shallow, the binding energies of this anisotropic system can be well described by the effective mass model.

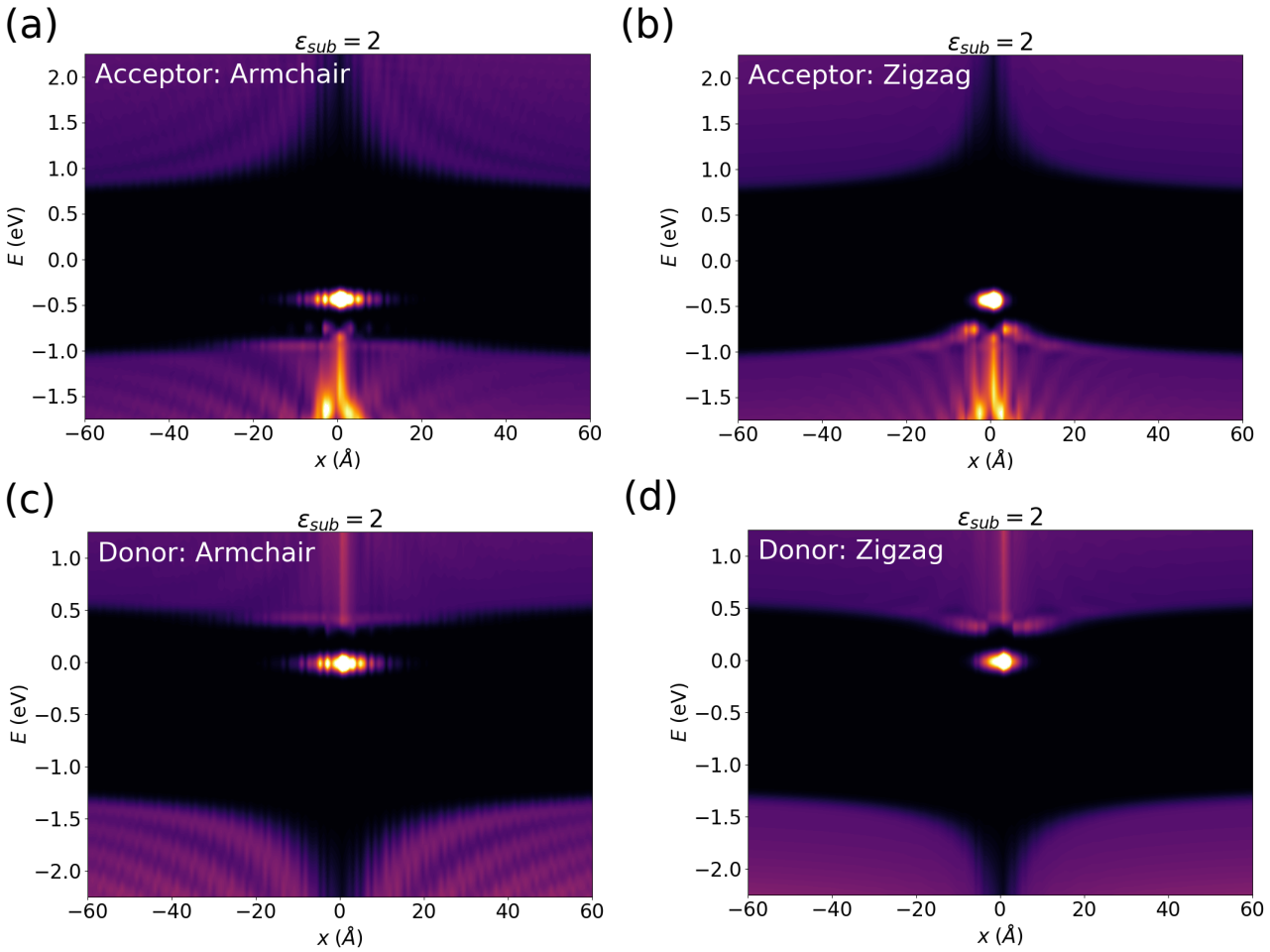



Figure 6.14: Local density of states for a charged defect a distance $d = 2$ Å above the top sublayer, for monolayer BP on a substrate with $\varepsilon_{\text{sub}} = 2$ for (a,b) acceptor defects and (c,d) donor defects. This is shown separately along the (a,c) armchair and (b,d) zigzag directions.

### 6.3.4 Monolayer BP Local Density of States

To view the wavefunctions collectively, the local density of states (LDOS) can be used to highlight relative importance of individual defect states within the bound spectrum, and provide a prediction for experimental signatures of charged defects that can be observed in scanning tunnelling experiments. In Fig. 6.14, The LDOS of monolayer BP with a charged defect of height $d = 2$ Å above the top sublayer is shown in Fig. 6.14 on a substrate with dielectric $\varepsilon_{\text{sub}} = 2$ for both the acceptor defect (a,b) and donor defect (c,d), resolved along either the armchair direction (a,c) or along the zigzag direction (b, d). For acceptor defects, Fig. 6.14(a) and (b) shows that when $\varepsilon_{\text{sub}} = 2$, a very well defined peak that corresponds to the $1s$ state in Fig. 6.9(i) is present which is followed by a series of lobed states closely spaced in energy

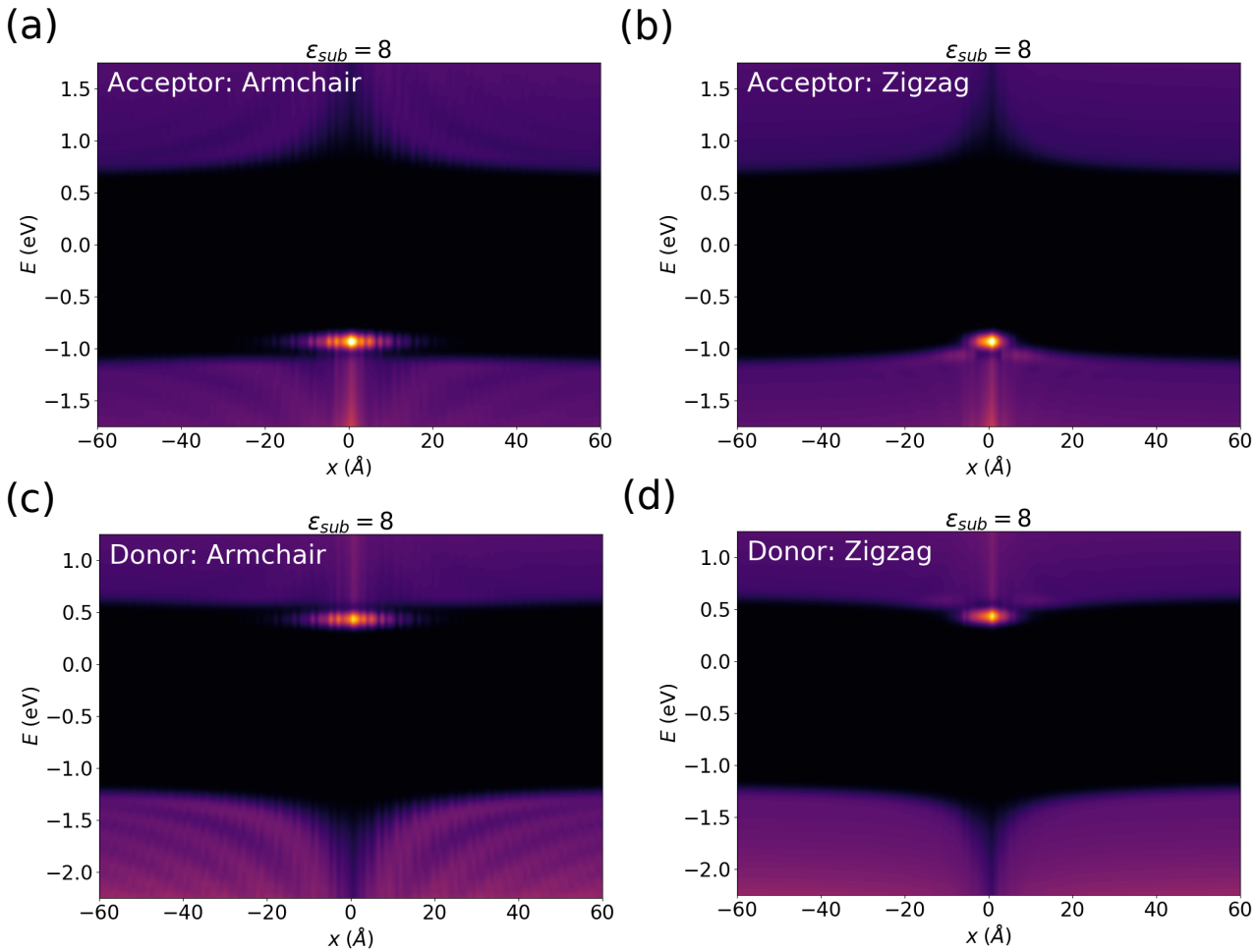



Figure 6.15: Local density of states for a charged defect a distance $d = 2$ Å above the top sublayer, for monolayer BP on a substrate with $\varepsilon_{\text{sub}} = 8$ for (a,b) acceptor defects and (c,d) donor defects. This is shown separately along the (a,c) armchair and (b,d) zigzag directions.

near the valence band maximum. This exhibits similarities with the hydrogen model, where consecutive bound states of increasing principal quantum numbers are decreasingly separated in binding energy, pertaining to the Coulombic nature of the defect potential. Additionally, the conduction band manifests strong defect-induced band-bending, being a result of the strong localised negative potential that repels electrons that would tunnel into the conduction band in an STM experiment. Comparing the signature of this defect spectrum in the armchair and zigzag direction, the anisotropy of the localisation can clearly be seen, where the LDOS along the armchair ($x$) direction shows a more delocalised electron distribution than along the zigzag ($y$) direction.

A larger dielectric constant of the substrate results in the potential being screened more and thus should result in bound states from a charged defect in BP having lower binding energies.

This is shown in Fig. 6.15, where $\varepsilon_{\text{sub}} = 8$, and it becomes apparent when looking at the zigzag directed LDOS, that the lobed states in the gap are very close to the valence band maximum, such that they are only just visible in Fig. 6.15(d). Additionally, compared to $\varepsilon_{\text{sub}} = 2$, it can be seen that the $1s$ state sits closer to the valence band and that the defect-induced band bending in the conduction band becomes less steep, directly reflecting the changes to the defect potential when the substrate dielectric constant is vastly increased. The same analysis can be performed on the donor defect, observing in Fig. 6.15(c-d) that the bound states instead sit close to the conduction band and qualitatively mirror the features of the acceptor defect. The donor defect LDOS spectrum shows that the lobed states are less pronounced and sit even closer to the band extremum than in the acceptor case, as well as displaying states that are slightly less anisotropic with respect to their spatial localisation, which results from the smaller disparity between the effective masses in the $x$ and $y$ direction (Table 6.1).

### 6.3.5 Bilayer BP Defect Wavefunctions

For an acceptor charged adsorbate with height 2 Å above the top sublayer of atoms in bilayer black phosphorus (BP), with an associated defect potential as shown in Fig. 6.8, several states forming within the band gap are displayed in Fig. 6.16(i-v) for both the top and bottom layers. These states are similar in shape and nodal structure to those of the monolayer acceptor case, forming a localised $1s$ state followed by a series of lobed states. Additionally, the wavefunction in the bottom layer mirrors that of the top layer, but to a lesser degree, such that in the $1s$ state, there is comparably negligible electron distribution on the bottom layer with respect to the top layer. This comes as a result of the strong screening exhibited by the layer above, resulting in a potential on the bottom layer that is significantly less deep, which can be seen in Fig. 6.8. Like the monolayer case, these states are constructed primarily from pristine system states in the vicinity of the $\Gamma$ point in the BZ, and because of the higher effective mass in the $y$-direction, states with $y$-oriented lobes are more strongly bound to the defect. The length scale over which the freestanding bilayer bound states extend, is notably larger than the case of the monolayer when placed on a substrate with dielectric constant $\varepsilon_{\text{sub}} = 2$, which also results from

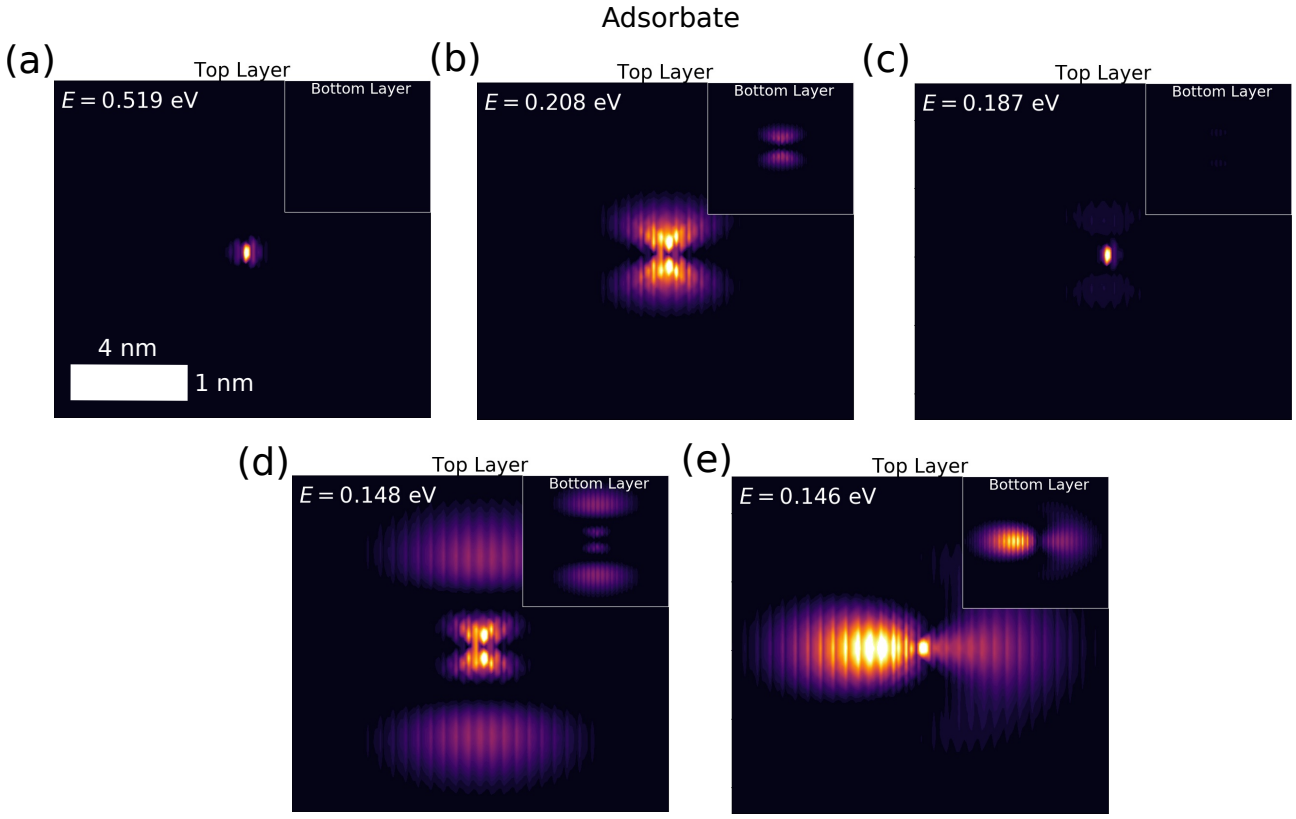



Figure 6.16: Top layer wavefunction of bilayer BP for acceptor states for a charged adsorbate with height $d = 2$ Å from the top sublayer of the top layer, in order a-e of most to least strongly bound. Binding energy is displayed in the top left, and the bottom layer wavefunction is shown in the inset.

a generally shallower potential. For the donor case, the wavefunctions and binding energies of this parameter set are very similar but with the states in iv and v in Fig. 6.16 being reversed in order.

The defect wavefunctions of a negatively charged intercalant are shown in Fig. 6.17. As expected, the wavefunctions for this system have a similar intensity on both layers. Interestingly, the wavefunction of the 1s state exhibits two peaks in the top layer, but only a single peak in the bottom layer, see Fig. 6.17(i). The splitting of the $1s$ wavefunction into two peaks is an interference effect caused by the location of the intercalant below the centre of a zigzag bond. The three most strongly bound states of the acceptor intercalant have a similar nodal structure as in the adsorbate case. However, the fourth and the fifth states look very different to the adsorbate states. However, this does not account for deformation of the structure, which has been shown to slightly warp and change the size of the interlayer gap by $\sim 0.1$ Å in first-principles calculations. The binding energies for charged adsorbates and intercalated defects seem to be

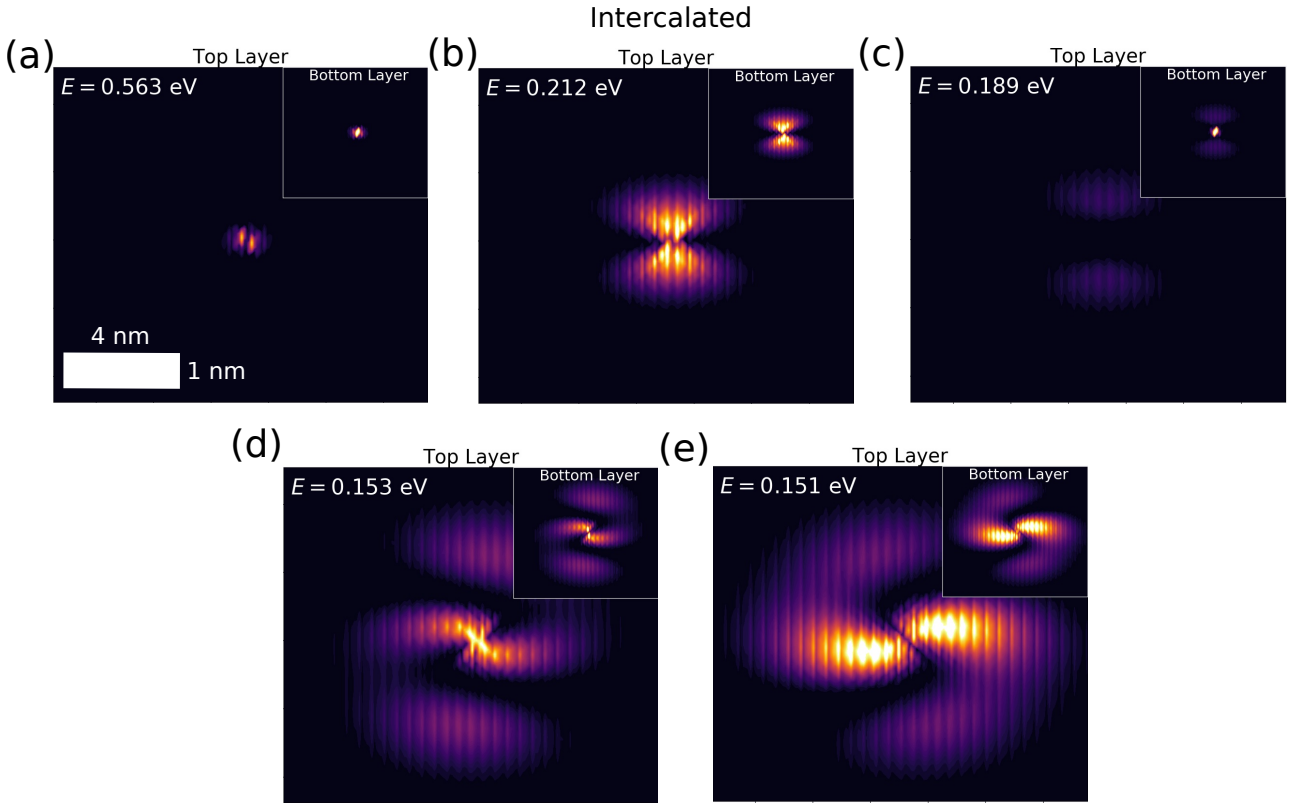



Figure 6.17: Top layer wavefunction of bilayer BP for acceptor states for a charged intercalated defect placed $d_{\text{int}} = 2.7$ Å below the top effective layer, in order a-e of most to least strongly bound. Binding energy is displayed in the top left, and the bottom layer wavefunction is shown in the inset.

very similar in their spectra, indicating that the binding energy could be mostly independent of out-of-plane positioning in the system due to their extended range.

### 6.3.6 Bilayer BP Adsorbate Binding Energies

For both acceptor and donor adsorbate defects on freestanding bilayer BP, the binding energy of the top five most bound states is shown in Fig. 6.18 compared to the monolayer, with the band gaps for bilayer and monolayer shown in red solid and red dashed lines, respectively. For the donor case in Fig. 6.18(a), the binding energies for the $1s$ defect state, with respect to the conduction band of pristine bilayer BP, decrease in binding energy with increasing defect height $d$. For $d = 1.5$ Å, the bilayer donor $1s$ states are not shown as they become resonant with the valence band, similarly to the monolayer, with the binding energy exceeding the band gap. As $d$ increases, an approximately consistent energy gap between 0.4-0.5 eV exists between the $1s$

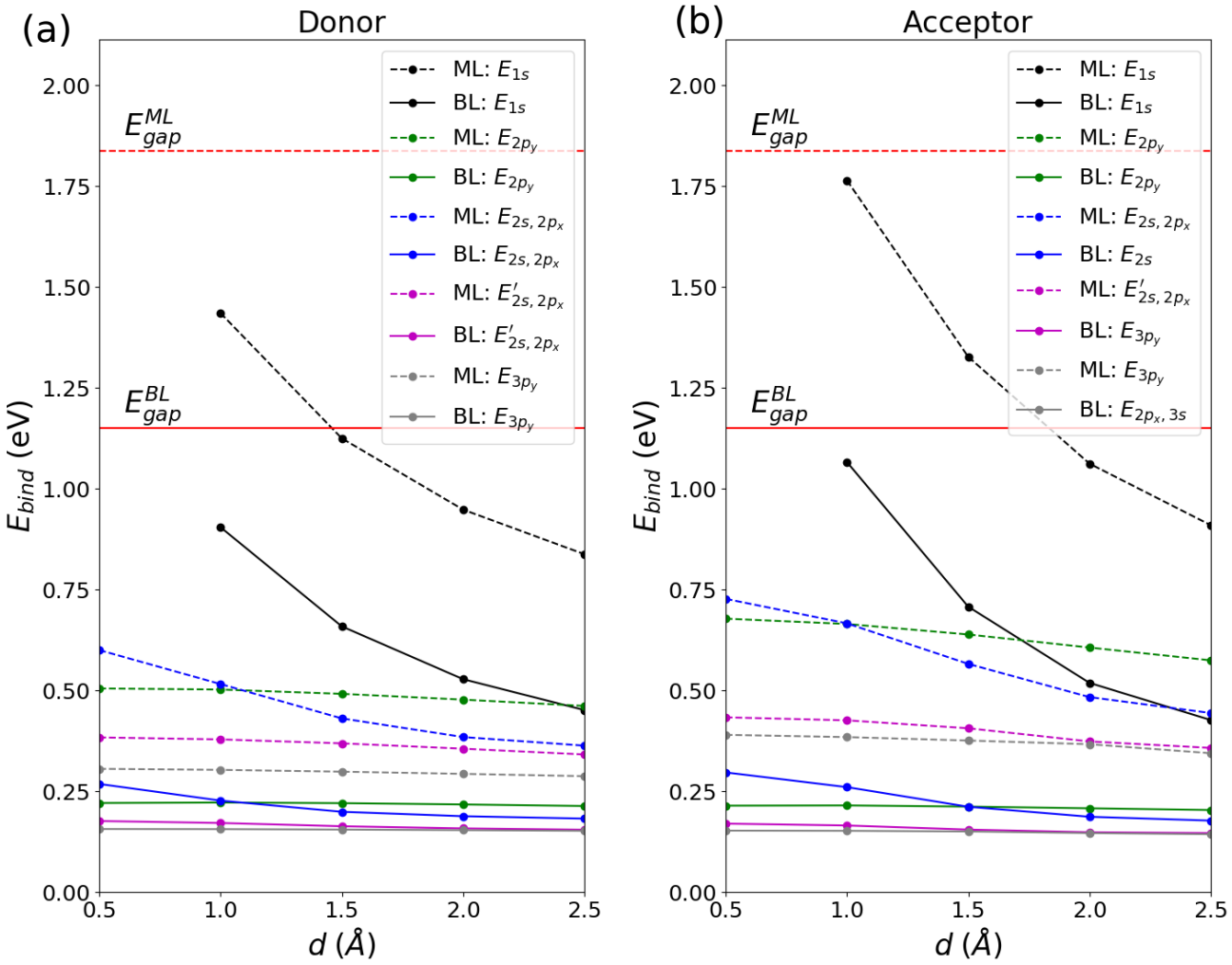



Figure 6.18: Defect energy levels as a function of defect height $d$ above the top sublayer of freestanding monolayer BP (dashed) and freestanding bilayer BP (solid) for (a) donor and (b) acceptor defects, showing the monolayer band gap (dashed) and bilayer band gap (solid).

donor states of the monolayer and bilayer. The binding energy of the $1s$ defect states strongly depend on the potential experienced in the top layer, as seen in Fig. 6.16(a), and for $\varepsilon_{\text{sub}} = 1$ these states are strongly localised to the defect site on this top layer. As a result of this, only the local region in the screened potential close to the defect will control the energy, and can be approximated by $\approx \frac{C}{d}$ where $C$ will depend on the short-wavelength dielectric screening, which differs between the bilayer and monolayer system. Conversely, different behaviour is observed for the lobed states that exist below their respective $1s$ states in energy. In Fig. 6.18(a), these levels remain approximately constant for the bilayer as $d$ is tuned, with the exception of the state strongly associated with the $2s$ nodal structure due to its central peak, that makes its binding energy more sensitive to $d$. Compared to those of the monolayer, the donor binding

energies in the bilayer behave similarly, but with a generally reduced magnitude. This would most likely be a result of the shallower defect potential in the bilayer corresponding to the weaker screening, which as a result causes the defect states to extend further from the defect. The secondary lobed states, having substantially smaller magnitudes of their wavefunctions at the defect site, will not have binding energies that are particularly sensitive to a change in defect height. When the defect instead has an acceptor nature (See Fig. 6.18(b)), it is observed that despite the generally larger effective mass in the conduction band of the bilayer system (See Table 6.1), the acceptor defect binding energies of the bilayer do not conform to the same monotonic increase of the binding energy with effective mass found in the monolayer case. Instead, the binding energy for the $1s$ state at $d = 2$ Å is larger for the acceptor case than for the donor case, whereas the donor binding energy of the $1s$ state is larger than in the acceptor case for $d = 3.5$ Å by 24 meV. This phenomenon occurs due to the non-parabolicity of the bilayer valence bands in the zigzag direction for wavevectors beyond approximately $\frac{1}{2}\Gamma Y$, where there is a crossing between the upper and lower valence bands. For stronger potentials in the vicinity of the defect, caused by smaller values of $d$, the reciprocal-space projections and thus the Bloch composition of the $1s$ includes states further away from the $\Gamma$ point. This means that for highly localised states, they will project more strongly onto both valence bands, and the acceptor binding energies will not be as accurately described by the effective mass approximation. By looking at the projections of the bilayer $1s$ acceptor defect states onto both valence bands, it can be seen that that this higher contribution from the second VBM is more pronounced for smaller $d$.

### 6.3.7 Bilayer BP Local Density of States

Fig. 6.19 shows the local density of states (LDOS) $\rho(E, \mathbf{x})$ of an acceptor adsorbate defect on bilayer BP as a function of energy, for several distances from the defect in both the (a) armchair and (b) zigzag directions. The most prominent feature of Fig. 6.19 is the large resonance that occurs approximately 0.5 eV from the valence band, where the LDOS exhibits a sharp peak that decays by an order of magnitude over 3-4 Å away from the defect. This peak is the signature

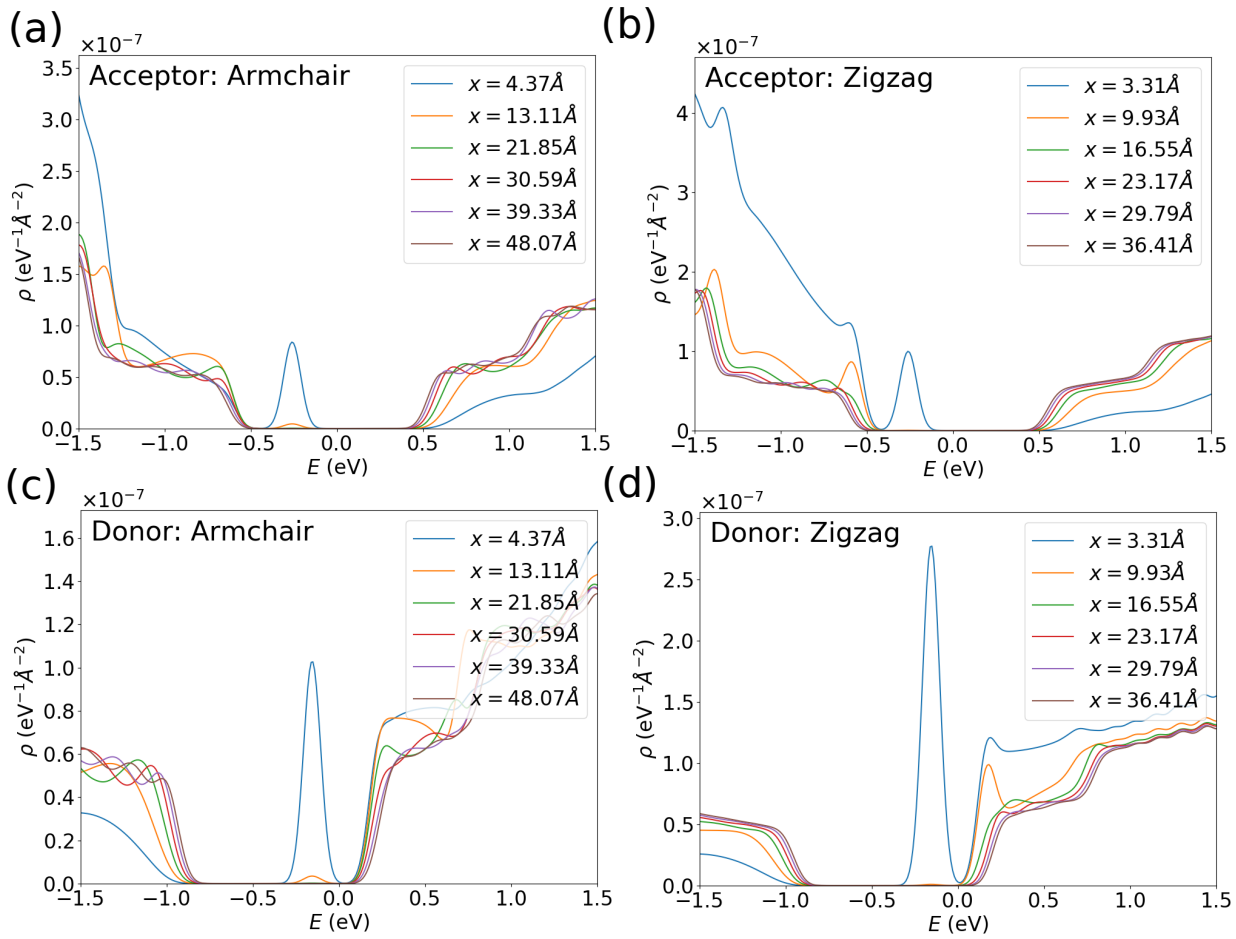



Figure 6.19: Local density of states (LDOS) for a defect charge placed 2 Å above the top sublayer in the top layer of bilayer BP, shown for the acceptor case along the (a) armchair and (b) zigzag directions, and shown for the donor case along the (c) armchair and (d) zigzag directions.

of the 1$s$ defect state and the only difference in its decay between the armchair and zigzag directions of bilayer BP is a slightly lesser decay in the armchair direction, which is noticeable at $\approx 8$ Å. Additionally, it can be seen that the collection of defect states close to the extremum has almost no significant presence in the armchair direction, whereas in the zigzag, the defect states manifest as strong resonances in the LDOS. This indicates that the majority of electronic signatures of the defects, arise from the 1$s$ bound state and those with zigzag-oriented lobes, as seen in Fig. 6.16(b, d). In the conduction band, the presence of the defect charge potential results in the flattening of the LDOS and upward bending of the bands, as commonly seen in previous work on defect calculations [2,14,91]. As the distance away from the defect increases, it is seen in both the armchair and zigzag direction that the LDOS converges to that of the pristine system. For the donor case, shown in Fig. 6.19 along (c) armchair and (d) zigzag

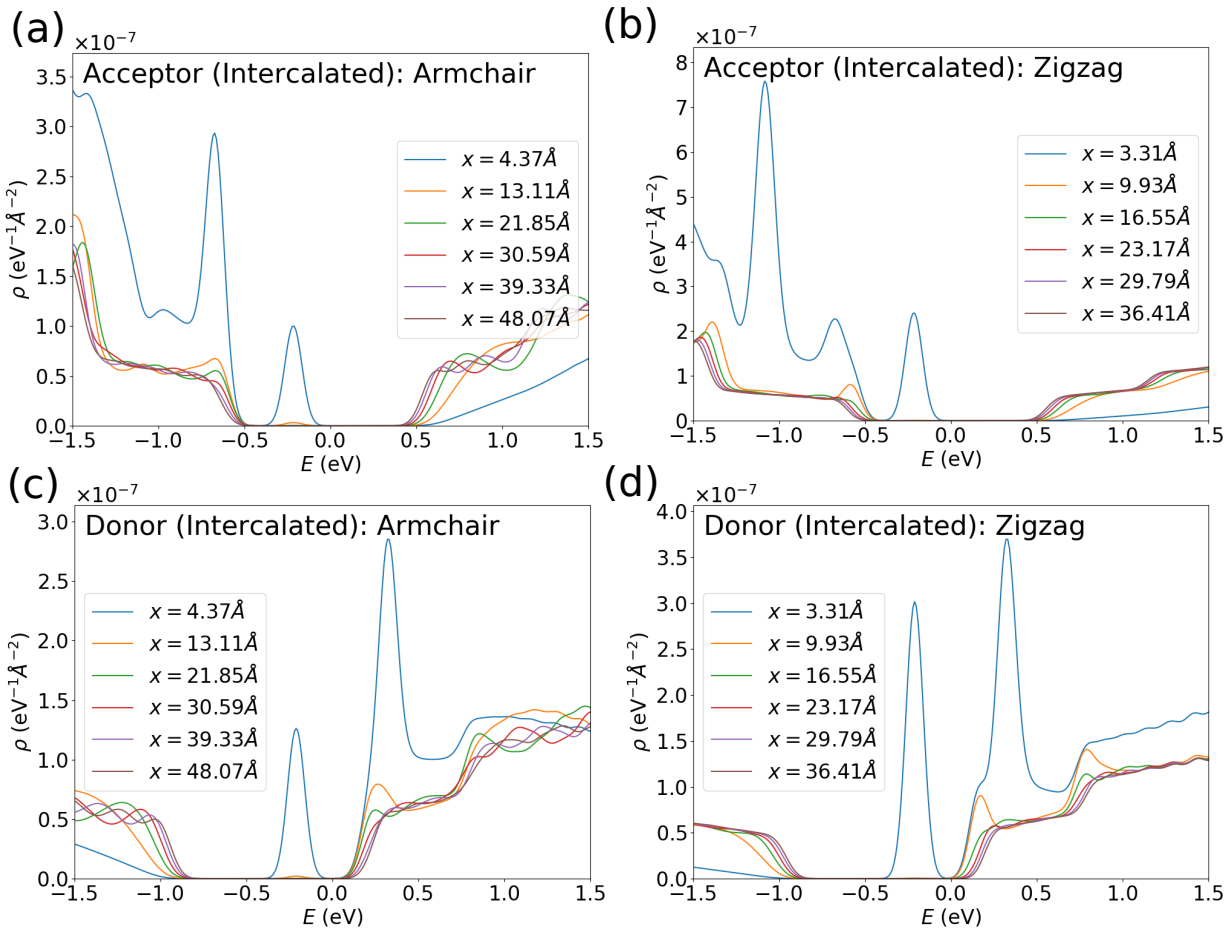



Figure 6.20: Local density of states (LDOS) for a charged intercalated defect placed $d_{\text{int}} = 2.7$ Å below the top layer of bilayer BP, shown for the acceptor case along the (a) armchair and (b) zigzag directions, and shown for the donor case along the (c) armchair and (d) zigzag directions.

directions, the prominent $1s$ resonance decays less swiftly with distance, and is less sharp than that of the acceptor case. However, the decay of the LDOS signature of the donor $1s$ state is more disparate between the two directions, owing to the slightly greater difference in effective mass of the zigzag ($y$) direction compared to the armchair ($x$) direction. Very similarly to the acceptor case, a cluster of defect signatures can be seen near the conduction band that is substantially more present along the zigzag than the armchair direction.

The LDOS for the intercalated charged defects are shown in Fig. 6.20, and while the localised in-gap $1s$ peak sits at the same energy, interesting electronic features arise which are not present for the adsorbate case. Along both armchair (a) and zigzag (b) directions, the LDOS for the intercalated acceptor defect exhibits several strong peaks that are highly localised to the defect, arising in the valence band continuum. These resonant states, unique to the intercalated defect,

decay quickly with distance from the defect, but are as strong as the $1s$ peak. Similarly, extra $1s$-type localised states appear in the intercalated donor defect spectrum along the (c) armchair and (d) zigzag directions that appear in addition to the conduction band LDOS. More evidently so in the donor case, a cluster of secondary states that appear to be lobed along the zigzag direction are seen at the second shoulder of the conduction band LDOS, in an almost identical way to that of the primary shoulder at the conduction band minima. The difference in electronic response between a defect adsorbed to the outer side of the top layer and one intercalated between the layers, can be explained in terms of the secondary conduction and valence band extrema at the $\Gamma$ point in the bilayer system, seen in Fig. 6.6(b). From previous work [14], it is understood that the presence of a charged defect in a two-dimensional semiconductor results in bound states appearing in the band gap which are constructed primarily from the pristine states close to the band extrema, consistent with concepts in the treatment of charged defects within the effective mass approximation [29]. It can be seen from Fig. 6.19 and Fig. 6.20 that, while the charged adsorbate strongly induces a set of bound states constructed from states in the primary extrema at $\Gamma$ in the Brillouin zone, the charged intercalated defect does so additionally in the secondary extrema, inducing defect states resonant with the primary extrema. This occurs due to the fact that in the pristine bilayer system, the secondary maxima in both the conduction and valence bands near the $\Gamma$ point have a higher orbital composition from the $p_z$ orbitals of the inner phosphorus atoms, while the primary band extrema have a higher orbital composition from the $p_z$ orbitals on the outer phosphorus atoms. However in this framework, unlike for the adsorbate defect, there is a noticeable asymmetry between the electronic signatures of the donor and acceptor in the intercalated case, with multiple peaks appearing for the acceptor case. This can be attributed to the effective mass of the secondary valence band at $\Gamma$ being negative along the zigzag direction ($-4.41m_0$). Conversely, the secondary conduction band at $\Gamma$ has very similar effective masses in both the armchair ($0.19m_0$) and zigzag ($0.91m_0$) directions to those of the primary conduction band (see Table 6.1). As a result, the signature seen near the secondary conduction band minimum for the intercalated donor defect mirrors the one near the primary conduction band minimum.

# Chapter 7

# Conclusions and Outlook

## 7.1 Conclusions

In this thesis, I have presented an approach for modelling the electronic properties of charged defects in two-dimensional (2D) semiconductors which combines the effectiveness and scalability of a highly parameterised minimal-basis tight-binding model with an accurate first-principles treatment of the electrostatic screening in the material. With this, I aimed to provide an intermediary description of these systems which bridges the computationally costly but chemically thorough picture provided by density-functional theory, and the long-range but inherently phenomenological framework of continuum models. In constructing large enough supercells to capture bound defect states, I have modelled the electronic effects of an isolated charged defect, such as an adsorbate, on both monolayer transition metal dichalcogenides (TMDCs) and few-layer black phosphorus (BP). Through the simulations presented in this thesis, I have developed an understanding of how charged defects change the electronic structure of atomically thick semiconductors, and indicated how specific defect levels can be engineered for applications in nanoelectronic devices.

For the case of shallow acceptor defects in monolayer $MoS_2$, the presence of a secondary valence band maximum (VBM) that lies close in energy to the primary VBM results in multiple sets of in-gap states which have envelope functions possessing hydrogenic nodal structure. This

was consistent with the effective mass approximation which dictates that the envelopes of the defect state wavefunctions are the solutions to a single-particle Schrödinger equation, where the potential is the screened Coulomb potential. By projecting the in-gap defect states onto the pristine BZ, it was observed that the peaks of the projection for each state are centred on either the primary or secondary valence band maxima, situated at the $K/K'$ and the $\Gamma$ points in the BZ, respectively. The bound states associated with the $\Gamma$ point displayed significantly different behaviour to those found at the $K/K'$ points, including more strongly localised defect states and a higher sensitivity of the binding energy to changes in the defect potential. Furthermore, despite the energy of the $1s$ state from $\Gamma$ being resonant with the $K/K'$ continuum for small charges, it was found for physically reasonably defect heights that as the charge strength is increased, the energy of the $1s$ state from the $\Gamma$ point becomes the deepest acceptor state into the band gap, surpassing the defect level of the $1s$ state from the $K/K'$ at some non-zero charge. This is due to the much larger effective mass of the $\Gamma$ point compared to the $K/K'$ points in the BZ. This was verified for shallow defects using a variational effective mass model to simulate the binding energy curves of the two $1s$ states, distinguished only by the energy and effective mass of the VBM they are most strongly constructed from, which reproduced the crossover and showed a good agreement with the atomistic calculations at smaller charges. Since the Bloch states associated with the VBM at $\Gamma$ and $K/K'$ have a dominant orbital character of $d_{z^2}$ and $d_{xy/x^2-y^2}$, respectively, it is understood that the orbital character of the most strongly bound acceptor state can be easily tuned by the magnitude of the defect charge. The choice of dielectric substrate however, was found to provide significantly less control on the ordering of the most strongly bound states.

Using this framework, the asymmetry between the electronic structure of the donor and acceptor defect states can be explained by the significant differences between the conduction and valence band structure. The spin-orbit splitting of the conduction band at the same location in the BZ is negligible, which results in a hybridisation effect between the spectrum of defect states from the $K$ and $K'$ subzone, causing pairs of modulated donor states whose splitting increases with the charge strength. This was not observed in the acceptor defect spectrum due to the strong spin-orbit coupling in the valence band at $K/K'$ which prevents interaction between same-

spin states at opposite primary valleys. Similar to the case of the acceptor defect, bound donor states arise in the gap which are constructed from combinations of the six secondary conduction band minima at the highly anisotropic $Q$ points in the BZ. Since the secondary minima have an overall larger effective mass and are quite energetically far away from the primary minima, a crossover point of the orbital character of the most strongly bound state is also seen in the donor case. However, compared to the acceptor case, a larger separation in energy between the two species of minima, coupled with a smaller ratio of effective masses, means that a larger charge strength is needed for a hybridised state from the $Q$ point to become the most strongly bound donor state.

Experimental signatures of donor and acceptor defects were determined for particular sample cases of adsorbate atoms on monolayer $MoS_2$ when on a $SiO_2$ substrate. This was done through the local density of states (LDOS), which is proportional to the gradient of current in scanning tunnelling experiments. In addition to highlighting the bound states, the LDOS showed that the presence of a donor adsorbate, such as lithium, induces downward band bending of the valence band, which converges back to the pristine case with increasing distance from the defect. Generally, this work has demonstrated that the effective defect charge strength, modified through either external fields or dielectric substrates, is an important parameter that can sensitively tune the size and ordering of defect spectra of charged adsorbates.

The understanding gained from studying the static electronic properties of charged defects in monolayer TMDCs was applied to the case of an unknown acceptor defect in monolayer $WS_2$ observed in scanning tunnelling experiments. By modelling the graphene+SiC substrate, and accounting for the poor tunnelling matrix element into states with large momenta, both bound and resonant states were identified and simulated to produce good agreement with experiment. It was found that while the experimental tunnelling spectra exhibited two resonances that behaved like localised $1s$ bound states of different binding energies within the gap, a ring-shaped $2p$-like state was found to be resonant with the valence band, and constructed primarily from $\Gamma$-point states. These resonant states were predicted to trap mobile holes for approximately 30 ps, which would impair the carrier mobility of transport devices [2].

Additionally, this work has explored how the defect state spectrum arising in the band gap plays a role in the optical properties of monolayer TMDCs, specifically $MoS_2$ on either a $SiO_2$ or diamond substrate. The optical conductivity of the pristine system is characterised by two primary excitonic resonances in the monolayer $MoS_2$ spectrum, named the $A$ and $B$ peak which arise from the strong spin-orbit splitting in the valence band. In the presence of an acceptor defect, the $A$ and $B$ peak were found to be significantly constructed from transitions from the strongly bound $1s$ acceptor states from both $\Gamma$ and $K/K'$. Additionally, the presence of in-gap defect states results in defect excitons that are comprised entirely from transitions from the bound $1s$ states, with much stronger binding energies than the $A$ and $B$ peaks. This is consistent with peaks seen in experimental literature, which are suspected to be drawn in from transitions between in-gap states. While these supercell calculations were sufficient in size to capture the lowest energy bound states from band extrema and model how they contribute to the optical properties, the general results of this section of the thesis can be improved with larger supercells, since the largest size of the Hamiltonian for the Bethe-Salpeter equation (BSE) was limited by computational resources. Further work to parallelise the diagonalisation of the BSE will allow for the increase in accuracy of the optical spectrum of charged defects in monolayer TMDCs.

The concepts developed in this work while studying charged defects in TMDCs were also applied to the case of monolayer and bilayer black phosphorus (BP), considering both acceptor and donor defects adsorbed to the surface. In the monolayer results, the screened Coulomb potential from the defect results in strongly bound states with wavefunctions that exhibit lobed hydrogenic nodal structure. The variation of their binding energy with the substrate dielectric constant has been demonstrated for different heights of the defect above the system. It is found that the acceptor states of the monolayer system are generally more strongly bound than those of the donor, given the same parameters of the defect, which is attributed to the large effective mass in the zigzag direction of the valence band. By comparing this to the binding energies extracted from a variational model within the effective mass approximation, it was found that for environments that allow for deep defect potentials, the $1s$ states become localised enough such that they are constructed from states in non-parabolic regions of the Brillouin zone. It

is within this region in the parameter space that the effective mass approximation fails to adequately model the behaviour of the charged defect states, whereas for the case of shallow potentials, the effective mass approximation can describe the results seen in the tight-binding model reasonably well. The local density of states of the charged defects on the monolayer demonstrated the disparity in decay scales of the states due to the anisotropy of the system. This also showed the proximity of secondary lobed states to the conduction and valence band extrema for donor and acceptor defects respectively, as well as to each other, possibly observed in tunnelling experiments as a single signature. Finally, a model of charged defects in the bilayer BP system demonstrates strong similarities with the monolayer system in terms of spatial nodal structure of the defect state, but stark differences in binding energy and decay scale of their wavefunction. If the defect is instead intercalated between the two layers, additional sets of bound resonant defect states are found in our calculations. These arise from the secondary band extrema which are characterised more strongly by the orbitals of the inner atoms of the bilayer.

## 7.2 Further Work

### 7.2.1 Further Study of Optical Properties of Charged Defects on Monolayer TMDCs

In this work I have covered a limited range of study on how the presence of charged defects influences the optical properties of TMDCs, namely the optical conductivity of monolayer $MoS_2$ on silicon dioxide and diamond substrates. This has been achieved with an $18 \times 18$ supercell which, while approximately spanning 2 nm either side of the defect that allows the localised $1s$-like states to be captured, is limited in its convergence of higher-order defect states. Additionally, a larger $N_k \times N_k$ sampling of the $N_c \times N_c$ supercell Brillouin zone (BZ) will allow for a better convergence on quantities such as the optical conductivity. However, an increase in both the supercell size and the sampling size of the BZ will incur large computational costs, on account of the basis size $M$ of the Bethe-Salpeter equation obeying $M \propto N_c^4 N_k^2$, and hence a

significant memory requirement. The current calculations were done using the standard Numpy diagonalisation routine which performs on a single processor with access to a fixed memory, limiting how large a matrix can be diagonalised in the calculation. This can be resolved by writing the matrix to disk and then using the parallel diagonalisation library available in `SCALAPACK` (accessed with a script written in `Fortran 90`), which will allow for the matrix to be divided into submatrices that are distributed across different machines each with their own memory, meeting the large memory demand of the calculation. Once this is achieved, optical calculations over a significantly larger area of monolayer $MoS_2$ can be performed. In addition to greater convergence, more study can be undertaken to understand the sensitivities of the defect excitons to changes in light-polarisation, defect height, defect site and which TMDC is used. Also, pristine $MoS_2$ has been shown to exhibit circular dichroism, in which the two valleys at $K$ or $K'$ absorb more strongly photons with left ($\sigma^+$) or right ($\sigma^-$) handed polarisation, respectively [104]. Further study into how this is changed by the presence of in-gap states induced by charged defects could result in interesting predictions for experimental efforts.

### 7.2.2 Doped Systems: Formulation of Thomas-Fermi Screening

The presence of doping in a semiconductor raises the Fermi level $E_F$, and results in a partially filled conduction or valence band, depending on whether the system has been doped with electrons or hole respectively. Partially filled bands give the electrons/holes occupying it a greater susceptibility to external electrostatic potentials, as electrons can more readily transition to higher or lower energy states to screen these external perturbations. The effects of doping on the screened defect potential has been recently studied for graphene [91, 92] for a variety of screening models. One such screening model is the Lindhard function, which is calculated from linear-response theory within the random-phase approximation (RPA).

Another continuum screening model, known as the Thomas-Fermi (TF) approximation, assumes electrons can be treated semiclassically as moving particles in a slow-varying potential, comprising of an external potential $V_{\text{ext}}(\mathbf{r})$ and an induced potential $V_{\text{ind}}(\mathbf{r})$. In TF-theory, the screened potential $V_{\text{scr}}(\mathbf{r}) = V_{\text{ext}}(\mathbf{r}) + V_{\text{ind}}(\mathbf{r})$ acting on the electrons causes a change in the homogeneous

density $n(\mu)$ where $\mu$ is the chemical potential, constant everywhere [115, 155]. The assumption of a slow-varying potential, compared to the Fermi wavelength [23], means that electron energies $E_{\mathbf{k}}$ are shifted locally to $E_{\mathbf{k}} + V_{scr}(\mathbf{r})$, changing the density [23] to $n\left[\mu - V_{\mathrm{scr}}(\mathbf{r})\right]$. For general non-linear TF-theory, where exchange-correlation effects are ignored [155], $n_{ind}(\mathbf{r})$ at chemical potential $\mu_0$ is the density difference between the perturbed and unperturbed system:

$$n_{ind}(\mathbf{r}) = n\left[\mu_0 - V_{\mathrm{scr}}(\mathbf{r})\right] - n(\mu_0) = -\left[\frac{\partial n}{\partial \mu}\right]_{\mu=\mu_0} V_{\mathrm{scr}}(\mathbf{r}) + \frac{1}{2}\left[\frac{\partial^2 n}{\partial \mu^2}\right]_{\mu=\mu_0} V_{\mathrm{scr}}^2(\mathbf{r}) + \cdots . \quad (7.1)$$

Having expanded this to sufficiently high order, the Fourier transform of the density can be used to calculate the dielectric function. For non-linear TF theory, this requires self-consistent calculations, whereas for linear TF theory the calculation can be performed reasonably quickly. This method is a promising candidate for studying the effects of doping on the bound states of adatoms on TMDCs, as it has produced experimentally verified results for the LDOS of calcium adatoms on graphene [91, 92].

This method would be applied to TMDCs, potentially using a quartic approximation to the low energy band structure. This can be done by expanding the formula for the massive Dirac Fermion band structure, taking the form:

$$E(q) = \pm\sqrt{\Delta^2 + (vq)^2} = \pm\Delta^2\sqrt{1 + \left(\frac{vq}{\Delta^2}\right)^2} \quad (7.2)$$

$$= \pm\Delta(1 + \frac{1}{2}\frac{(vq)^2}{\Delta^2} - \frac{1}{8}\frac{(vq)^4}{\Delta^4} + \cdots) \quad (7.3)$$

$$\approx \Delta + \frac{v^2q^2}{2\Delta} - \frac{v^4q^4}{8\Delta^3}, \quad (7.4)$$

where $v$ is a parameter to be fit to the band structure, and $\Delta = E_g/2$ is half the band gap. This can be rewritten as a quadratic to be solved for $q$:

$$E(q) = \Delta + Aq^2 - Bq^4, \quad A = \frac{v^2}{2\Delta},\ B = \frac{v^4}{8\Delta^3} \quad (7.5)$$

$$q^2 = \frac{1}{2B}\left(A \pm \sqrt{A^2 - 4B(E-\Delta)}\right) \quad (7.6)$$

$$q = \pm\left[\frac{1}{2B}\left(A - \sqrt{A^2 - 4B(E-\Delta)}\right)\right]^{\frac{1}{2}}, \quad (7.7)$$

where the negative solution of $q^2$ is taken such that $q$ lies in the region of the quartic curve closest to the origin. To use this in the Thomas-Fermi model, the carrier density $n$ is required, which can be obtained from integrating the density of states per unit area:

$$\rho(E) = \frac{g_s g_v}{4\pi^2}(2\pi k)\frac{\mathrm{d}k}{\mathrm{d}E} = \frac{g_s g_v}{2\pi}\frac{2\Delta^3}{v^4\sqrt{\frac{3\Delta}{2} - E}} \tag{7.8}$$

$$n(\mu) = \int_{E_{\min}}^{\mu} \mathrm{d}E\ \rho(E) = \quad \text{const.} \quad - \frac{g_s g_v \Delta^3}{2\sqrt{2}\pi v^4}\sqrt{3\Delta - 2\mu}, \tag{7.9}$$

where $g_s = 2$ and $g_v = 2$ are the spin and valley degeneracy, respectively, and $\mu$ is the chemical potential. This can be inserted into the expression for $n_{\mathrm{ind}}(q)$ which can then be used to obtain the Fourier transform $V(q)$ of the total defect potential, using self-consistent calculations, for a charge $Z$, the height $d$ of the impurity above the monolayer, and the chemical potential $\mu$. As performed by Corsetti *et al.* [91], a calculation with ONETEP would be used to extract a screened defect potential, which would be used to parameterise the screening model determined by both the screening from interband transitions accounted for in the undoped calculations (RPA), and the TF approximation. This would then allow similar analysis to be performed as the work done so far, but for specific atoms on $MoS_2$. The final result of this would be the local density of states, which as mentioned throughout this thesis, can be directly compared to STS measurements of adatoms on TMDCs.

# Bibliography


[1] G.-B. Liu, W.-Y. Shan, Y. Yao, W. Yao, and D. Xiao. Three-band tight-binding model for monolayers of group-vib transition metal dichalcogenides. *Phys. Rev. B*, 88:085433, 2013.

[2] M. Aghajanian, B. Schuler, K. A. Cochrane, J.-H. Lee, C. Kastl, J. B. Neaton, A. Weber-Bargioni, A. A. Mostofi, and J. Lischner. Resonant and bound states of charged defects in two-dimensional semiconductors. *Phys. Rev. B*, 101:081201, 2020.

[3] K. F. Mak, C. Lee, J. Hone, J. Shan, and T. F. Heinz. Atomically thin $MoS_2$: A new direct-gap semiconductor. *Phys. Rev. Lett.*, 105:136805, 2010.

[4] Y. Zhang, T.-R. Chang, B. Zhou, Y.-T. Cui, H. Yan, Z. Liu, F. Schmitt, J. Lee, R. Moore, Y. Chen, H. Lin, H.-T. Jeng, S.-K. Mo, Z. Hussain, A. Bansil, and Z.-X. Shen. Direct observation of the transition from indirect to direct bandgap in atomically thin epitaxial $MoSe_2$. *Nature Nanotech*, 9:111–115, 2014.

[5] G.-B. Liu, D. Xiao, Y. Yao, X. Xu, and W. Yao. Electronic structures and theoretical modelling of two-dimensional group-vib transition metal dichalcogenides. *Chem. Soc. Rev.*, 44:2643–2663, 2015.

[6] E. Ridolfi, D. Le, T. S. Rahman, E. R. Mucciolo, and C. H. Lewenkopf. A tight-binding model for $MoS_2$ monolayers. *Journal of Physics: Condensed Matter*, 27(36):365501, 2015.

[7] R. Addou, L. Colombo, and R. M. Wallace. Surface defects on natural $MoS_2$. *ACS Applied Materials and Interfaces*, 7(22):11921–11929, 2015.

[8] D. Edelberg, D. Rhodes, A. Kerelsky, B. Kim, J. Wang, A. Zangiabadi, C. Kim, A. Abhinandan, J. Ardelean, M. Scully, D. Scullion, L. Embon, R. Zu, E. J. G. Santos, L. Balicas, C. Marianetti, K. Barmak, X. Zhu, J. Hone, and A. N. Pasupathy. Approaching the intrinsic limit in transition metal diselenides via point defect control. *Nano Letters*, 19(7):4371–4379, 2019.

[9] W. H. Blades, N. J. Frady, P. M. Litwin, S. J. McDonnell, and P. Reinke. Thermally induced defects on $WSe_2$. *Journal of Physical Chemistry C*, 124(28):15337–15346, 2020.

[10] D. Y. Qiu, da Jornada F. H., and S. G. Louie. Screening and many-body effects in two-dimensional crystals: Monolayer $MoS_2$. *Phys. Rev. B*, 93:235435, 2016.

[11] Y. Li, A. Chernikov, X. Zhang, A. Rigosi, H. M. Hill, A. M. van der Zande, D. A. Chenet, E.-M. Shih, J. Hone, and T. F. Heinz. Measurement of the optical dielectric function of monolayer transition-metal dichalcogenides. *Phys. Rev. B*, 90:205422, 2014.

[12] D. Y. Qiu, F. H. da Jornada, and S. G. Louie. Optical spectrum of $MoS_2$: many-body effects and diversity of exciton states. *Phys. Rev. Lett.*, 111:216805, 2013.

[13] P. K. Chow, R. B. Jacobs-Gedrim, J. Gao, T.-M. Lu, B. Yu, and H. Terrones. Defect-induced photoluminescence in monolayer semiconducting transition metal dichalcogenides. *ACS Nano*, 9(2):1520–1527, 2015.

[14] M. Aghajanian, A. A. Mostofi, and J. Lischner. Tuning electronic properties of transition-metal dichalcogenides via defect charge. *Scientific Reports*, 8:13611, 2018.

[15] T. H. Lee, S. Y. Kim, and H. W. Jang. Black phosphorus: Critical review and potential for water splitting photocatalyst. *Nanomaterials*, 6(11):194, 2016.

[16] H. Liu, A. T. Neal, Z. Zhu, Z. Luo, X. Xu, D. Tománek, and P. D. Ye. Phosphorene: An unexplored 2D semiconductor with a high hole mobility. *ACS Nano*, 8(4):4033–4041, 2014.

[17] A. N. Rudenko, S. Brener, and M. I. Katsnelson. Intrinsic charge carrier mobility in single-layer black phosphorus. *Phys. Rev. Lett.*, 116:246401, 2016.

[18] L. Liang, J. Wang, W. Lin, B. G. Sumpter, V. Meunier, and M. Pan. Electronic bandgap and edge reconstruction in phosphorene materials. *Nano Letters*, 14(11):6400–6406, 2014.

[19] C. Q. Han, M. Y. Yao, X. X. Bai, L. Miao, F. Zhu, D. D. Guan, S. Wang, C. L. Gao, C. Liu, D. Qian, Y. Liu, and J.-F. Jia. Electronic structure of black phosphorus studied by angle-resolved photoemission spectroscopy. *Phys. Rev. B*, 90:085101, 2014.

[20] G. Long, D. Maryenko, J. Shen, S. Xu, J. Hou, Z. Wu, W. K. Wong, T. Han, J. Lin, Y. Cai, R. Lortz, and N. Wang. Achieving ultrahigh carrier mobility in two-dimensional hole gas of black phosphorus. *Nano Letters*, 16(12):7768–7773, 2016.

[21] Y. Deng, Z. Luo, N. J. Conrad, H. Liu, Y. Gong, S. Najmaei, P. M. Ajayan, J. Lou, X. Xu, and P. D. Ye. Black phosphorus-monolayer $MoS_2$ van der Waals heterojunction p-n diode. *ACS Nano*, 8(8):8292–8299, 2014.

[22] Z. Qiu, H. Fang, A. Carvalho, A. S. Rodin, Y. Liu, S. J. R. Tan, M. Telychko, P. Lv, J. Su, Y. Wang, A. H. Castro Neto, and J. Lu. Resolving the spatial structures of bound hole states in black phosphorus. *Nano Letters*, 17(11):6935–6940, 2017.

[23] N. W. Ashcroft and N. D. Mermin. *Solid State Physics*, pages 340–342, 562–579. Harcourt Publishing, 1976.

[24] T. Mattila and A. Zunger. Deep electronic gap levels induced by isovalent P and As impurities in GaN. *Phys. Rev. B*, 58:1367–1373, 1998.

[25] Y. Zhang. Electronic structures of impurities and point defects in semiconductors. *Chinese Physics B*, 27(11):117103, 2018.

[26] W. Kohn. Shallow impurity states in silicon and germanium. *Solid State Physics*, 5:257–320, 1957.

[27] H. J. Hrostowski and R. H. Kaiser. *Bull. Am. Phys. Soc.*, 2(66), 1957.

[28] S. T. Pantelides. The electronic structure of impurities and other point defects in semiconductors. *Rev. Mod. Phys.*, 50:797–858, 1978.

[29] F. Bassani, G. Iadonisi, and B. Preziosi. Electronic impurity levels in semiconductors. *Rep. Prog. Phys.*, 37(9):1009–1210, 1974.

[30] T.-I. Jeon and D. Grischkowsky. Nature of conduction in doped silicon. *Phys. Rev. Lett.*, 78:1106–1109, 1997.

[31] Ü. Özgür, Y. I. Alivov, C. Liu, A. Teke, M. A. Reshchikov, S. Doğan, V. Avrutin, S.-J. Cho, and H. Morko. A comprehensive review of ZnO materials and devices. *Journal of Applied Physics*, 98(4):041301, 2005.

[32] E. G. Seebauer and K. W. Noh. Trends in semiconductor defect engineering at the nanoscale. *Materials Science and Engineering: R: Reports*, 70(3):151–168, 2010.

[33] K. S. Novoselov, A. K. Geim, S. V. Morozov, D. Jiang, Y. Zhang, S. V. Dubonos, I. V. Grigorieva, and A. A. Firsov. Electric field effect in atomically thin carbon films. *Science*, 306(5696):666–669, 2004.

[34] T. Ando, A. B. Fowler, and F. Stern. Electronic properties of two-dimensional systems. *Rev. Mod. Phys.*, 54:437–672, 1982.

[35] K. I. Bolotin, K. J. Sikes, Z. Jiang, M. Klima, G. Fudenberg, J. Hone, P. Kim, and H. L. Stormer. Ultrahigh electron mobility in suspended graphene. *Solid State Communications*, 146(9):351–355, 2008.

[36] K. S. Novoselov, S. V. Morozov, T. M. G. Mohinddin, L. A. Ponomarenko, D. C. Elias, R. Yang, I. I. Barbolina, P. Blake, T. J. Booth, D. Jiang, J. Giesbers, E. W. Hill, and A. K. Geim. Electronic properties of graphene. *Physica Status Solidi (B) Basic Research*, 244(11):4106–4111, 2007.

[37] M. D. Stoller, S. Park, Y. Zhu, J. An, and R. S. Ruoff. Graphene-based ultracapacitors. *Nano Letters*, 8(10):3498–3502, 2008.

[38] F. Schwierz. Graphene transistors. *Nature Nanotechnology*, 5(7):487–496, 2010.

[39] L. Liao, J. Bai, R. Cheng, Y.-C. Lin, S. Jiang, Y. Huang, and X. Duan. Top-gated graphene nanoribbon transistors with ultrathin high- $\kappa$ dielectrics. *Nano Letters*, 10(5):1917–1921, 2010.

[40] V. B. Mohan, K. tak Lau, D. Hui, and D. Bhattacharyya. Graphene-based materials and their composites: A review on production, applications and product limitations. *Composites Part B: Engineering*, 142:200–220, 2018.

[41] G. D. Förster, F. Rabilloud, and F. Calvo. Adsorption of metal nanoparticles on carbon substrates and epitaxial graphene: Assessing models for dispersion forces. *Phys. Rev. B*, 91:245433, 2015.

[42] T. Xu and L. Sun. Structural defects in graphene. *Defects in Advanced Electronic Materials and Novel Low Dimensional Structures*, 5:137–160, 2018.

[43] L. G. Cançado, A. Jorio, E. H. Martins Ferreira, F. Stavale, C. A. Achete, R. B. Capaz, M. V. O. Moutinho, A. Lombardo, T. S. Kulmala, and A. C. Ferrari. Quantifying defects in graphene via Raman spectroscopy at different excitation energies. *Nano Letters*, 11(8):3190–3196, 2011.

[44] A. Hashimoto, K. Suenaga, A. Gloter, K. Urita, and S. Iijima. Direct evidence for atomic defects in graphene layers. *Nature*, 430(7002):870–873, 2004.

[45] F. Bonaccorso, Z. Sun, T. Hasan, and A. C. Ferrari. Graphene photonics and optoelectronics. *Nature Photonics*, 4(9):611–622, 2010.

[46] A. K. Geim. Graphene: Status and prospects. *Science*, 324(5934):1530–1534, 2009.

[47] K. S. Novoselov, A. Mishchenko, A. Carvalho, and A. H. Castro Neto. 2D materials and van der Waals heterostructures. *Science*, 353(6298):aac9439, 2016.

[48] K. Dolui, I. Rungger, C. D. Pemmaraju, and S. Sanvito. Possible doping strategies for $MoS_2$ monolayers: An ab initio study. *Phys. Rev. B*, 88:075420, 2013.

[49] Z. Lin, B. R. Carvalho, E. Kahn, R. Lv, R. Rao, H. Terrones, M. A. Pimenta, and M. Terrones. Defect engineering of two-dimensional transition metal dichalcogenides. *2D Mater.*, 3(2):022002, 2016.

[50] J. Davies. *The Physics of Low-Dimensional Semiconductors*. Cambridge University Press, 1998.

[51] M. Chhowalla, H. S. Shin, G. Eda, L.-J. Li, K. P. Loh, and H. Zhang. The chemistry of two-dimensional layered transition metal dichalcogenide nanosheets. *Nature Chemistry*, 5(4):263–275, 2013.

[52] B. Sipos, A. F. Kusmartseva, A. Akrap, H. Berger, L. Forró, and E. Tutĭ. From Mott state to superconductivity in-1T-$TaS_2$. *Nature Materials*, 7(12):960–965, 2008.

[53] Q. H. Wang, K. Kalantar-Zadeh, A. Kis, J. N. Coleman, and M. S. Strano. Electronics and optoelectronics of two-dimensional transition metal dichalcogenides. *Nature NanoTech.*, 7(11):699–712, 2012.

[54] Y. Shi, H. Zhang, W.-H. Chang, H. S. Shin, and L.-J. Li. Synthesis and structure of two-dimensional transition-metal dichalcogenides. *MRS Bulletin*, 40(7):566–576, 2015.

[55] W. Choi, N. Choudhary, G. H. Han, J. Park, D. Akinwande, and Y. H. Lee. Recent development of two-dimensional transition metal dichalcogenides and their applications. *Materials Today*, 20(3):116–130, 2017.

[56] J. Park, N. Choudhary, J. Smith, G. Lee, M. Kim, and W. Choi. Thickness modulated $MoS_2$ grown by chemical vapor deposition for transparent and flexible electronic devices. *Applied Physics Letters*, 106(1):012104, 2015.

[57] A. L. Elías, N. Perea-López, A. Castro-Beltrán, A. Berkdemir, R. Lv, S. Feng, A. D. Long, T. Hayashi, Y. A. Kim, M. Endo, H. R. Gutiérrez, N. R. Pradhan, L. Balicas, T. E. Mallouk, F. López-Urías, H. Terrones, and M. Terrones. Controlled synthesis and transfer of large-area $WS_2$ sheets: From single layer to few layers. *ACS Nano*, 7(6):5235–5242, 2013.

[58] S. Wang, A. Robertson, and J. H. Warner. Atomic structure of defects and dopants in 2D layered transition metal dichalcogenides. *Chem. Soc. Rev.*, 47:6764–6794, 2018.

[59] J. Hong, Z. Hu, M. Probert, K. Li, D. Lv, X. Yang, L. Gu, N. Mao, Q. Feng, L. Xie, J. Zhang, D. Wu, Z. Zhang, C. Jin, and W. Ji. Exploring atomic defects in molybdenum disulphide monolayers. *Nature Communications*, 6(1):6293, 2015.

[60] D. Jariwala, V. K. Sangwan, L. J. Lauhon, T. J. Marks, and M. C. Hersam. Emerging device applications for semiconducting two-dimensional transition metal dichalcogenides. *ACS Nano*, 8(2):1102–1120, 2014.

[61] A. Nipane, D. Karmakar, N. Kaushik, S. Karande, and S. Lodha. Few-layer $MoS_2$ p-type devices enabled by selective doping using low energy phosphorus implantation. *ACS Nano*, 10(2):2128–2137, 2016.

[62] B. Radisavljevic, A. Radenovic, J. Brivio, V. Giacometti, and A. Kis. Single-layer $MoS_2$ transistors. *Nature Nanotechnology*, 6(3):147–150, 2011.

[63] B. N. Szafranek, D. Schall, M. Otto, D. Neumaier, and H. Kurz. High on/off ratios in bilayer graphene field effect transistors realized by surface dopants. *Nano Letters*, 11(7):2640–2643, 2011.

[64] B. Radisavljevic and A. Kis. Mobility engineering and a metal-insulator transition in monolayer $MoS_2$. *Nature Materials*, 12(9):815–820, 2013.

[65] S. Das, H.-Y. Chen, A. V. Penumatcha, and J. Appenzeller. High performance multilayer $MoS_2$ transistors with scandium contacts. *Nano Letters*, 13(1):100–105, 2013.

[66] S. Wachter, D. K. Polyushkin, O. Bethge, and T. Mueller. A microprocessor based on a two-dimensional semiconductor. *Nature Communications*, 8(1):14948, 2017.

[67] H. Tian, M. L. Chin, S. Najmaei, Q. Guo, F. Xia, H. Wang, and M. Dubey. Optoelectronic devices based on two-dimensional transition metal dichalcogenides. *Nano Research*, 9(6):1543–1560, 2016.

[68] O. Lopez-Sanchez, D. Lembke, M. Kayci, A. Radenovic, and A. Kis. Ultrasensitive photodetectors based on monolayer $MoS_2$. *Nature Nanotechnology*, 8(7):497–501, 2013.

[69] W. Zhu, T. Low, Y.-H. Lee, H. Wang, D. B. Farmer, J. Kong, F. Xia, and P. Avouris. Electronic transport and device prospects of monolayer molybdenum disulphide grown by chemical vapour deposition. *Nature Communications*, 5(1):3087, 2014.

[70] M. M. Furchi, D. K. Polyushkin, A. Pospischil, and T. Mueller. Mechanisms of photoconductivity in atomically thin $MoS_2$. *Nano Letters*, 14(11):6165–6170, 2014.

[71] A. R. Klots, A. K. M. Newaz, B. Wang, D. Prasai, H. Krzyzanowska, J. Lin, D. Caudel, N. J. Ghimire, J. Yan, B. L. Ivanov, K. A. Velizhanin, A. Burger, D. G. Mandrus, N. H. Tolk, S. T. Pantelides, and K. I. Bolotin. Probing excitonic states in suspended two-dimensional semiconductors by photocurrent spectroscopy. *Scientific Reports*, 4(1):6608, 2014.

[72] S. Tongay, J. Zhou, C. Ataca, K. Lo, T. S. Matthews, J. Li, C. Grossman, and J. Wu. Thermally driven crossover from indirect toward direct bandgap in 2D semiconductors: $MoSe_2$ versus $MoS_2$. *Nano Letters*, 12(11):5576–5580, 2012.

[73] J. P. Perdew, K. Burke, and M. Ernzerhof. Generalized gradient approximation made simple. *Phys. Rev. Lett.*, 77(18):3865–3868, 1996.

[74] A. Kormányos, V. Zólyomi, N. D. Drummond, P. Rakyta, G. Burkard, and V. I. Fal'ko. Monolayer $MoS_2$: Trigonal warping, the Γ-valley, and spin-orbit coupling effects. *Phys. Rev. B*, 88:045416, 2013.

[75] E. S. Kadantsev and P. Hawrylak. Electronic structure of a single $MoS_2$ monolayer. *Solid State Communications*, 152(10):909–913, 2012.

[76] W. Zhao, Z. Ghorannevis, L. Chu, M. Toh, C. Kloc, P.-H. Tan, and G. Eda. Evolution of electronic structure in atomically thin sheets of $WS_2$ and $WSe_2$. *ACS Nano*, 7(1):791–797, 2013.

[77] F. Zahid, L. Liu, Y. Zhu, J. Wang, and H. Guo. A generic tight-binding model for monolayer, bilayer and bulk $MoS_2$. *AIP Advances*, 3(5):052111, 2013.

[78] A. C. Dias, F. Qu, D. L. Azevedo, and J. Fu. Band structure of monolayer transition-metal dichalcogenides and topological properties of their nanoribbons: Next-nearest-neighbor hopping. *Phys. Rev. B*, 98:075202, 2018.

[79] H. Rostami, A. G. Moghaddam, and R. Asgari. Effective lattice Hamiltonian for monolayer $MoS_2$: Tailoring electronic structure with perpendicular electric and magnetic fields. *Phys. Rev. B*, 88:085440, 2013.

[80] E. Cappelluti, R. Roldan, J. A. Silva-Guillen, P. Ordejon, and F. Guinea. Tight-binding model and direct-gap/indirect-gap transition in single-layer and multi-layer $MoS_2$. *Phys. Rev. B*, 88:075409, 2013.

[81] J. Heyd, G. E. Scuseria, and M. Ernzerhof. Hybrid functionals based on a screened Coulomb potential. *Journal of Chemical Physics*, 118(18):8207–8215, 2003.

[82] H. Y. Jeong, Y. Jin, S. J. Yun, J. Zhao, J. Baik, D. H. Keum, H. S. Lee, and Y. H. Lee. Heterogeneous defect domains in single-crystalline hexagonal $WS_2$. *Advanced Materials*, 29(15):1605043, 2017.

[83] H. Fang, M. Tosun, G. Seol, T. C. Chang, K. Takei, J. Guo, and A. Javey. Degenerate n-doping of few-layer transition metal dichalcogenides by potassium. *Nano Letters*, 13(5):1991–1995, 2013.

[84] T. Komesu, D. Le, I. Tanabe, E. F. Schwier, Y. Kojima, M. Zheng, K. Taguchi, K. Miyamoto, T. Okuda, H. Iwasawa, K. Shimada, T. S. Rahman, and P. A. Dowben. Adsorbate doping of $MoS_2$ and $WSe_2$: The influence of Na and Co. *J. Phys.: Cond. Matt.*, 29(28):285501, 2017.

[85] C. Krull. *Electronic structure of metal phthalocyanines on Ag(100)*, chapter Experimental Techniques, pages 9–29. Springer International Publishing, 2014.

[86] K. T. Chan, J. B. Neaton, and M. L. Cohen. First-principles study of metal adatom adsorption on graphene. *Phys. Rev. B*, 77:235430, 2008.

[87] S. Xinxiang, Y. Guang, D. Meifeng, H. Mimura, L. Chun, and N. Mang. First principles study the effects of alkali metal and chlorine adatoms on the opposite surface of graphene. *Chemical Physics Letters*, 694:1 – 6, 2018.

[88] P. Rastogi, S. Kumar, S. Bhowmick, A. Agarwal, and Y. S. Chauhan. Ab-initio study of doping versus adsorption in monolayer $MoS_2$. *IEEE 2nd International Conference on Emerging Electronics (ICEE)*, 2014.

[89] J. Chang, S. Larentis, E. Tutus, L. F. Register, and S. K. Banerjee. Atomistic simulation of the electronic states of adatoms in monolayer $MoS_2$. *Appl. Phys. Lett.*, 104(14):141603, 2014.

[90] C. Ataca and S. Ciraci. Functionalization of single-layer $MoS_2$ honeycomb structures. *J. Phys. Chem. C*, 115(27):13303–13311, 2011.

[91] F. Corsetti, A. A. Mostofi, and J. Lischner. First-principles multiscale modelling of charged adsorbates on doped graphene. *2D Mater.*, 4(2):025070, 2017.

[92] D. Wong, F. Corsetti, Y. Wang, V. W. Brar, H. Tsai, Q. Wu, R. K. Kawakami, A. Zettl, A. A. Mostofi, J. Lischner, and M. F. Crommie. Spatially resolving density-dependent screening around a single charged atom in graphene. *Phys. Rev. B*, 95:205419, 2017.

[93] G. Henkelman, A. Arnaldsson, and H. Jónsson. A fast and robust algorithm for Bader decomposition of charge density. *Computational Materials Science*, 36(3):354–360, 2006.

[94] R. Carbo-Dorca and P. Bultinck. Quantum mechanical basis for Mulliken population analysis. *Journal of Mathematical Chemistry*, 36(3):231–239, 2004.

[95] S. Saha, R. K. Roy, and P. W. Ayers. Are the Hirshfeld and Mulliken population analysis schemes consistent with chemical intuition? *International Journal of Quantum Chemistry*, 109(9):1790–1806, 2009.

[96] S. Salehi and A. Saffarzadeh. Surface science atomic defect states in monolayers of $MoS_2$ and $WS_2$. *Surface Science*, 651:215–221, 2016.

[97] C. Varvenne, F. Bruneval, M.-C. Marinica, and E. Clouet. Point defect modeling in materials: Coupling ab initio and elasticity approaches. *Phys. Rev. B*, 88:134102, 2013.

[98] J. Lindhard. On the properties of a gas of charged particles. *Danske Matematisk-fysiske Meddeleiser*, 28(8):1–57, 1954.

[99] L. V. Keldysh. Coulomb interaction in thin semiconductor and semimetal films. *JETP Lett.*, 29:658, 1979.

[100] N. S. Rytova. Screened potential of a point charge in a thin film. *Moscow University Physics Bulletin*, 3(3):18, 1967.

[101] T. Berkelbach, M. S. Hybertsen, and D. R. Reichman. Theory of neutral and charged excitons in monolayer transition metal dichalcogenides. *Phys. Rev. B*, 88:045318, 2013.

[102] S. Ismail-Beigi. Truncation of periodic image interactions for confined systems. *Phys. Rev. B*, 73:233103, 2006.

[103] U. Roessler. *Solid State Theory: An Introduction.* Springer-Verlag Berlin Heidelberg, 2009.

[104] G. Wang, A. Chernikov, M. M. Glazov, T. F. Heinz, X. Marie, T. Amand, and B. Urbaszek. Colloquium: Excitons in atomically thin transition metal dichalcogenides. *Reviews of Modern Physics*, 90(2), 2018.

[105] T. C. Berkelbach and D. R. Reichman. Optical and excitonic properties of atomically thin transition-metal dichalcogenides. *Annual Review of Condensed Matter Physics*, 9(1):379–396, 2018.

[106] A. Splendiani, L. Sun, Y. Zhang, T. Li, J. Kim, C. Y. Chim, G. Galli, and F. Wang. Emerging photoluminescence in monolayer $MoS_2$. *Nano Letters*, 10(4):1271–1275, 2010.

[107] F. Wu, F. Qu, and A. H. MacDonald. Exciton band structure of monolayer $MoS_2$. *Phys. Rev. B*, 91:075310, 2015.

[108] P. Hohenberg and W. Kohn. Inhomogeneous electron gas. *Phys. Rev.*, 136:B864–B871, Nov 1964.

[109] W. Kohn and L. J. Sham. Self-consistent equations including exchange and correlation effects. *Phys. Rev.*, 140:A1133–A1138, 1965.

[110] Richard M. Martin. *Electronic Structure: Basic Theory and Practical Methods*. Cambridge University Press, 2004.

[111] J. P. Perdew. Generalized gradient approximations for exchange and correlation: A look backward and forward. *Physica B: Physics of Condensed Matter*, 172(1):1–6, 1991.

[112] D. R. Hamann. Optimized norm-conserving Vanderbilt pseudopotentials. *Phys. Rev. B*, 88:085117, 2013.

[113] D. Bohm and D. Pines. A collective description of electron interactions. I. magnetic interactions. *Phys. Rev.*, 82:625–634, 1951.

[114] G. F. Giuliani and G. Vignale. *Quantum Theory of the Electron Liquid*, pages 191–198. Cambridge University Press, 2005.

[115] J. Solyom. *Fundamentals of Physics in Solids: Volume III*. Springer-Verlag Berlin Heidelberg, 2010.

[116] S. L. Adler. Quantum theory of the dielectric constant in real solids. *Phys. Rev.*, 126:413–420, 1962.

[117] B. Wunsch, T. Stauber, F. Sols, and F. Guinea. Dynamical polarization of graphene at finite doping. *New Journal of Physics*, 8(12):318–318, 2006.

[118] C. Hwang, D. A. Siegel, S.-K. Mo, W. Regan, A. Ismach, Y. Zhang, A. Zettl, and A. Lanzara. Fermi velocity engineering in graphene by substrate modification. *Scientific Reports*, 2(1):590, 2012.

[119] K. V. Emtsev, A. Bostwick, K. Horn, J. Jobst, G. L. Kellogg, L. Ley, J. L. McChesney, T. Ohta, S. A. Reshanov, J. Röhrl, E. Rotenberg, A. K. Schmid, D. Waldmann, H. B. Weber, and T. Seyller. Towards wafer-size graphene layers by atmospheric pressure graphitization of silicon carbide. *Nature Materials*, 8(3):203–207, 2009.

[120] T. L. Yoon, T. L. Lim, T. K. Min, S. H. Hung, N. Jakse, and S. K. Lai. Epitaxial growth of graphene on 6H-silicon carbide substrate by simulated annealing method. *The Journal of Chemical Physics*, 139(20):204702, 2013.

[121] I. Radović, L. Hadžievski, and Z. L. Mišković. Polarization of supported graphene by slowly moving charges. *Phys. Rev. B*, 77:075428, 2008.

[122] L. Patrick and W. J. Choyke. Static dielectric constant of SiC. *Phys. Rev. B*, 2:2255–2256, 1970.

[123] O. Madelung and B. C. Taylor. *Introduction to Solid-State Theory*, pages 78–80. Springer Series in Solid-State Sciences. Springer, 1978.

[124] W. A. Harrison. Tight-binding methods. *Surface Science*, 299-300:298–310, 1994.

[125] P. Vogl, H. P. Hjalmarson, and J. D. Dow. A semi-empirical tight-binding theory of the electronic structure of semiconductors. *Journal of Physics and Chemistry of Solids*, 44(5):365–378, 1983.

[126] R. E. Allen and J. D. Dow. Unified theory of point–defect electronic states, core excitons, and intrinsic electronic states at semiconductor surfaces. *Journal of Vacuum Science and Technology*, 19(3):383–387, 1981.

[127] H. P. Hjalmarson, P. Vogl, D. J. Wolford, and J. D. Dow. Theory of substitutional deep traps in covalent semiconductors. *Phys. Rev. Lett.*, 44(12):810–813, 1980.

[128] A. Carvalho and A. H. Castro Neto. Donor and acceptor levels in semiconducting transition-metal dichalcogenides. *Phys. Rev. B*, 89:081406, 2014.

[129] N. V. Smith. Photoemission spectra and band structures of *d*-band metals. VII. Extensions of the combined interpolation scheme. *Phys. Rev. B*, 19:5019–5027, 1979.

[130] E. Ridolfi, C. H. Lewenkopf, and V. M. Pereira. Excitonic structure of the optical conductivity in $MoS_2$ monolayers. *Physical Review B*, 97(20):205409, 2018.

[131] T. Olsen, S. Latini, F. Rasmussen, and K. S. Thygesen. Simple screened hydrogen model of excitons in two-dimensional materials. *Phys. Rev. Lett.*, 116:056401, 2016.

[132] X. L. Yang, S. H. Guo, F. T. Chan, K. W. Wong, and W.-Y. Ching. Analytic solution of a two-dimensional hydrogen atom. I. Nonrelativistic theory. *Phys. Rev. A*, 43(3):1186–1196, 1991.

[133] F. Bassani, G. Iadonisi, and B. Preziosi. Band Structure and Impurity States. *Phys. Rev.*, 186:735–746, 1969.

[134] A. Kormányos, G. Burkard, M. Gmitra, J. Fabian, V. Zólyomi, N. D. Drummond, and V. Fal'ko. k·p theory for two-dimensional transition metal dichalcogenide semiconductors. *2D Materials*, 2(2):022001, 2015.

[135] H. Asahina and A. Morita. Band structure and optical properties of black phosphorus. *J. Phys. C: Solid State Phys.*, 17(11):1839–1852, 1984.

[136] J. Qiao, X. Kong, Z.-X. Hu, F. Yang, and W. Ji. High-mobility transport anisotropy and linear dichroism in few-layer black phosphorus. *Nature Communications*, 5(1):4475, 2014.

[137] S. Bagheri, N. Mansouri, and E. Aghaie. Phosphorene: A new competitor for graphene. *International Journal of Hydrogen Energy*, 41(7):4085–4095, 2016.

[138] A. Brown and S. Rundquist. Refinement of the crystal structure of black phosphorus. *Acta Crystallographica*, 19(4):684–685, 1965.

[139] A. Cupo and V. Meunier. Quantum confinement in black phosphorus-based nanostructures. *Journal of Physics: Condensed Matter*, 29(28):283001, 2017.

[140] R. Fang, X. Cui, M. A. Khan, C. Stampfl, S. P. Ringer, and R. Zheng. Strain-engineered ultrahigh mobility in phosphorene for terahertz transistors. *Advanced Electronic Materials*, 5(3):1800797, 2019.

[141] J. He, D. He, Y. Wang, Q. Cui, M. Z. Bellus, H. Y. Chiu, and H. Zhao. Exceptional and anisotropic transport properties of photocarriers in black phosphorus. *ACS Nano*, 9(6):6436–6442, 2015.

[142] G. Wang, W. J. Slough, R. Pandey, and S. P. Karna. Degradation of phosphorene in air: Understanding at atomic level. *2D Materials*, 3(2):025011, 2016.

[143] A. Favron, E. Gaufrès, F. Fossard, A. L. Phaneuf-Laheureux, N. Y. W. Tang, P. L. Lévesque, A. Loiseau, R. Leonelli, S. Francoeur, and R. Martel. Photooxidation and quantum confinement effects in exfoliated black phosphorus. *Nature Materials*, 14(8):826–832, 2015.

[144] W. Zhu, M. N. Yogeesh, S. Yang, S. H. Aldave, J. S. Kim, S. Sonde, L. Tao, N. Lu, and D. Akinwande. Flexible black phosphorus ambipolar transistors, circuits and AM demodulator. *Nano Lett.*, 15(3):1883–1890, 2015.

[145] B. Kiraly, N. Hauptmann, A. N. Rudenko, M. I. Katsnelson, and A. A. Khajetoorians. Probing single vacancies in black phosphorus at the atomic level. *Nano Letters*, 17(6):3607–3612, 2017.

[146] J. V. Riffle, C. Flynn, B. St Laurent, C. A. Ayotte, C. A. Caputo, and S. M. Hollen. Impact of vacancies on electronic properties of black phosphorus probed by STM. *Journal of Applied Physics*, 123(4):044301, 2018.

[147] J. Gaberle and A. L. Shluger. Structure and properties of intrinsic and extrinsic defects in black phosphorus. *Nanoscale*, 10(41):19536–19546, 2018.

[148] A. S. Rodin, A. Carvalho, and A. H. Castro Neto. Excitons in anisotropic two-dimensional semiconducting crystals. *Phys. Rev. B*, 90:075429, 2014.

[149] X. B. Li, P. Guo, T. F. Cao, H. Liu, W. M. Lau, and L. M. Liu. Structures, stabilities, and electronic properties of defects in monolayer black phosphorus. *Scientific Reports*, 5(1):10848, 2015.

[150] X. Sun and Z. Wang. Sodium adsorption and diffusion on monolayer black phosphorus with intrinsic defects. *Applied Surface Science*, 427:189–197, 2018.

[151] Z. Tian, Y. Gan, T. Zhang, B. Wang, H. Ji, Y. Feng, and J. Xue. Isotropic charge screening of anisotropic black phosphorus revealed by potassium adatoms. *Phys. Rev. B*, 100:085440, 2019.

[152] N. Wiser. Dielectric constant with local field effects included. *Phys. Rev.*, 129:62–69, 1963.

[153] A. N. Rudenko and M. I. Katsnelson. Quasiparticle band structure and tight-binding model for single and bilayer black phosphorus. *Phys. Rev. B*, 89:201408, 2014.

[154] A. N. Rudenko, S. Yuan, and M. I. Katsnelson. Toward a realistic description of multilayer black phosphorus: From GW approximation to large-scale tight-binding simulations. *Phys. Rev. B*, 92:085419, 2015.

[155] M. I. Katsnelson. Nonlinear screening of charge impurities in graphene. *Phys. Rev. B*, 74:201401, 2006.

# Appendix A

# Copyright Permissions

All copyrighted material adapted or otherwise used in this thesis is clearly cited.

1. LICENSE #: RNP/21/AUG/043114
    - Order Date: 08/08/2021
    - *Physical Review Letters*
    - Mak *et al.* [3]
    - Used in Fig. 2.2

2. LICENSE #: RNP/21/AUG/043115
    - Order Date: 08/08/2021
    - *Physical Review B*
    - Liu *et al.* [1]
    - Used in Fig. 2.5(b-d)

3. LICENSE #: RNP/21/AUG/043116
    - Order Date: 08/08/2021
    - *Physical Review B*
    - Qiu *et al.* [10]
    - Used in Fig. 2.9

4. LICENSE #: RNP/21/AUG/043117
    - Order Date: 08/08/2021
    - *Physical Review B*
    - Yilei Li *et al.* [11]
    - Used in Fig. 2.10

5. LICENSE #: RNP/21/AUG/043118
    - Order Date: 08/08/2021
    - *Physical Review Letters*
    - Qiu *et al.* [12]
    - Used in Fig. 2.11

6. LICENSE #: RNP/21/AUG/043119
    - Order Date: 08/08/2021
    - *Physical Review B*
    - Aghajanian *et al.* [2]
    - Used in Fig. 5.3, Fig. 5.4, Fig. 5.6 and Fig. 5.7

7. LICENSE #: RNP/21/AUG/043121
    - Order Date: 08/08/2021
    - *Physical Review B*
    - Rudenko *et al.* [154]
    - Used in Fig. 6.2(a)

8. LICENSE #: RNP/21/AUG/043122
    - Order Date: 08/08/2021
    - *Physical Review B*
    - Han *et al.* [19]
    - Used in Fig. 6.2(c, d)

9. LICENSE #: 1139125-1
    - Order Date: 08/08/2021
    - *Journal of Physics: Condensed Matter*
    - Ridolfi *et al.* [6]
    - Used in Fig. 2.5(a)

10. LICENSE #: 1139123-1
    - Order Date: 08/08/2021
    - *Chemical Society Reviews*
    - Liu *et al.* [5]
    - Used in Fig. 2.4

11. LICENSE #: 5124291236026
    - Order Date: 08/08/2021
    - *Nature Technology*
    - Zhang *et al.* [4]
    - Used in Fig. 2.3